Doctoral Thesis

Thermal and Mechanical Properties of High Burnup Oxide Fuels
(高燃焼度酸化物燃料の熱物性・機械的特性に関する基礎研究)

Ken Kurosaki

Department of Nuclear Engineering,
Graduate School of Engineering,
Osaka University

2003

Doctoral Thesis

Thermal and Mechanical Properties of High Burnup Oxide Fuels
(高燃焼度酸化物燃料の熱物性・機械的特性に関する基礎研究)

Ken Kurosaki

Department of Nuclear Engineering,
Graduate School of Engineering,
Osaka University

2003

Table of Contents

Chapter 1
General Introduction

1. General Introduction

The trend of an oxide nuclear fuel development is to extend the burnup for the economic and environmental reason. It is required to reduce the cost performance of the fuel production and to reduce the volume of the spent fuel. Today, the maximum burnups of the oxide nuclear fuel for the fuel assembly are 55 GWd/t in BWR fuel and 48 (partly 55) GWd/t in PWR fuel, respectively. At the following stage, it is expected that the burnups may be applied to 65 GWd/t in BWR and 60 GWd/t in PWR, respectively.

In order to propel this high burnup program, it is important to understand the thermal and mechanical properties of the fuel at the high burnup conditions, which is affected by the fission product (FP) and transuranium (TRU) elements. Especially, a large amount of FP elements that is generated under irradiation changes the composition, phase relation, and physical properties of the fuel. In particular, the thermal and mechanical properties of the fuel pellet such as the thermal conductivity and elastic modulus are very important. For example, the thermal conductivity controls the fuel operating temperature, and therefore it influences very important processes such as the gas release, swelling, and grain growth, and it also limits the linear power. On the other hand, the knowledge of the elastic modulus and hardness of the fuel pellet is absolutely essential for the pellet-cladding interaction (PCI).

The previous studies reveal that three kinds of solid state FP elements are formed in the irradiated oxide nuclear fuels [1]:

(1) Oxides dissolved in the fuel matrix: Y, La, Ce, Nd, Mo, Zr, etc.,

(2) Oxides precipitated in the fuel: Ba, Sr, Zr, Mo, etc.,

(2) Metals precipitated in the fuel: Mo, Ru, Rh, Pd, Tc, etc.,

In the matrix phase, the actinide and rare earth elements are incorporated as solid solutions. Some amounts of Sr, Ba, and Zr are also soluble in this phase. The majority of BaO and SrO appears to the oxide precipitates as a perovskite type oxide with the chemical form of $(Ba,Sr)ZrO_3$, in which a minor amount of rare earth elements, Mo, U, and Pu would be soluble [2]. The formation of the metallic precipitates seems to be considerably complex. The metallic precipitates produced in the fuel are mixture of two or more phases, which mainly consist of Mo, Tc, Ru, Rh, and Pd. The composition of the phase is changed by the circumstance in the fuel pellet, especially the oxygen potential. The oxygen potential of the fuel, characterized by the oxygen-to-metal (O/M) ratio, is important factor, because it determines the chemical behavior of the fuel during the operation.

The gray oxide phase with a perovskite type structure, $(Ba,Sr)(U,Pu,Zr,RE,Mo)O_3$ and white metallic inclusions composed of Mo, Ru, Rh, and Pd have been observed in the irradiated oxide fuels [1,3]. The SEM images of the high burn up oxide fuels and metallic inclusion are shown in Figs. 1 and 2 [4,5], and the compositions of the oxide and metallic inclusions

determined by a post irradiation examination (PIE) are shown in Figs. 3 and 4 [1,4-7], respectively. Although the thermodynamic properties and phase equilibria of the high burnup oxide fuel have been studied until now, the thermal and mechanical properties such as the thermal conductivity and elastic modulus have been scarcely studied. Therefore, in the present study, the effects of the solid state FP elements on the thermal and mechanical properties of the high burnup oxide fuels are systematically studied.

In Chapter 2, the simulated fuel materials have been prepared and their thermal and mechanical properties have been measured.

A simulated high burnup UO_2 based fuel (SIMFUEL) has been prepared and their thermal and mechanical properties have been studied. The effect of the annealing oxygen potentials on the phase equilibria of the SIMFUEL has been evaluated. The effects of the burnup and annealing oxygen potential on the properties of the SIMFUEL have also been studied (Chapter 2.1).

The thermophysical properties of the oxide and metallic inclusions have been studied. The perovskite type oxides, $BaUO_3$, $BaZrO_3$, $BaCeO_3$, and $BaMoO_3$ have been prepared and their thermal and mechanical properties have been measured. For the simulated materials of the metallic precipitates, the alloys composed of Mo, Ru, Rh, and Pd have been prepared and their thermal conductivity and mechanical properties have been measured (Chapter 2.2).

In order to obtain the nanoscale mechanical properties such as the reduced modulus and nanohardness of the oxide nuclear fuels, the nanoindentation tests have been performed. The nanoscale mechanical properties of the single crystal UO_2, single crystal UO_2 (111) plane, polycrystalline UO_2, $(U,Ce)O_2$, and $BaUO_3$ have been evaluated. The nanoindentation tests have also been performed for the SIMFUEL (Chapter 2.3).

In Chapter 3, the characteristics of the oxide nuclear fuels have been evaluated by the computer simulations.

The compositions and phase equilibria of the high burnup oxide fuel have been evaluated. An ORIGEN-2 code has been used to calculate the FP inventories. The thermodynamic equilibrium calculation has been performed by using ChemSage program to evaluate the phase equilibria of the high burnup oxide fuels (Chapter 3.1).

In order to evaluate the thermal and mechanical properties of the oxide fuel more efficiently, it is necessary to develop a new technique to evaluate the properties of the fuel. In Chapter 3.2, the molecular dynamics (MD) calculations have been performed to UO_2, PuO_2, $(U,Pu)O_2$ solid solution, and the perovskite type oxides. The applicability of the MD method to evaluation of the thermal and mechanical properties of the oxide nuclear fuels has been studied.

In order to understand the phase equilibria of the high burnup oxide fuels, the phase diagram of O-Pu-U ternary system is very important. In Chapter 3.3, the thermodynamic

modelling has been carried out for the O-Pu-U ternary system. The possible ternary phase diagrams for the O-Pu-U system have been calculated.

The thermal and mechanical properties modeling of the high burnup oxide fuels have been carried out by using a finite elements method (FEM). The quantitative discussion about the effect of the inclusions on the thermal conductivity and Young's modulus of the fuel pellet has been performed.

In Chapter 4, the present study has been summarized.

References

[1] H. Kleykamp, J. Nucl. Mater., 131 (1985) 221.

[2] C. Sari, C.T. Walker, and G. Schumacher, J. Nucl. Mater., 79 (1979) 255.

[3] H. Kleykamp, Nucl. Technol., 80 (1988) 412.

[4] I. Sato, H. Furuya, T. Arima, K. Idemitsu, and K. Yamamoto, J. Nucl. Sci. Technol., 36 (1999) 775.

[5] I. Sato, H. Furuya, T. Arima, K. Idemitsu, and K. Yamamoto, J. Nucl. Mater., 273 (1999) 239.

[6] H. Kleykamp, J.O. Paschoal, R. Pejsa, and F. Thummler, J. Nucl. Mater., 130 (1985) 426.

[7] J.O.A. Paschoal, Kernforschungszentrum Karlsruhe, report KfK-3473 (1983).

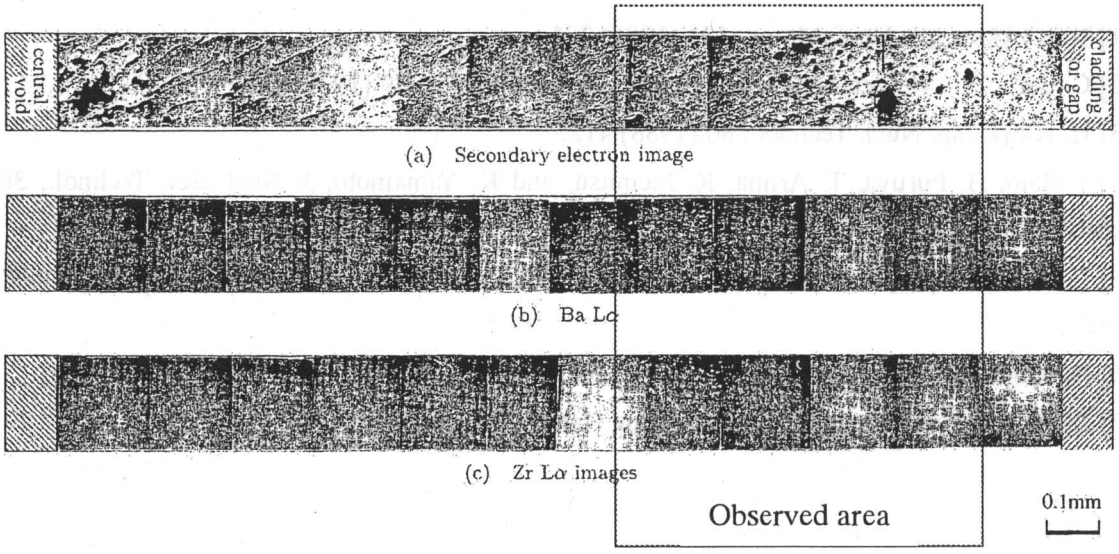

Figure 1. SEM image and EDX analysis of high burnup oxide fuel (13.3 at.%-burnup) [4]. The oxide precipitates composed of mainly Ba and Zr have been observed in the high burnup oxide fuel.

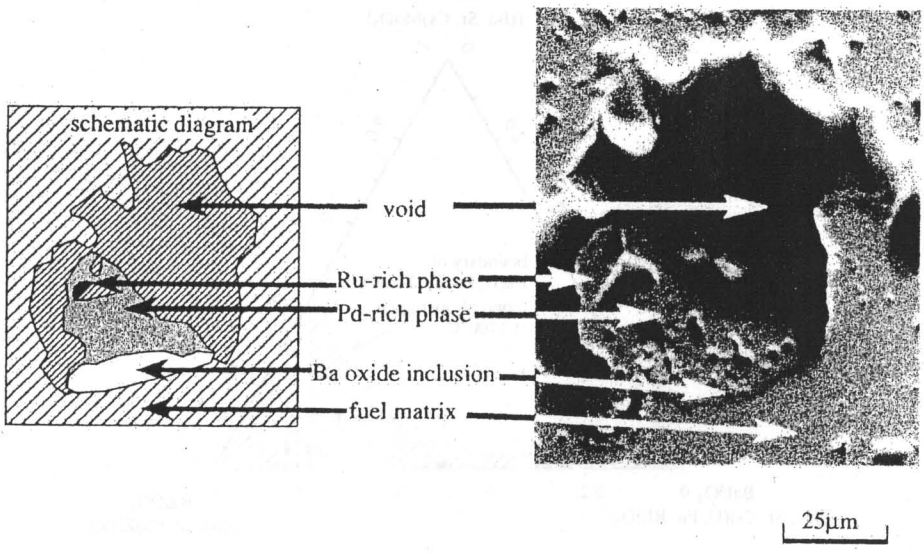

Figure 2. A metallic inclusion composed of mainly Mo, Ru, and Pd observed at the periphery region of high burnup oxide fuel (9.6 at.%-burnup) [5].

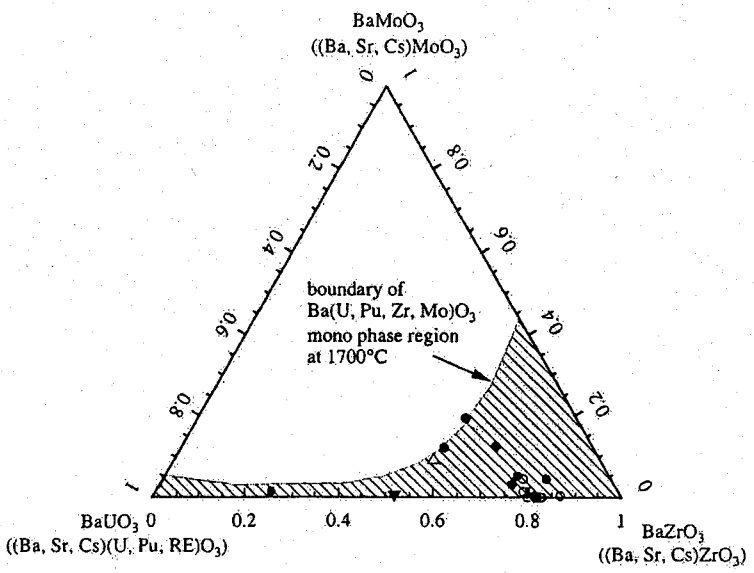

Figure 3. Compositions of the perovskite type oxides precipitated in irradiated oxide fuels projected onto the $BaUO_3$-$BaZrO_3$-$BaMoO_3$ isothermal section at 1973 K [1,4-7].

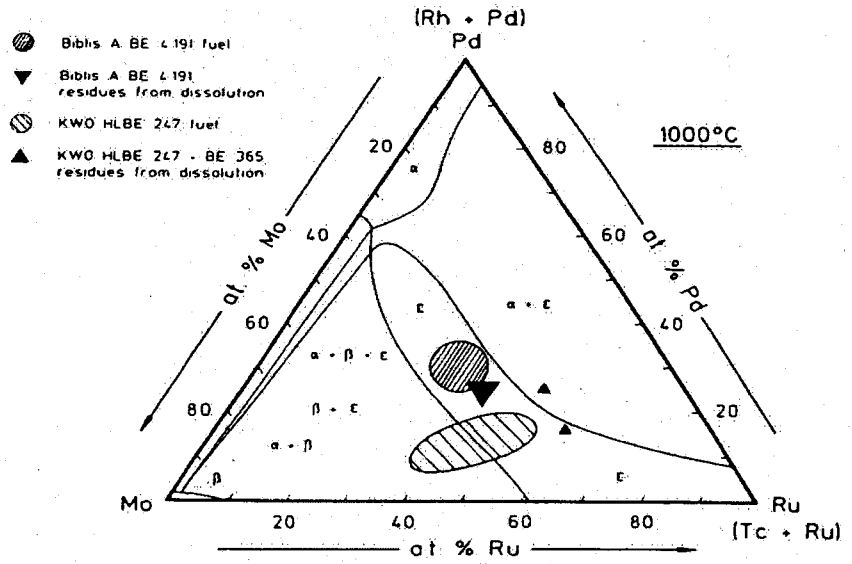

Figure 4. Compositions of the metallic Mo-Tc-Ru-Rh-Pd precipitates in irradiated oxide fuels, projected onto the Mo-(Tc+Ru)-(Rh+Pd) isothermal section at 1273 K [1].

Chapter 2

Preparation of Simulated Fuel Materials and Their Properties

2.1. Simulated High Burnup Oxide Fuel (SIMFUEL)

2.1.1. Introduction of SIMFUEL

In order to evaluate the fuel safety and performance, it is very important to understand the behavior of fission product (FP) and transuranium (TRU) elements in an irradiated oxide nuclear fuel, because the physical and chemical properties of the fuel are affected by the FP and TRU elements. In particular, the thermal conductivity is one of the very important properties, because it controls the fuel operating temperature, and therefore it influences on very important processes such as the gas release, swelling, and grain grows, and limits the linear power. On the other hand, in terms of the pellet-cladding interaction (PCI), the knowledge of the elastic modulus and hardness of the fuel is very important.

In case of the simple system composed of UO_2 and one kind of FP element, it is easy to estimate or examine what kinds of phase and compound exist under the specified temperature and oxygen potential. However, in the irradiated nuclear fuel, there are 30-40 kinds of FP elements, and their amounts and the oxygen potential of the fuel are changed with the burnup. The chemical composition and phase relation of the irradiated fuel are changed by the FP elements as shown in Fig. 1.

Post irradiation examinations (PIE) by using the real irradiated fuels provide important data on the thermodynamics and chemistry of the FP elements at high burnups. However, the practical difficulties such as the radioactivity of the fuel have limited the propellant of these studies. In addition, a high cost performance is required to carry out the PIE.

The SIMFUEL has an advantage to study high burnup effects on the irradiated fuel. The SIMFUEL provides a convenient way to study the thermal and mechanical properties of the irradiated fuels. The SIMFUEL is a material that replicates the chemical states and phase relation of the high burnup oxide fuels. The effect of the gaseous FP elements and radiation damages are not simulated by the SIMFUEL. By using the SIMFUEL, we can evaluate the effect of the FP elements to the physical and chemical properties of the fuel in the laboratory, without the complication of the intense radiation fields.

The SIMFUEL has been studied since 1962 [1], the aim of this first study being to perform dry-reprocessing and re-fabrication experiments. Previous investigations on the SIMFUEL have examined the matrix and precipitated phases [2-4], the effect of the oxygen potential on the crystalline structure [5], and the thermal conductivity [6], etc. Recently, Lucuta et al. [6] and Matzke et al. [7] have studied the effect of the FP elements to the thermophysical and -chemical properties of the fuel by using the SIMFUEL with equivalent simulated burnups of 3 at.% (corresponding to 28 GWd/t) and 8 at.% (corresponding to 75 GWd/t).

In the present study, in order to evaluate the effect of the solid state FP elements on the thermal and mechanical properties of the irradiated fuel, the SIMFUEL has been prepared and

its various properties have been studied.

References

[1] S. Strasberg and T.E. Luebben, Multicycle Reprocessing and Refabrication Experiments on Simulated UO_2-Fissia Pellets, US report, Atomics International-Division of North American Aviation, Inc., NAA-SR-7138 (1962).

[2] T. Muromura, T. Adachi, H. Takeishi, Z. Yoshida, T. Yamamoto, and K. Ueno, J. Nucl. Mater., 151 (1988) 318.

[3] T. Adachi, T. Muromura, H. Takeishi, and T. Yamamoto, J. Nucl. Mater., 160 (1988) 81.

[4] P.G. Lucuta, R.A. Verral, Hj. Matzke, and B.J. Palmer, J. Nucl. Mater., 178 (1991) 48.

[5] K. Une and M. Oguma, J. Nucl. Sci. Technol., 20 (1983) 844.

[6] P.G. Lucuta, Hj. Matzke, and R.A. Verral, J. Nucl. Mater., 223 (1995) 51.

[7] Hj. Matzke, P.G. Lucuta, R.A. Verrall, and J. Henderson, J. Nucl. Mater., 247 (1997) 121.

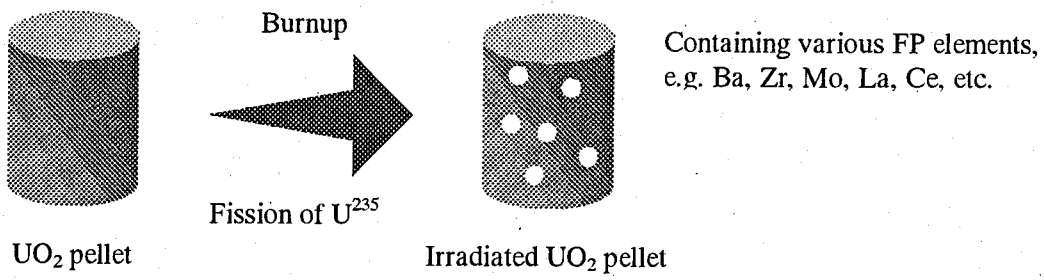

Figure 1. Irradiation of UO_2 fuel pellet.

2.1.2. Preparation and Phase Equilibria of SIMFUEL

In this section, the SIMFUEL with simulated burnups of 50, 100, and 150 GWd/t were prepared. The composition of the SIMFUEL was determined. The phase equilibria of the SIMFUEL were studied by an X-ray diffraction and SEM/EDX analysis, and the results were compared with the results of the thermodynamic equilibrium calculation performed in Chapter 3.1. The effect of the oxygen potential on the phase equilibria of the SIMFUEL was also studied.

2.1.2.1. Experimental

The composition of the SIMFUEL was determined by using ORIGEN-2 code [1]. The compositions of the SIMFUEL with simulated burnups of 50, 100, and 150 GWd/t are shown in Table 1. Appropriate amounts of high-purity oxides of the representative elements listed in Table 2 were mechanically mixed with UO_2 powder and calcined at 2023 K. The SIMFUEL powder thus obtained was pressed into a pellet under a uniaxial pressure. The pellet was sintered in a reducing atmosphere at 2023 K. Note that the starting materials were mixed as oxides except for Ba that was mixed as a carbonic acid salt ($BaCO_3$). In order to evaluate the effect of the oxygen potential on the phase equilibria of the SIMFUEL, the samples were annealed at 1400 K (40 hours), under three kinds of oxygen potentials (-390, -340, and -220 kJ/mol). Various oxygen potentials were obtained by using a dissociative reaction of H_2O and H_2, which is continuously measured by a solid ZrO_2 electrolyte oxygen sensor. The annealing conditions of the oxygen potential are summarized in Table 3. The UO_2 pellet, which does not contain the FP elements, was also annealed at same conditions for comparison.

The phase identification of the SIMFUEL was carried out by a powder X-ray diffraction method using a Cu-Kα radiation at room temperature. The lattice parameter, a, of the cubic matrix phase was determined from the diffraction patterns.

The total oxygen content in the SIMFUEL was measured by using an oxygen and nitrogen analyzer (EMGA-550, HORIBA Co. ltd.). In this apparatus, a sample wrapped with a nickel capsule is heated above 3000 K, and the amount of infrared absorption of the oxygen in the form of CO is determined.

In order to determine the compositions of each phase in the SIMFUEL, the surface observation and elemental analysis were performed using a scanning electron microscope, SEM (S-2600H, HITACHI Ltd.) and an energy dispersive X-ray microanalyzer, EDX (EX-200, HORIBA Ltd.).

2.1.2.2. Results and Discussion

Figure 1 (a)-(c) show the X-ray diffraction patterns of the SIMFUEL for certain

burnups under three kinds of annealing conditions. For comparison, the X-ray diffraction patterns of UO_2, $BaZrO_3$, $BaMoO_4$, and $Mo_{0.34}Ru_{0.32}Rh_{0.08}Pd_{0.26}$ (ε-phase) are shown in Fig. 1 (d). There are some peaks corresponding to the matrix phase (fluorite type structure) and oxide precipitates in all the SIMFUEL samples. It is considered that the oxide precipitates form a perovskite-type oxide structure expressed as the chemical formula of $BaMO_3$ (M: U, Zr, Mo) at the annealing oxygen potentials of -390 and -340 and a scheelite-type oxide structure expressed as the chemical formula of $BaMO_4$ (M: U, Mo) at the annealing oxygen potentials of -220 kJ/mol. The metallic precipitates considered being the ε-phase is clearly observed in the SIMFUEL annealed under the oxygen potentials of -390 and -340 kJ/mol.

The lattice parameters of UO_{2+x} and the matrix phase of the SIMFUEL are shown in Table 4. Figure 2 shows the lattice parameter of the samples annealed under the various oxygen potentials as a function of burnups. In this figure, the curves (1)-(3) show the reported lattice parameters of the SIMFUEL (burnup: 5-30 %FIMA) [2] and the curve (4) shows the empirical equation (Δa= -0.07 pm per percent burnup) from the results of the irradiated UO_2 fuel up to 8 % burnup [3]. The lattice parameter of the oxide fuel with the fluorite type structure is known to be affected by; (a) O/M ratio, (b) dissolution of solid state FP elements, and (c) accumulation of radiation damages. In general, the lowering in O/M ratio and the accumulation of radiation defects increase the lattice parameter, while dissolution of soluble FP elements decreases it. The lattice parameters of the matrix phase of the SIMFUEL with simulated burnups of 50, 100, and 150 GWd/t linearly decrease from 0.5470 nm (corresponds to UO_2) with increasing burnup. Concerning the effect of the annealing oxygen potential, the lattice parameter slightly decreases as the oxygen potential increases. This would be predominantly due to the formation of higher valency ions with smaller ionic radii under the high oxygen potentials. The lattice parameter of the matrix phase of the SIMFUEL decreases with increasing both the burnup and annealing oxygen potential, which corresponds to literature data. However, the absolute values of the lattice parameter measured in the present study are slightly higher than those in literatures. This is due to the difference of the dissolved FP elements and their fraction in the SIMFUEL.

Assuming that the matrix phase and precipitates of the SIMFUEL exist as shown in Table 5, the amounts of the dissolved FP elements in the matrix phase of the SIMFUEL with simulated burnups of 50, 100, and 150 GWd/t annealed under the oxygen potentials of -390 kJ/mol are estimated to be about 4, 7.5, and 11.0 mol%, respectively. Figure 3 shows the comparison of the lattice parameters between the matrix phase of the SIMFUEL annealed under the oxygen potential of -390 kJ/mol and $(U,Ce)O_2$ solid solution [4,5]. For the matrix phase of the SIMFUEL, the lattice parameter is shown as a function of the simulated burnup (lower horizontal axis), while for $(U,Ce)O_2$ that is shown as a function of the CeO_2 content (upper horizontal axis). In this figure, the upper horizontal axis roughly corresponds to the lower

horizontal axis. The lattice parameter of the matrix phase of the SIMFUEL annealed under the oxygen potential of -390 kJ/mol shows good agreement with that of $(U,Ce)O_2$ when the amount of the dissolved FP elements is transposed to the amount of Ce.

Table 6 shows the densities of UO_{2+x} and SIMFUEL pellets after the annealing procedure. The bulk densities of the samples were calculated from the measured weight and dimensions. Assuming that all the FP elements in the SIMFUEL are composed with the fluorite structure, the theoretical densities of these samples are estimated by the following equation:

$$\rho_{th} = \frac{zM}{a^3 N_A}, \quad (1)$$

where z is the molecular number in the unit cell (= 4), M is the molecular weight, a is the lattice parameter, and N_A is the Avogadro constant. The measured bulk densities of the UO_{2+x} and SIMFUEL are around 83-84 %TD and 90-94 %TD, respectively.

Figure 4 shows the relationship between the oxygen potential of UO_{2+x} and the oxygen-to-metal (O/M) ratio. The O/U ratios of UO_{2+x} annealed under the oxygen potentials of -390, -340, and -220 kJ/mol at 1400 K are 2.00, 2.002, and 2.03, respectively.

The O/M ratio of the matrix phase of the SIMFUEL was determined based on the results of the thermodynamic equilibrium calculation performed in Chapter 3.1. The O/M ratio of the matrix phase is calculated using the following equation:

$$\left(\frac{O}{M}\right)_{matrix} = \frac{\%M_{total} - \%M_{oxide\ precipitate} - \%M_{metallic\ precipitate}}{1 - M_{oxide\ precipitate} - M_{metallic\ precipitate}}, \quad (2)$$

where M_x is the molecular weight of the precipitated phase x. In the present study, the samples annealed at the oxygen potentials of -390 and -340 kJ/mol are assumed to have the oxide precipitates formed $Ba(U_{0.5}Zr_{0.5})O_3$ with all amounts of Ba and the metallic precipitates formed Mo-Ru-Rh-Pd alloy with all amounts of Mo, Ru, Rh, and Pd. All amounts of Y, La, Ce, Nd, and remained Zr are assumed to exist in the matrix phase. Table 7 shows the calculated results of the O/M ratio of the matrix phase.

The SEM image and results of the EDX analysis of the matrix phase, oxide precipitates, and metallic precipitates observed in the SIMFUEL surface with simulated burnup of 50 GWd/t annealed at the oxygen potentials of -390 and -220 kJ/mol are shown in Figs. 5, 6, and 7.

A large part of the matrix phase is UO_2 and the small amount of additional elements, Nd, Ce, La, etc. is fully or partially dissolved in the matrix phase as shown in Fig. 5.

It is confirmed that the oxide precipitates annealed at the oxygen potential of -390 kJ/mol is mainly consisted of Ba, U, Zr, and Mo. On the other hand, the oxide precipitates annealed at the oxygen potential of -220 kJ/mol is mainly consisted of Ba, Mo, and U. Based on

the results of the X-ray diffraction analysis, they correspond to the $BaMO_3$ (M: U, Zr, Mo) and $BaMO_4$ (M: Mo, U), respectively.

The average compositions of the perovskite-type oxide precipitates annealed at the oxygen potential of -390 kJ/mol are graphically presented in Fig. 8, together with the result of the thermodynamic equilibrium calculation (Burnup: 100 GWd/t) performed in Chapter 3.1. In this figure, the effect of the burnup on the composition of the oxide precipitates is not clearly observed. The fraction of $BaMoO_3$ in the oxide precipitates is about 10 %, irrespective of the burnups. Figure 9 shows the compositions of the (Ba,Sr,Cs)([U,Pu,RE],Zr,Mo)O_3 precipitates observed in irradiated HTR and FBR fuels projected onto the isothermal section of the pseudo-ternary $BaUO_3$-$BaZrO_3$-$BaMoO_3$ system at 1973 K [6-9]. It is confirmed that the compositions of the perovskite-type oxide precipitates obtained in the present study are located within the cubic mono-phase region of the pseudo-ternary $BaUO_3$-$BaZrO_3$-$BaMoO_3$ section.

The Scheelite-type oxide precipitates would be caused by the oxidation of Mo in the perovskite-type oxide precipitates. The MoO_3 thus produced would react BaO in UO_2 and/or in the perovskite-type oxide precipitates, and the scheelite-type oxide precipitates will be produced. The reaction may be expressed as:

$$BaMoO_{3(Perovskite)} + \frac{1}{2}O_2 \rightarrow BaMoO_{4(Scheelite)}. \quad (3)$$

As a first approximation, the oxygen potential of the reaction is obtained as follows [2]:

$$\Delta G(O_2)(kJ/mol) = -302 + 0.0656T. \quad (4)$$

From above equation, it is suggested that the scheelite-type oxide precipitates would be formed instead of the perovskite-type oxide precipitates under the oxygen potential above -210 kJ/mol at 1400 K, which is slightly higher than the present experimental condition.

The metallic precipitates observed in the SIMFUEL annealed at the oxygen potentials of -390 and -220 kJ/mol are mainly composed of Mo, Ru, Rh, and Pd, as shown in Fig 7. Figure 10 shows the average compositions of the metallic precipitates in the SIMFUEL annealed at the oxygen potentials of (a): -390 kJ/mol and (b): -220 kJ/mol, together with the result of the thermodynamic equilibrium calculation (Burnup: 100 GWd/t) performed in Chapter 3.1. The Mo concentration in the metallic precipitates is clearly affected by the annealing oxygen potential. The Mo concentration decreases with increasing oxygen potential, which is due to the oxidation of Mo in the metallic precipitates. These experimental results show good agreement with the results of the thermodynamic equilibrium calculation. Figure 11 shows the compositions of the metallic precipitates with the chemical form of Mo-Tc-Ru-Rh-Pd alloy in irradiated LWR fuels, which is projected onto the isothermal section of the ternary Mo-Ru-Pd system at 1273 K [10]. The metallic precipitates observed in the SIMFUEL annealed at the oxygen potential of -390 kJ/mol are located in around the ε-phase in consideration of

experimental error. It has been reported by many workers that this phase is a Ru-based alloy, and its main components are Ru, Mo, Tc, and Pd [9]. Assuming that the oxygen potential in LWR is about -400 kJ/mol, this experimental result is valid considerably.

2.1.2.4. Conclusion

The phase equilibria of the SIMFUEL annealed at three kinds of oxygen potential have been studied by using the X-ray diffraction analysis, SEM observation, EDX analysis, and oxygen chemical analysis. The behavior of the FP elements in the SIMFUEL well agrees with the results of the thermodynamic calculation. The lattice parameter of the matrix phase linearly decreases from 0.5470 nm (corresponds to UO_2) with increasing both the burnup and oxygen potential, which corresponds to literature data. The O/U ratios of UO_{2+x} annealed under the oxygen potentials of -390, -340 and -220 kJ/mol at 1400 K are 2.00, 2.002, and 2.03, respectively. The chemical compositions of the oxide and metallic inclusions measured in the present study almost correspond to the PIE results.

References

[1] M.J. Bell, ORIGEN-2 Code, Oak Ridge National Laboratories, Report ORNL-TM4397 (1973).

[2] T. Muromura, T. Adachi, H. Takeishi, Z. Yoshida, T. Yamamoto, and K. Ueno, J. Nucl. Mater., 151 (1988) 318.

[3] K. Une, K. Nogita, S. Kashibe, and M. Imamura, J. Nucl. Mater., 188 (1992) 65.

[4] K. Yamada, S. Yamanaka, T. Nakagawa, M. Uno, and M. Katsura, J. Nucl Mater., 247 (1997) 289.

[5] T.L. Markin, R.S. Street, and J. Inorg, Nucl. Chem., 32 (1970) 59.

[6] H. Kleykamp, J.O. Paschoal, R. Pejsa, and F. Thummler, J. Nucl. Mater., 130 (1985) 426.

[7] I. Sato, H. Furuya, T. Arima, K. Idemitsu, and K. Yamamoto, J. Nucl. Sci. Technol., 36 (1999) 775.

[8] J.O.A. Paschoal, Kernforschungszentrum Karlsruhe, report KfK-3473 (1983).

[9] H. Kleykamp, J. Nucl. Mater., 131 (1985) 221.

[10] H. Kleykamp, J. Nucl. Mater., 167 (1989) 49.

Table 1

Compositions of the SIMFUEL (6.2 wt.%-U235) calculated by ORIGEN2-code

6.2 wt.%-U235	Burmp 50.0 GWd/tM 5.24 at.%		100.0 GWd/tM 10.46 at.%		150.0 GWd/tM 15.47 at.%	
Representative elements	mol%	wt.%	mol%	wt.%	mol%	wt.%
U (+Pu)	92.48	96.20	85.428	92.34	78.90	88.48
Ba (+Sr)	0.762	0.457	1.363	0.850	1.944	1.257
Zr (+Nb)	1.430	0.570	2.427	1.005	3.227	1.387
Mo (+Tc)	1.456	0.611	2.653	1.156	3.655	1.652
Ru	0.723	0.320	1.679	0.771	2.688	1.280
Rh	0.127	0.057	0.146	0.068	0.140	0.068
Pd	0.303	0.141	1.130	0.546	2.108	1.057
Y	0.208	0.081	0.319	0.129	0.392	0.164
La (+Am, Cm)	0.325	0.197	0.726	0.458	1.147	0.751
Ce (+Np)	0.747	0.457	1.348	0.858	1.797	1.186
Nd (+other REs)	1.436	0.905	2.779	1.820	3.998	2.716
TOTAL	100.00	100.00	100.00	100.00	100.00	100.00

Table 2

Representative elements and their belonging groups

Groups	Representative elements
Ba+Sr	Ba
Zr+Nb	Zr
Mo+Tc	Mo
Ru	Ru
Rh	Rh
Pd	Pd
Y	Y
La+Am+Cm	La
Ce+Np	Ce
Nd+other REs.	Nd

Table 3

Annealing conditions of UO_{2+x} and the SIMFUEL

Oxygen potential (kJ/mol)	Estimated O/M ratio	Preparation conditions		
		Gas mixture	Temperature (K)	Annealing time (h)
-390	2.000	Ar-7 %H_2-H_2O (Dew point: 278 K)	1400	18
-340	2.003	Ar-3 %H_2-H_2O (Dew point: 298 K)	1400	18
-220	2.030	Ar-H_2O (Dew point: 278 K)	1400	18

Table 4

Lattice parameters (nm) of UO_{2+x} and the SIMFUEL (matrix phase)

Oxygen potentials (kJ/mol)	UO_2	Simulated burnups		
		50 GWd/t	100 GWd/t	150 GWd/t
-390	0.54725	0.54691	0.54664	0.54639
-340	0.54714	0.54697	0.54650	0.54622
-220	0.54727	0.54685	0.54650	0.54600

Table 5

Compositions of the SIMFUEL at various oxygen potentials based on the results of the thermodynamic equilibrium calculation performed in Chapter 3.1.

Representative elements	Oxygen potentials (kJ/mol)	
	-220	-340 and -390
U	MO_2, $BaUO_4$	MO_2, $Ba(U_{0.5}Zr_{0.5})O_3$
Zr	MO_2	MO_2, $Ba(U_{0.5}Zr_{0.5})rO_3$
Y		MO_2
La		
Ce		
Nd		
Ba	$Ba(Mo_{0.95}U_{0.5})O_4$	$Ba(U_{0.5}Zr_{0.5})O_3$
Mo	$BaMoO_4$, MoO_2	Mo-Ru-Rh-Pd alloy
Ru	Ru-Rh-Pd alloy	
Rh		
Pd		

Table 6

Bulk densities (g/cm^3) of UO_{2+x} and the SIMFUEL

Oxygen potentials (kJ/mol)	UO_2	Simulated burnups		
		50 GWd/t	100 GWd/t	150 GWd/t
-390	9.23 (84.3 %T.D.)	9.58 (91.0 %T.D.)	8.91 (87.9 %T.D.)	8.58 (87.7 %T.D.)
-340	-	9.57 (90.9 %T.D.)	9.27 (91.3 %T.D.)	9.09 (92.8 %T.D.)
-220	9.12 (83.2 %T.D.)	9.76 (92.5 %T.D.)	9.14 (89.9 %T.D.)	9.05 (92.1 %T.D.)

Table 7

O/M ratio of the matrix phase in UO_{2+x} and the SIMFUEL

Oxygen potentials		Simulated burnups		
(kJ/mol)	UO_2	50 GWd/t	100 GWd/t	150 GWd/t
-390	2.001	2.000	2.000	2.001
-340	2.003	2.004	2.001	2.002
-220	2.029	2.027	2.027	2.028

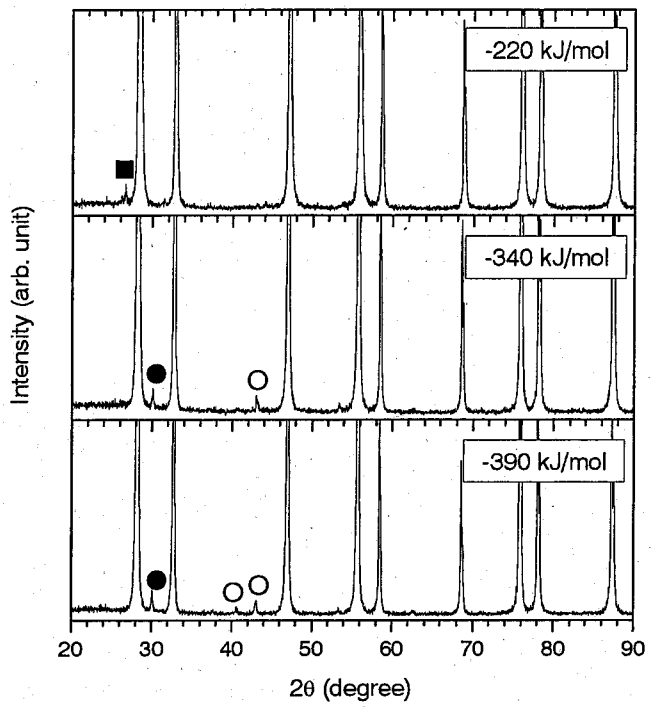

Figure 1 (a). X-ray diffraction patterns of the SIMFUEL with simulated burnup of 50 GWd/t. (The open circle, solid circle, and solid square represent Mo-Me (Me: Ru, Rh, Pd) alloy, $BaMO_3$ (M: U, Zr, Mo), and $BaMoO_4$ (M: U, Mo), respectively.)

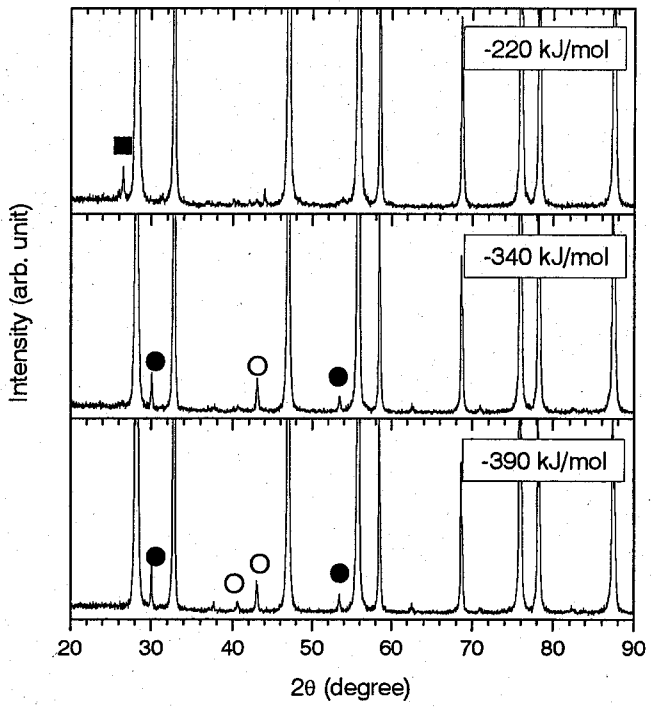

Figure 1 (b). X-ray diffraction patterns of the SIMFUEL with simulated burnup of 100 GWd/t. (The open circle, solid circle, and solid square represent Mo-Me (Me: Ru, Rh, Pd) alloy, $BaMO_3$ (M: U, Zr, Mo), and $BaMoO_4$ (M: U, Mo), respectively.)

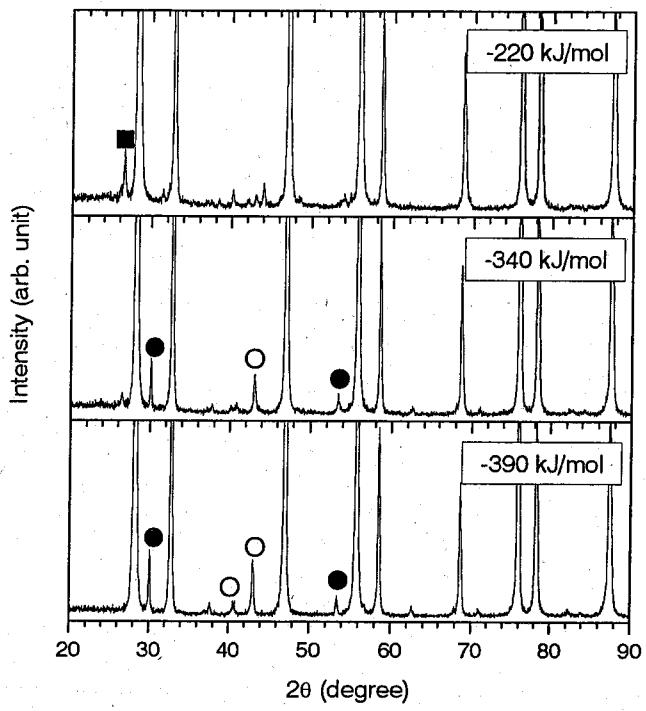

Figure 1 (c). X-ray diffraction patterns of the SIMFUEL with simulated burnup of 150 GWd/t. (The open circle, solid circle, and solid square represent Mo-Me (Me: Ru, Rh, Pd) alloy, $BaMO_3$ (M: U, Zr, Mo), and $BaMoO_4$ (M: U, Mo), respectively.)

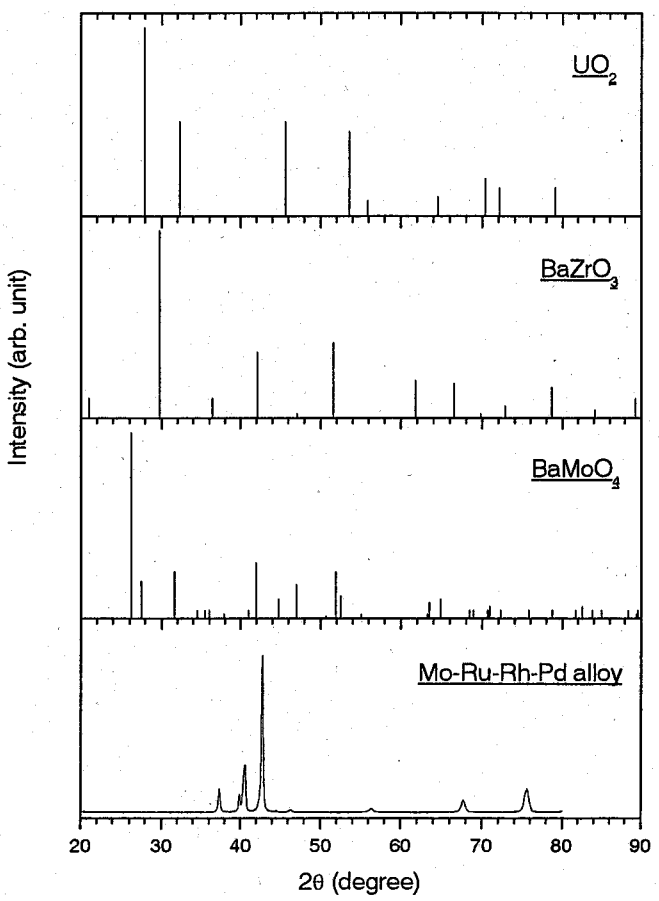

Figure 1 (d). X-ray diffraction patterns of UO_2, $BaZrO_3$, $BaMoO_4$, and Mo-Ru-Rh-Pd alloy.

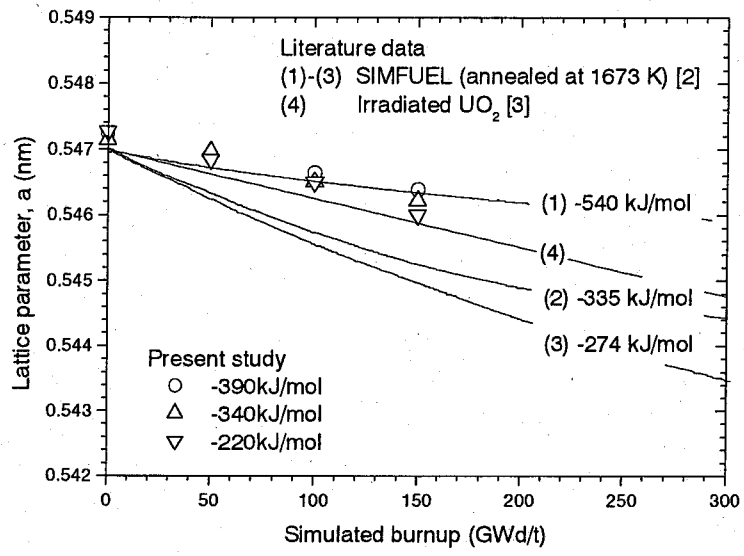

Figure 2. Lattice parameters of the matrix phase under the various oxygen potentials as a function of simulated burnup.

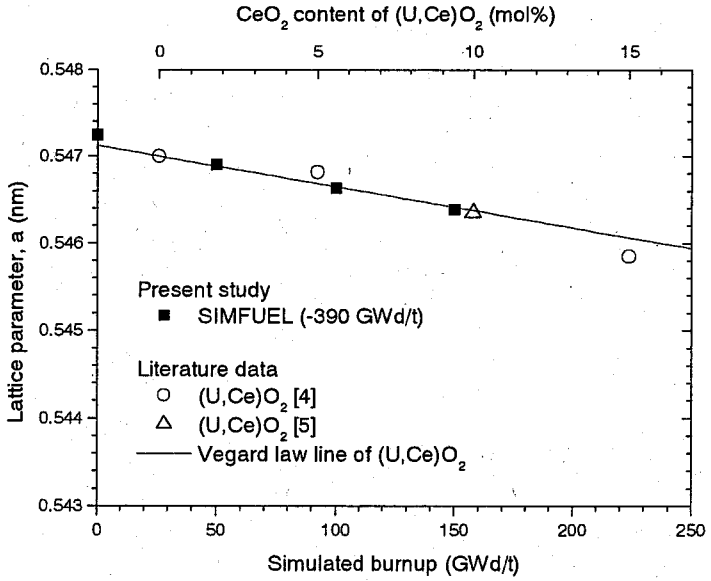

Figure 3. Comparison of lattice parameters between the matrix phase of the SIMFUEL (-390 GWd/t) and $(U,Ce)O_2$.

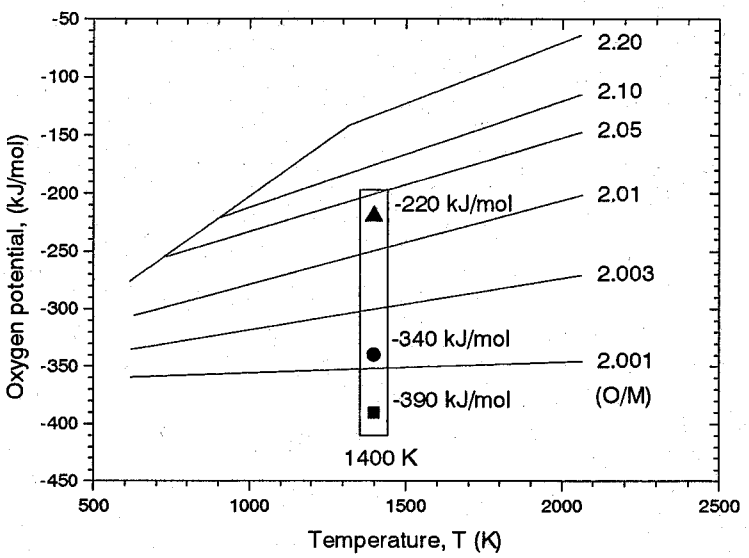

Figure 4. Relationship between the oxygen potential of UO_{2+x} and O/U ratio.

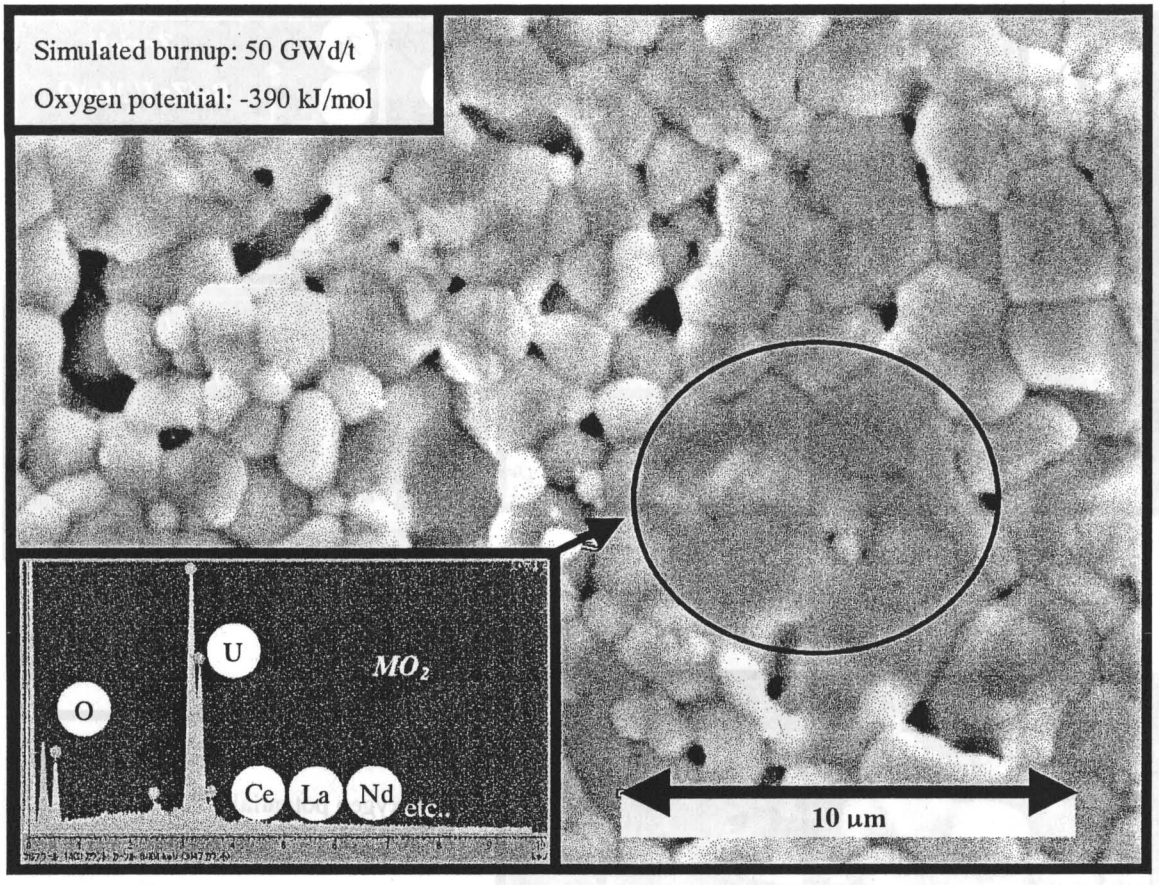

Figure 5. SEM image and EDX analysis of the matrix phase of the SIMFUEL with simulated burnup of 50 GWd/t annealed at the oxygen potential of -390 kJ/mol.

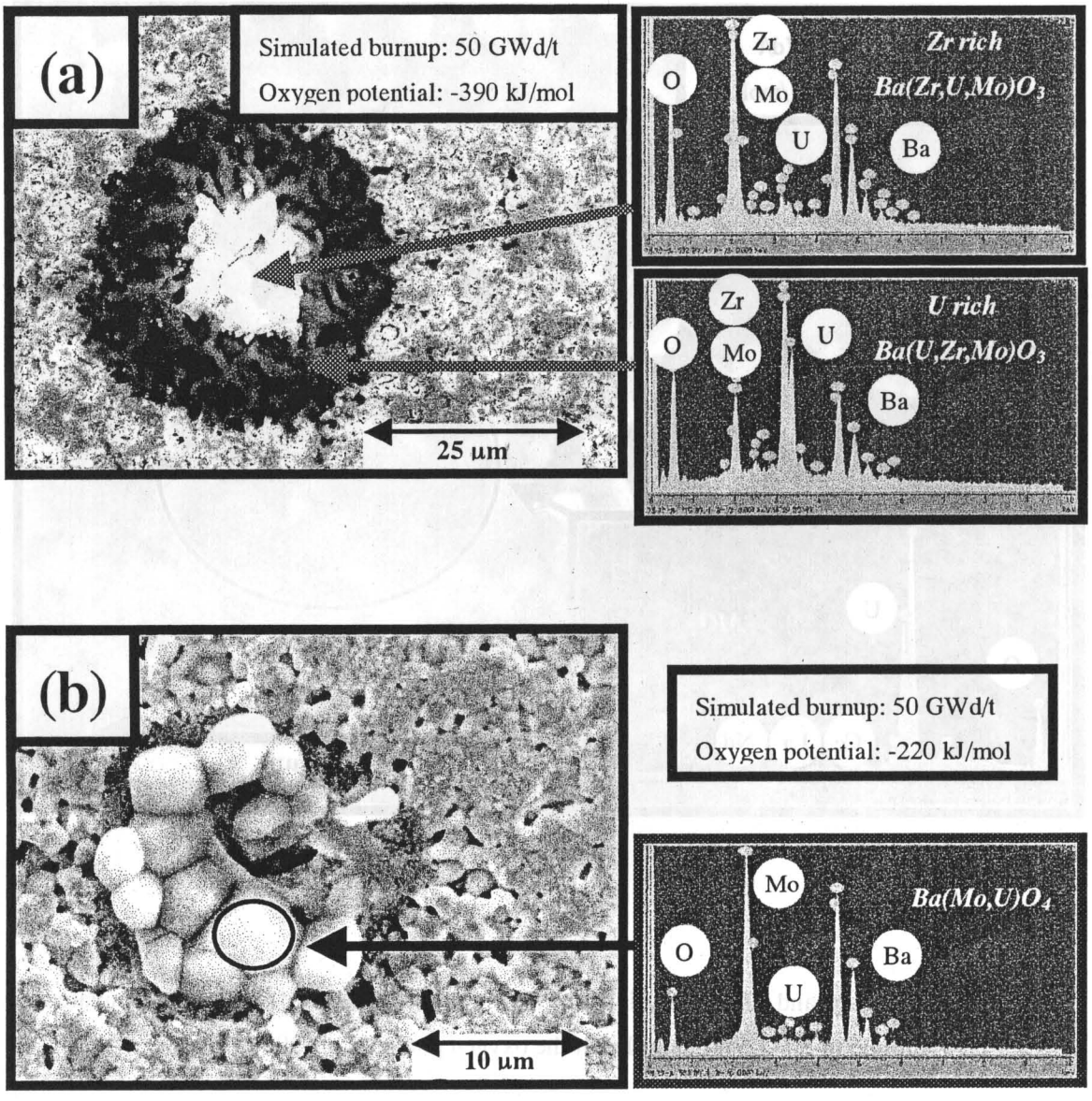

Figure 6. SEM image and EDX analysis of the oxide precipitates in the SIMFUEL with simulated burnup of 50 GWd/t: (a) annealed at the oxygen potential of -390 kJ/mol, (b) annealed at the oxygen potential of -220 kJ/mol.

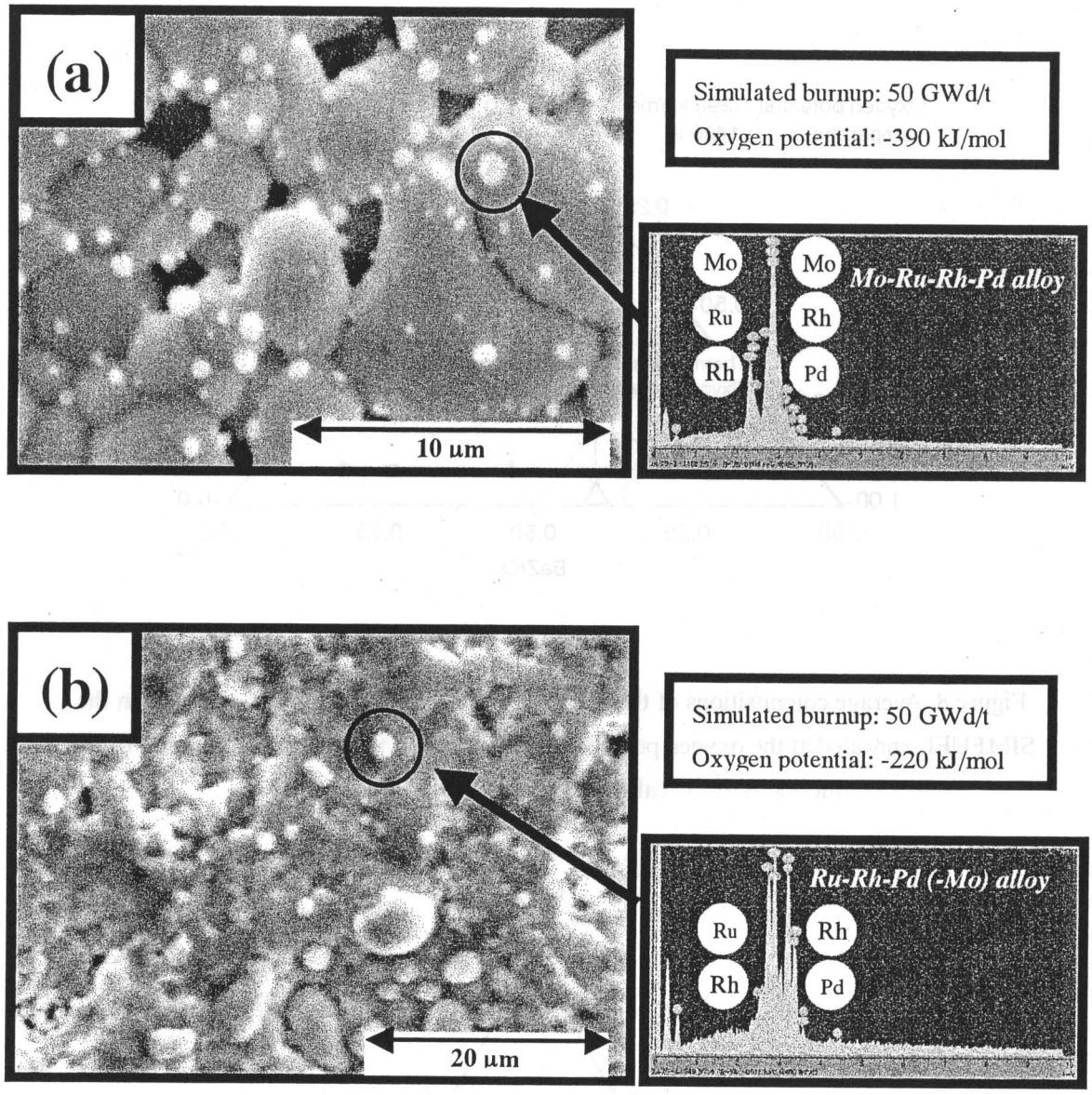

Figure 7. SEM image and EDX analysis of the metallic precipitates in the SIMFUEL with simulated burnup of 50 GWd/t: (a) annealed at the oxygen potential of -390 kJ/mol, (b) annealed at the oxygen potential of -220 kJ/mol.

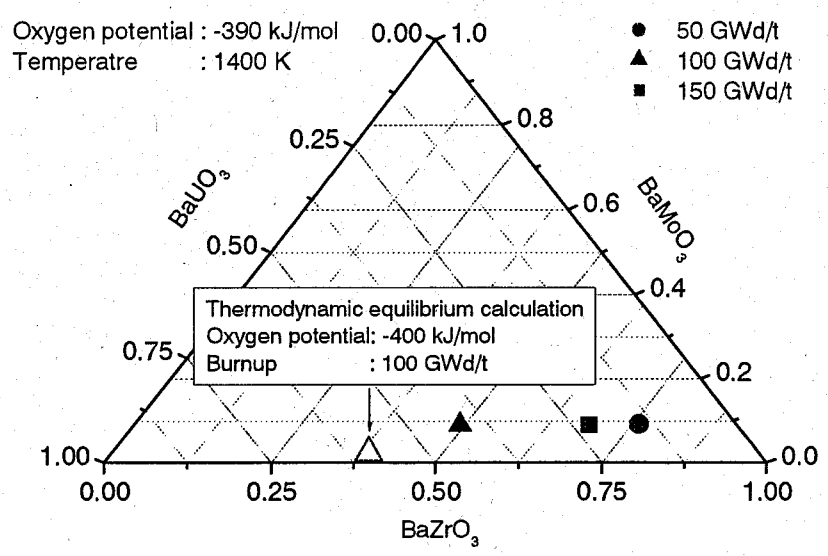

Figure 8. Average compositions of the perovskite-type oxide precipitates observed in the SIMFUEL annealed at the oxygen potential of -390 kJ/mol, together with the result of the thermodynamic calculation performed in Chapter 3.1.

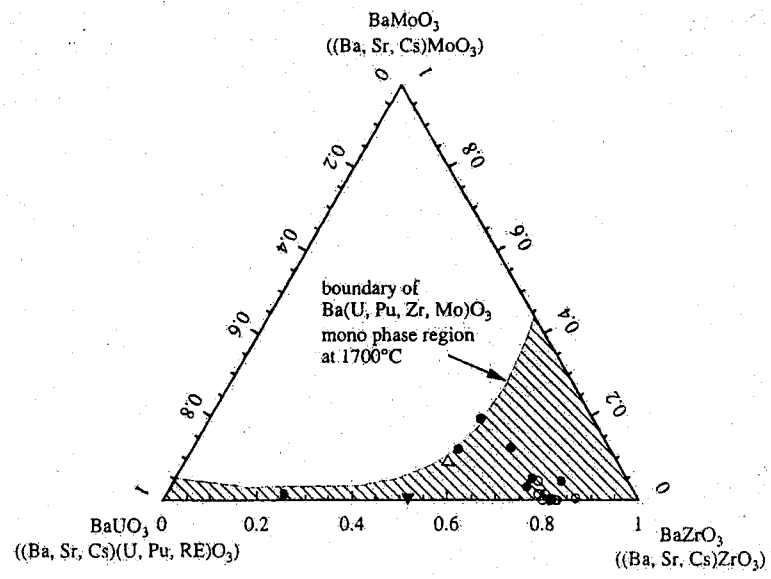

Figure 9. Compositions of the perovskite type oxides precipitated in irradiated oxide fuels projected onto the $BaUO_3$-$BaZrO_3$-$BaMoO_3$ isothermal section at 1973 K [6-9].

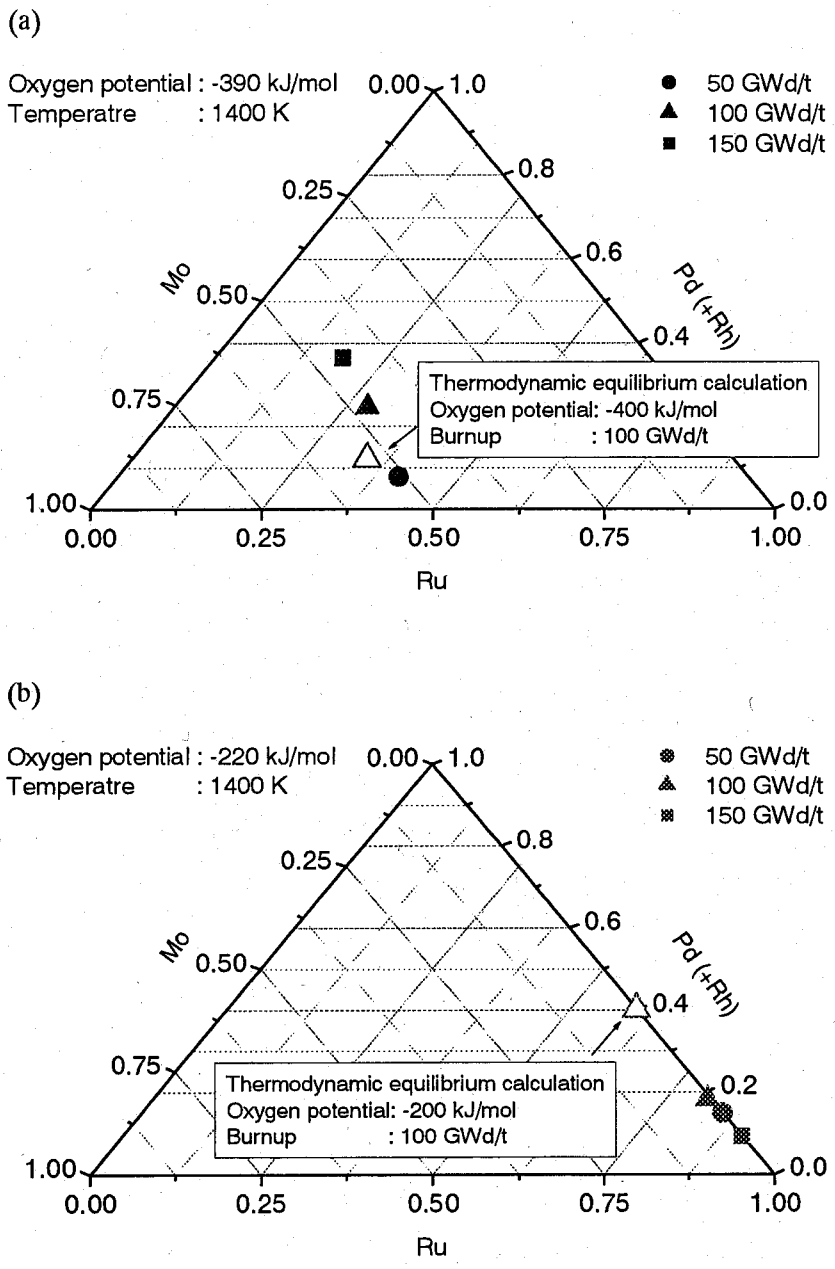

Figure 10. Average compositions of the metallic precipitates observed in the SIMFUEL annealed at the oxygen potential of (a): -390 kJ/mol and (b): -220 kJ/mol, together with the result of the thermodynamic calculation performed in Chapter 3.1.

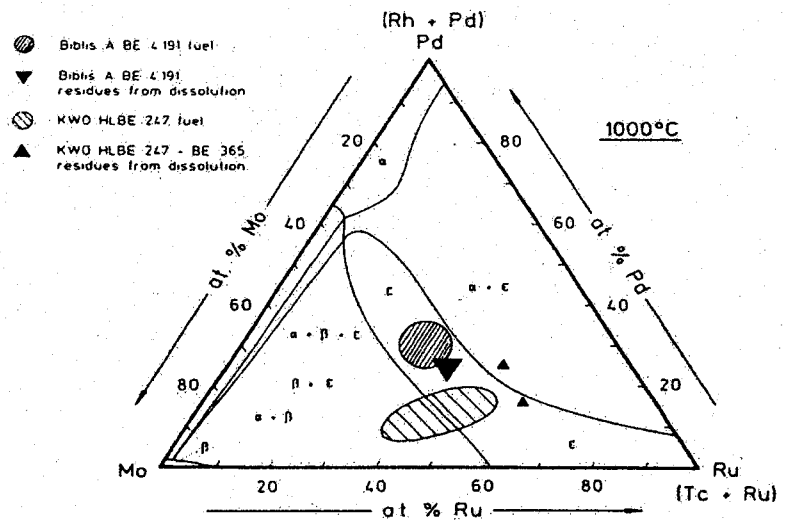

Figure 11. Compositions of the metallic Mo-Tc-Ru-Rh-Pd precipitates in irradiated LWR fuels, that are projected onto the isothermal section of the ternary Mo-(Tc+Ru)-(Rh+Pd) system at 1273 K [9].

2.1.3. Thermophysical Properties of SIMFUEL

As mentioned in the previous section, the SIMFUEL with the simulated burnups of 50, 100, and 150 GWd/t were prepared and annealed at the oxygen potentials of -390, -340, and -220 kJ/mol. The effects of the simulated burnup and annealing oxygen potential on the phase equilibria of the SIMFUEL were studied.

In the present section, the thermophysical properties, viz., the thermal diffusivity, specific heat capacity, thermal conductivity, elastic modulus, and micro Vickers hardness of the SIMFEL have been measured. The effects of the simulated burnup and annealing oxygen potential on the thermophysical properties of the SIMFUEL have been studied.

2.1.3.1. Experimental

2.1.3.1.1. Thermal Diffusivity

The thermal diffusivities of UO_{2+x} and the SIMFUEL were measured by a laser flash method from room temperature to about 1800 K in vacuum (10^{-4} Pa) by using ULVAC TC-7000 (ULVAC-RIKO Inc.).

This technique consists of a rapid heating of the surface of the sample with an energy pulse from a ruby laser (as shown in Fig. 1). Subsequently, the temperature change on the rear-surface is monitored with an indium antimonide infrared detector. The ambient temperature of the sample is established and controlled by a high temperature electric furnace. The temperature is measured with a Pt versus Pt-10%/Rh thermocouple. In the present study, a logarithmic method [1] is used to solve the thermal diffusion equation. This method is utilized to determine the thermal diffusivity α, from the experimental rear-surface temperature history of the sample after being flashed by a laser pulse, using the following equation:

$$\log\left(T_1 t^{\frac{1}{2}}\right) = \log\left[2T_{\max}\left(\frac{L^2}{\pi\alpha}\right)^{\frac{1}{2}}\right] - \left(\frac{L^2}{4\alpha}\right)\frac{1}{t}, \qquad (1)$$

where $t_{1/2}$ is the time to one-half of the maximum temperature rise, T_{max} is the temperature at rear-surface of the sample, T_1 is the temperature at rear-surface of the sample at the time t, and L is the sample thickness. $L^2/4\alpha$ (= ω) is determined by the slope of $\log(t_{1/2}T)$ versus 1/t plot, then the thermal diffusivity α is expressed by the following simple equation:

$$\alpha = \frac{L^2}{4\omega}. \qquad (2)$$

The effects of a heat leak from the sample and non-uniform heating by the pulse laser are much less than those case of a half time method used often in the laser flash technique.

In the present study, for thermal diffusivity measurements, about 10 mm in diameter and about 1 mm thickness of disc shape sample was sliced from the pellet. The thermal

diffusivities at a temperature obtained at the heating process were checked during the cooling cycle.

2.1.3.1.2. Specific Heat Capacity

The specific heat capacities of UO_{2+x} and the SIMFUEL annealed at the oxygen potentials of -390 and -220 kJ/mol were measured by a differential scanning calorimeter (DSC, ULVAC-RIKO Inc.) apparatus, in the temperature range from room temperature to about 1200 K in Ar flow atmosphere.

The apparatus has a "triple-cell" system and an adiabatic temperature control system, which was originally developed by Takahashi et al. [2]. In this apparatus, there are three cells for sample, reference material, and empty. The temperature differences between the sample and empty sides and between the reference and empty sides are detected simultaneously by R-type thermocouples under the condition of constant heating rate. The specific heat capacity of the sample is determined by comparing each of the signals. The principle of the apparatus is briefly summarized as follows [3].

The conceptual construction of the DSC is illustrated in Fig. 2. The fundamental thermal equations for the system are given by the following equations:

$$\frac{1}{R_1'}(T_h - T_{1m}) = C_{1m}\frac{dT_{1m}}{dt} + C_1\frac{dT_1}{dt}, \tag{3}$$

$$\frac{1}{R_2'}(T_h - T_{2m}) = C_{2m}\frac{dT_{2m}}{dt} + C_2\frac{dT_2}{dt}, \tag{4}$$

$$\frac{1}{R_3'}(T_h - T_{3m}) = C_{3m}\frac{dT_{3m}}{dt} + C_3\frac{dT_3}{dt}, \tag{5}$$

where the subscripts indicate the empty, reference, and sample side, respectively. T_i is the temperature of the sample, T_h the temperature of the isothermal plate, T_{im} is the temperature of the sample-pan holder, R_i' is the thermal resistance between the holder and isothermal plate, C_{im} is the specific heat capacity of the holder, and C_i is the heat capacity of the sample. Suppose that an empty sample pan is placed on the empty side, a pan filled with reference material (α-Al_2O_3) on the reference side, and a pan filled with the sample on the sample side, these pans are then heated from the heat source through the thermal resistances R and R'. Assuming that $R_i<R_i'$, $R_1'=R_2'=R_3'$, and the heating rate is equal to dT_h/dt everywhere on the isothermal plate during the scan, we can obtain the heat capacity of the sample C_S from only a single run using the following equation:

$$C_S = C_r\frac{T_{1m} - T_{3m}}{T_{1m} - T_{2m}}, \tag{6}$$

where C_r is the heat capacity of the reference material, (T_{1m}-T_{3m}) is the observed temperature

difference between the sample and empty pans, and (T_{1m}-T_{2m}) is the observed temperature difference between the reference and empty pans.

Even when the condition of $R_1'=R_2'=R_3'$ fails, only two separate runs are needed in the system. The first run is carried out with three empty sample pans on all the sides (blank run). The temperature differences observed in this case are given by the following equations:

$$\Delta T_{2m}^{B} = (T_{2m} - T_{1m})^{B} = \left(1 - \frac{R_2'}{R_1'}\right)(T_h - T_{1m}), \tag{7}$$

$$\Delta T_{3m}^{B} = (T_{3m} - T_{1m})^{B} = \left(1 - \frac{R_3'}{R_1'}\right)(T_h - T_{1m}), \tag{8}$$

where the subscript B indicates the result of a "blank run". The second run is then performed with the empty pan on the empty side, the pan filled with the reference material on the reference side, and pan filled with the sample on the sample side. The temperature differences are represented by the following equations:

$$\Delta T_{2m} = (T_{2m} - T_{1m}) = \left(1 - \frac{R_2'}{R_1'}\right)(T_h - T_{1m}) - R_2'(C_2 - C_1)\frac{dT}{dt}, \tag{9}$$

$$\Delta T_{3m} = (T_{3m} - T_{1m}) = \left(1 - \frac{R_3'}{R_1'}\right)(T_h - T_{1m}) - R_3'(C_3 - C_1)\frac{dT}{dt}. \tag{10}$$

By subtracting the equations (7) and (8) from the equations (9) and (10), respectively, we can obtain the following equations:

$$\Delta T_{3m} - \Delta T_{3m}^{B} = -R_3'(C_3 - C_1)\frac{dT}{dt}, \tag{11}$$

$$\Delta T_{2m} - \Delta T_{2m}^{B} = -R_2'(C_2 - C_1)\frac{dT}{dt} - R_2'(C_2 - C_1)\frac{dT}{dt}. \tag{12}$$

The C_S is thus given by the following equation:

$$C_S = C_r \frac{R_2'}{R_3'} \frac{\Delta T_{3m} - \Delta T_{3m}^{B}}{\Delta T_{2m} - \Delta T_{2m}^{B}}. \tag{13}$$

Therefore, knowing the value of R_2'/R_3', the C_S can be determined from two separate runs, including the blank run. The descriptions above refer to the principle of the scanning method can be also applied to the enthalpy method. Figure 3 shows the schematic diagram for the enthalpy and scanning methods. The enthalpy method refers to heat capacity measurements in which all the output signals during a temperature scan are integrated to give the total enthalpy change (ΔH) for the given temperature interval (ΔT). The quantity $\Delta H/\Delta T$ is taken as the value of the heat capacity at the middle point of the temperature interval. The scanning method refers to heat capacity measurements in which the output signals are continuously converted to the

heat capacity values over the range of the temperature scan. For a given temperature range of a scan, the quantities required that must be recorded are the difference in ordinate displacement between the reference and blank, and between the sample and blank.

Takahashi et al. [3] have been measured the heat capacities of some material from 300 K to 1500 K using this "triple-cell" DSC. They determined the precision of the measurement by the enthalpy method and scanning method is within ±3 % and ±5 %, respectively. It is indicated that the heat capacity determined by the enthalpy method is more precise than that determined by the scanning method. However, using the scanning method, it is possible to determine the profile of the heat capacity anomalies more using the enthalpy method.

In the present study, for the specific heat capacity measurements, the sample with a column shape of about 5 mm diameter and 4 mm in height was cut from the pellet. The specific heat capacity measurement was carried out in a high purity argon (99.999 %) atmosphere with a flow rate of 100 ml/min. The sample was heated with small and large temperature intervals as shown in Fig. 4. The specific heat capacity was calculated by the enthalpy method. Furthermore, we calculated the specific heat capacity by the scanning method at individual temperatures in the large interval region. In order to check the accuracy of the apparatus, the heat capacity of α-Al_2O_3 was measured.

2.1.3.1.3. Thermal Conductivity

The thermal conductivity was calculated from the thermal diffusivity, heat capacity, and density using the following standard expression:

$$\lambda = \alpha C_P \rho . \qquad (14)$$

In the present study, the thermal conductivity was evaluated from room temperature to about 1200 K. The specific heat capacity evaluated by fitting of the experimental scanning data was used for computing the thermal conductivity. For the density evaluation at high temperatures, the recommended following equations [4,5] for UO_2 were used:

$$\rho(T) = \rho(273)\left(9.9734\times10^{-1} + 9.802\times10^{-6}T - 2.705\times10^{-10}T^2 + 4.391\times10^{-13}T^3\right)^{-3} \quad (kg/m^3)$$

(In the temperature range between 273 K and 923 K), (15)

$$\rho(T) = \rho(273)\left(9.9672\times10^{-1} + 1.179\times10^{-5}T - 2.429\times10^{-9}T^2 + 1.219\times10^{-12}T^3\right)^{-3} \quad (kg/m^3)$$

(In the temperature above 923 K), (16)

where $\rho(273)$ is the density at room temperature. These equations are derived from the thermal expansion data. In the present study, the difference in the thermal expansion between UO_2 and the SIMFUEL is considered to be small.

The thermal conductivity was normalized to 95 % of the theoretical density using the

Maxwell-Eucken relationship [6,7]:

$$\lambda_{95} = 0.8636\lambda_M \frac{1+2p}{1-p}, \quad (17)$$

where λ_M is the thermal conductivity with porosity of p (=1-ρ/ ρ_{TD}).

2.1.3.1.4. Elastic Modulus

An ultrasonic pulse-echo measurement was carried out by using Echometer 1062 (NIHON MATECH Inc.) to evaluate the elastic moduli of UO_{2+x} and the SIMFUEL at room temperature in air.

The schematic view of the apparatus is shown in Fig. 5. The sample is cemented to the SiO_2 buffer, and the other end of the buffer is bonded to the 5 MHz transducer connected to the Echometer. The sound velocity in the sample is estimated from the sample length and time separation between the ultrasonic echoes t obtained from the Echometer. The glue joint between the transducer and buffer is Sonicoat-SHN13 (Nichigo Acetylene. Corp.).

The longitudinal sound velocity V_L and shear sound velocity V_S are calculated by:

$$V_L = \frac{2L}{T_2 - T_1}, \quad (18)$$

$$V_S = \left[\left(\frac{T_3 - T_2}{D}\right)^2 + \left(\frac{T_2 - T_1}{2L}\right)^2\right]^{-\frac{1}{2}}, \quad (19)$$

where T_1 is the reflection time of the longitudinal sound velocity from bottom face of the sample, T_2 is the reflection time of the longitudinal sound velocity from top face of the sample, T_3 is the reflection time of the shear sound velocity from top face of the sample, D is the diameter of the sample, and L is the length of the sample.

For isotropic media, the shear modulus G and Young's modulus E are expressed in terms of the measured longitudinal sound velocities V_L and shear sound velocities V_S as:

$$G = \rho V_S^2, \quad (20)$$

$$E = G\left(\frac{3V_L^2 - 4V_S^2}{V_L^2 - V_S^2}\right), \quad (21)$$

where ρ is the sample density.

The measurements were performed three times over changing the sample position, and the error in the sound velocity calculated from t was within 20 m/s.

2.1.3.1.5. Micro Vickers Hardness

The Vickers hardness measurement was carried out using MHT-1 Vickers hardness

tester supplied by MATSUZAWA SEIKI Co. The Vickers hardness, H_V was measured by loading a diamond pyramid-type (with apex 136°) indenter into the surface of the specimen, which is defined by:

$$H_V = \frac{2p_H \sin\phi}{d^2}, \tag{22}$$

where d is the mean diagonal length of the diamond-shaped impression made in the indented surface (see Fig. 24). In the present study, the applied load and loading time were chosen to be 1 kg (9.8 N) and 30 sec, respectively. The measurements were repeated 12 times for all the samples, and the average was gotten from the data except for the maximum and minimum values.

2.1.3.2. Results and Discussion

2.1.3.2.1. Thermal Diffusivity

The temperature dependences of the thermal diffusivities of UO_{2+x} and the SIMFUEL with simulated burnups of 50, 100, and 150 GWd/t annealed at the oxygen potentials of -390 and -220 kJ/mol are shown in Figs. 6 and 7, respectively. In these figures, the measured thermal diffusivities, α_M are normalized to 95 % of the theoretical density considering the porosity correlation which can be derived from the following equation:

$$\alpha_{95} = 1.158\alpha_M \frac{(1+2p)}{(1-0.05)}. \tag{23}$$

In Fig. 6, the thermal diffusivity of stoichiometric UO_2 measured by Lucuta et al. [8] is shown for comparison. The thermal diffusivity of $UO_{2.001}$ measured in the present study is in good agreement with that of stoichiometric UO_2 [8]. The thermal diffusivities of the SIMFUEL are lower than that of UO_2, for the specimens annealed at same oxygen potential. The difference is especially marked at low temperatures.

2.1.3.2.2. Specific Heat Capacity

Figure 8 shows the temperature dependence of the specific heat capacity of α-Al_2O_3 determined by both the enthalpy method in the small interval region and the scanning method in the large interval region. The measured values well agree with literature data [9] within ±3%.

The temperature dependences of the specific heat capacities of UO_{2+x} and the SIMFUEL are shown in Figs. 9, 10, 11, 12, 13, and 14. In these figures, the plotted values represent the specific heat capacity calculated by the enthalpy method, and the smooth lines represent the fitting results by using the scanning data. The fitting equations for UO_{2+x} and the SIMFUEL are listed in Table 1.

Figure 9 shows the specific heat capacity of UO_{2+x}, together with literature data [10].

The specific heat capacity of $UO_{2.001}$ measured in the present study is in good agreement with that of stoichiometric UO_2 [10]. The measured specific heat capacity of $UO_{2.029}$ is slightly higher than that of stoichiometric UO_2, but the difference is inconspicuous.

Figures 10 and 11 show the specific heat capacities of the SIMFUEL annealed at the oxygen potentials of -390 and -220 kJ/mol, respectively. All the SIMFUEL samples show an increase in specific heat capacity with increasing temperature, and have the same trend as UO_2. The specific heat capacity of the SIMFUEL with simulated burnup of 50 GWd/t is lower than that of UO_2, and the specific heat capacities of the SIMFUEL increase with increasing the simulated burnup. The specific heat capacity of the SIMFUEL with simulated burnup of 150 GWd/t is at the same level as that of UO_2.

The specific heat capacities of the SIMFUEL with simulated burnups of 50, 100, and 150 GWd/t are represented in Figs. 12, 13, and 14, respectively. It is confirmed that the specific heat capacities of the SIMFUEL increase with increasing the oxygen content.

2.1.3.2.3. Thermal Conductivity

Figure 15 shows the temperature dependence of the thermal conductivities of UO_{2+x} annealed at the oxygen potentials of -390 and -220 kJ/mol. The thermal conductivity of $UO_{2.001}$ is slightly higher below 500 K, but is good agreement above 500 K in comparison with literature data [8]. The thermal conductivities of UO_{2+x} decrease with increasing O/U ratio due to the formation of interstitial oxygen atoms and/or U^{5+} ions in order to maintain the electrical neutrality. For $UO_{2.029}$, a change in the slope of the curve of the thermal conductivity is observed at around 800 K. This change is considered to be the phase transition from $UO_2+U_4O_9$ to UO_{2+x} single phase. The same behavior has also observed in literatures [8,11]. For UO_2 fuel with defects of deviations from the stoichiometric composition, Carbojo et al. [12] has recommended the following correlation, which combines the lattice term recommended by Lucuta et al. [13] and the ambipolar term recommended by Ronchi [14]:

$$\lambda_0 = \frac{1}{0.0257 + 3.336x + (2.206 - 6.85x)t/10} + 1.158\frac{6400}{t^{5/2}}\exp\left(-16.35/t\right), \text{ (W/m/K)}, \qquad (24)$$

where t = T/1000, T is the temperature in K and x is the deviation from stoichiometry. This equation is for 100 % of the theoretical density of UO_2. The thermal conductivity of $UO_{2.029}$ was calculated by using above equation. The result, which is corrected to the data of 95 % of the theoretical density, is shows in Fig. 15. The thermal conductivity of $UO_{2.029}$ measured in the present study is good agreement with the calculated result, above about 800 K.

The normalized thermal conductivities to 95 % of the theoretical density of UO_{2+x} and the SIMFUEL annealed at the oxygen potentials of -390, -340, and -220 kJ/mol are shown in Figs. 16, 17, and 18, respectively. The thermal conductivity of the SIMFUEL annealed at the

oxygen potential of -340 kJ/mol was calculated using the specific heat capacity of the SIMFUEL annealed at the oxygen potential of -390 kJ/mol, because the difference of the specific heat capacities is very small.

The thermal conductivities of the SIMFUEL decrease with increasing temperature, indicating a phonon conduction characteristic. The thermal conductivities of the SIMFUEL also decrease with increasing the simulated burnup, which is due to the phonon scattering caused by the dissolved FP elements. These characteristics are always observed, regardless of the annealing oxygen potential.

As shown in Figs. 16, 17, and 18, the reduction rate of the thermal conductivities caused by the burnup increasing appears to be small with increasing burnup. In general, the degradation is caused primarily by the dissolved FP elements and possibly by the oxide precipitates, and the metallic precipitates should increase the thermal conductivity. (It is expected that the thermal conductivity of the metallic precipitates is about 10 times larger than that of the matrix phase at room temperature reported in Chapter 3.2. of this thesis.) Since the volume fraction of these precipitates is very small, they will have only a small effect. For example, according to a literature [15], the contribution of the metallic precipitates is about 1 % increase in the thermal conductivity for each 1 at.% (equivalent to 9.375 GWd/t) burnup. In the present study, the SIMFUEL has the metallic precipitates about 2.0 to 3.0 vol.% for the simulated burnup of 50 GWd/t, 5.0 to 6.0 vol.% for the simulated burnup of 100 GWd/t, and 8.0 to 9.0 vol.% for the simulated burnup of 150 GWd/t. The amount of the metallic precipitates in the SIMFUEL prepared in the present study is higher than that with the simulated burnup of 14 to 75 GWd/t reported by Lucuta et al. [8,16]. (In the literature, for example, the volume fraction of the metallic precipitates is 2.0 to 3.0 vol.% for 75 GWd/t.) Consequently, it is considered that the contribution of a large amount of metallic precipitates reduces the reduction effect by the dissolved FP elements on the thermal conductivity with increasing burnup.

Figures 19, 20, and 21 show the effect of the oxygen potential on the thermal conductivity for a given burnup. The thermal conductivities of the hyperstoichiometric SIMFUEL are lower than that of the stoichiometric SIMFUEL. A similar characteristic observed for UO_{2+x} is found due to the formation of the interstitial oxygen and/or high valency ions.

2.1.3.2.4. Elastic Modulus

The calculated shear modulus G and Young's modulus E of stoichiometric and hyperstoichiometric UO_{2+x} and the SIMFUEL from the longitudinal and shear sound velocities were normalized to 100 % of the theoretical density by using the correlation of the elastic modulus of UO_2 as a function of the porosity [17]:

$$G = 82\left(1 - 2.03p\right), \qquad (25)$$

$$E = 220(1 - 2.34p), \quad (26)$$

where, p is the porosity.

In Fig. 22, the normalized values of the shear and Young's moduli are shown as a function of the simulated burnup. It is found that the elastic moduli decrease linearly with increasing the simulated burnup. The effect of the annealing oxygen potential on the elastic modulus is not confirmed. The reduction rates in the elastic moduli of the SIMFUEL are about 6.5 % per 50 GWd/t burnup for the shear modulus and about 7 % per 50 GWd/t burnup for the Young's modulus, respectively.

The effects of the solid FP elements on the elastic modulus have been studied by using the solid solutions between UO_2 and appropriate FP oxides [18-20]. Boocock et al. [19] has reported that the addition of 6 wt.% of the FP elements, comprising transition metals and lanthanides, to the mixed oxide reduced both the shear and Young's moduli by less than 10 %. We have also studied that the effect of the rare earth FP elements on the elastic modulus using $(U,Ce)O_2$ solid solution with the CeO_2 contents ranging from 0 to 20 mol%. Figure 23 shows the shear and Young's moduli of $(U,Ce)O_2$ solid solution, as a function of the CeO_2 content. It can be seen that the shear and Young's moduli decrease with increasing CeO_2 content. As compared to the elastic moduli of the SIMFUEL obtained in the present study, the reduction rate in the elastic moduli with simulated burnup of 50 GWd/t corresponds to about 3.5 mol% CeO_2 in case of $(U,Ce)O_2$ solid solution. This correlation and the reduction rate are the same as the case of the lattice parameter described in previous section.

2.1.3.2.5. Micro Vickers Hardness

Figure 24 shows the micro Vickers hardness of UO_{2+x} and the SIMFUEL as a function of the simulated burnup. The Vickers hardness of the SIMFUEL decreases with increasing the simulated burnup. In general, the hardness of the ceramic material is known to increase with the density. The SIMFUEL indicates lower hardness than that of UO_2. (The density of UO_2 is lower than that of the SIMFUEL.) Therefore, it is confirmed that the dissolved FP elements lead lower hardness. The effect of the annealing oxygen potential on the Vickers hardness of the SIMFUEL is not confirmed in the present study.

For various materials, the Vickers hardness H_V is associated with the Young's modulus E. For some oxide and carbide ceramics, H_V is found to be proportional to E with the values of [21]:

$$\frac{H_V}{E} \approx 0.05. \quad (27)$$

The values of the Vickers hardness for UO_2 and the SIMFUEL with simulated burnups of 50, 100, and 150 GWd/t are plotted in Fig. 25, as a function of the normalized Young's modulus. As

shown in this figure, it is found that the relationship between the Vickers hardness and Young's modulus for the SIMFUEL is located ranging from about 0.04 to 0.05, indicating typical ceramics characteristics.

2.1.3.3. Conclusion

The thermophysical properties of UO_2 and the SIMFUEL have been measured and the effects of the simulated burnup and annealing oxygen potential on the properties have been studied. The specific heat capacity of the SIMFUEL measured by the "triple cell" DSC shows that the simulated burnup increases the specific heat capacity of the SIMFUEL. The specific heat capacity of the SIMFUEL with the simulated burnup of 150 GWd/t nearly equals to that of UO_2. The specific heat capacity of the SIMFUEL slightly increases with increasing the oxygen content. The thermal conductivity of the SIMFUEL decreases with burnup increasing. The reduction rate of the thermal conductivity is appeared to be small with increasing burnup. The excess oxygen decreases the thermal conductivity of the SIMFUEL. The elastic moduli and Vickers hardness of the SIMFUEL decrease with increasing the simulated burnup. The effects of the annealing oxygen potential on the mechanical properties of the SIMFUEL are not clearly confirmed.

References

[1] Y. Takahashi et al., Netsusokutei, 15 (1988) 103.

[2] Y. Takahashi, M. Asou, T. Terai, T. Yoneoka, M. Kamimoto, and A. Maesono, Proc. 12th Japan Symp. on Thermophysical Properties, Kyoto, 1991, p. 339.

[3] Y. Takahashi and M. Asou, Thermochimica Acta, 223 (1993) 7.

[4] J.J. Carbajo, G.L. Yoder, S.G. Popov, and V.K. Ivanov, J. Nucl. Mater., 299 (2001) 181.

[5] D.G. Martin, J. Nucl. Mater., 152 (1988) 94.

[6] Y. Philipponneau, J. Nucl. Mater., 188 (1992) 194.

[7] C. Duriez, J.-P. Alessandri, T. Gervais, and Y. Philipponneau, J. Nucl. Mater., 277 (2000) 143.

[8] P.G. Lucuta, Hj. Matzke, and R.A. Verral, J. Nucl. Mater., 223 (1995) 51.

[9] SGTE Pure Substance Database (Edit. 1998), Provided by GTT Technol., Herzogenrath, Germany (1998).

[10] Hj. Matzke, P.G. Lucuta, R.A. Verrall, and J. Henderson, J. Nucl. Mater., 247 (1997) 121.

[11] M. Amaya, T. Kubo, and Y. Korei, J. Nucl. Sci. Technol., 33 (1996) 636.

[12] J.J. Carbojo, G.L. Yoder, S.G. Popov, and V.K. Ivanov, J. Nucl. Mater., 299 (2001) 181.

[13] P.G. Lucuta, H.J. Matzke, and I.J. Hastings, J. Nucl. Mater., 232 (1996) 166.

[14] C.Ronchi, M. Sheindlin, M. Musella, and G.J. Hyland, J. Appl. Phys., 85 (1999) 776.

[15] P.G. Lucuta, Hj. Matzke, and R.A. Verrall, J. Nucl. Mater., 217 (1994) 279.

[16] P.G. Lucuta, R.A. Verral, Hj. Matzke, and B.J. Palmer, J. Nucl. Mater., 178 (1991) 48.

[17] V. Roque, B. Cros, D. Baron, and P. Dehaudt, J. Nucl. Mater., 277 (2000) 211.

[18] K. Yamada, S. Yamanaka, T. Nakagawa, M. Uno, and M. Katsura, J. Nucl Mater., 247 (1997) 289.

[19] J. Boocock, A.S. Furzer, and J.R. Matthews, Harwell memo AERE-M2565 (1972).

[20] S. Yamanaka, S. Yoshida, K. Kurosaki, M. Uno, K. Yamamoto, and T. Namekawa, J. Alloys and comp., 327 (2001) 281.

[21] K. Tanaka, H. Koguchi, and T. Mura, Int. J. Eng. Sci., 27 (1989) 11.

Table 1

Empirical equation of the specific heat capacity C_P of UO_2 and the SIMFUEL evaluated by fitting the experimental scanning data (323-1200 K).

Sample	Specific heat capacity C_P ($JK^{-1}g^{-1}$) = $a+bT+cT^2+dT^{-2}$			
	a	$b\times10^{-4}$	$c\times10^{-8}$	$d\times10^{3}$
$UO_{2.001}$	0.25174	1.40	-5.8	-4.38
$UO_{2.029}$	0.24631	1.30	-4.14	-3.24
50 SIM $_{2.000}$	0.28445	3.00	-0.978	-4.24
50 SIM $_{2.027}$	0.31766	-0.20	1.96	-6.24
100 SIM $_{2.000}$	0.35401	-0.80	3.91	-7.82
100 SIM $_{2.027}$	0.33276	-0.50	3.33	-5.80
150 SIM $_{2.001}$	0.30472	0.30	-1.12	-5.94
150 SIM $_{2.028}$	0.31733	0.051	0.35	-5.89

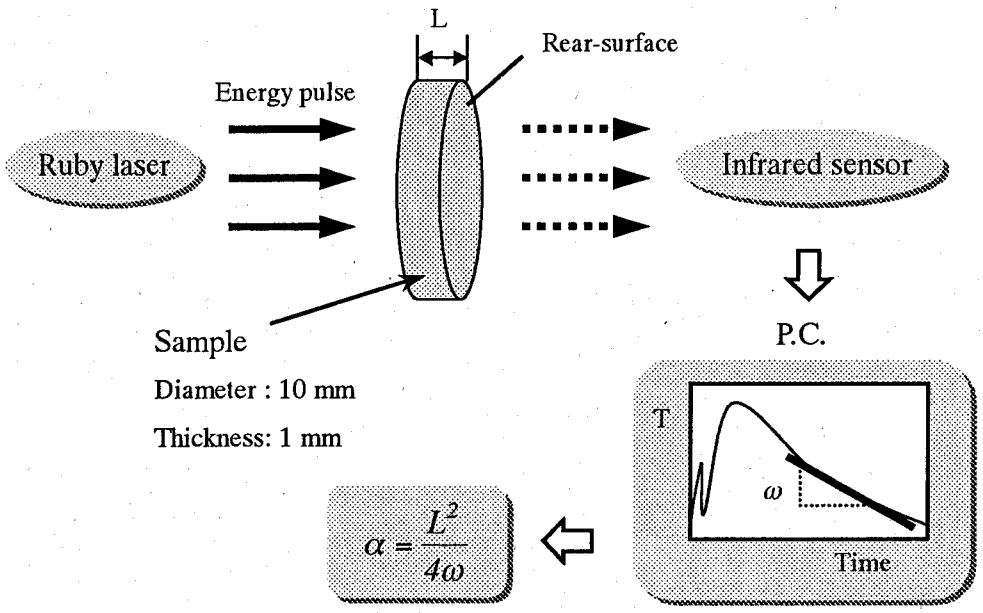

Figure 1. Schematic view of the laser flush method.

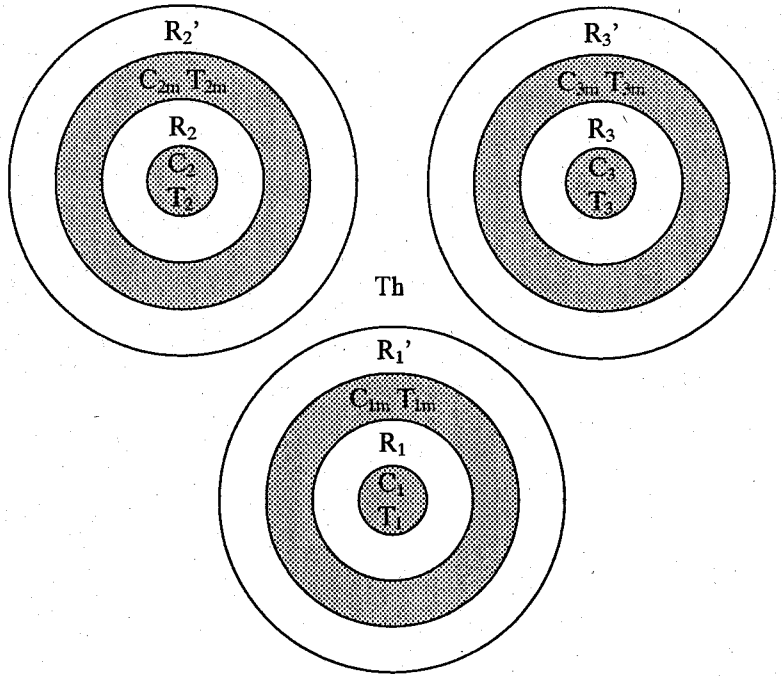

Figure 2. Conceptual diagram of the "triple-cell" DSC. T_1, T_2, and T_3 are the temperatures of the sample; T_{1m}, T_{2m}, and T_{3m} are the temperatures of the holder; T_h, is the temperature of the isothermal plate; C_1, C_2, and C_3 are the heat capacities of the sample; C_{1m}, C_{2m}, and C_{3m} are the heat capacities of the holder; R_1, R_2, and R_3 are the thermal resistances between the holder and sample; R_1', R_2', and R_3' are the thermal resistances between the holder and isothermal plate; Subscripts 1, 2, and 3 indicate the empty side, reference side, and sample side, respectively.

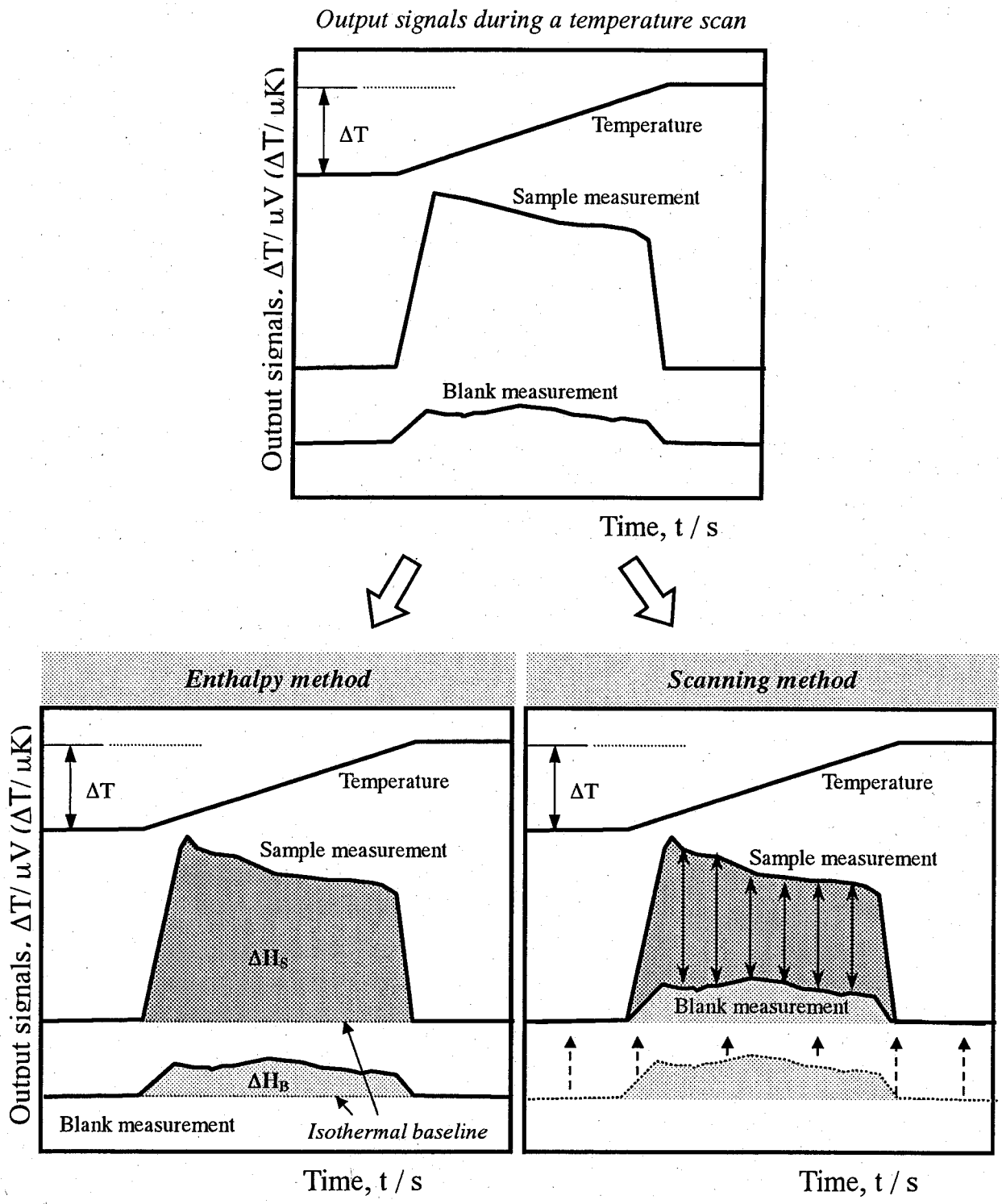

Figure 3. Schematic diagrams for the enthalpy method and scanning method.

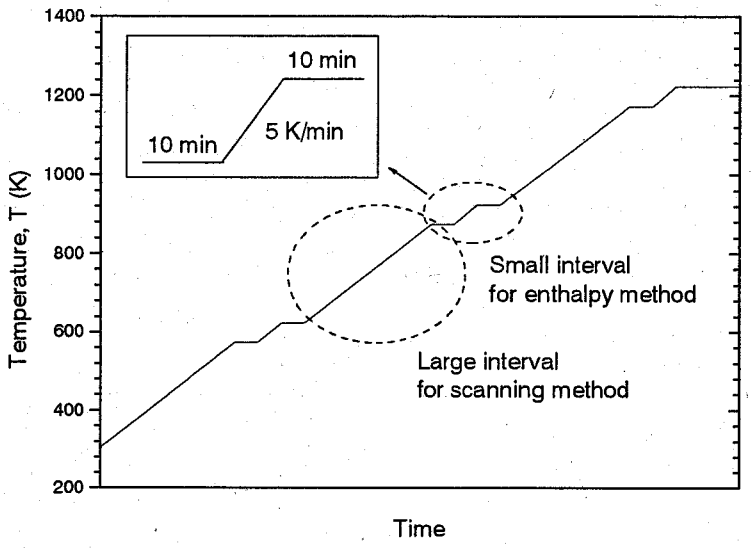

Figure 4. Schematic diagram of the time-temperature curve.

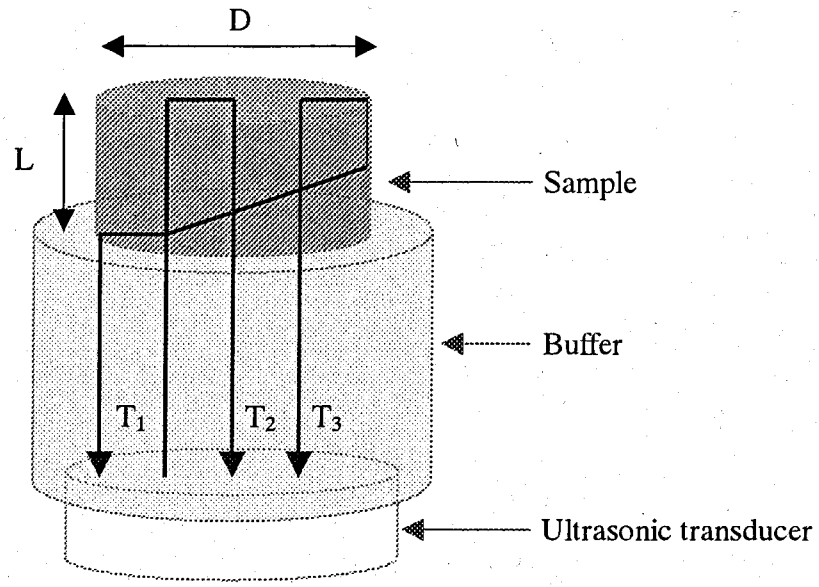

Figure 5. Schematic view of the ultrasonic pulse echo method. The longitudinal sound velocity V_L and shear sound velocity V_S can be calculated by using T_1, T_2, T_3, D, and L, as follows:

$$V_L = \frac{2L}{T_2 - T_3} \quad \text{and} \quad V_S = \frac{1}{\sqrt{\frac{(T_3 - T_2)^2}{D^2} + \frac{(T_2 - T_1)^2}{4L^2}}}.$$

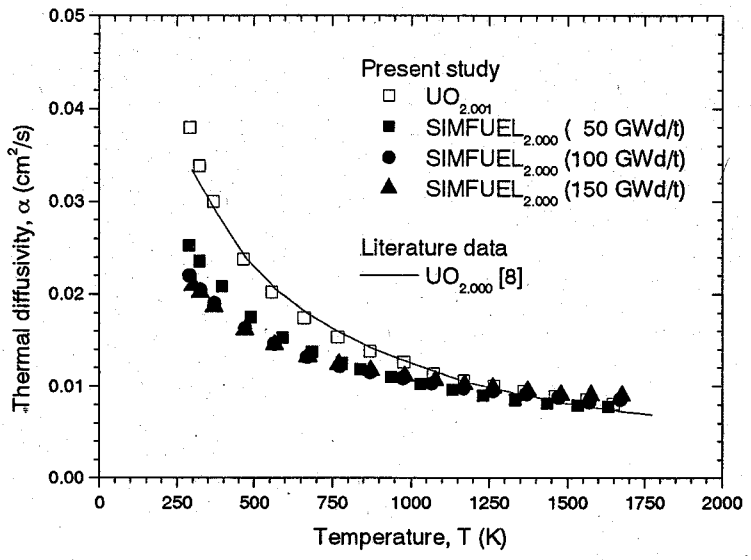

Figure 6. Temperature dependence of the thermal diffusivities of UO_{2+x} and the SIMFUEL with simulated burnup of 50, 100, and 150 GWd/t annealed at the oxygen potential of -390 kJ/mol.

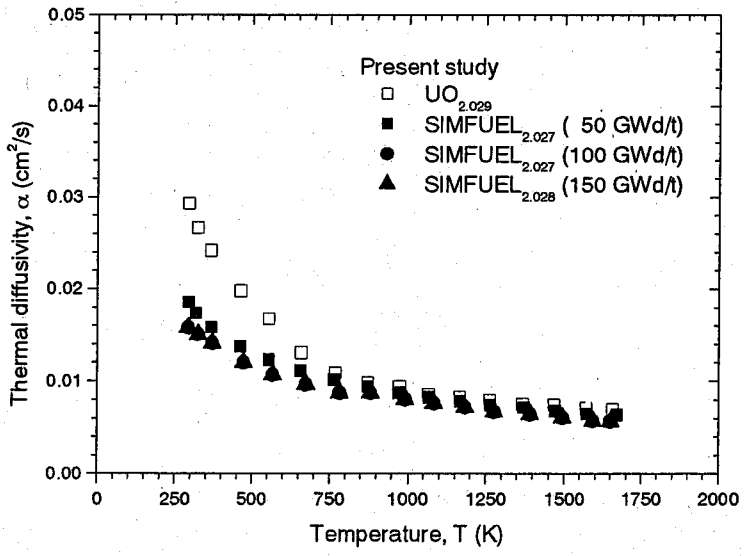

Figure 7. Temperature dependence of the thermal diffusivities of UO_{2+x} and the SIMFUEL with simulated burnup of 50, 100, and 150 GWd/t annealed at the oxygen potential of -220 kJ/mol.

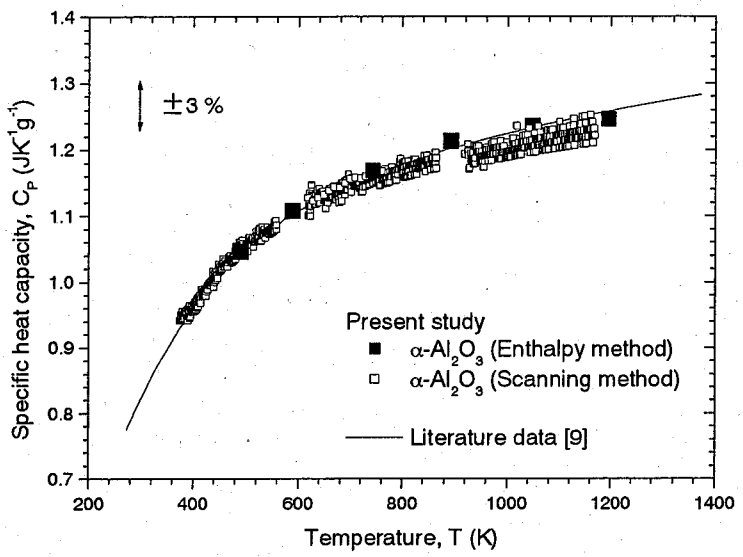

Figure 8. Temperature dependence of the specific heat capacity of α-Al_2O_3 measured in the present study.

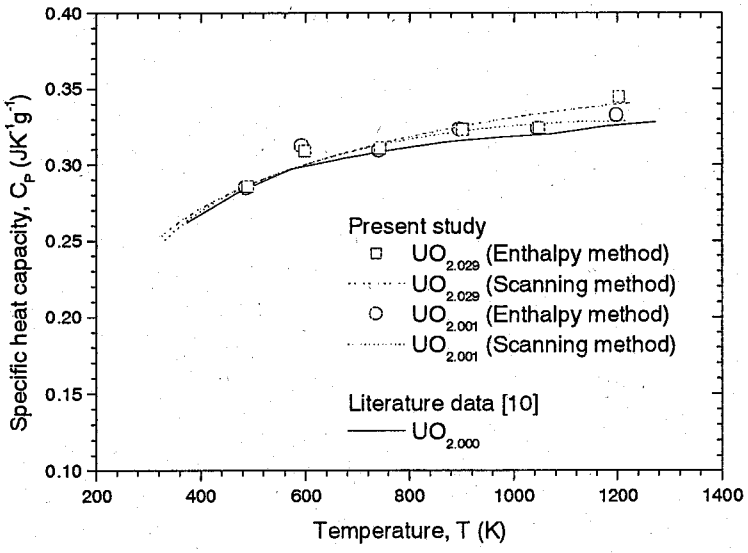

Figure 9. Temperature dependence of the specific heat capacities of UO_{2+x} annealed at the oxygen potentials of -390 and -220 kJ/mol.

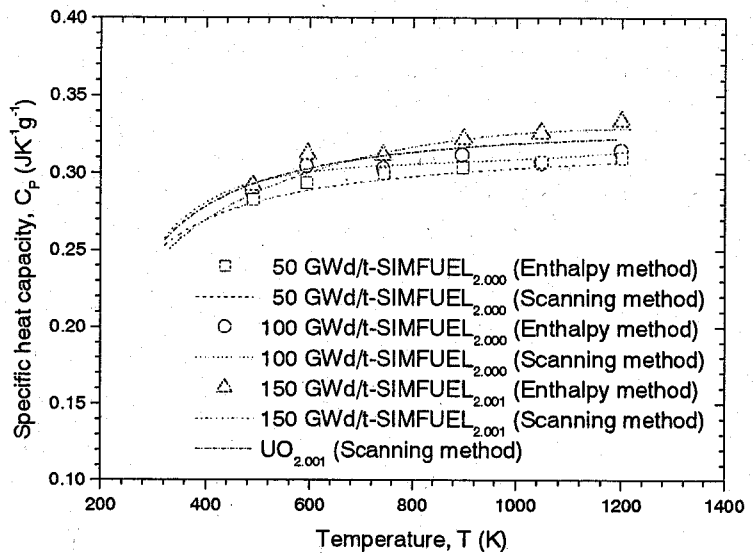

Figure 10. Temperature dependence of the specific heat capacities of the SIMFUEL with simulated burnups of 50, 100, and 150 GWd/t annealed at the oxygen potential of -390 kJ/mol.

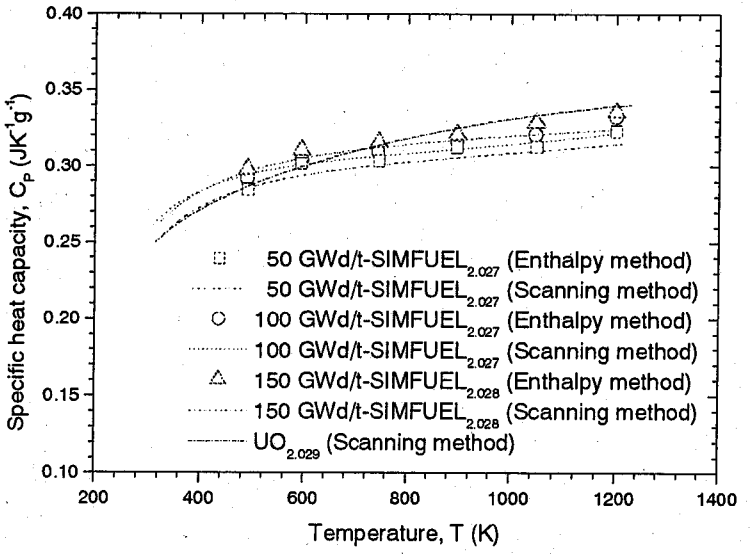

Figure 11. Temperature dependence of the specific heat capacities of the SIMFUEL with simulated burnups of 50, 100, and 150 GWd/t annealed at the oxygen potential of -220 kJ/mol.

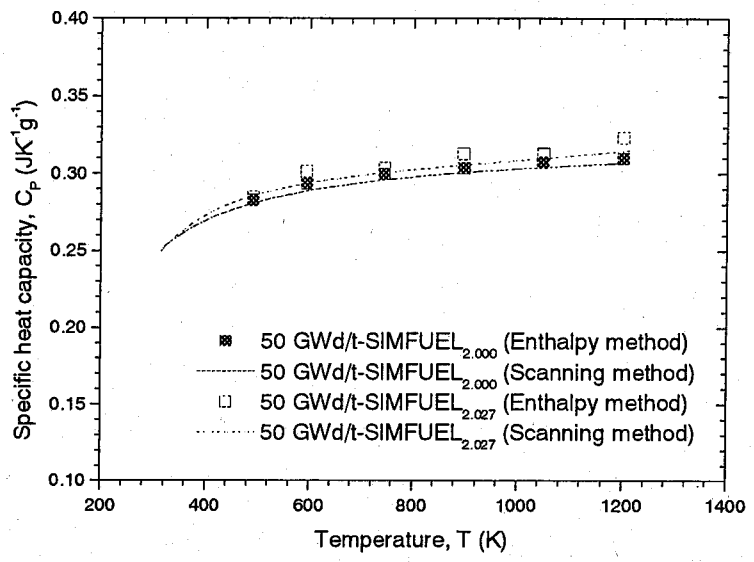

Figure 12. Temperature dependence of the specific heat capacities of the SIMFUEL with simulated burnup of 50 GWd/t annealed at the oxygen potentials of -390 and -220 kJ/mol.

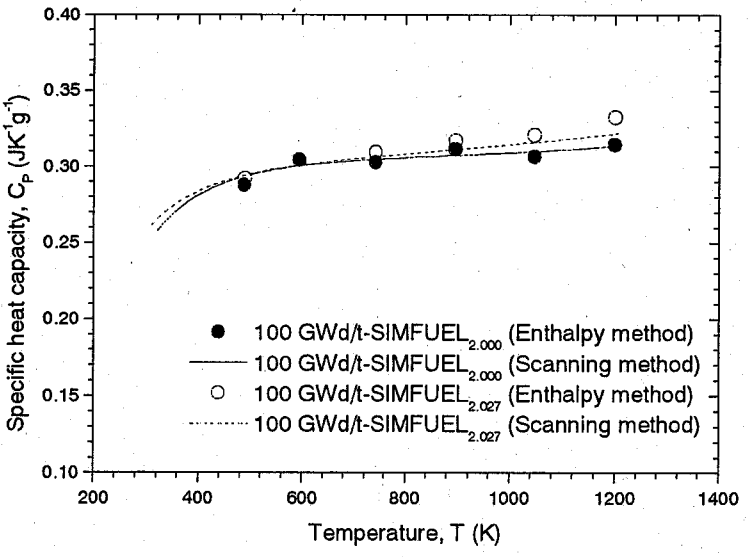

Figure 13. Temperature dependence of the specific heat capacities of the SIMFUEL with simulated burnup of 100 GWd/t annealed at the oxygen potentials of -390 and -220 kJ/mol.

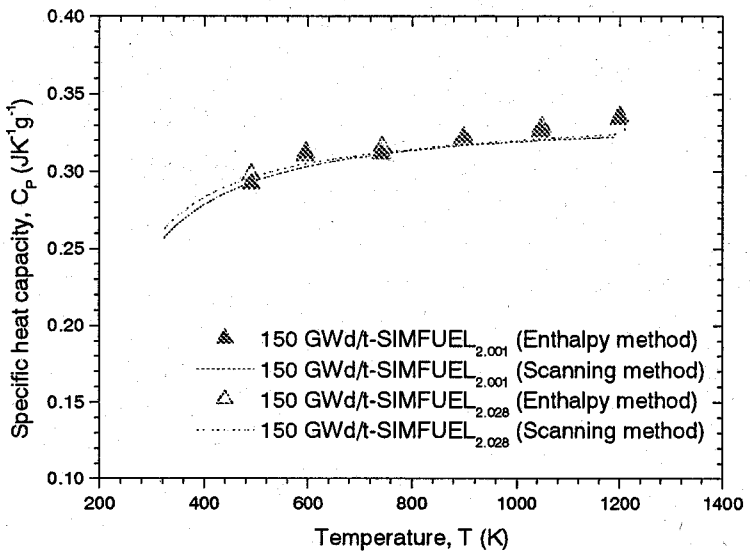

Figure 14. Temperature dependence of the specific heat capacities of the SIMFUEL with simulated burnup of 150 GWd/t annealed at the oxygen potentials of -390 and -220 kJ/mol.

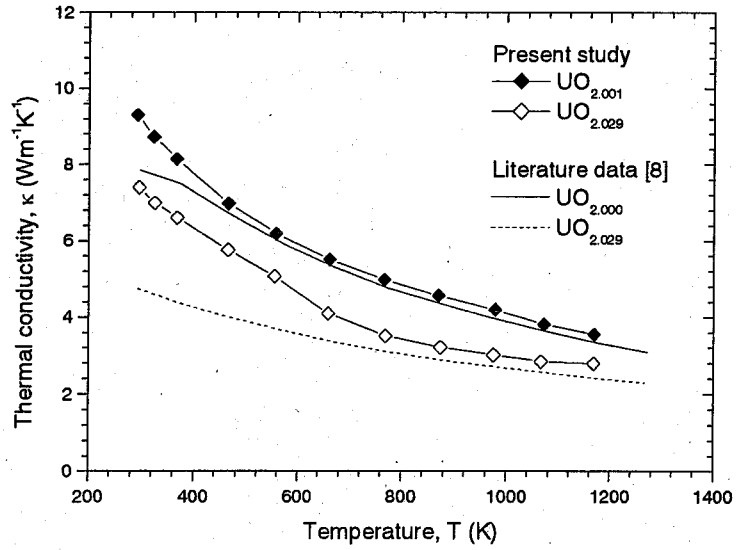

Figure 15. Temperature dependence of the thermal conductivities of UO_{2+x} annealed at the oxygen potentials of -390 and -220 kJ/mol.

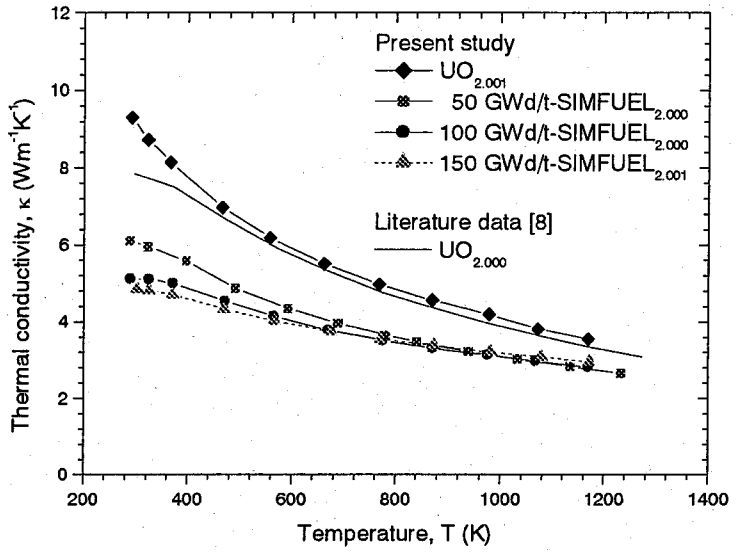

Figure 16. Temperature dependence of the thermal conductivities of UO_{2+x} and the SIMFUEL (50, 100, and 150 GWd/t-burnup) annealed at the oxygen potential of -390 kJ/mol.

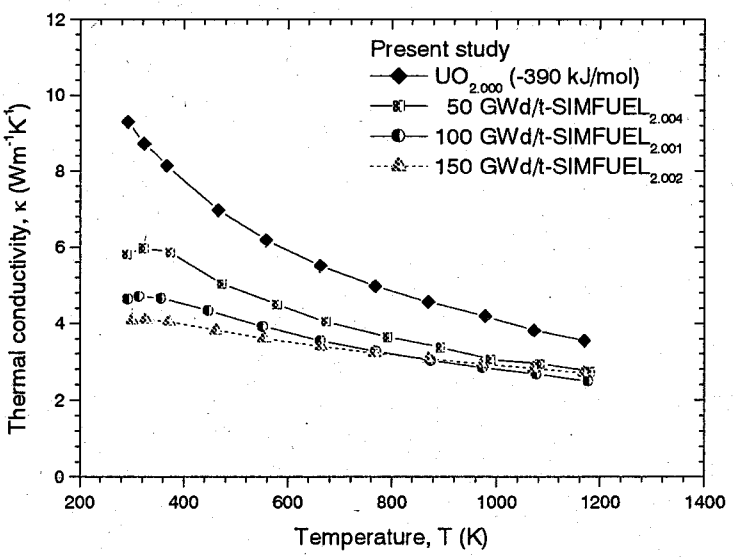

Figure 17. Temperature dependence of the thermal conductivities of UO_{2+x} and the SIMFUEL (50, 100, and 150 GWd/t-burnup) annealed at the oxygen potential of -340 kJ/mol.

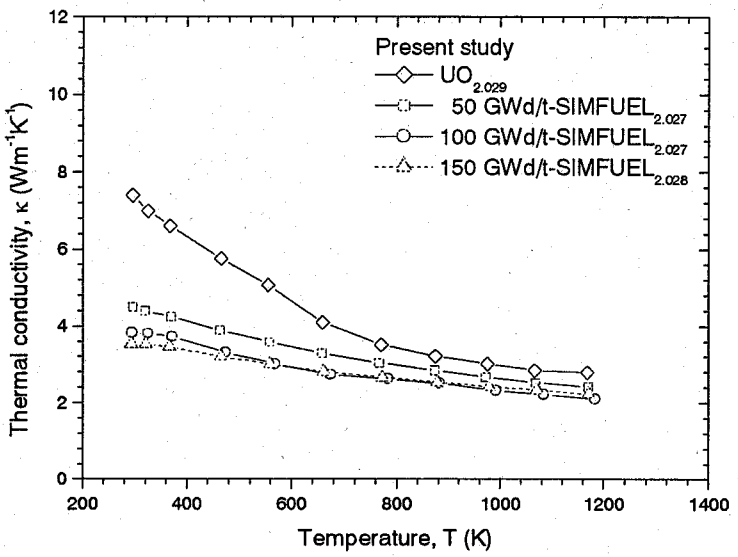

Figure 18. Temperature dependence of the thermal conductivities of UO_{2+x} and the SIMFUEL (50, 100, and 150 GWd/t-burnup) annealed at the oxygen potential of -220 kJ/mol.

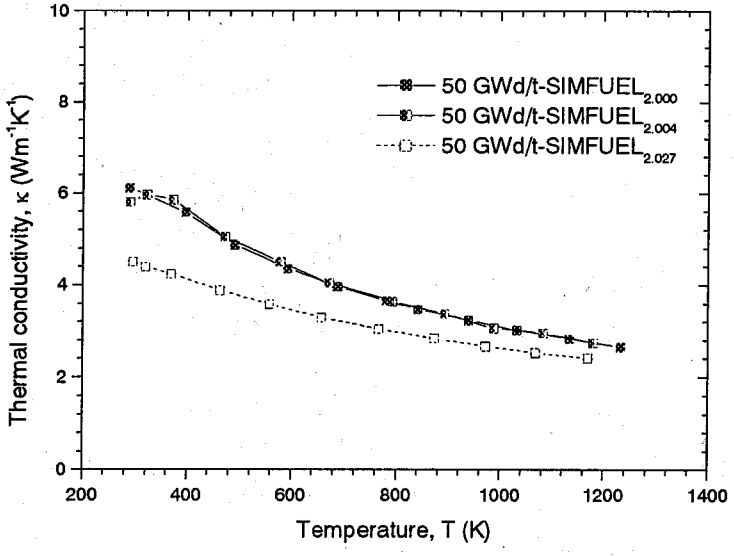

Figure 19. Temperature dependence of the thermal conductivities of the SIMFUEL with simulated burnup of 50 GWd/t annealed at three oxygen potentials.

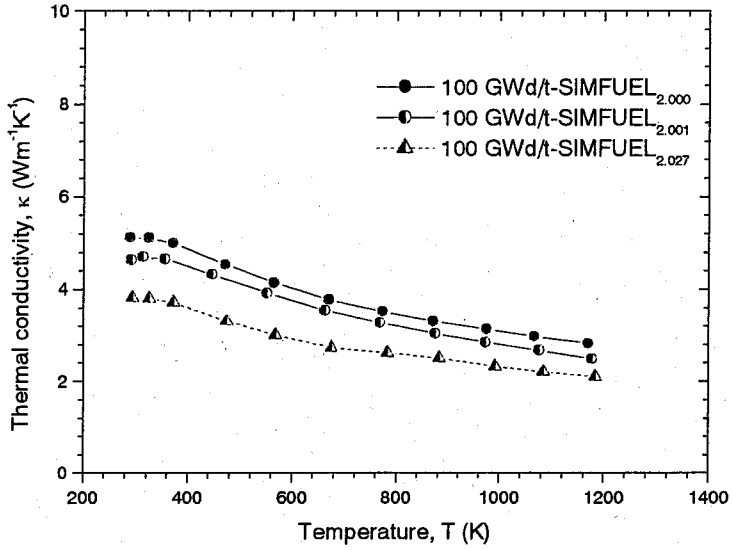

Figure 20. Temperature dependence of the thermal conductivities of the SIMFUEL with simulated burnup of 100 GWd/t annealed at three oxygen potentials.

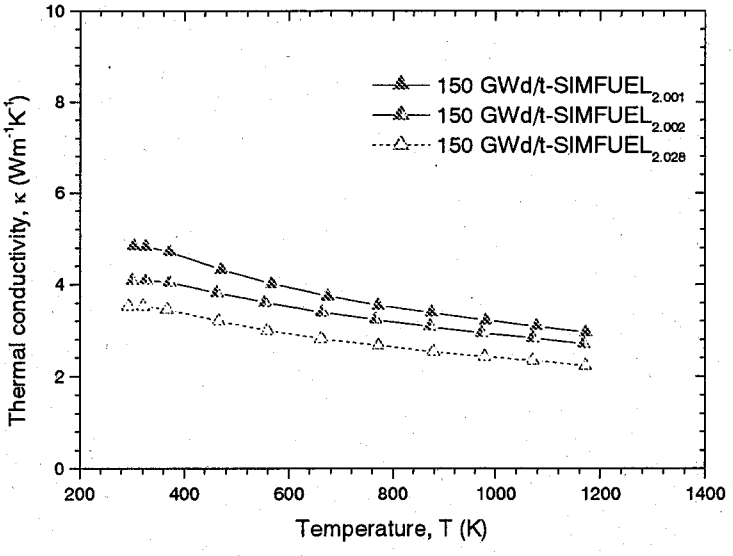

Figure 21. Temperature dependence of the thermal conductivities of the SIMFUEL with simulated burnup of 150 GWd/t annealed at three oxygen potentials.

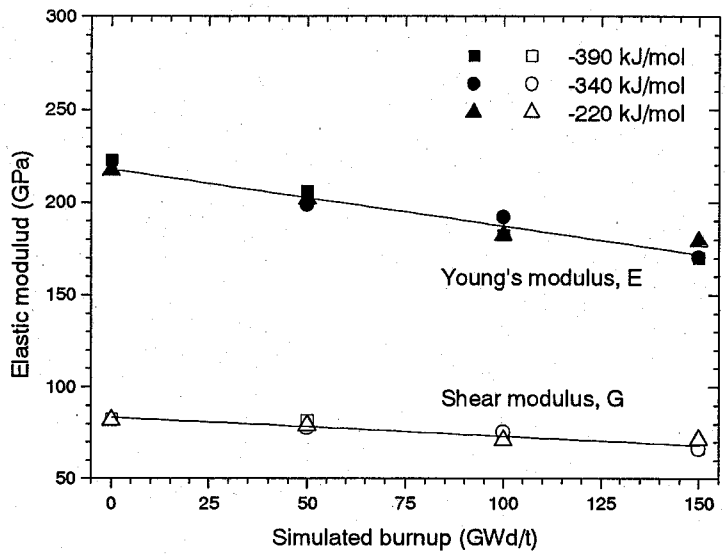

Figure 22. Change in the elastic moduli of UO_2 and the SIMFUEL with simulated burnups with simulated burnup of 50, 100, and 150 GWd/t annealed at the oxygen potentials of -390, -340, and -220 kJ/mol. The values of the elastic moduli are normalized to 100 % of the theoretical density using the correlation for the elastic modulus of UO_2 as a function of the porosity [17]. The straight lines show the least-square fitting results of all the data, irrespective the annealing oxygen potentials.

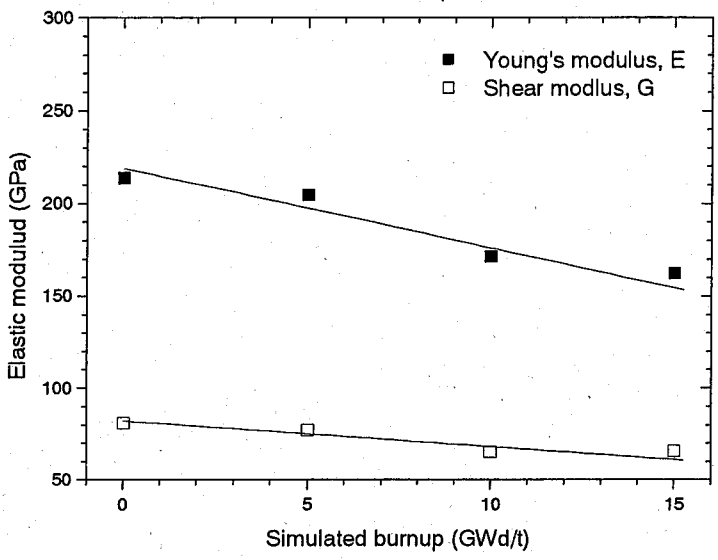

Figure 23. Elastic moduli of $(U,Ce)O_2$ solid solution as a function of the CeO_2 content. The values of the elastic moduli are normalized to 100 % of the theoretical density [18].

(a)

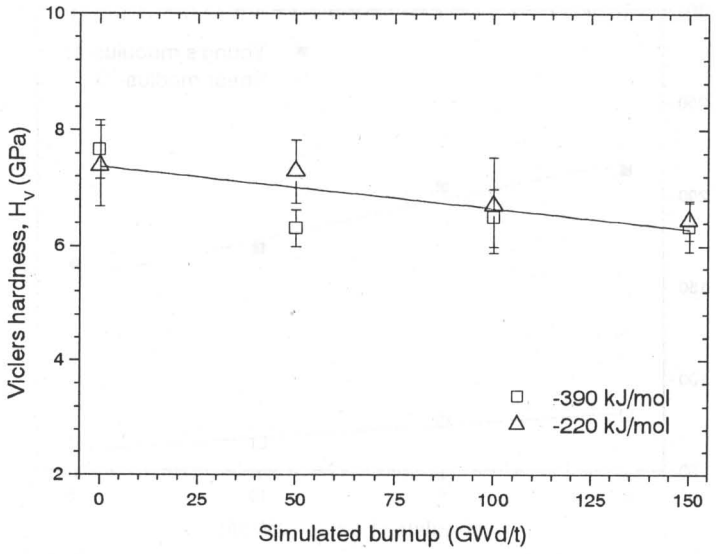

(b)

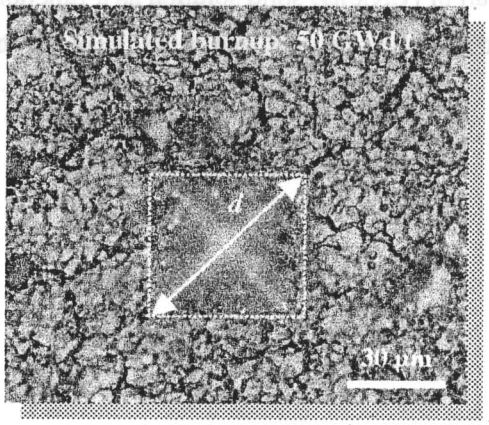

Figure 24. (a) Vickers hardness of UO_2 and the SIMFUEL annealed at the oxygen potentials of -390 and -220 kJ/mol as a function of the simulated burnup. The straight line shows the least-square fitting results of all the data, irrespective the annealing oxygen potentials. (b) An impression at the SIMFUEL surface (50 GWd/t) observed after the Vickers hardness measurement.

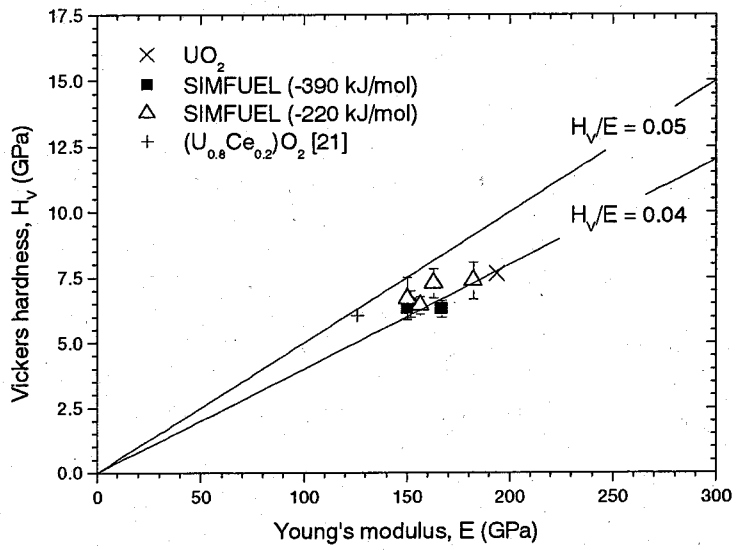

Figure 25. Relationships between the Vickers hardness and Young's modulus of UO_2 and the SIMFUEL.

2.2. Oxide and Metallic Precipitates

2.2.1. Thermal and Mechanical Properties of Oxide Inclusions

2.2.1.1. Introduction

In an irradiated nuclear fuel, a number of fission product (FP) elements are produced and they affect the fuel performance. Especially the FP elements precipitated in the fuel matrix, such as oxide and metallic inclusions, have a great influence on the thermal and mechanical properties of the fuel. Therefore, the behavior of FP elements and the properties of their compounds are very important for evaluation of the safety of the fuels. It is known that some FP elements are soluble in the fuel matrix and others form the oxide or metallic inclusions [1-6]. The white metallic precipitates composed of Mo-Tc-Ru-Rh-Pd alloys and the oxide precipitates with a perovskite type structure of (Ba,Sr)(U,Pu,Zr,RE,Mo)O_3 have been observed in the irradiated oxide fuels. It is considered that the inclusions affect the thermochemical and -physical properties of the fuel.

We have systematically studied the thermophysical and -chemical properties of Ba series perovskite type oxides until now [7-15]. In the present paper, the thermal and mechanical properties, viz. the thermal expansion coefficient, melting point, elastic modulus, microhardness, heat capacity, and thermal conductivity of $BaUO_3$, $BaZrO_3$, $BaCeO_3$, and $BaMoO_3$ are studied.

2.2.1.2. Experimental

Polycrystalline perovskite type oxides, $BaUO_3$, $BaZrO_3$, and $BaCeO_3$ were prepared by mixing the appropriate amounts of UO_2, ZrO_2, CeO_2, and $BaCO_3$ followed by reacting at 1273 K and sintering at 1773 K. Polycrystalline $BaMoO_3$ was prepared by a reduction of $BaMoO_4$ (supplied by Furuuchi Chemical Co., Ltd.) under 4 % H_2-Ar atmosphere at 1523 K.

The crystal structure of the samples was analyzed by both the powder X-ray diffraction method and Raman spectroscopy. The powder X-ray diffraction was performed at room temperature using Cu-Kα radiation. The Raman spectra were recorded by using a NR-1600 (JASCO Co. Ltd.) using an argon laser with a wavelength of 514 nm operated at 100 mW. In order to determine the chemical composition, the SEM-EDX analysis was performed using a HITACHI S-2600H SEM instrument equipped with an energy-dispersive HORIBA EX-200 system. The oxygen analysis was also performed by using HORIBA EMGA-550 to identify the oxygen concentration of the samples. For measurements of the thermal conductivities and heat capacities, appropriate shapes of the samples were cut from the sintered pellets. The bulk density was determined by the weight and geometric measured volume.

The thermal expansion coefficient was evaluated by using a dilatometer in the temperature range from room temperature to about 1000 K under a reduction atmosphere. The melting point was measured by a thermal arrest method under a reduction atmosphere. The

longitudinal and shear sound velocities were measured by an ultrasonic pulse-echo method at room temperature, which enables us to evaluate the elastic moduli and the Debye temperature. From the obtained sound velocities of the sintered pellets with porosity, the elastic moduli and Debye temperature for 100 % of the theoretical density were estimated by using a finite element method. Hardness measurements were also performed, at room temperature, using a micro-Vickers hardness tester. The heat capacity was measured by using a differential scanning calorimeter, DSC (ULVAC Co. Ltd.) with triple cells in a high purity argon atmosphere. The samples were heated with small and large temperature intervals. The heat capacity was determined by both enthalpy and scanning methods at individual temperatures. The thermal diffusivity was measured by a laser flash method by using an ULVAC TC-7000 in the temperature range from room temperature to 1400 K in vacuum. The thermal conductivity was evaluated from the heat capacity, thermal diffusivity, and density.

2.2.1.3. Results and Discussion

The powder X-ray diffraction patterns at room temperature of $BaUO_3$, $BaZrO_3$, $BaCeO_3$, and $BaMoO_3$ are shown in Fig. 1. It is found that the perovskite type single phase is obtained in the present study.

The conventional parameter describing the geometric distortion of a perovskite type compound is defined as a tolerance factor, t:

$$t = \frac{r_A + r_O}{\sqrt{2}(r_B + r_O)}, \qquad (1)$$

where r_A, r_B, r_O are the ionic radii of each atom. Ordinarily, the value of "t" is within 0.75 to 1.1 for the perovskite type oxides. The cubic structure has a value near 1. As the value of "t" shifts from 1, a geometric distortion becomes gradually large. The values of the tolerance factor "t" of $BaUO_3$, $BaZrO_3$, $BaCeO_3$, and $BaMoO_3$ are shown in Table1. The Shannon's values of the ionic radius [16] are referred in the present study.

It is reported that the crystal structure of $BaCeO_3$ at room temperature is orthorhombic (*Pnma*), equivalent to a small distortion of the cubic structure [17]. On the other hand, $BaUO_3$, $BaZrO_3$, and $BaMoO_3$ are cubic at room temperature. The Raman spectra of $BaZrO_3$ and $BaCeO_3$ are shown in Fig. 2, together with the XRD patterns. The Raman spectrum of $BaZrO_3$ shows a very low intensity, showing that this substance has a cubic structure (*Pm3m*), while the Raman-active modes of the orthorhombic structure are easily observed in the Raman spectrum of $BaCeO_3$. These results are similar to those in literatures [18,19]. The crystal structures of $BaZrO_3$ and $BaCeO_3$ are shown in Fig. 3.

The lattice parameters evaluated from the X-ray diffraction patterns correspond to the previously reported values [17,19-21]. The bulk densities of the samples are about 90 % of the

theoretical densities calculated from the lattice parameters. The chemical composition of the samples does not deviate from the stoichiometric composition. The lattice parameters and O/M ratios of the samples are shown in Table 1.

Figure 4 shows the relationship between the molar volume and ionic radius of M^{4+} for $BaMO_3$ type perovskite type oxides. The values of the ionic radius are obtained from a literature [16]. The molar volume increases linearly with increasing the ionic radius of M^{4+} ions.

The thermal expansions of the samples measured by the dilatometer are shown in Fig. 5, together with the data of UO_2 [22]. The thermal expansions of $BaUO_3$ and $BaCeO_3$ nearly equal that of UO_2, while $BaZrO_3$ and $BaMoO_3$ show slightly lower thermal expansion. From the slope of the thermal expansion curves shown in Fig. 5, the linear thermal expansion coefficients α_l of the samples were evaluated as shown in Table 1.

The melting points T_m measured by the thermal arrest method of $BaUO_3$, $BaZrO_3$, $BaCeO_3$, and $BaMoO_3$ are shown in Table 1. In the present study, the melting point of $BaZrO_3$ was not evaluated because of the unclear thermal arrest signal, so the reference value [23] is shown in Table 1. It is empirically confirmed that the linear thermal expansion coefficient varies inversely as the melting point for many substances, and for some substances the following relationships between α_l and T_m in K have been reported [24]:

$$\alpha_l \cdot T_m = 0.019 \quad \text{(for metals)}, \tag{2}$$

$$\alpha_l \cdot T_m = 0.030 \quad \text{(for fluorite type oxides)}. \tag{3}$$

The relationship between α_l and T_m for $BaUO_3$, $BaZrO_3$, $BaCeO_3$, and $BaMoO_3$ is shown in Fig. 6, together with the data of UO_2 [7]. For $BaZrO_3$ and $BaCeO_3$, the products of α_l and T_m show approximately same value (= 0.022). The product of α_l and T_m for $BaUO_3$ shows slightly higher value (= 0.027) than those for $BaZrO_3$ and $BaCeO_3$, while that for $BaMoO_3$ shows slightly lower value (= 0.017).

For isotropic media, the shear modulus G, Young's modulus E, compressibility β, and Debye temperature θ_D can be written in terms of the longitudinal sound velocity V_L and shear sound velocities V_S as [25-27]:

$$G = \rho V_S^{\,2}, \tag{4}$$

$$E = \frac{G\left(3V_L^{\,2} - 4V_S^{\,2}\right)}{\left(V_L^{\,2} - V_S^{\,2}\right)}, \tag{5}$$

$$\beta = \frac{1}{\rho\left(V_L^{\,2} - \frac{4}{3}V_S^{\,2}\right)}, \tag{6}$$

$$\theta_D = \left(\frac{h}{k_B}\right)\cdot\left[\frac{9N}{4\pi V\cdot\left(V_L^{\,-3} + 2V_S^{\,-3}\right)}\right]^{\frac{1}{3}}, \tag{7}$$

where ρ is the sample density, h is the Plank constant, k_B is the Boltzmann constant, N is the number of atoms in a unit cell, and V is the unit cell volume. The longitudinal and shear sound velocities of $BaZrO_3$ and $BaCeO_3$ were measured at room temperature and in air. The elastic moduli and Debye temperature evaluated in the present study are shown in Table 1. Figure 7 shows the relationship between the Young's modulus E and tolerance factor t for the perovskite type oxides. The Young's modulus becomes small as the tolerance factor deviates from 1, indicating that the symmetry of the crystal affects the elastic properties.

For some substances, Young's modulus E is proportional to $q(RT_m/V_m)$ [28], where q is the number of atoms in the chemical formula, T_m is the melting temperature in K, V_m is the molar volume, and R is the gas constant. For pure metals, we have obtained the following relationship [29]:

$$E = 97.9 \cdot q\left(\frac{RT_m}{V_m}\right), \tag{8}$$

which is in good agreement with the results of Frost and Ashby [28]. In the present study, the melting point of $BaZrO_3$ is referred to literature data [23]. The Young's moduli E of $BaUO_3$, $BaZrO_3$, $BaCeO_3$, and $BaMoO_3$ are shown in Fig. 8 as a function of $q(RT_m/V_m)$, together with the data of UO_2 [10]. In the relationship between E and $q(RT_m/V_m)$, $BaZrO_3$, $BaCeO_3$, and $BaMoO_3$ show similar characteristics and the proportionality is almost identical. Although $BaUO_3$ has the same crystal structure as $BaZrO_3$ and $BaMoO_3$, the proportionality between E and $q(RT_m/V_m)$ is almost identical with that of SiO_2 glass.

It is known that the Debye temperature θ_D can be related to the melting temperature T_m in K, the molar mass M, and the molar volume V_m by a Lindemann relationship [30]. The relationships were reexamined for the perovskite type oxides, and the ratio of θ_D to $q^{5/6}(T_m/(MV_m^{2/3}))^{1/2}$ was evaluated to be 1.60 [31], where q is the number of atoms in the chemical formula. Figure 9 shows this relationship for $BaUO_3$, $BaZrO_3$, $BaCeO_3$, and $BaMoO_3$, together with the data of other substances [10,32]. The proportionality constants of $BaZrO_3$, $BaCeO_3$, and $BaMoO_3$ are almost identical (around 1.60), indicating typical characteristics of the perovskite type oxides. However, the tendency differs between $BaUO_3$ and other perovskite type oxides, which apparently shows the glass-like characteristics of $BaUO_3$.

The hardness is associated with the resistance of a material to plastic deformation. The measurements were repeated ten times for a given sample, and the applied load and loading time were chosen to be 9.8 N and 30 s. The values of the Vickers microhardness obtained for $BaUO_3$, $BaZrO_3$, $BaCeO_3$, and $BaMoO_3$ are shown in Table 1.

For some oxides and carbides, the hardness H is found to be proportional to Young's modulus E with the following relationship [33]:

$$H/E \approx 0.05. \tag{9}$$

We have estimated the H/E for pure metals using literature data [34] and obtained the values of 0.006, 0.003, and 0.004 for bcc, fcc, and hcp metals, respectively [29]. The values of H for the perovskite type oxides are plotted in Fig. 10 as a function of Young's modulus E, together with other substances data [10,32]. Since both the hardness and elastic modulus are affected by the sample density at the same level, therefore, the non-correcting values of the Young's modulus are plotted in Fig. 10. $BaZrO_3$, $BaCeO_3$, and $BaMoO_3$ show similar characteristics, and the proportionality constants are around 0.03. However, the relationship between the Vickers hardness and Young's modulus for $BaUO_3$ is similar to that of SiO_2 glass.

Figure 11 shows the temperature dependence of the heat capacity of $BaUO_3$ determined by the enthalpy method. The C_p of $BaUO_3$ measured in the present study well agrees with the estimated values using the data of Cordfunke et al. [35], but shows slightly higher values than those using the data from MALT2 [36]. The difference comes from the C_p values of BaO, in which it decreases with increasing temperature in MALT2. The temperature dependence of the C_p values of $BaUO_3$, in the temperature range of 373-873K, is determined from the experimental values as follows:

$$C_P(JK^{-1}mol^{-1}) = 126.6 + 1.61\times10^{-2}T - 1.42\times10^{6}/T^2. \quad (10)$$

The temperature dependence of the heat capacity of $BaZrO_3$ determined by the enthalpy and scanning methods is shown in Fig. 12, together with literature data [23,35,37]. The experimental values obtained in the present study well agree with the data of Nagarajan et al. [37] and Vassen et al. [23], while are slightly lower than that of Cordfunke et al. [35]. In the temperature range between 300 K and 1400 K, the empirical equation for the C_P of $BaZrO_3$ is determined from the experimental values as follows:

$$C_P(JK^{-1}mol^{-1}) = 111.1 + 1.21\times10^{-2}T - 6.22\times10^{5}/T^2. \quad (11)$$

The temperature dependence of the heat capacity of $BaCeO_3$ determined by the enthalpy and scanning methods is shown in Fig. 13, together with literature data [38,39]. The experimental values obtained in the present study are slightly lower than those in literatures. Three signals associated with the phase transitions are observed in our experimental data determined by the scanning methods. It is reported that $BaCeO_3$ evolves slowly toward ideal cubic perovskite structure with increasing temperature. Knight [20] examined the phase transition of $BaCeO_3$ by a neutron diffraction method, and reported that the phase transitions occur at 560 K (orthorhombic, *Imma*), at 670 K (rhombohedral, $R\bar{3}c$), and at 1170 K (cubic, $Pm3m$). In the present study, the transition temperatures observed in the C_P curve of $BaCeO_3$ are 540 K, 600 K, and 1180 K, which almost agree with the previously reported values.

The temperature dependence of the heat capacity of $BaMoO_3$ determined by the enthalpy and scanning methods is shown in Fig. 14. Cordfunke and Konings have estimated the heat capacity at room temperature from a comparison with $BaZrO_3$ and recommended 101.7

$JK^{-1}mol^{-1}$ at 298.15 K [35]. Agarwal et al., has evaluated the heat capacity from the Enthalpy increment [40]. In the present study, the empirical equation for the C_P of $BaMoO_3$ up to 800 K is determined from the experimental values as follows:

$$C_P(JK^{-1}mol^{-1}) = 131.8 + 9.36\times10^{-3}T - 4.33\times10^{6}/T^2. \quad (12)$$

Our experimental data is slightly lower than literature data. On the other hand, it well agrees with the data obtained from Newmann Kopp's rule based on the heat capacities of the constituent binary oxides, BaO and MoO_2, taken from Kubaschewski [41].

The heat capacity at constant pressure C_P can be evaluated from the following relationship:

$$C_P = C_h + C_d + C_{others}, \quad (13)$$

where C_h is the harmonic term, C_d is the lattice dilation term, and C_{others} is the residual term. The harmonic term C_h is expressed by using the Debye temperature θ_D as follows:

$$C_h = 3nRD\left(\theta_D/T\right), \quad (14)$$

where n is the number of atoms per molecule, R is the gas constant, and $D(\theta_D/T)$ is the Debye function. The lattice dilatational term C_d can be calculated from the volumetric thermal expansion coefficient α_V and compressibility β as follows:

$$C_d = \frac{\alpha_V{}^2 V_m T}{\beta}, \quad (15)$$

where V_m is the molar volume and T is the absolute temperature.

The temperature dependences of the C_P, C_h, and $(C_h + C_d)$ of $BaUO_3$ and $BaZrO_3$ are shown in Fig. 15. It is confirmed that the measured C_P of $BaZrO_3$ is nearly consistent with the $(C_h + C_d)$. On the other hand, the measured C_P of $BaUO_3$ is higher than the $(C_h + C_d)$, indicating the existence of other contributions. The residual term C_{others} of $BaUO_3$ is approximately evaluated to be proportional to the absolute temperature.

The thermal conductivity λ was calculated from the thermal diffusivity D, heat capacity C_P, and density ρ by using the following relationship:

$$\lambda = DC_P\rho. \quad (16)$$

The thermal diffusivity was measured by the laser flash method. The temperature dependence of the thermal conductivities of $BaUO_3$, $BaZrO_3$, $BaCeO_3$, and $BaMoO_3$ are shown in Fig. 16, together with that of UO_2 [42]. The thermal conductivities were corrected to 100 % of the theoretical density by using Schulz's equation [43]. The thermal conductivities of $BaZrO_3$, $BaCeO_3$, and $BaMoO_3$ decrease with increasing temperature, showing a phonon conduction mechanism. The thermal conductivities of $BaUO_3$, $BaZrO_3$, and $BaCeO_3$ are lower than that of UO_2 in the whole temperature range, especially that for $BaUO_3$ shows the extremely low values. The thermal conductivity at room temperature of $BaUO_3$ is around 1 $Wm^{-1}K^{-1}$, which is about

10 times lower than that of UO_2. On the other hand, $BaMoO_3$ shows the extremely high values, in which the thermal conductivity at room temperature of $BaMoO_3$ is around 30 $Wm^{-1}K^{-1}$.

The electrical resistivity and Seebeck coefficient of $BaUO_3$ and $BaMoO_3$ were measured simultaneously by using ULVAC ZEM-1 in He atmosphere. The electrical resistivities of $BaZrO_3$ and $BaCeO_3$ are too high to measure by using our apparatus. The temperature dependence of the electrical resistivities of $BaUO_3$ and $BaMoO_3$ is shown in Fig. 17, together with the data of other substances [44-46]. The electrical resistivity of $BaUO_3$ shows semiconducting characteristics with the negative temperature coefficient, while that of $BaMoO_3$ shows metallic characteristics with the positive temperature coefficient. The electrical resistivity of $BaUO_3$ is higher by approximately five to seven orders of magnitude than that of $BaMoO_3$.

The temperature dependence of the Seebeck coefficients of $BaUO_3$ and $BaMoO_3$ is shown in Fig. 18, together with the data of other substances [44-46]. The Seebeck coefficients of $BaUO_3$ and $BaMoO_3$ are negative in the whole temperature range, showing that the majority of charge carriers are electrons. The absolute value of the Seebeck coefficient of $BaUO_3$ increases with increasing temperature, while that of $BaMoO_3$ keeps constant. The absolute value of the Seebeck coefficient of $BaUO_3$ reaches a maximum value of about 170 μVK^{-1} at 900 K, which is relatively high value comparable to the currently used thermoelectric materials.

It is well known that the total thermal conductivity λ_{total} of solids can be written as follows:

$$\lambda_{total} = \lambda_{lat} + \lambda_{el} + \cdots, \quad (17)$$

where λ_{lat} is the lattice contribution and λ_{el} is the electronic contribution. The electronic part of the thermal conductivity λ_{el} is calculated from the Wiedemann Franz Lorenz relation:

$$\lambda_{el} = L\sigma T, \quad (18)$$

where L is the Lorenz number, σ is the electrical conductivity, and T is the absolute temperature. The λ_{el} of $BaUO_3$ and $BaMoO_3$ evaluated from the measured electrical resistivities are shown in Figs. 19 and 20, together with the measured total thermal conductivity λ_{total}. For $BaUO_3$, the λ_{el} is not significant compared to the measured total thermal conductivity throughout all temperature range. For $BaMoO_3$, however, the λ_{el} is about 40 % of the λ_{total} at room temperature and it decreases gradually with increasing temperature. The high thermal conductivity of $BaMoO_3$ is due to the large electronic component of the thermal conductivity.

2.2.1.4. Conclusion

The thermal and mechanical properties of $BaUO_3$, $BaZrO_3$, $BaCeO_3$, and $BaMoO_3$ have been measured and the relationships between the properties have been studied. The thermal expansions of $BaUO_3$ and $BaCeO_3$ nearly equal that of UO_2, while $BaZrO_3$ and $BaMoO_3$ show slightly lower thermal expansion. In the relationship between α_l and T_m, the

product of α_l and T_m for $BaUO_3$ shows slightly higher value (= 0.027) than those for $BaZrO_3$ and $BaCeO_3$, while that for $BaMoO_3$ shows slightly lower value (= 0.017). In the relationship between E and $q(RT_m/V_m)$, $BaZrO_3$, $BaCeO_3$, and $BaMoO_3$ show similar characteristics and the proportionality is almost identical. Although $BaUO_3$ has the same crystal structure as $BaZrO_3$ and $BaMoO_3$, the proportionality between E and $q(RT_m/V_m)$ is almost identical with that of SiO_2 glass. The heat capacities of $BaUO_3$, $BaZrO_3$, $BaCeO_3$, and $BaMoO_3$ have been measured by the DSC. It is confirmed that the measured C_P of $BaZrO_3$ is nearly consistent with the $(C_h + C_d)$. On the other hand, the measured C_P of $BaUO_3$ is higher than the $(C_h + C_d)$, indicating the existence of other contributions. The thermal conductivities of $BaUO_3$, $BaZrO_3$, and $BaCeO_3$ are lower than that of UO_2 in the whole temperature range, especially that for $BaUO_3$ shows the extremely low values. The thermal conductivity at room temperature of $BaUO_3$ is around 1 $Wm^{-1}K^{-1}$, which is about 10 times lower than that of UO_2. On the other hand, $BaMoO_3$ shows the extremely high values, in which the thermal conductivity at room temperature of $BaMoO_3$ is around 30 $Wm^{-1}K^{-1}$.

References

[1] F.T. Ewart, R.G. Taylor, J.M. J.M. Horspool, and G. James, J. Nucl. Mater., 61 (1976) 254.

[2] H. Kleykamp, J.O. Paschoal, R. Pejsa, and F. Thummler, J. Nucl. Mater., 130 (1985) 426.

[3] H. Kleykamp, J. Nucl. Mater., 131 (1985) 221.

[4] D.R. O'boyle, F.L. Browm, and A.E. Dwight, J. Nucl. Mater., 35 (1970) 257.

[5] I. Sato, H. Furuya, T. Arima, K. Idemitsu, and K. Yamamoto, J. Nucl. Mater., 273 (1999) 239.

[6] I. Sato, H. Furuya, T. Arima, K. Idemitsu, and K. Yamamoto, J. Nucl. Sci. Technol., 36 (1999) 775.

[7] S. Yamanaka, K. Kurosaki, T. Matsuda, and M. Uno, J. Nucl. Mater., 294 (2001) 99.

[8] K. Kurosaki, T. Matsuda, M. Uno, S. Kobayashi, and S. Yamanaka. J. Alloys and Comp., 319 (2001) 271.

[9] T. Matsuda, S. Yamanaka, K. Kurosaki, M. Uno, and S. Kobayashi, J. Alloys and Comp., 322 (2001) 77.

[10] S. Yamanaka, T. Matsuda, K. Kurosaki, and M. Uno, J. Nucl. Sci. Technol., Supl.3 (2002) 709.

[11] K. Kurosaki, S. Yamanaka, T. Matsuda, and M. Uno, J. Nucl. Sci. Technol., Supl.3 (2002) 807.

[12] K. Kurosaki, T. Oyama, T. Matsuda, M. Uno, and S. Yamanaka, J. Nucl. Sci. Technol., Supl.3 (2002) 815.

[13] T. Matsuda, S. Yamanaka, K. Kurosaki, S. Kobayashi, and M. Uno, J. Nucl. Sci. Technol., Supl.3 (2002) 823.

[14] S. Yamanaka, T. Hamaguchi, T. Oyama, T. Matsuda, S. Kobayashi, and K. Kurosaki, J. Alloys and Comp., in press (JALCOM9660).

[15] S. Yamanaka, M. Fujikane, T. Hamaguchi, H. Muta, T. Oyama, T. Matsuda, S. Kobayashi, and K. Kurosaki, J. Alloys and Comp., in press (JALCOM####).

[16] R.D. Shannon, Acta Cryst., A32 (1976) 751.

[17] A.J. Jacobson, B.C. Tofield, and B.E.F. Fender, Acta Cryst. B28 (1972) 956.

[18] F. Genet, S. Loridamt, and G. Lucazeau, J. Raman Spectroscopy, 28 (1997) 255.

[19] I. Charrier-Cougoulic, T. Pagnier, and G. Lucazeau, J. Solid State Chem., 142 (1999) 220.

[20] K.S. Knight, Solid State Ion., 74 (1994) 109.

[21] K. Kamata, T. Nakamura, and T. Sata, Mat. Res. Bull., 10 (1975) 373.

[22] D.G. Martin, J. Nucl. Mater., 152 (1988) 94.

[23] R. Vassen, X. Cao, F. Tietz, D. Basu, and D. Stover, J. Am. Ceram. Soc., 83 (2000) 2023.

[24] L.G. Van Uitert et al., Mat. Res. Bull., 12 (1977) 261.

[25] K. Yamada, S. Yamanaka, and M. Katsura, Tech. Rep. Osaka Univ., 47 (1997) 181.

[26] M. Fukuhara and I. Yamauchi, J. Mater. Sci., 28 (1993) 4681.
[27] H. Inaba and T. Yamamoto, Netsu Sokutei, 10 (1983) 132.
[28] H.J. Frost and M.F. Ashby, Deformation-Mechanism Maps, Pergamon Press, Oxford, 1982.
[29] S. Yamanaka, K. Yamada, T. Tsuzuki, T. Iguchi, M. Katsura, Y. Hoshino, and W. Saiki, J. Alloys and Compounds, 271-273 (1998) 549.
[30] F.A. Lindemann, Physikalische Zeitschrift, No.14, pp. 609, (1910).
[31] The Chemical Society of Japan ed., Kikan Kagaku Sousetsu, Perovskite-Related Compounds, No. 32, pp. 37-51, (1997).
[32] A. Bartolotta, G. Carini, G. D'Angelo, A. Fontana, F. Rossi, and G. Tripodo, J. Non-Crystalline Solids, 245 (1999) 9.
[33] K. Tanaka, Int. J. Eng. Sci., 27 (1989) 11.
[34] S. Yamamoto, Atarashii Zairyoukagaku, Shouwadou, Kyoto, (1990).
[35] E.H.P. Cordfunke and R.J.M. Konings, editor, "Thermochemical data for Reactor Materials and Fission Products", 1990, North-Holland, Amsterdam.
[36] Japan Thermal Measurement Society, Thermodynamics database for personal computer MALT2, (1992).
[37] K. Nagarajan, R. Saha, R. Babu, and C.K. Mathews, Thermochimica Acta, 90 (1985) 297.
[38] R. Saha, R. Babu, K. Nagarajan, and C.K. Mathews, Thermochimica Acta, 120 (1987) 29.
[39] R. Venkata Krishnan, K. Nagarajan, and P.R. Vasudeva Rao, J. Nucl. Mater., 299 (2001) 28.
[40] R. Agarwal, Z. Singh, and V. Venugopal, J. Alloys and Comp., 282 (1999) 231-235.
[41] O. Kubaschewski, C.B. Alcock, and P.J. Spencer, Metallurgical Thermochemistry, 6th ed., Pergamon Press, Oxford, 1993, Xii, p. 363, ISBN 0-08-041888-0.
[42] MATPRO-Version 11 (Revision 2), NUREG/CR-0497, TREE-1280, Rev. 2, August (1981).
[43] B. Schulz, High Temp.-High Press., 13 (1981) 649.
[44] R.S. Caputo and V.C. Truscello, Proc. IECEC, (1974) 637.
[45] B. Abeles and R.W. Cohen, J. Appl. Phys., 35 (1964) 247.
[46] J.P. Dismukes, L. Ekstrom, E.F. Steigmeier, I. Kudman, and D.S. Beers, J. Appl. Phys., 35 (1964) 2899.

Table 1

Thermophysical properties of the perovskite type oxides

			$BaUO_3$	$BaZrO_3$	$BaCeO_3$	$BaMoO_3$
Tolerance factor		t	0.935	1.011	0.943	1.047
Crystal system			Cubic	Cubic	Orthorhombic	Cubic
Lattice parameters	(nm)	a	0.4404	0.4192	0.8786	0.4040
		b	-	-	0.6251	-
		c	-	-	0.6220	-
O/M ratio			2.96±0.02	3.01±0.01	3.06±0.07	2.97±0.07
Linear thermal expansion coefficient	(K^{-1})	α_l	1.10×10^{-5}	7.13×10^{-6}	1.12×10^{-5}	9.46×10^{-6}
Melting temperature	(K)	T_m	2450	2978 [23]	2016	1791
Shear modulus	(GPa)	G	45.8	103	58.7	94.3
Young's modulus		E	113	243	154	235
Compressibility	(GPa^{-1})	β	0.0138	0.00786	0.00723	0.00648
Debye temperature	(K)	θ_D	302	544	394	512
Vickers hardness	(GPa)	H_V	5.46	4.95	2.34	3.23

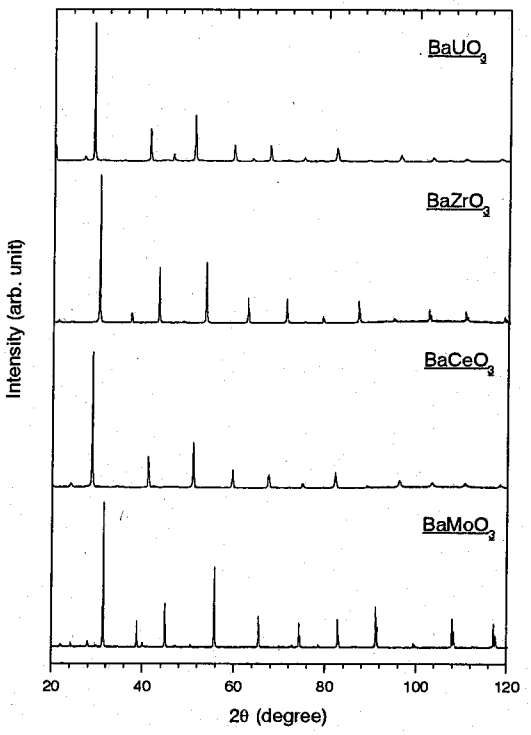

Figure 1. X-ray diffraction patterns of $BaUO_3$, $BaZrO_3$, $BaCeO_3$, and $BaMoO_3$ at room temperature.

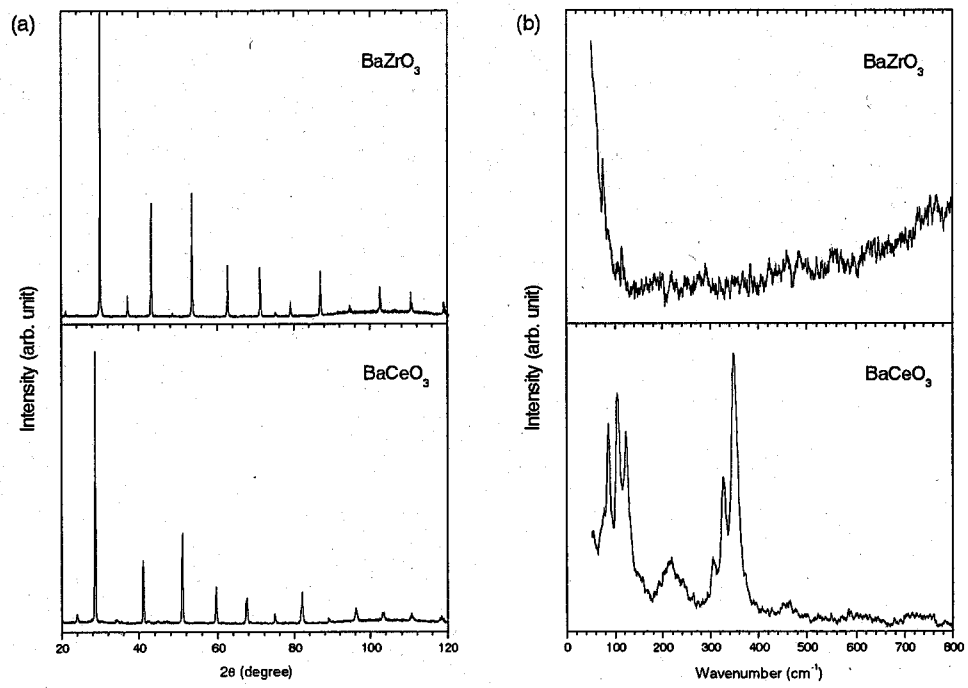

Figure 2. X-ray diffraction patterns (a) and Raman spectra (b) of $BaZrO_3$ and $BaCeO_3$ at room temperature.

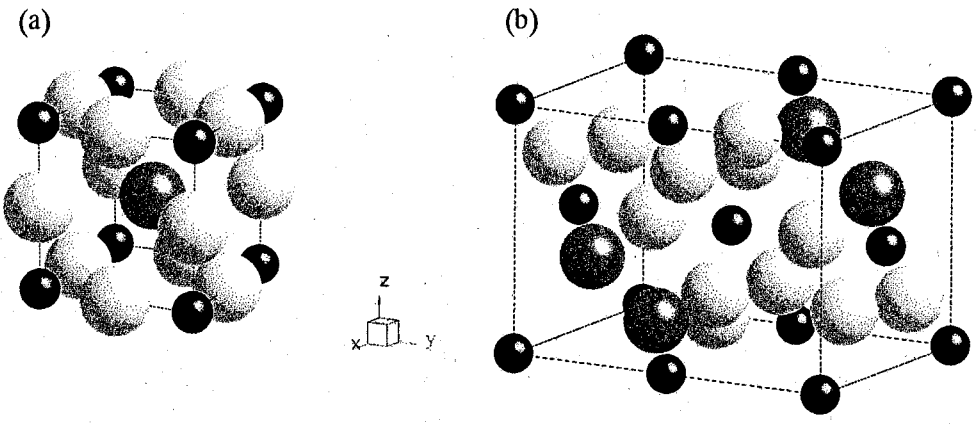

Figure 3. Crystal structures of (a) $BaZrO_3$ and (b) $BaCeO_3$: The black, dark gray, and light gray spheres show zirconium or cerium atoms, barium atoms, and oxygen atoms, respectively.

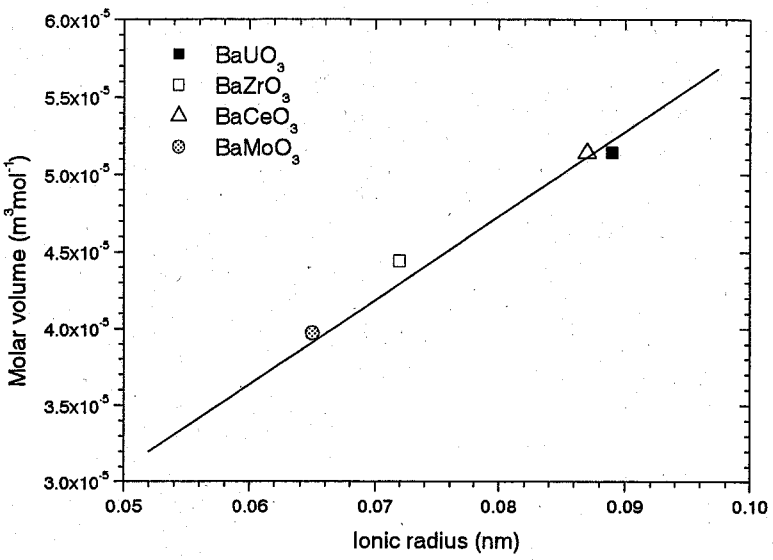

Figure 4. Relationship between molar volume and ionic radius of M^{4+} for $BaMO_3$ type perovskite type oxides.

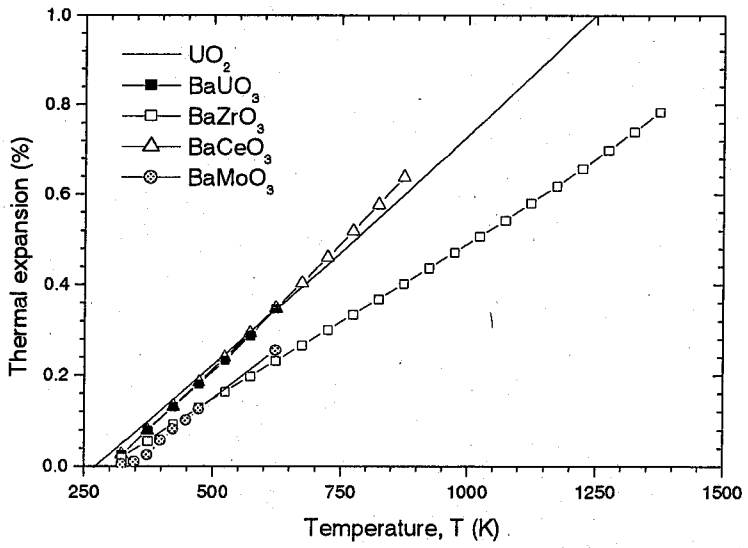

Figure 5. Thermal expansions of the perovskite type oxides and UO_2.

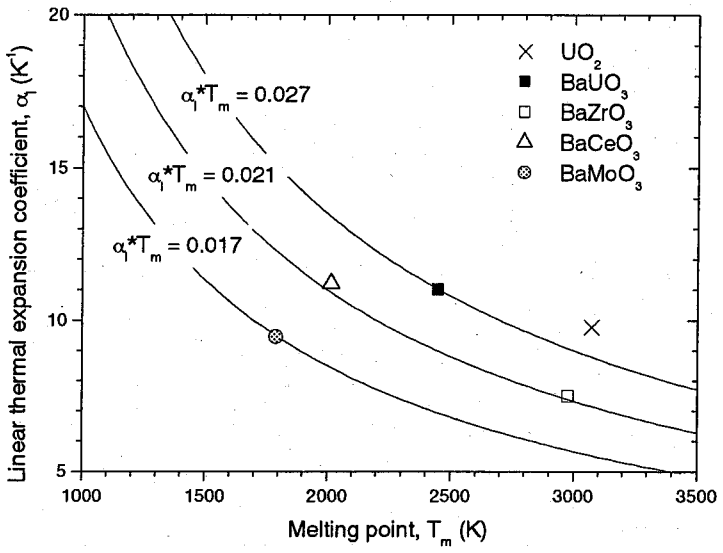

Figure 6. Relationship between linear thermal expansion coefficient α_l and melting point T_m for the perovskite type oxides and UO_2.

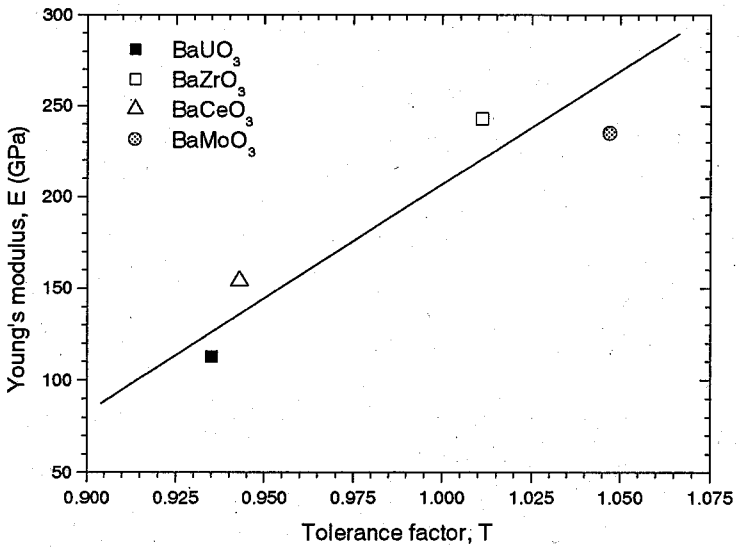

Figure 7. Relationship between Young's modulus E and tolerance factor t for $BaUO_3$, $BaZrO_3$, $BaCeO_3$, and $BaMoO_3$.

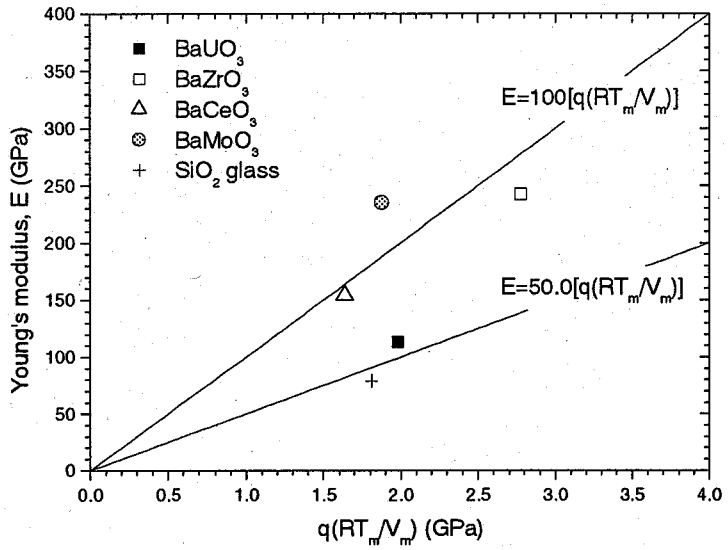

Figure 8. Relationship between Young's modulus E and $q(RT_m/V_m)$ for the perovskite type oxides and SiO_2 glass.

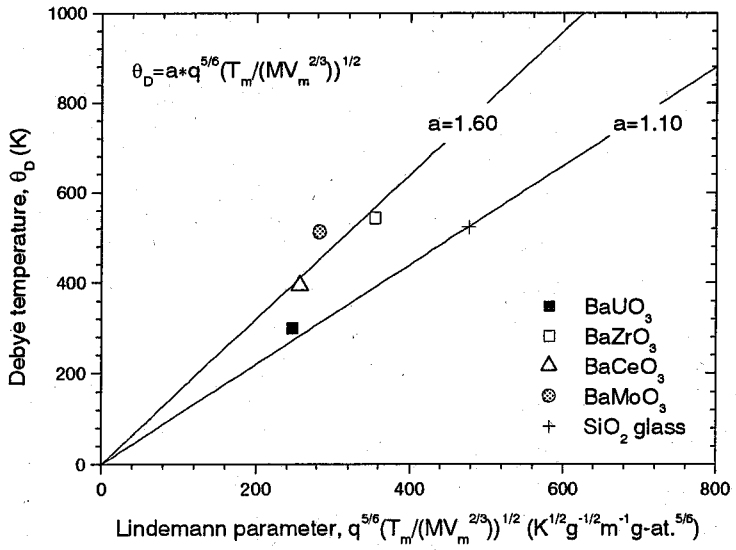

Figure 9. Relationship between Debye temperature θ_D and Lindemann parameter $q(T_m/(MV_m^{2/3}))^{1/2}$ for the perovskite type oxides and SiO_2 glass.

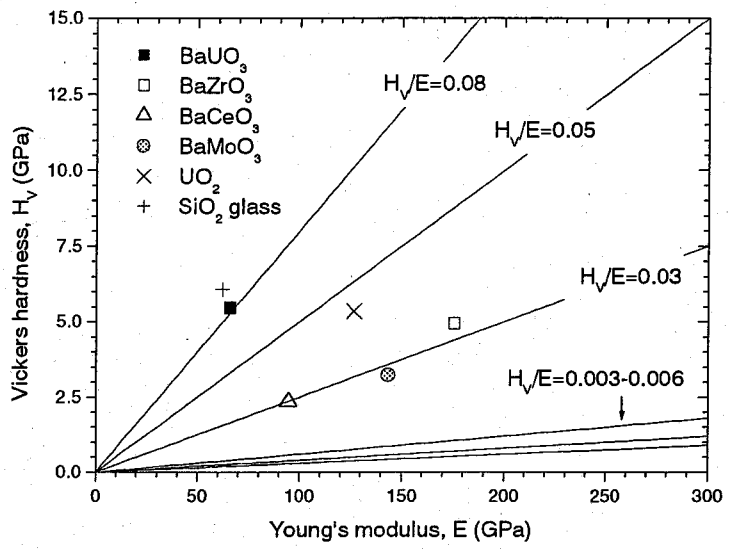

Figure 10. Relationship between Vickers hardness H_V and Young's modulus E for the perovskite type oxides and other materials.

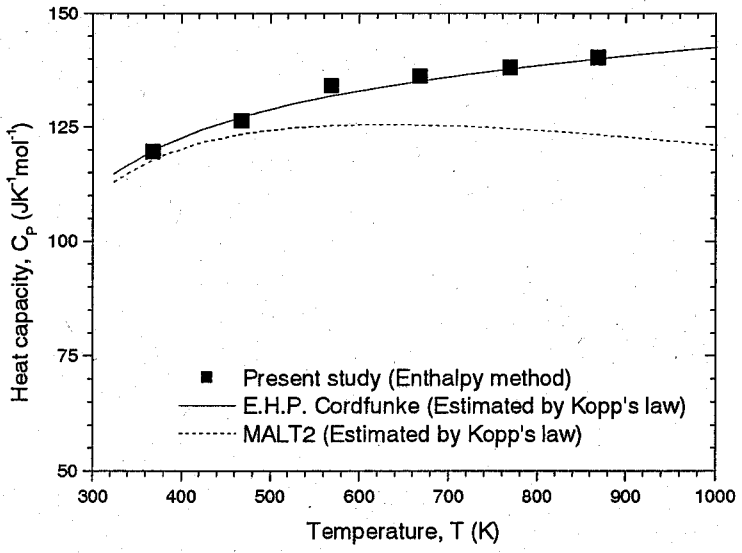

Figure 11. Temperature dependence of the heat capacity of $BaUO_3$.

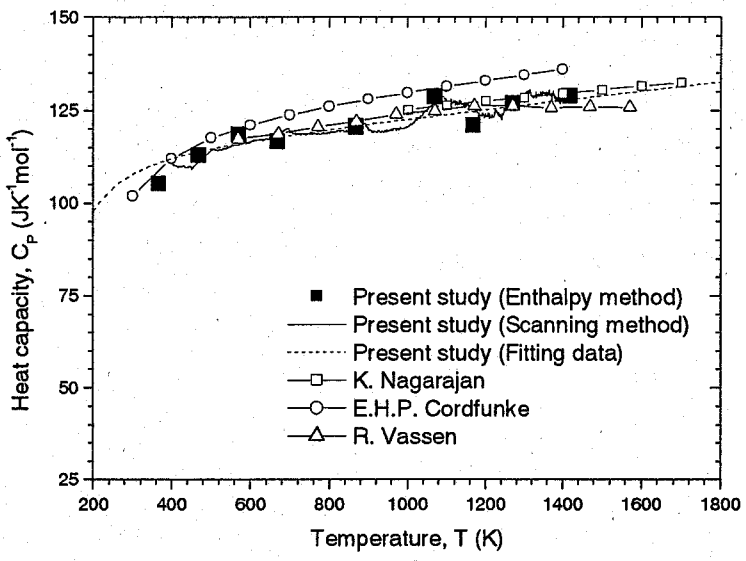

Figure 12. Temperature dependence of the heat capacity of $BaZrO_3$.

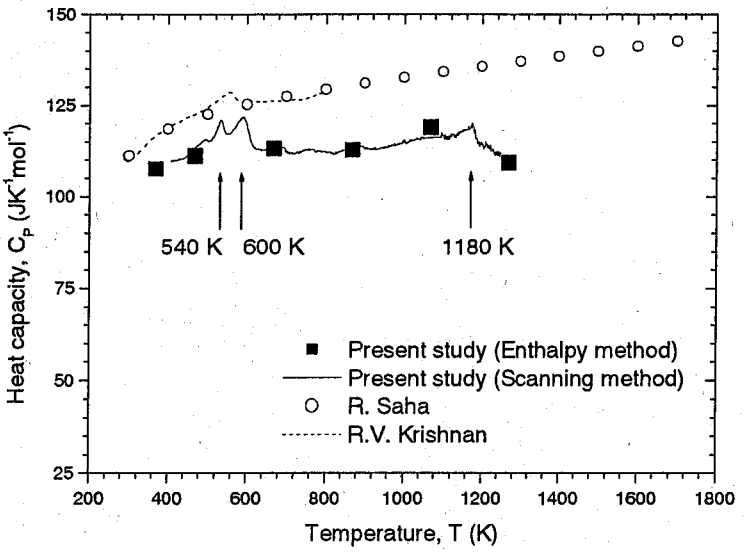

Figure 13. Temperature dependence of the heat capacity of $BaCeO_3$.

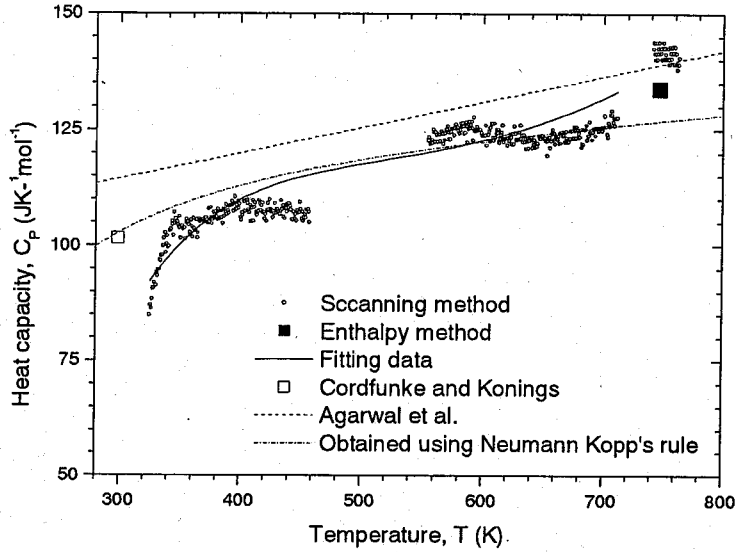

Figure 14. Temperature dependence of the heat capacity of $BaMoO_3$.

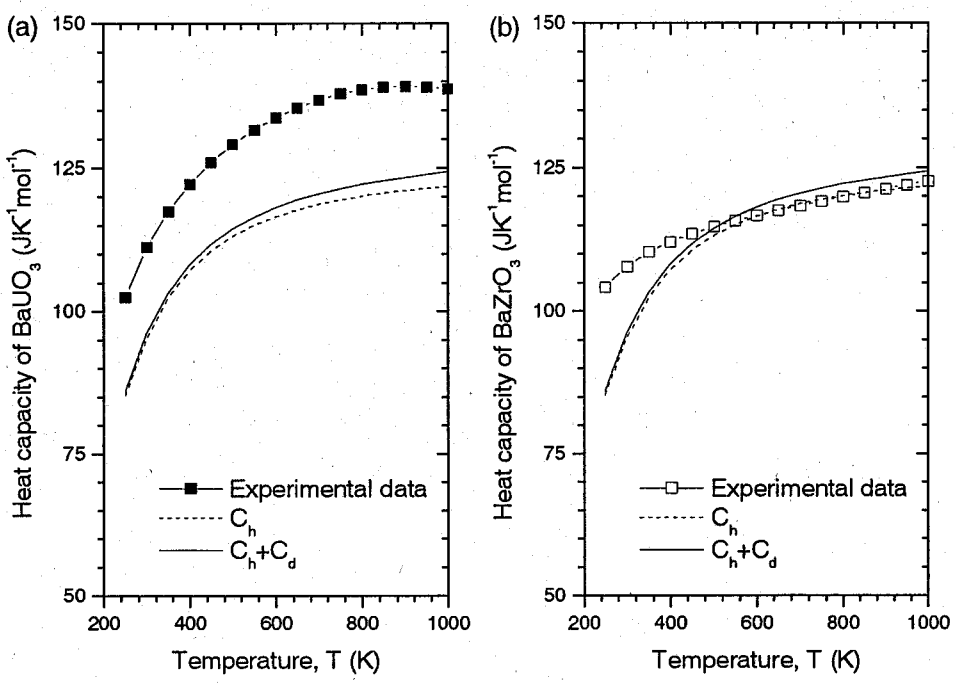

Figure 15. Temperature dependence of the heat capacities of (a) $BaUO_3$ and (b) $BaZrO_3$.

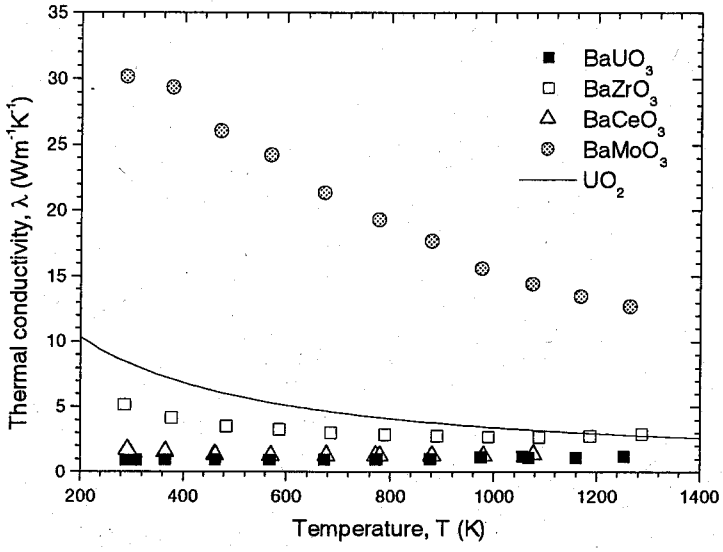

Figure 16. Temperature dependence of the thermal conductivities of the perovskite type oxides and UO_2.

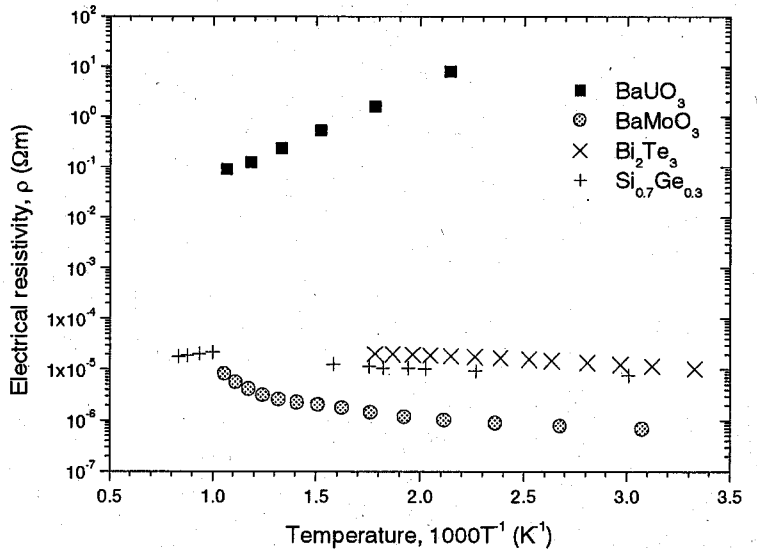

Figure 17. Temperature dependence of the electrical resistivities of $BaUO_3$, $BaMoO_3$, and other substances.

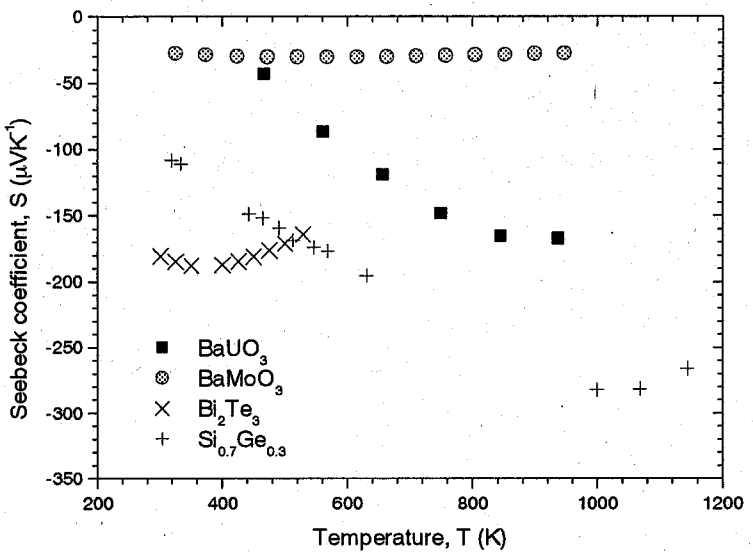

Figure 18. Temperature dependence of the Seebeck coefficients of $BaUO_3$, $BaMoO_3$, and other substances.

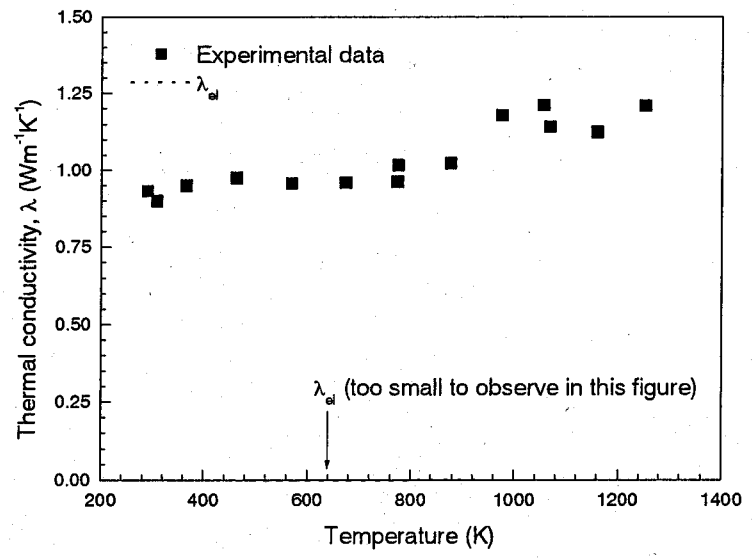

Figure 19. Temperature dependence of the thermal conductivity of $BaUO_3$.

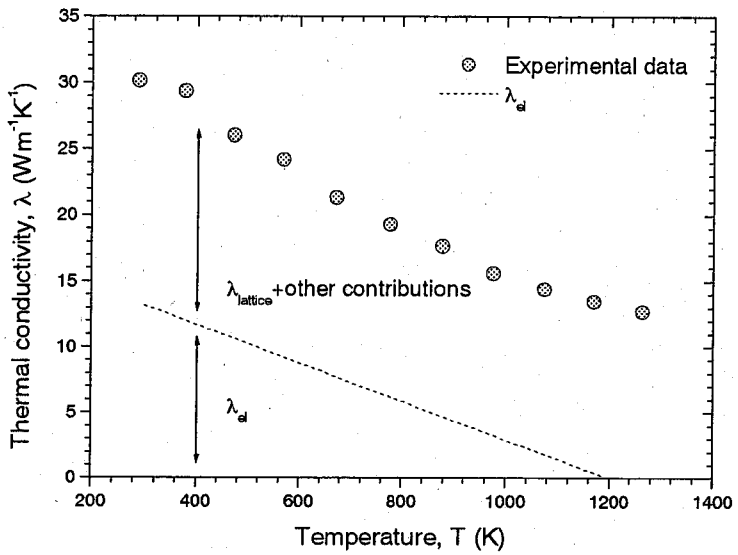

Figure 20. Temperature dependence of the thermal conductivity of $BaMoO_3$.

2.2.2. Thermal Conductivities of Metallic Inclusions

2.2.2.1. Introduction

In an irradiated oxide nuclear fuel, a number of fission product (FP) elements are produced and they affect the fuel performance. Especially the FP elements precipitated in the fuel matrix, such as oxide and metallic inclusions, have a great influence on the thermal and mechanical properties of the fuel. Therefore, it is very important to understand the thermophysical properties of the oxide and metallic inclusions. For the oxide inclusions, gray oxide phases with a perovskite type structure of $(Ba,Sr)(U,Pu,Zr,RE,Mo)O_3$ have been observed in the irradiated fuel [1-4]. In our previous studies, the thermal and mechanical properties of the perovskite type oxides have been systematically studied [5-10]. On the other hand, for the metallic inclusions, white metallic precipitates composed of Mo-Tc-Ru-Rh-Pd alloys have been observed in irradiated fuels [1-3,11,12]. Although the thermodynamic and -chemical properties of the alloys have been studied until now [13-18], information on the thermophysical properties is scarcely reported. In the present study, therefore, the thermal and mechanical properties of Mo-Ru-Rh-Pd alloys, specifically the thermal conductivity, were examined.

2.2.2.2. Experimental

The samples of Mo-Ru-Rh-Pd alloys were prepared by high vacuum induction melting followed by annealing at 1073 K for 10 h in vacuum below 10^{-5} Pa. The purities of the starting materials are above 99.9 %. The crystal structure of the samples was analyzed by a powder X-ray diffraction method at room temperature using Cu-Kα radiation. SEM-EDX analysis was performed by using a HITACHI S-2600H SEM instrument equipped with an energy-dispersive HORIBA EX-200 system. For measurements of the thermophysical properties, appropriate shapes of the samples were cut from the annealed ingots. The density of the samples was calculated from the measured weight and dimensions.

The longitudinal and shear sound velocities were measured by an ultrasonic pulse-echo method at room temperature to evaluate the elastic moduli and Debye temperature. The hardness was measured at room temperature using a micro-Vickers hardness tester. The thermal diffusivity was measured by a laser flash method (ULVAC TC-7000) in the temperature range from 300 K to 1300 K in vacuum. The thermal conductivity was evaluated from the heat capacity, density, and thermal diffusivity. The heat capacity was evaluated from the Neumann-Kopp law using literature data [19,20] of Mo, Ru, Rh, and Pd. In the temperature range from room temperature to about 1000 K, the electrical resistivity and Seebeck coefficient of the samples were measured simultaneously by using ULVAC ZEM-1 in He atmosphere. The Seebeck coefficient was measured in a temperature gradient of about 10 K.

4.3.3. Results and Discussion

The powder X-ray diffraction patterns at room temperature of the Mo-Ru-Rh-Pd alloys show that a hexagonal ε-phase is obtained in the present study. The lattice parameters evaluated from the X-ray diffraction patterns and the chemical compositions evaluated by the EDX analysis are summarized in Table 1. The bulk densities of the samples are 95-98 % of the theoretical density. The chemical compositions of the alloys prepared in the present study are $Mo_{35}Ru_{31}Rh_9Pd_{25}$, $Mo_{20}Ru_{54}Rh_{15}Pd_{11}$, $Mo_{30}Ru_{43}Rh_{14}Pd_{13}$, and $Mo_{43}Ru_{34}Rh_{12}Pd_{11}$. The chemical compositions are plotted on the Mo-Pd-($Ru_{0.7}Rh_{0.3}$) isothermal section as shown in Fig. 1, together with literature data [15]. Form this figure, it seems that the compositions of all the alloys approximately exist in the ε-phase region.

The longitudinal and shear sound velocities of the alloys were measured at room temperature, and the elastic moduli and Debye temperatures were evaluated [5,21,22]. The details of the method to evaluate the elastic moduli from the sound velocity are shown in the previous section. The elastic moduli and Debye temperatures of the alloys are summarized in Table 2.

The micro-Vickers hardness measurements were repeated ten times for a given sample, and the applied load and loading time were chosen to be 4.75 N and 30 s. The values of the hardness obtained for the alloys are given in Table 1.

For some ceramics and glasses, the Vickers hardness H_V has been found to be proportional to the Young's modulus E with the values of [23]:

$$\frac{H_V}{E} \approx 0.05 \quad \text{(for ceramics)}, \tag{1}$$

$$\frac{H_V}{E} \approx 0.08 \quad \text{(for glasses)}. \tag{2}$$

We have evaluated the H_V/E for pure metals and obtained the values of 0.006, 0.003 and 0.004 for bcc, fcc and hcp metals, respectively [24]. The values of H_V for the Mo-Ru-Rh-Pd alloys are plotted in Fig. 2 as a function of the Young's modulus E, together with the data of UO_2 and $(U_{0.8}Ce_{0.2})O_2$ [25]. The relationship between H_V and E for $Mo_{35}Ru_{31}Rh_9Pd_{25}$, $Mo_{30}Ru_{43}Rh_{14}Pd_{13}$, and $Mo_{43}Ru_{34}Rh_{12}Pd_{11}$ show the metallic characteristics, while that for $Mo_{20}Ru_{54}Rh_{15}Pd_{11}$ show the intermediate characteristics between metals and ceramics. In either case, it is found that the mechanical properties of the Mo-Ru-Rh-Pd alloys differ from those of UO_2 and $(U_{0.8}Ce_{0.2})O_2$.

The temperature dependence of the thermal conductivities λ of the alloys is shown in Fig. 3, together with the data of UO_2 [26]. The thermal conductivities of all the alloys almost linearly increase with increasing temperature, showing metallic behavior. The thermal conductivity of $Mo_{20}Ru_{54}Rh_{15}Pd_{11}$ is slightly larger than those of $Mo_{35}Ru_{31}Rh_9Pd_{25}$, $Mo_{30}Ru_{43}Rh_{14}Pd_{13}$, and $Mo_{43}Ru_{34}Rh_{12}Pd_{11}$. The thermal conductivities of all the alloys are

tenfold or above larger than that of UO_2 above about 1000 K.

The temperature dependencies of the electrical resistivities ρ and Seebeck coefficients S of the alloys are shown in Figs. 4 and 5, respectively. The electrical resistivities of all the alloys increase with increasing temperature, showing metallic behavior. The values of the electrical resistivities are of an order of magnitude of about 10^{-6} (Ωm). The Seebeck coefficients of the alloys are positive in the whole temperature range, showing that the majority of charge carriers are holes.

It is well known that the total thermal conductivity λ_{total} of solids can be written as follows:

$$\lambda_{total} = \lambda_{lat} + \lambda_{el} \cdots, \quad (3)$$

where λ_{lat} is the lattice contribution and λ_{el} is the electronic contribution. λ_{el} can be calculated from the Wiedemann-Franz-Lorenz relation:

$$\lambda_{el} = L\sigma T, \quad (4)$$

where L is the Lorenz number, σ is the electrical conductivity, and T is the absolute temperature. λ_{lat} is obtained by subtracting λ_{el} from λ_{total}. As an example, the temperature dependence of the λ_{total}, λ_{el}, and λ_{lat} of $Mo_{35}Ru_{31}Rh_9Pd_{25}$ is shown in Fig. 6. The temperature dependence of λ_{lat} follows a 1/T law, indicating that the λ_{lat} is composed of phonon contribution. It is found that the electronic contribution is more predominant than the lattice contribution in the whole temperature range.

In the present study, it is confirmed that the characteristics of the mechanical and thermal properties of the Mo-Ru-Rh-Pd alloys differ from that of UO_2, which means that if the Mo-Ru-Rh-Pd alloys were precipitated in the irradiated fuel, they probably affect the thermal and mechanical properties of the fuel. In Chapter 3.4, we have performed the FEM (Finite Element Method) analysis to quantitatively evaluate the effect of the precipitates to the thermal and mechanical properties of the irradiated fuels.

4.3.4. Conclusion

The thermal, mechanical and electrical properties, viz., the thermal conductivity, elastic modulus, microhardness, electrical resistively, and Seebeck coefficient, of the Mo-Ru-Rh-Pd alloys with the compositions of $Mo_{35}Ru_{31}Rh_9Pd_{25}$, $Mo_{20}Ru_{54}Rh_{15}Pd_{11}$, $Mo_{30}Ru_{43}Rh_{14}Pd_{13}$, and $Mo_{43}Ru_{34}Rh_{12}Pd_{11}$ have been evaluated. The relationships between the micro-Vickers hardness and the Young's modulus for the alloys show the metallic characteristics. The thermal conductivities of all the alloys almost linearly increase with increasing temperature, showing metallic behavior. Above about 1000 K, the thermal conductivities are tenfold or above larger than that of UO_2. The electronic contribution to the thermal conductivity was evaluated from the Wiedemann-Franz-Lorenz relation by using the electrical resistivity. The electronic

contribution is more predominant than the lattice contribution in the whole temperature range. It is confirmed that the characteristics of the thermal and mechanical properties of the Mo-Ru-Rh-Pd alloys differ from that of UO_2.

References

[1] F.T. Ewart, R.G. Taylor, J.M. J.M. Horspool, and G. James, J. Nucl. Mater., 61 (1976) 254.

[2] H. Kleykamp, J.O. Paschoal, R. Pejsa, and F. Thummler, J. Nucl. Mater., 130 (1985) 426.

[3] H. Kleykamp, J. Nucl. Mater., 131 (1985) 221.

[4] I. Sato, H. Furuya, T. Arima, K. Idemitsu, and K. Yamamoto, J. Nucl. Sci. Technol., 36 (1999) 775.

[5] S. Yamanaka, K. Kurosaki, T. Matsuda, and M. Uno, J. Nucl. Mater., 294 (2001) 99.

[6] T. Matsuda, S. Yamanaka, K. Kurosaki, M. Uno, and S. Kobayashi, J. Alloys and Comp., 322 (2001) 77.

[7] S. Yamanaka, T. Matsuda, K. Kurosaki, and M. Uno, J. Nucl. Sci. Technol., Suppl. 3 (2002) 709.

[8] T. Matsuda, S. Yamanaka, K. Kurosaki, S. Kobayashi, and M. Uno, J. Nucl. Sci. Technol., Suppl. 3 (2002) 823.

[9] K. Kurosaki, S. Yamanaka. T. Matsuda, and M. Uno, J. Nucl. Sci. Technol., Suppl. 3 (2002) 807.

[10] K. Kurosaki, T. Oyama, T. Matsuda, M. Uno, and S. Yamanaka, J. Nucl. Sci. Technol., Suppl., 3 (2002) 815.

[11] D.R. O'boyle, F.L. Browm, and A.E. Dwight, J. Nucl. Mater., 35 (1970) 257.

[12] I. Sato, H. Furuya, T. Arima, K. Idemitsu, and K. Yamamoto, J. Nucl. Mater., 273 (1999) 239.

[13] H. Kleykamp, J. Less-Common Met., 144 (1988) 79.

[14] M. Yamawaki, Y. Nagai, T. Kogai, and M. Kanno, Thermodynamics of Nuclear Materials, 1979, IAEA, 1 (1980) 249.

[15] H. Kleykamp, J. Nucl. Mater., 167 (1989) 49-63.

[16] E.H.P. Cordfunke and R.J.M. Konings, Thermochimica Acta, 139 (1989) 99.

[17] T. Matsui and K. Naito, Thermochimica Acta, 139 (1989) 299.

[18] T. Matsui and K. Naito, J. Nucl. Sci. Technol., 26 (1989) 1102.

[19] Japan Thermal Measurement Society, Thermodynamics database for personal computer MALT2, (1992).

[20] The SGTE Pure Substance and Solution databases, GTT-DATA SERVICES, (1994).

[21] S. Yamanaka, H. Kobayashi, and K. Kurosaki, J. Alloys and Comp., 350 (2003) 269.

[22] S. Yamanaka, A. Kosga, and K. Kurosaki, J. Alloys and Comp., 350 (2003) 288.

[23] Materials and Fracture, edited by Materials Science Society of Japan, Shokabo, Tokyo, p. 100, (1989).

[24] S. Yamanaka, K. Yamada, T. Tsuzuki, T. Iguchi, M. Katsura, Y. Hoshino, and W. Saiki, J. Alloys and Comp., 271-273 (1998) 549.

[25] K. Yamada, S. Yamanaka and M. Katsura, J. Alloys and Comp., 271-273 (1998) 697.
[26] MATPRO-Version 11 (Revision 2), NUREG/CR-0497, TREE-1280, Rev. 2, August (1981).

Table 1

Sample characteristics of Mo-Ru-Rh-Pd alloys

Sample No.	Chemical composition (at.%)				Hexagonal lattice parameters	
	Mo	Ru	Rh	Pd	a (nm)	c (nm)
1	35	31	9	25	0.2738	0.4381
2	20	54	15	11	0.2731	0.4344
3	30	43	14	13	0.2749	0.4383
4	43	34	12	11	0.2751	0.4408

Sample No.	X-ray density	Bulk density	
	(gcm^{-3})	(gcm^{-3})	(%T.D.)
1	11.771	11.257	95.6
2	11.948	11.638	97.4
3	11.638	11.446	98.3
4	11.462	11.211	97.8

Table 2

Mechanical properties of Mo-Ru-Rh-Pd alloys

Sample No.	Longitudinal sound velocity	Shear sound velocity	Shear modulus	Young's modulus	Bulk modulus
	V_L (ms^{-1})	V_S (ms^{-1})	G (GPa)	E (GPa)	K (GPa)
1	4723	2695	81.7	206	142
2	5153	3035	107	265	166
3	4823	2865	93.9	231	141
4	5158	2773	86.2	224	183

Sample No.	Poisson's ratio	Debye temperature	Micro hardness
	ν	θ_D (K)	H_V (GPa)
1	0.259	368	1.63
2	0.234	415	4.84
3	0.227	389	0.98
4	0.297	379	1.45

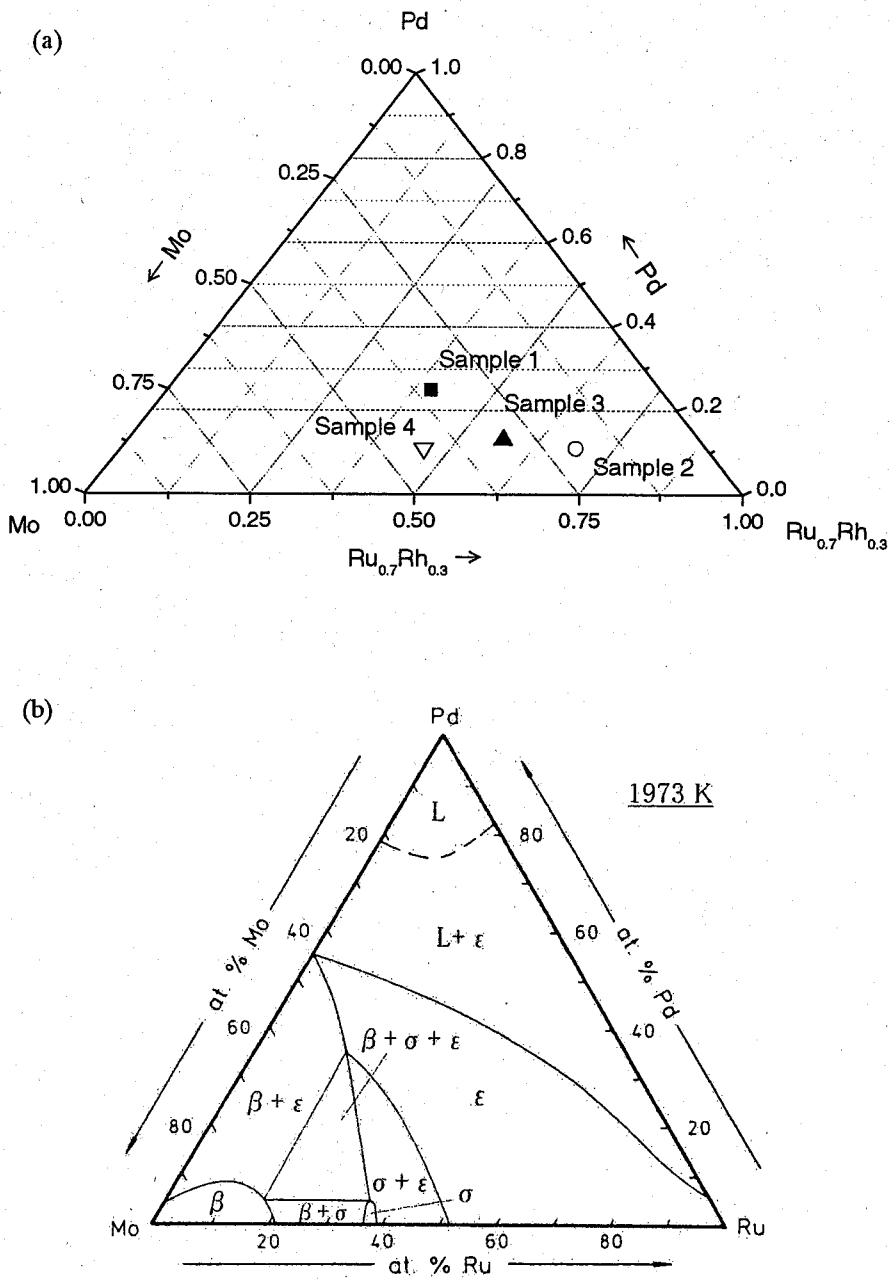

Figure 1. Chemical compositions of Mo-Ru-Rh-Pd alloys,
(a): Determined by the EDX analysis, (b): Phase diagram of Mo-Ru-Pd system at 1973 K [15].

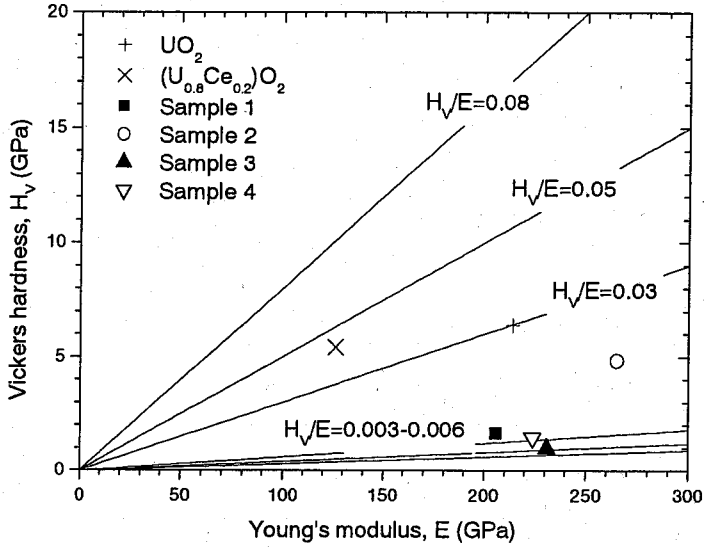

Figure 2. Relationship between the Vickers hardness H_V and Young's modulus E of Mo-Ru-Rh-Pd alloys.

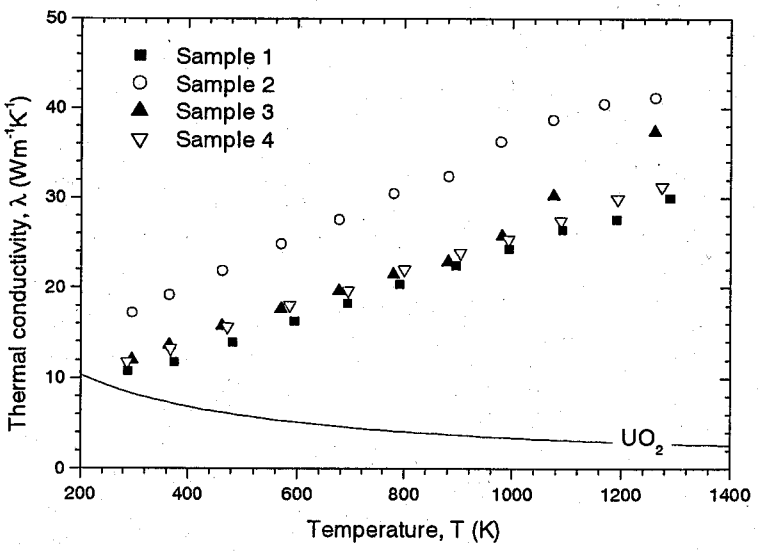

Figure 3. Temperature dependence of the thermal conductivity λ of Mo-Ru-Rh-Pd alloys.

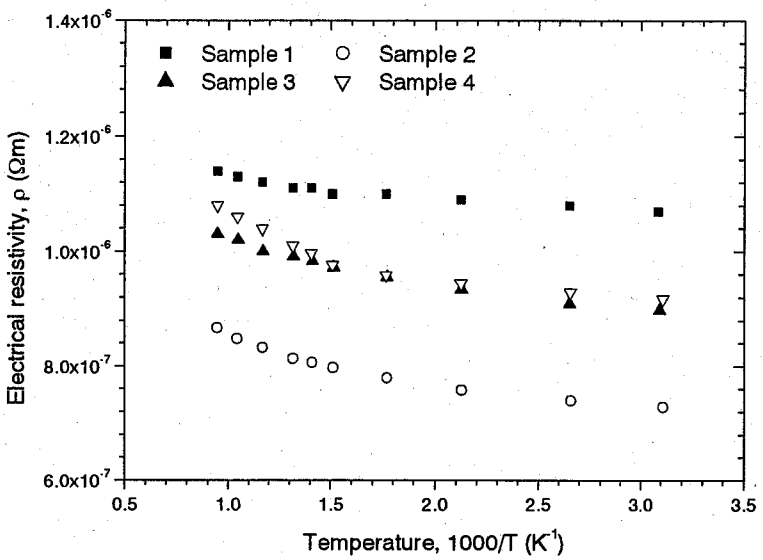

Figure 4. Temperature dependence of the electrical resistivity ρ of Mo-Ru-Rh-Pd alloys.

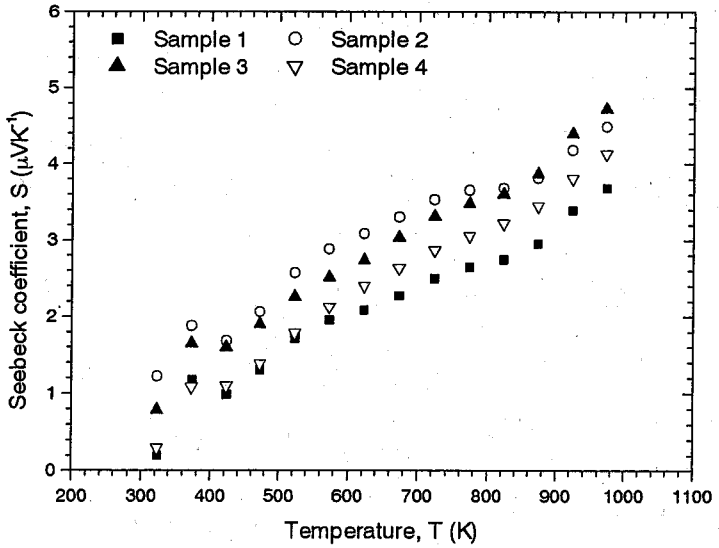

Figure 5. Temperature dependence of the Seebeck coefficient S of Mo-Ru-Rh-Pd alloys.

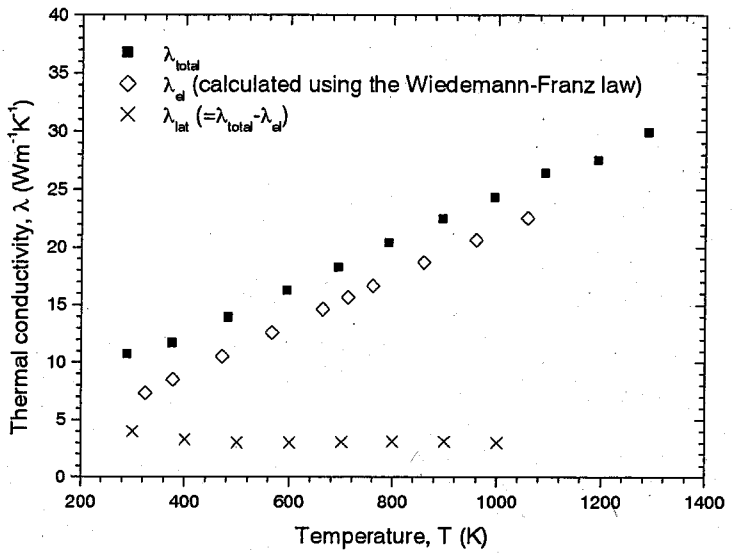

Figure 6. Temperature dependence of the λ_{total}, λ_{el}, and λ_{lat} of $Mo_{35}Ru_{31}Rh_9Pd_{25}$ (sample No. 1).

2.3. Nanomechanical Properties of Oxide Nuclear Fuels

2.3.1. Introduction

In traditional research area of nuclear fuels and materials, the advanced materials such as high burnup fuels and claddings have been developed from the viewpoint of their bulk properties. For example, a lot of studies have been performed on the mechanical properties of UO_2 fuel pellets in order to evaluate the effects of the porosity [1-5], temperature dependence [6,7], accumulation of solid fission product (FP) elements [2,4,8], etc. In order to advance these studies, it is necessary to spread out the research area, and we propose the nanoscale properties in addition to bulk properties as shown in Fig. 1.

Now, there are several properties we can measure in the nanoscale, such as nanomechanical properties, nanoscale thermal conductivity, nanoscale gas analysis, and nanoscale FT-IR. By using the nanoscale properties, we can develop the advanced nuclear materials more effectively. The nanoscale properties can be measured using the scanning probe microscope (SPM) with several equipments. These systems are called "multifunction SPM" and are shown in Fig. 2. For example, we can perform the nanoindentation by using a diamond indenter instead of a cantilever of the AFM, and applying an ultra micro load to the surface of the sample. Similarly, by using appropriate systems, we can obtain the current imaging and heat flow imaging in nanoscale.

The nanoindentation technique [9-13] has been developed in some decades, and the mechanical properties within a sub-micron or nano scale are widely discussed. The techniques are expected to be useful for measurement of the mechanical properties of thin films or local structure of various materials. However, there are few attempts to apply the nanoindentation to evaluate the mechanical properties of the nuclear fuels and materials.

In the present study, the nanomechanical properties of the oxide fuels have been evaluated. The nanoindentation tests have been carried out for UO_2 single crystal, UO_2 single crystal with (111) plane, polycrystalline UO_2 pellet, and polycrystalline $(U,Ce)O_2$ pellet, and the relationship between nano- and bulk-mechanical properties has been studied. The nanoindentation tests have also been carried out for a simulated high burnup UO_2 based fuel (SIMFUEL). The nanoindentation technique enables us to evaluate the mechanical properties of the individual phases precipitated on the SIMFUEL surface. The objectives of the present study are as follows:

(1) To evaluate the direction effect on the nanomechanical properties of UO_2 single crystal.
(2) To evaluate the difference between single crystal and polycrystalline pellet in the nanomechanical properties of UO_2.
(3) To evaluate the CeO_2 doping effect on the nanomechanical properties of $(U,Ce)O_2$.
(4) To evaluate the mechanical properties of the matrix phase and oxide precipitate observed in

the SIMFUEL surface.

2.3.2. Experimental

Polycrystalline UO_2 pellet, UO_2 single crystal, UO_2 single crystal with (111) plane, and polycrystalline $(U,Ce)O_2$ pellet were selected as the samples. The SIMFUEL with the simulated burnup of 150 GWd/t was employed in the present study. The composition of the SIMFUEL with simulated burnup of 150 GWd/t was determined from the burnup calculation using ORIGEN-2 program as shown in Table 1. The preparation method and conditions of the SIMFUEL is described in Chapter 2.1. The SIMFUEL was annealed at the oxygen potential of -390 kJ/mol. The size of the samples is disc-shaped with a diameter of about 10 mm and a thickness of about 1.0 mm. The surface of all the samples is polished with 0.3 μm-diamond powders to a mirror-like surface.

The nanoindentation tests were performed at room temperature in air using the atomic force microscope (AFM) supplied by JEOL (JSPM-4200) with a nanoindenter named TriboScope (Hysitron Inc.). The appearance of the SPM apparatus is shown in Fig. 3. Our SPM has various observation modes: the contact mode AFM, AC mode AFM, and STM (scanning tunnel microscope) are equipped as standard. Under various conditions, such as atmospheric pressure (standard), in vacuum, gas flow, heating, and cooling, we can get the surface image of the sample in an atomic and molecular level. The appearance of the nanoindentation system is shown in Fig. 4. The nanoindenter is operated on the SPM head. A Berkovich type diamond indenter was used in the present study. The SEM image and geometrical characteristics of the indenter are shown in Fig. 5.

Figure 6 shows the typical load-displacement curves for the standard sample (fused SiO_2) in the load range between 250 μN and 1500 μN. According to the method proposed by Oliver and Pharr [9], the nanomechanical properties, viz. the reduced modulus and nanohardness, can be evaluated from the load-displacement curve. The derivation of the reduced modulus and nanohardness from the load-displacement curve is summarized in Fig. 7.

After an indentation, the load-displacement curve was obtained as shown in Fig. 7. The nanohardness, H_n is defined by dividing the maximum load, P_{max}, by the projected contacted area, A, of the indenter at the load P_{max}:

$$H_n = \frac{P_{max}}{A}. \quad (1)$$

If the indenter has an ideal geometry, the projected contact area of the Berkovich pyramidal indenter can be obtained from the actual contact depth, h_c, at the maximum load as follows:

$$A = 24.5 h_c^2. \quad (2)$$

The actual contact depth, h_c, is different from the contact depth, h_{max}, at the maximum load in

the measured load-displacement curve, because the roundness is caused at the tip area of the indenter. The actual contact depth is obtained from the following relationship:

$$h_c = h_{\max} - \varepsilon \frac{P_{\max}}{S}. \quad (3)$$

where ε is a geometrical constant associated with the shape of the indenter. For the Berkovich pyramidal indenter, ε is equal 0.75. In this equation, S is the stiffness, which is equal to the slope of the unloading curve (dP/dh), given by:

$$S = \frac{dP}{dh} = \frac{2}{\sqrt{\pi}} E_r \sqrt{A}. \quad (4)$$

From the above consideration, we can get the following equation:

$$A = \frac{\pi}{4}\left(\frac{S}{E_r}\right)^2, \quad (5)$$

where E_r is the reduced modulus. The reduced modulus is given by:

$$\frac{1}{E_r} = \frac{1-\nu_s^2}{E_S} + \frac{1-\nu_i^2}{E_i}, \quad (6)$$

where, E and ν are the Young's modulus and Poisson's ratio, and the subscripts s and i represent a sample and an indenter. Assuming that the value of E_i= 1140 GPa and ν_i= 0.07 for the diamond tip, and ν_s= 0.3 for the sample, the calculated Young's modulus of the sample, E_s is considered to be about 10 % higher than the reduced modulus.

In order to obtain the accurate relationship between the indentation depth and projected contact area, it is necessary to perform the tip shape calibration based on a method suggested by Oliver and Pharr [9]. In the present study, to determine the area function, a series of the indentations at the various contact depths corresponding to the load of 2500 μN to 3500 μN were performed on the standard sample (fused SiO_2), and the projected contact area were calculated. The calculated area as a function of contact depth is plotted and a fitting procedure is employed with a fifth order polynomial as follows:

$$A = C_0 h_c^2 + C_1 h_c + C_2 h_c^{1/2} + C_3 h_c^{1/4} + C_4 h_c^{1/8} + C_5 h_c^{1/16}, \quad (7)$$

where C_i is the coefficients that are experimentally determined. C_0 is 24.5 for the Berkovich indenter. The fused SiO_2 with the elastic modulus of 72 GPa was used for calibration.

The loads in the range between 2500 μN and 3500 μN were applied for the nanoindentation tests of UO_2 and $(U,Ce)O_2$. In the case of the SIMFUEL, the load of 3000 μN was applied.

2.3.3. Results and Discussion

2.3.3.1. Nanomechanical Properties of UO_2 and $(U,Ce)O_2$

Figure 8 shows the typical load-displacement curves for UO_2 single crystal, UO_2 single crystal with (111) plane, and polycrystalline UO_2 pellet. The shapes of the curves are almost identical, but that for the polycrystalline UO_2 pellet is slightly deviated from other two curves to deeper direction. The indentation depth of these samples is about 110 to 120 nm, when the maximum load P_{max} is 3500 μN. The final depth due to the plastic deformation is about 75 to 85 nm, when the load is 3500 μN.

The calculated reduced modulus and nanohardness of the samples are plotted as a function of the contact depth as shown in Figs. 9 and 10, respectively. The indentation size effects, in which the nanohardness decreases with increasing the indentation depth, have reported by Oliver and Pharr for aluminum [9], Mante et al. for titanium single crystal [14], and Page et al. for silicon single crystal [15]. In the present study, the indentation size effect of the nanohardness is also observed for both UO_2 single crystal and polycrystalline UO_2 pellet. The mean values of the reduced modulus for UO_2 single crystal, UO_2 single crystal with (111) plane, and polycrystalline UO_2 pellet are 223.5±7 GPa, 220.3±7 GPa, and 223.1±7 GPa, respectively. For the reduced modulus, there is no difference between the single crystal and pellet for UO_2.

On the other hand, the difference between the single crystal and pellet of the nanohardness is clearly observed. The mean value of the nanohardness for polycrystalline UO_2 pellet is 8.5±0.4 GPa, but those of UO_2 single crystal and UO_2 single crystal with (111) plane are 9.4±0.2 GPa and 10.0±0.3 GPa, respectively. The nanohardness of polycrystalline UO_2 pellet is lower than that of UO_2 single crystal.

The typical load-displacement curves for polycrystalline UO_2 and $(U,Ce)O_2$ pellets are shown in Fig. 11. The curves of $(U,Ce)O_2$ are deviated from that of UO_2 in deeper direction with increasing CeO_2 content. The reduced modulus and nanohardness of polycrystalline $(U,Ce)O_2$ pellet are plotted as a function of the contact depth as shown in Figs. 12 and 13, respectively. Both the reduced modulus and nanohardness decrease with increasing CeO_2 content. Figures 14 and 15 show the bulk-elastic modulus and Vickers hardness of $(U,Ce)O_2$ pellet as a function of CeO_2 content [8,16], evaluated by the author's group. The elastic modulus of the sample was measured by an ultrasonic pulse echo method. It is observed that both the elastic modulus and Vickers hardness of $(U,Ce)O_2$ decrease with increasing CeO_2 content. The effects of the CeO_2 content on the reduced modulus and nanohardness of polycrystalline $(U,Ce)O_2$ pellet are shown in Figs. 16 and 17, respectively. As shown in these figures, the reduced modulus and nanohardness decrease with increasing CeO_2 content, in which the same tendency is observed in the nanoscale mechanical properties as that in the bulk-mechanical properties.

Figure 18 shows the relationship between the Nanohardness and Vickers hardness for all the materials measured in the present study (solid circles), together with the reported bcc single crystals (open circles) measured by Ohmura et al. [17]. The nanohardness of all materials

measured in the present study are about two times higher than the micro Vickers hardness. These results correspond to the results for bcc single crystals.

2.3.3.2. Nanomechanical Properties of SIMFUEL

Figures 19 shows the SEM image of the SIMFUEL surface with simulated burnup of 150 GWd/t after polishing. It is observed that the oxide inclusion is precipitated on the SIMFUEL surface, while the metallic inclusion is not observed. The composition of the oxide inclusion is reported in Chapter 2.1. Of course, the metallic inclusion also exists in the SIMFUEL, but unfortunately it is removed in the polishing process before nanoindentations. Figure 20 shows the AFM image of the SIMFUEL surface. In the AFM image, it is observed that the oxide inclusion exists beside the matrix phase. The traces of the indentation at the oxide inclusion and matrix phase are shown in Figs, 20(a) and (b), respectively. The triangle traces with the side length of about 500 nm and the depth of about 100 nm are observed.

The load-displacement curves obtained from the nanoindentations performed on the SIMFUEL surface are shown in Fig. 21. In these curves, there are two patterns, one is shown by solid lines and the other is shown by dashed lines. The number of the solid curves is about 90 % of all the curves. From the SEM/EDX analysis, about 90 % of the surface area of the SIMFUEL is the matrix phase, and about 10 % of that is the oxide inclusion. Therefore, it is decided that the solid curves represent the matrix phase, and the dashed curves represent the oxide inclusion.

The calculated reduced modulus and nanohardness of the matrix phase and oxide inclusion of the SIMFUEL as a function of the contact depth are shown in Figs. 22 and 23, respectively. Both the reduced modulus and nanohardness of the matrix phase are higher than those of the oxide inclusion. The mean values of the reduced modulus and nanohardness of the matrix phase are 217.4±20 GPa and 10.86±1.5 GPa, respectively. The mean values of the reduced modulus and nanohardness of the oxide inclusion are 196.5±17 GPa and 8.16±0.5 GPa, respectively. The values of the nanomechanical properties of the matrix phase and oxide inclusion of the SIMFUEL obtained in the present study are summarized in Table 2.

Figure 24 and 25 show the bar graphs of the reduced modulus and nanohardness of the matrix phase and oxide inclusion, together with those of $(U_{0.9}Ce_{0.1})O_2$ and $BaUO_3$. The nanomechanical properties of $BaUO_3$ have also been measured in the same condition described above. The values of the reduced modulus and nanohardness of the matrix phase and oxide inclusion differ from those of $(U_{0.9}Ce_{0.1})O_2$ and $BaUO_3$. It is considered that this difference is due to the chemical compositions. For example, a lot of dissolved FP elements such as La and Nd exist in the matrix phase of the SIMFUEL, and the chemical composition of the oxide inclusion in the SIMFUEL is very complicate such as $(Ba,Sr)(U,Zr,Mo)O_3$.

In the present study, we can directly measure the nanomechanical properties of the

individual phases existed in the SIMFUEL surface. The nanoindentation method enables in situ measurements of the nanomechanical properties of the matrix phase and oxide inclusion in the SIMFUEL.

2.3.4. Conclusion

In the present study, the nanomechanical properties, viz., the reduced modulus and nanohardness of polycrystalline UO_2 pellet, UO_2 single crystal, UO_2 single crystal with (111) plane, polycrystalline $(U,Ce)O_2$ pellet, and SIMFUEL have been evaluated by the nanoindentation system. The SIMFUEL with the simulated burnup of 150 GWd/t has been employed in the present study. The nanoindentation tests have been performed at room temperature and in air using the AFM with the nanoindenter named TriboScope. For the reduced modulus, there is no difference between the single crystal and pellet of UO_2. The nanohardness of polycrystalline UO_2 pellet is lower than that of UO_2 single crystal. Both the reduced modulus and nanohardness of polycrystalline $(U,Ce)O_2$ pellet decrease with CeO_2 content. The same tendency is observed in the nanoscale mechanical properties of $(U,Ce)O_2$ as that in the bulk-mechanical properties. The nanoindentation method enables in situ measurements of the nano-mechanical properties of the matrix phase and oxide inclusion in the SIMFUEL.

References

[1] V. Roque, B. Cros, D. Baron, and P. Dehaudt, J. Nucl. Mater., 277 (2000) 211.

[2] J. Boocock, A.S. Furzer, and J. R. Matthews, Harwell memo AERE-M2565 (1972).

[3] K. Tanaka, H. Koguchi, and T. Mura, Int. J. Eng. Sci., 27 (1989) 11.

[4] S. Yamanaka, S. Yoshida, K. Kurosaki, M. Uno, K. Yamamoto, and T. Namekawa, J. Alloys and compounds, 327 (2001) 281.

[5] D.G. Martin, High Temp.-High Press., 21 (1989) 13.

[6] K. Yamada, S. Yamanaka, and M. Katsura, J. Alloys and compounds, 275-277 (1998) 725.

[7] A. Padel and C.H. de Novison, J. Nucl. Mater., 33 (1969) 40.

[8] K. Yamada, S. Yamanaka, T. Nakagawa, M. Uno, and M. Katsura, J. Nucl Mater., 247 (1997) 289.

[9] W.C. Oliver and G.M. Pharr, J. Mater. Res., 7 (1992) 1564.

[10] M. Nishibori and K. Kinoshita, Thin Solid Films, 48 (1978) 325.

[11] D. Newey, M.A. Wilkins, and H.M. Pollock, J. Phys. E: Sci. Instrum., 15 (1982) 119.

[12] J.B. Pethica. In: V. Ashworth, W. Grant, and R. Procter, Editors, Ion Implantation into Metals, Pergamon Press, Oxford (1982), p. 147.

[13] J.B. Pethica, R. Hutchings, and W.C. Oliver, Phil. Mag., A48 (1983) 593.

[14] F.K. Mante, G.R. Baran, and B. Lucas, Biomaterials, 20 (1999) 1051.

[15] T.F. Page, W.C. Oliver, and C.J. McHargue, J. Mater. Res., 8 (1993) 1028.

[16] K. Yamada, S. Yamanaka, and M. Katsura, J. Alloys and Compounds, 271-273 (1998) 697.

[17] T. Ohmura, K. Tsuzaki, and S. Matsuoka, Scripta Materialia, 45 (2001) 889.

Table 1

Composition of the SIMFUEL with simulated burnup of 150 GWd/t

6.2 wt.%-U235	Burnups 50.0 GWd/t 5.24 at.%		100.0 GWd/t 10.46 at.%		150.0 GWd/t 15.47 at.%	
Representative elements	mol%	wt.%	mol%	wt.%	mol%	wt.%
U (+Pu)	92.48	96.20	85.428	92.34	78.90	88.48
Ba (+Sr)	0.762	0.457	1.363	0.850	1.944	1.257
Zr (+Nb)	1.430	0.570	2.427	1.005	3.227	1.387
Mo (+Tc)	1.456	0.611	2.653	1.156	3.655	1.652
Ru	0.723	0.320	1.679	0.771	2.688	1.280
Rh	0.127	0.057	0.146	0.068	0.140	0.068
Pd	0.303	0.141	1.130	0.546	2.108	1.057
Y	0.208	0.081	0.319	0.129	0.392	0.164
La (+Am, Cm)	0.325	0.197	0.726	0.458	1.147	0.751
Ce (+Np)	0.747	0.457	1.348	0.858	1.797	1.186
Nd (+other REs)	1.436	0.905	2.779	1.820	3.998	2.716
TOTAL	100.00	100.00	100.00	100.00	100.00	100.00

Table 2

Values of the nanomechanical properties of UO_2, $(U,Ce)O_2$, and the SIMFUEL

		Reduced Modulus E_r (GPa)	Nanohardness H_n (GPa)
SIMFUEL with simulated burnup of 150 GWd/t	Matrix phase	217.4±20	10.86±1.5
	Oxide inclusion	196.5±17	8.15±0.5
UO_2 single crystal		223.5±7	9.43±0.2
UO_2 single crystal with (111) plane		220.3±7	10.0±0.3
Polycrystalline UO_2 pellet		223.1±7	8.53±0.4
Polycrystalline $(U_{0.9}Ce_{0.1})O_2$ pellet		189.8±10	8.16±0.5
Polycrystalline $(U_{0.8}Ce_{0.2})O_2$ pellet		175.6±9	7.95±0.3

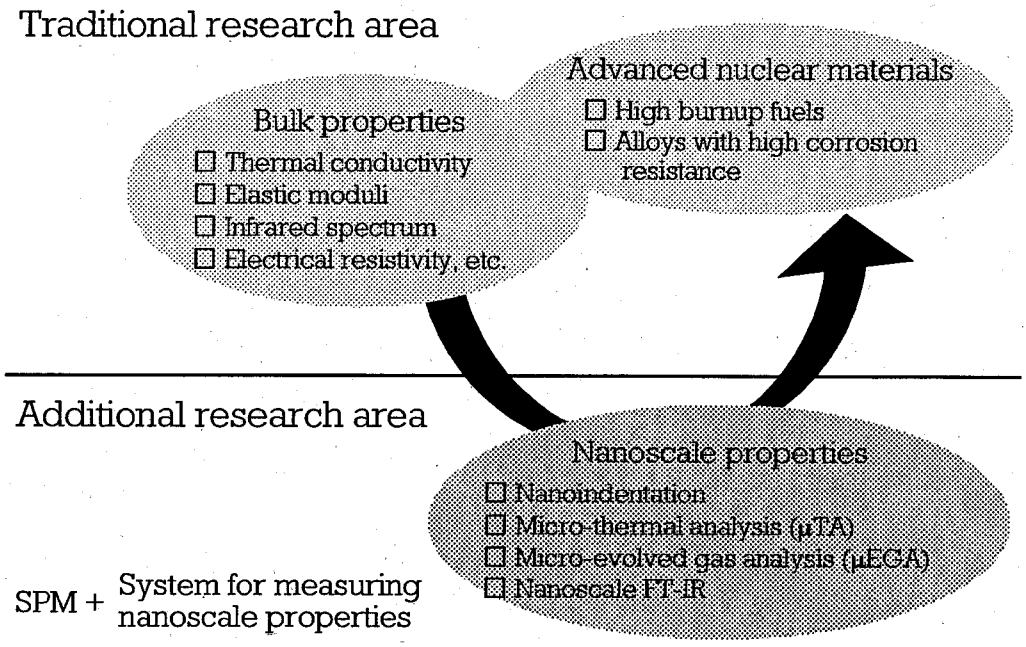

Figure 1. Background of the present study.

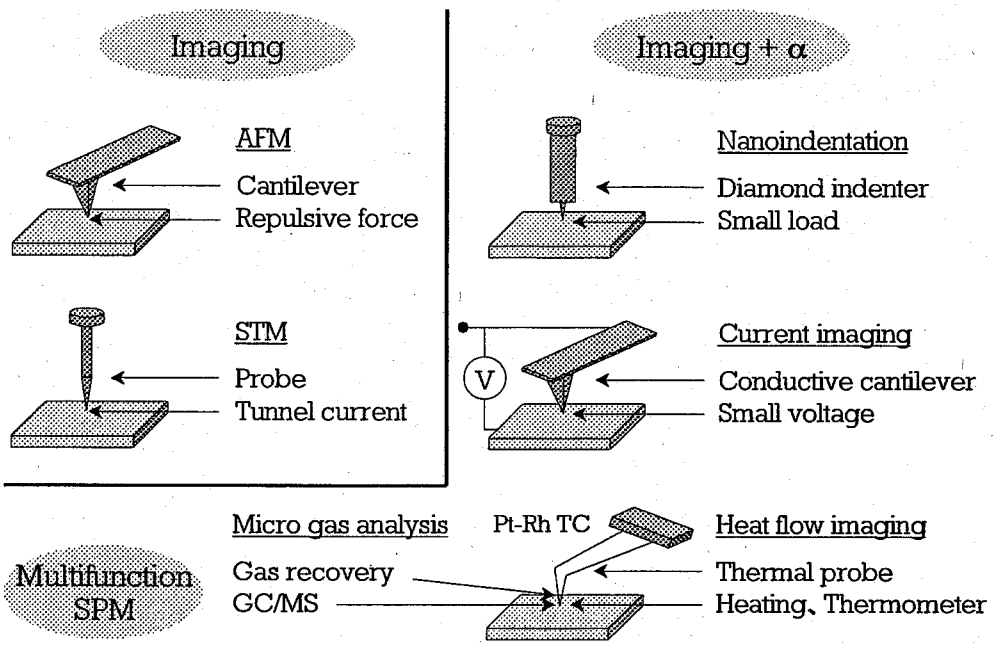

Figure 2. Nanoscale properties measuring system (Multifunction SPM).

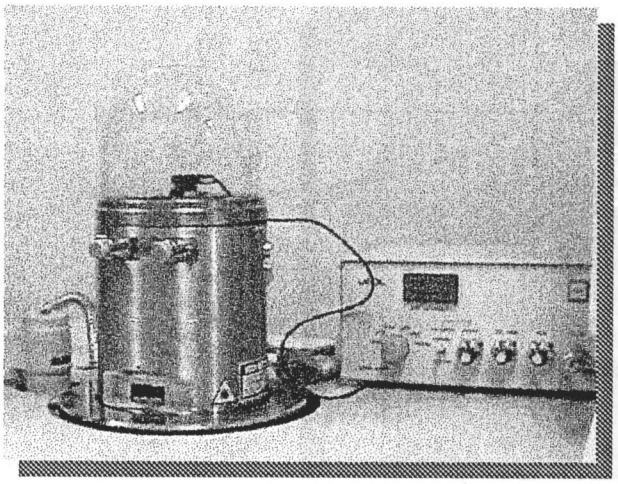

Specifications

#Resolution

AFM : Atomic resolution

STM : Atomic resolution

#X-Y scanning area

10 mm × 10 mm (Standard)

80 mm × 80 mm (Wide scanner)

#Sample size

10 mm × 10 mm × 3 mm (Standard)

Figure 3. Appearance and specifications of the scanning probe microscope (JSPM-4210 by JEOL Co. Ltd.,).

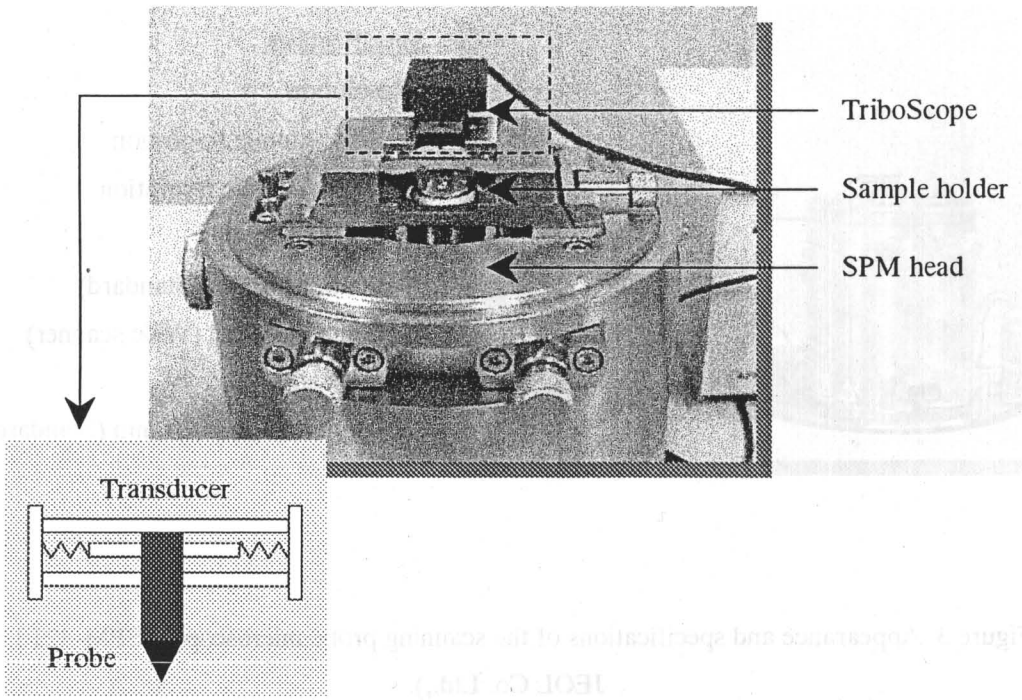

Figure 4. Appearance of the nanoindentation system (TriboScope by Hysitron Inc.).

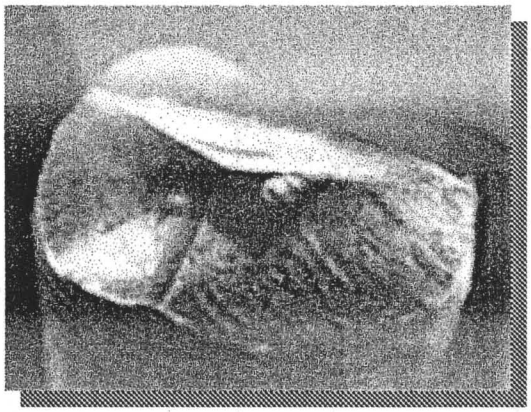

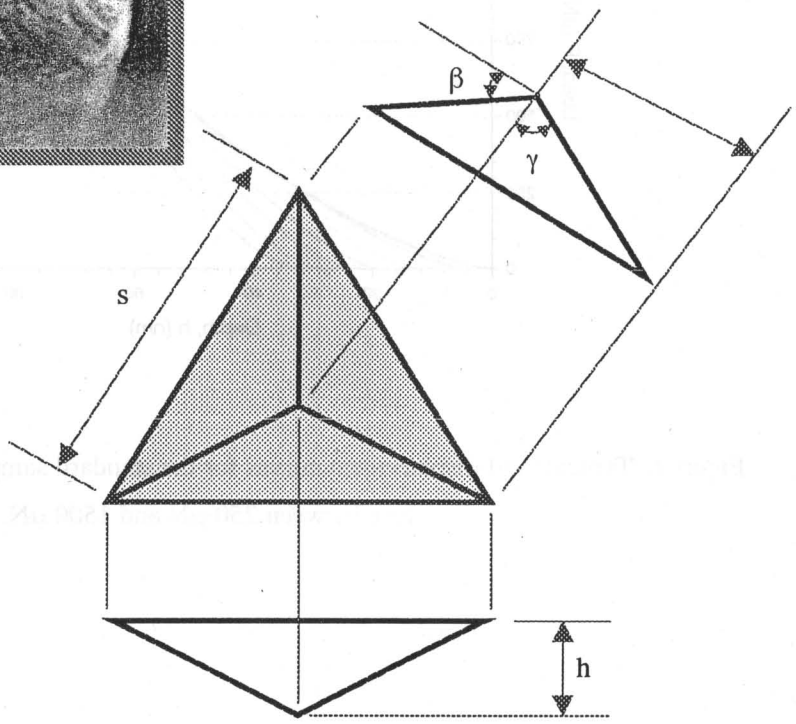

Geometrical characteristics		
Inclined face angle	β	24.7°
Apex angle	γ	77.1°
Projected area	$A_{projected}$	$24.5h^2$
Ratio of side length to depth	s/h	about 7.5
Projected edge length	a	2h/tanb

Figure 5. SEM image and geometrical characteristics of the Berkovich indenter.

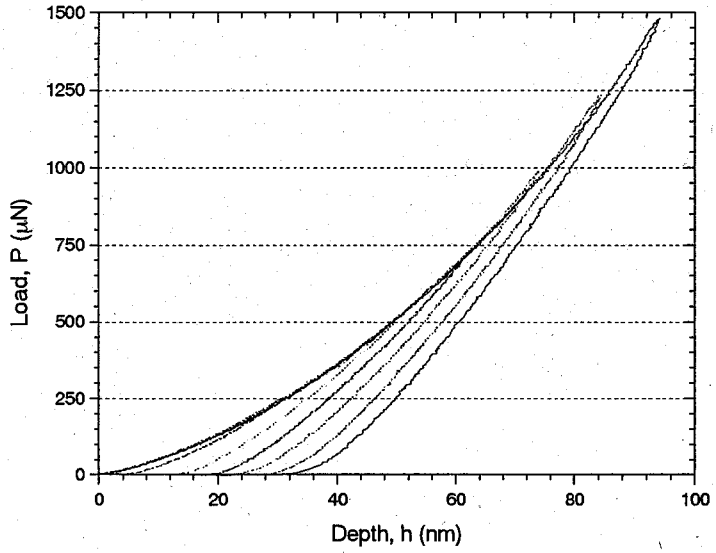

Figure 6. Typical load-displacement curves for the standard sample (fused SiO_2) in the load range between 250 μN and 1500 μN.

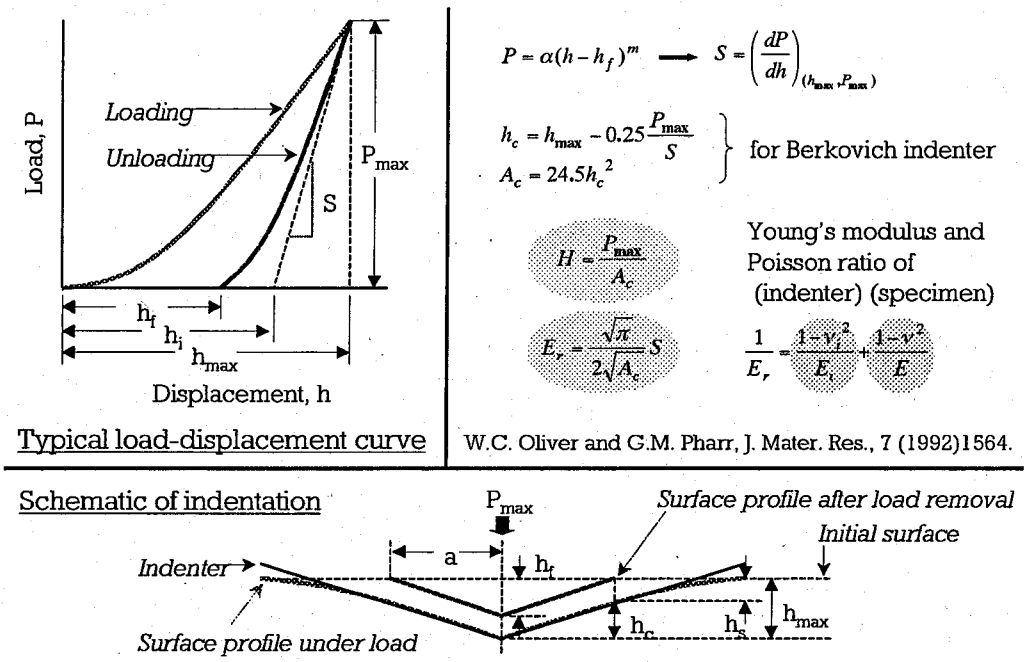

Figure 7. Derivation of the reduced modulus and nanohardness from the load-displacement curve.

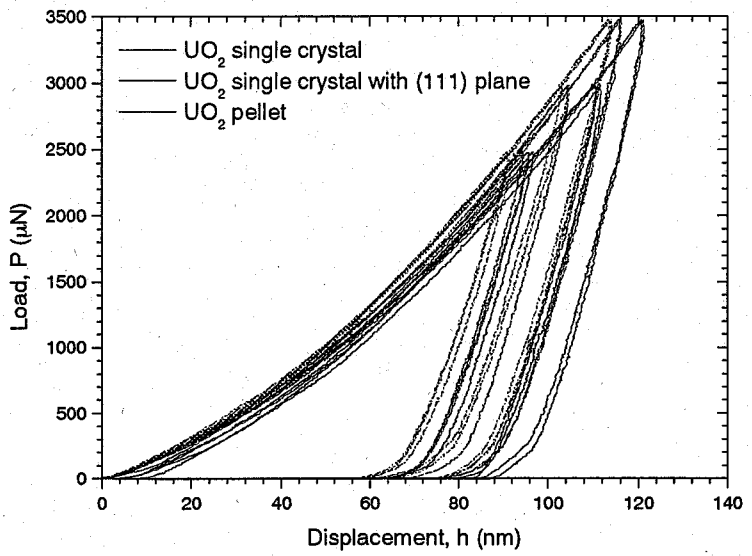

Figure 8. Load-displacement curves for UO_2 single crystal, UO_2 single crystal with (111) plane, and polycrystalline UO_2 pellet.

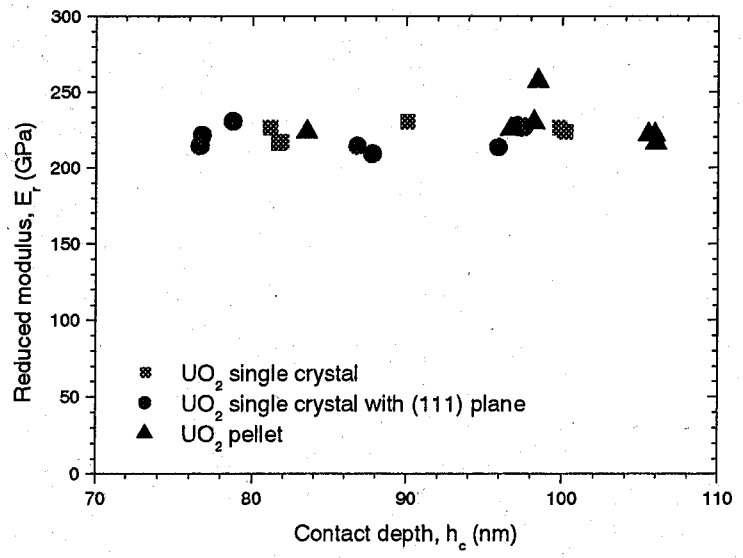

Figure 9. Reduced modulus of UO_2 single crystal, UO_2 single crystal with (111) plane, and polycrystalline UO_2 pellet as a function of contact depth.

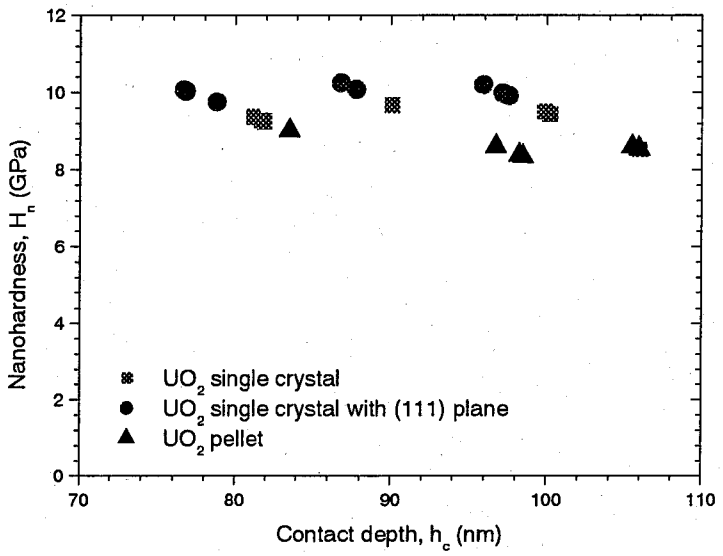

Figure 10. Nanohardness of UO_2 single crystal, UO_2 single crystal with (111) plane, and polycrystalline UO_2 pellet as a function of contact depth.

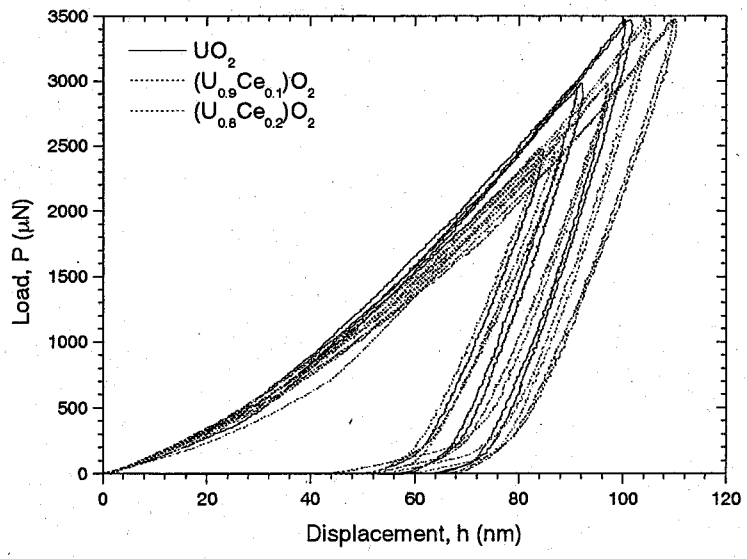

Figure 11. Load-displacement curves of polycrystalline UO_2 and $(U,Ce)O_2$ pellets.

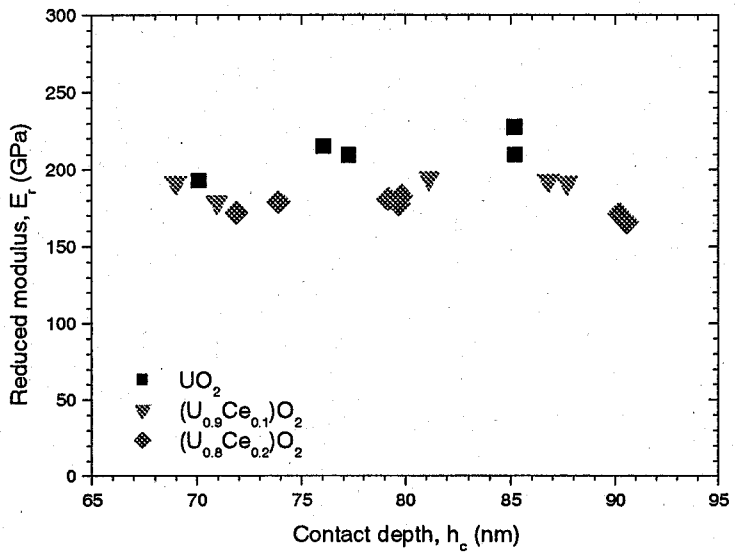

Figure 12. Reduced modulus of polycrystalline $(U,Ce)O_2$ pellet as a function of contact depth.

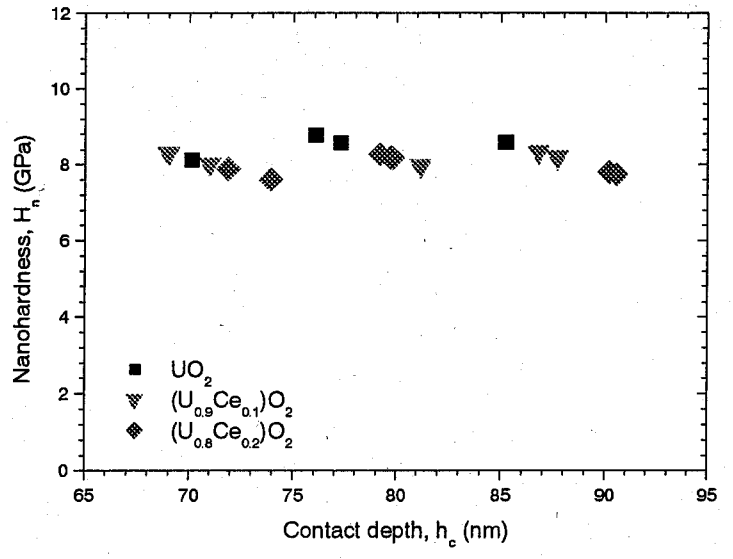

Figure 13. Nanohardness of polycrystalline $(U,Ce)O_2$ pellet as a function of contact depth.

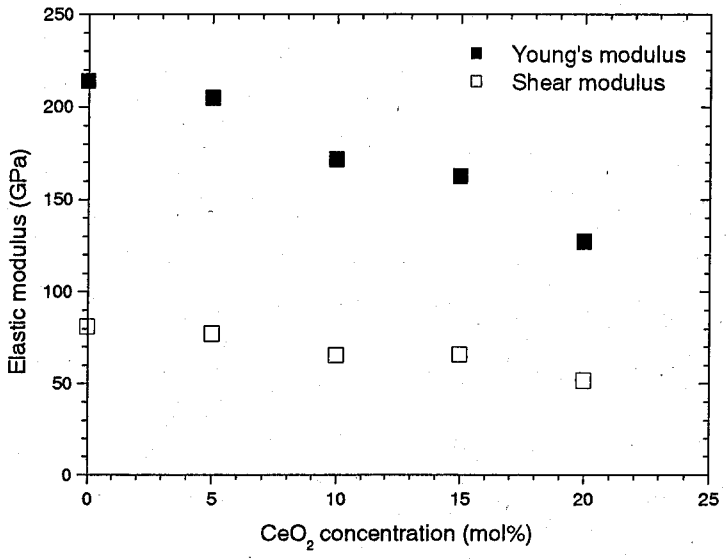

Figure 14. Bulk-elastic modulus of polycrystalline $(U,Ce)O_2$ pellet as a function of CeO_2 content.

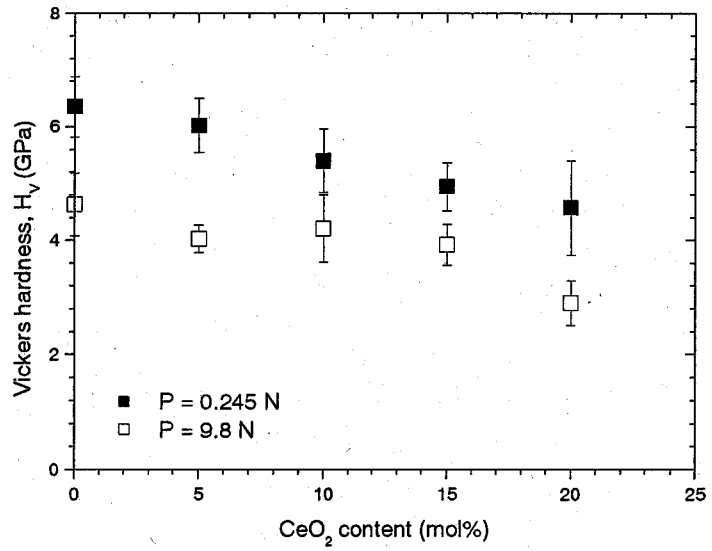

Figure 15. Vickers hardness of polycrystalline $(U,Ce)O_2$ pellet as a function of CeO_2 content.

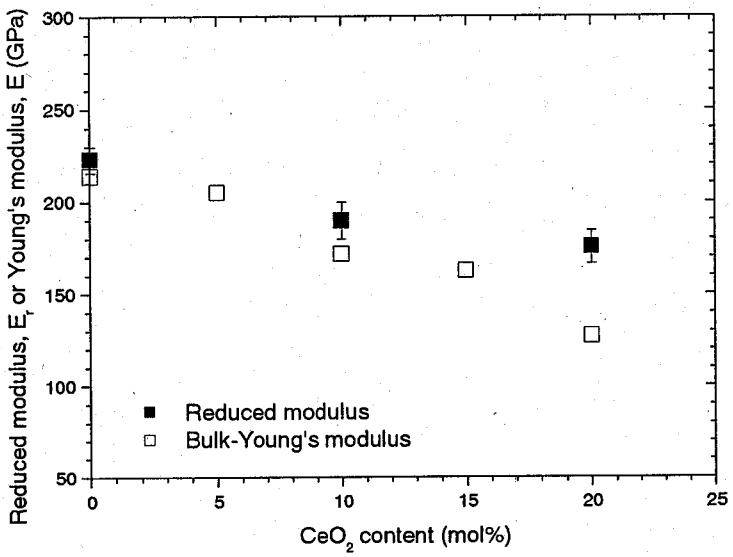

Figure 16. Effect of the CeO_2 content on the reduced modulus of polycrystalline $(U,Ce)O_2$ pellet, together with the data of bulk-Young's modulus.

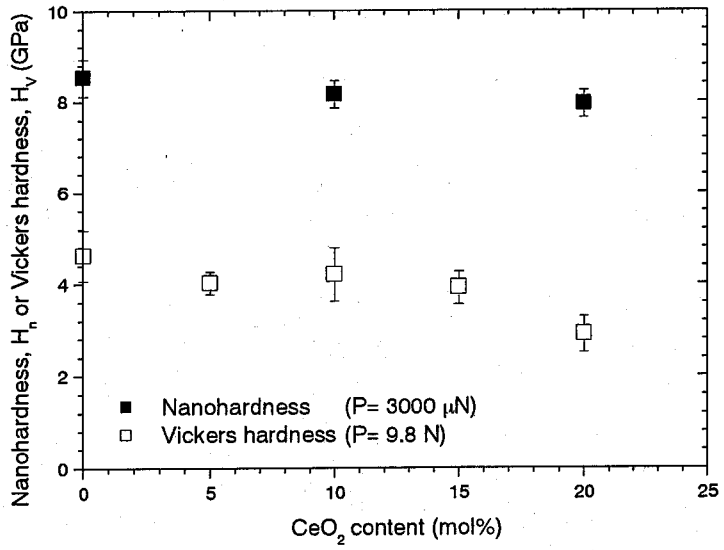

Figure 17. Effect of the CeO_2 content on the nanohardness of polycrystalline $(U,Ce)O_2$ pellet, together with the data of Vickers hardness.

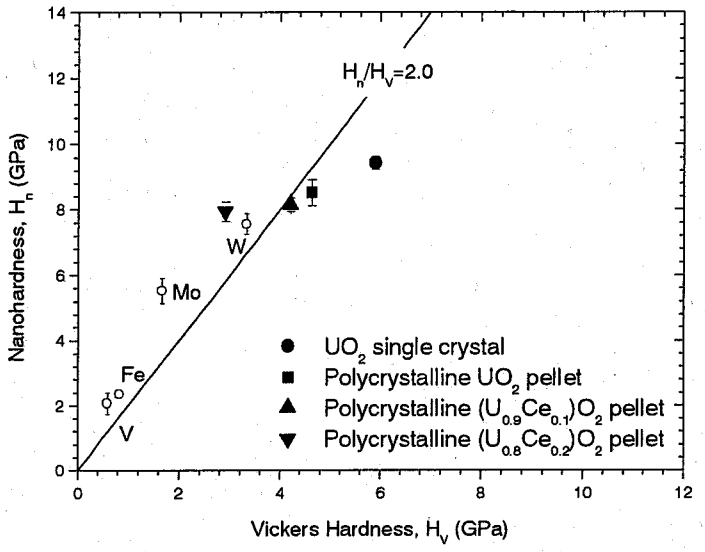

Figure 18. Relationship between the Nanohardness and Vickers hardness for UO_2 and $(U,Ce)O_2$ (solid circles), together with the reported bcc single crystals (open circles).

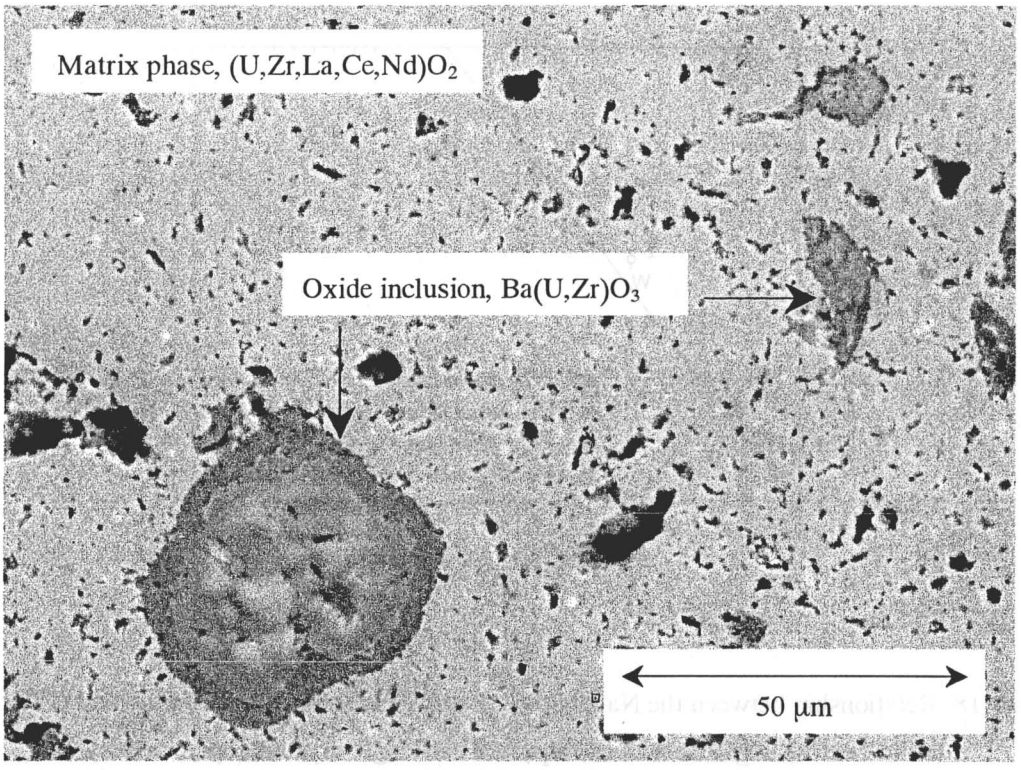

Figure 19. SEM image of the SIMFUEL surface with simulated burnup of 150 GWd/t after polishing.

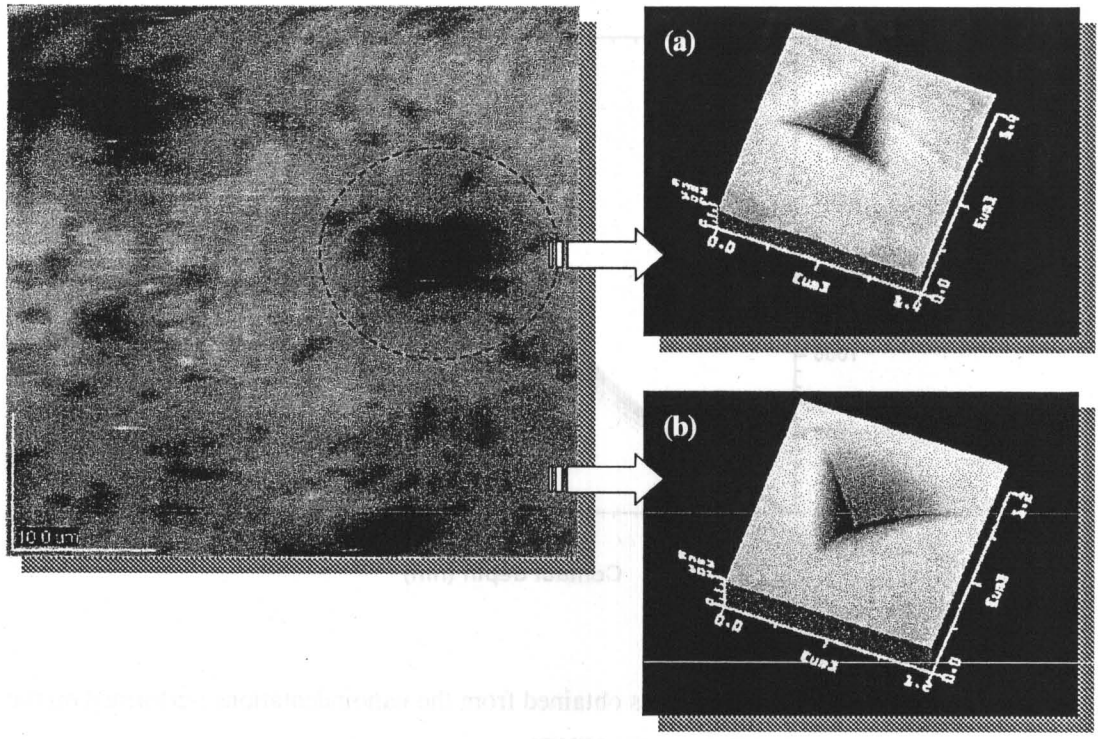

Figure 20. AFM image of the SIMFUEL surface: (a) a trace of the indentation at the oxide inclusion, (b) at the matrix phase.

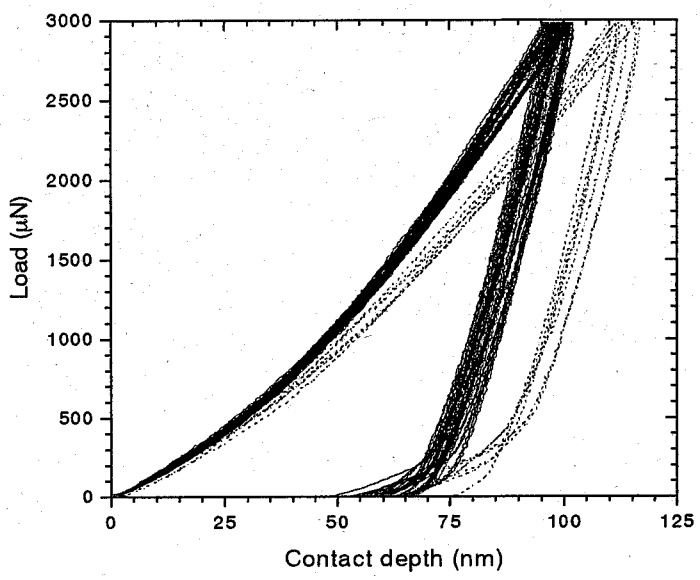

Figure 21. Load-displacement curves obtained from the nanoindentations performed on the SIMFUEL surface.

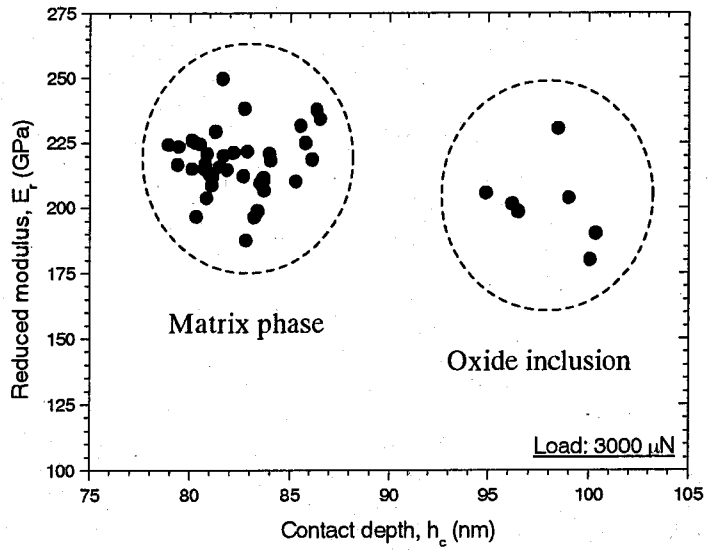

Figure 22. Reduced modulus of the SIMFUEL as a function of contact depth.

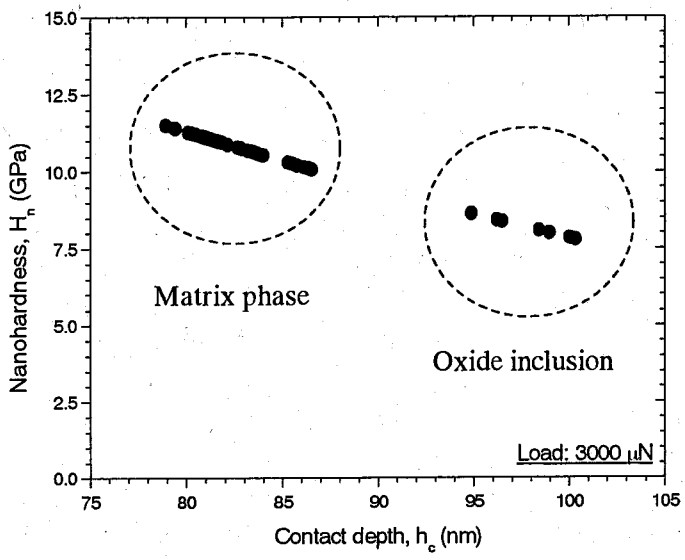

Figure 23. Nanohardness of the SIMFUEL as a function of contact depth.

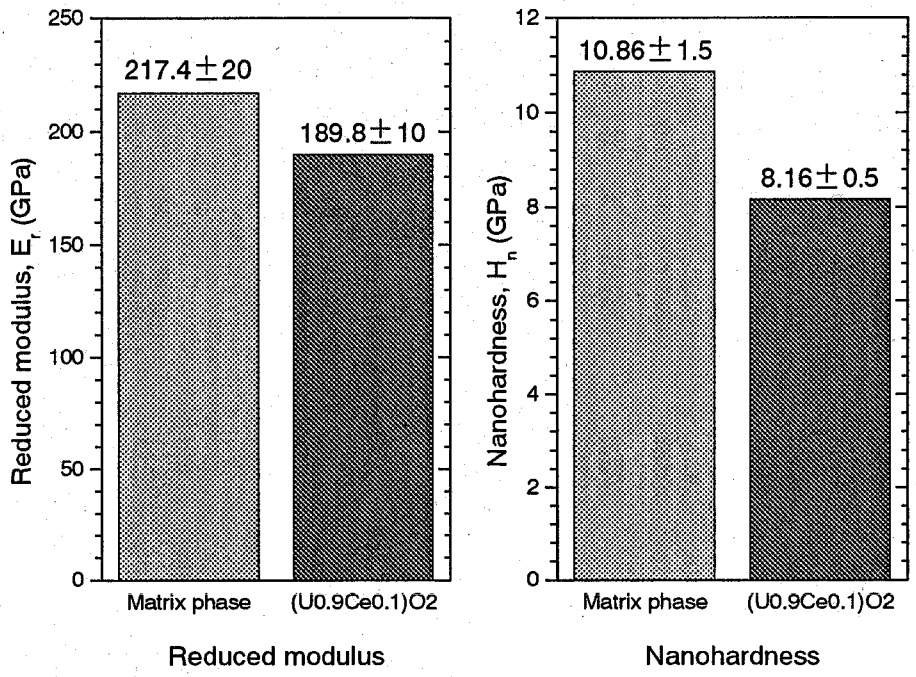

Figure 24. Reduced modulus and nanohardness of the matrix phase of the SIMFUEL and polycrystalline $(U_{0.9}Ce_{0.1})O_2$ pellet.

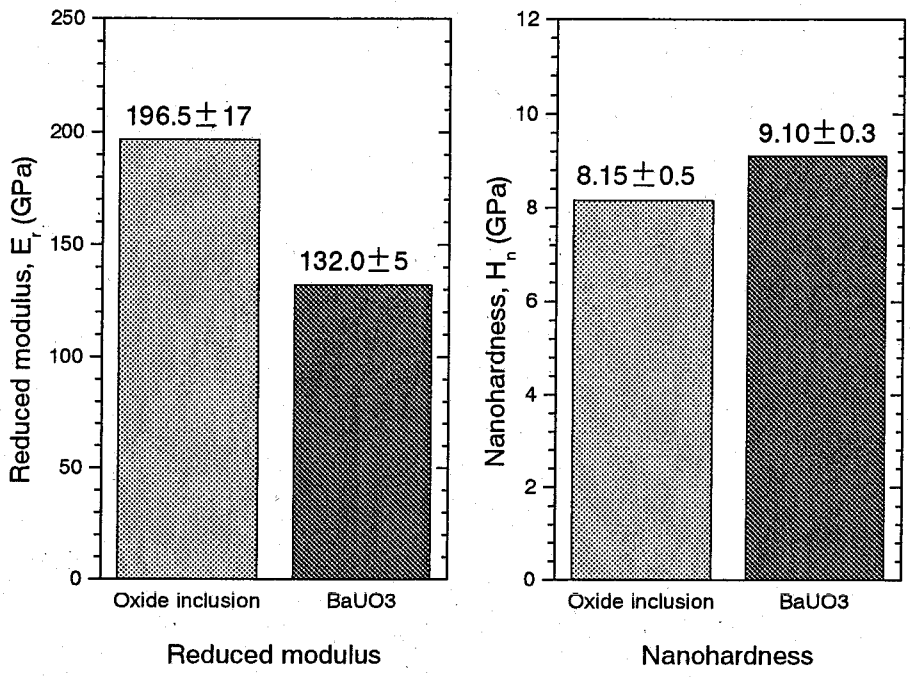

Figure 25. Reduced modulus and nanohardness of the oxide inclusion of the SIMFUEL and polycrystalline $BaUO_3$ pellet.

Chapter 3

Characterization of Oxide Nuclear Fuels by Computer Simulations

3.1. Thermodynamic Equilibrium Calculations of Oxide Nuclear Fuels

3.1.1. Phase Equilibria of High Burnup Oxide Fuels

3.1.1.1. Introduction

It is necessary to understand the behavior of fission product (FP) elements during the irradiation because they should strongly affect the physical and chemical properties of the fuel. The irradiated nuclear fuel forms a multi-component and -phase system containing more than 40 kinds of FP elements, and the chemical states of the FP elements are sensitively changed with the various conditions such as temperature, pressure, and oxygen potential in the fuel. The FP elements do not take a single chemical state but may be distributed into several phases, and each phase is usually composed of a number of elements. Therefore, it is very important to understand the phase equilibria of high burnup oxide fuels.

The purpose of the present study is to understand the chemical states of the FP elements in the high burnup oxide fuels. A thermodynamic equilibrium calculation for the multi-component and -phase system has been performed using ChemSage program [1]. The ChemSage program has been utilized to evaluate the equilibrium state of the multi-component system by finding the minimum of the total free energy of the system. The effect of the oxygen potential to the chemical states of the FP elements has been evaluated.

In this chapter, in order to evaluate the FP elements behavior in the irradiated fuel, the amount of the selective FP elements under the given burnup conditions has been calculated by using ORIGEN-2 code. The chemical states of the FP elements under the various oxygen potentials have been evaluated by the thermodynamics equilibrium calculation.

3.1.1.2. Calculation

The amount of the FP elements in the irradiated UO_2 fuel was determined by its starting enrichment and irradiation history. The ORIGEN-2 code [2] was used to calculate the FP inventories. In the present study, three kinds of the composition were considered; simulated burnups of 50, 100, and 150 GWd/t. A 6.2 wt.% of enrichment of UO_2 fuel, a constant power of 38.301 MW, and an neutron flux of 3.82×10^{14} N/cm^2-sec were selected under a BWR circumstance for the irradiation conditions. The operating cycle was determined to 653 days operating and 60 days checking (×6 cycles). The burnups of 50, 100, and 150 GWd/t were corresponded to 2, 4 and 6 cycle, respectively.

In the present study, ten FP elements listed in Table 1 were selected for the representative elements of all major FP elements, except for the volatile elements. This classification was referred to the previous study reported by Lucuta et al. [3]. In this case, the FP elements with similar chemical behavior were represented by a single element. For example, Ba represents Ba and Sr. For TRU elements, La represents itself and minor actinide (MA) elements;

Am and Cm. Np is represented by Ce. Nd represents all the rare earth elements except for La and Ce. Note that the amounts of the representative elements are summation of that of each FP element of the group.

The thermodynamic equilibrium calculation means to calculate what phases are stable and how many stable phases exist in the material under certain temperature and pressure. In the present study, the solution phases existed in the high burnup oxide fuels are treated as an ideal liquid model. The calculation was done based on a principle that a total free energy of the system show as the following equation indicates the lowest value:

$$G(T) = \sum_i n_i \left(G_i^0 + RT \ln a_i \right), \quad (1)$$

where n_i is the mole number of species i, G_i^0 is the standard free energy of the species i, R is the gas constant, T is the absolute temperature, and a_i is the activity of species i.

In the present study, ChemSage Ver. 4.0 (for MS-DOS) [1] was used for the thermodynamic equilibrium calculation. The ChemSage consists of the software and thermodynamic database.

The gas phase, matrix phase, oxide precipitate, metallic precipitate, and other solid phase were selected in the present calculation. The gas phase consists of single elements and oxides as an ideal gas (total 48 types). The matrix phase (MO_2) consists of UO_2, ZrO_2, Y_2O_3, La_2O_3, CeO_2, and Nd_2O_3 as an ideal solution. Assuming that the oxide precipitate exists as two kinds of chemical form, the first one is $BaMO_3$ (M: U, Zr, Mo) type and the other is $BaMO_4$ (M: U, Mo) type. The metallic precipitate is also assumed to exist as two kinds of chemical form, Mo-Me (Me: Ru, Rh, Pd) alloy and UMe_3 (Me: Ru, Rh, Pd) type intermetallic compound. Other solid phases (25 types) are assumed to exist as single elements, oxides, and intermetallic compounds. The selected species and phases in the present calculation are summarized as Table 2. SGTE pure database [4] and MALT2 [5] were used as the thermodynamic databases. In order to evaluate the effect of the oxygen potential on the phase equilibria of the high burnup oxide fuels, the oxygen potential is varied from -500 kJ/mol to -200 kJ/mol at 1273 K for the simulated burnup of 100 GWd/t. The total gaseous pressure in the system was fixed at one atmosphere. The details for the calculation conditions are summarized in Table 3.

3.1.1.3. Results and Discussion

Table 4 shows the results of the burnup calculations by using ORIGEN-2 code. The amounts of the FP elements show proportional relationship with burnup increasing. The burnups of 50, 100, and 150 GWd/t corresponded to 5.24, 10.46, and 15.47 at.%, respectively

The equilibrium phases obtained from the present calculation are shown in Table 5. It is found that the MO_2 phase that corresponds to the fuel matrix phase and Mo-Me alloy are

always stable under the whole conditions. The $BaMO_3$ phase, which corresponds to the gray oxide phase, does not exist as a stable phase under the high oxygen potentials, because MoO_2 and $BaMO_4$ phase are more stable chemical species in these conditions. At low oxygen potentials, the UMe_3 type intermetallic compound is stable in addition to the Mo-Me alloy as the metallic precipitate.

Table 6 shows the compositions of the matrix phase, MO_2 (M: U, Zr, Y, La, Ce, Nd), under the various oxygen potentials calculated in the present study. Figure 1 shows the chemical states of U and the compositions of the MO_2 phase at the oxygen potentials of -500 and -200 kJ/mol. About 94 % of the MO_2 phase is UO_2 and remain of 6 % of that is ZrO_2, Y_2O_3, La_2O_3, CeO_2, and Nd_2O_3 under the all oxygen potentials. Slight differences in the compositions of the MO_2 phase at different oxygen potentials are due to the amount of ZrO_2. Figure 2 shows the chemical states of Zr. The stable chemical forms of Zr are mainly MO_2 phase and $BaMO_3$ (M: U, Zr, Mo) phase. Although the MO_2 phase exists under any oxygen potentials, the $BaMO_3$ phase exists only under the oxygen potentials of -500 and -400 kJ/mol, as shown in Table 7, which is caused by the decrease of ZrO_2 in the MO_2 phase under the low oxygen potentials.

Tables 7 and 8 show the compositions of the $BaMO_3$ (M: U, Zr, Mo) phase and $BaMO_4$ (M: U, Mo) phase under the various oxygen potentials. The compositions of those are also shown in Figs. 3 and 4, together with the chemical states of Ba. These figures indicate that the $BaMO_3$ phase is stable under the low oxygen potentials (-500 and -400 kJ/mol), and the $BaMO_4$ phase is stable under the high oxygen potentials (-300 and -200 kJ/mol). About 60 % of the $BaMO_3$ phase is $BaUO_3$, and about 40 % of that is $BaZrO_3$. Certain quantity of $BaMoO_3$ (about 2.5 %) exists under the oxygen potential of -400 kJ/mol. About 95 % of the $BaMO_4$ phase is $BaMoO_4$, and about 5 % of that is $BaUO_4$.

As described before, the metallic precipitate in the irradiated oxide fuels consists of Mo, Tc, and the platinum family metals (Ru, Rh, Pd). Figure 5 shows the chemical states of Mo under the various oxygen potentials. This figure indicates that the Mo-Me (Me: Ru, Rh, Pd) alloy is stable under the low oxygen potentials, and MoO_2 or $BaMoO_4$ becomes stable with increasing the oxygen potential. Figure 6 shows the chemical states of Me such as Ru, Rh, and Pd. It is confirmed that Ru, Rh, and Pd exist in the UMe_3 type intermetallic compound or Mo-Me alloy at the oxygen potentials of -400 and -500 kJ/mol, and in the Mo-Me alloy at the oxygen potentials of -300 and -200 kJ/mol. The compositions of the Mo-Me alloy under the various oxygen potentials are shown in Table 9 and Fig. 7. Mo is scarcely contained in the Mo-Me alloy under the high oxygen potentials. It is considered that Mo is stable as MoO_2 or $BaMoO_4$ under the high oxygen potentials. The complicated behavior of Mo is reconfirmed in the present calculation.

Summary of the present calculation is shown in Table 10. Although the free energy of

each solution phase was treated by the ideal solution model, the present calculation results are validity compared with the post irradiation examination (PIE) results for the irradiated FBR, LWR, and HTR fuels [6-11].

3.1.1.4. Conclusion

In order to understand the chemical states of the FP elements in the irradiated high burnup oxide fuels, the phase equilibrium calculation has been performed using ChemSage program. The composition of the irradiated fuel with the burnups of 50, 100, and 150 GWd/t has been calculated by using ORIGEN-2 code. Although the free energy of each solution phase is treated as the ideal solution model, the calculated results almost agree with the PIE results. For example, Mo exits as Mo-Me (Me: Ru, Rh, Pd) alloy or $BaMO_3$ (M: U, Zr, Mo) under the low oxygen potentials and as $BaMO_4$ (M: U, Mo) under the high oxygen potentials. It is found that the multi-component and -phase thermodynamic equilibrium calculation between the fuel and the FP elements system is an effective tool for understanding the phase equilibria of the high burnup oxide fuels.

References

[1] G. Eriksson and K. Hack, Metallurgical Transactions B, 21B (1990) 1013.

[2] M.J. Bell, ORIGEN-2 Code, Oak Ridge National Laboratories, Report ORNL-TM4397 (1973).

[3] P.G. Lucuta, R.A. Verral, Hj. Matzke, and B.J. Palmer, J. Nucl. Mater., 178 (1991) 48.

[4] SGTE Pure Substance Database (Edit. 1998), Provided by GTT Technol., Herzogenrath, Germany (1998).

[5] Japan Thermal Measurement Society, Thermodynamics data base for personal computer MALT2.

[6] H. Kleykamp, J. Nucl. Mater., 131 (1985) 221.

[7] H. Kleykamp, Nucl. Technol., 80 (1988) 412.

[8] H. Kleykamp, J.O. Paschoal, R. Pejsa, and F. Thummler, J. Nucl. Mater., 130 (1985) 426.

[9] J.O.A. Paschoal, Kernforschungszentrum Karlsruhe, report KfK-3473 (1983).

[10] I. Sato, H. Furuya, T. Arima, K. Idemitsu, and K. Yamamoto, J. Nucl. Sci. Technol., 36 (1999) 775.

[11] I. Sato, H. Furuya, T. Arima, K. Idemitsu, and K. Yamamoto, J. Nucl. Mater., 273 (1999) 239.

Table 1

Representative elements and their groups

Groups	Representative elements
U+Pu	U
Ba+Sr	Ba
Zr+Nb	Zr
Mo+Tc	Mo
Ru	Ru
Rh	Rh
Pd	Pd
Y	Y
La+Am+Cm	La
Ce+Np	Ce
Nd+other REs.	Nd

Table 2

Chemical species treated in the present equilibrium calculation

Gas phase		Ideal gas composed of total 48 kinds of gaseous species
Matrix phase	MO_2	Ideal solid solution of UO_2, ZrO_2, Y_2O_3, La_2O_3, CeO_2, and Nd_2O_3
Oxide precipitates	$BaMO_3$	Ideal solid solution of $BaUO_3$, $BaZrO_3$, and $BaMoO_3$
	$BaMO_4$	Ideal solid solution of $BaUO_4$ and$BaMoO_4$
Metallic precipitates	Mo-Me alloy	Ideal solid solution of Mo and Me (Ru, Rh, Pd)
	UMe_3	Ideal solid solution of URu_3, URh_3,and UPd_3
Other solid species		Other oxides and intermetallic compounds (total 25 kinds of species)

Table 3

Calculation conditions

Burnup conditions (GWd/t)	100	
Oxygen potential (kJ/mol)	-200, -300, -400, -500	
Temperature (K)	1273	
Chemical forms	Gas phase	Ideal gas
	Matrix phase	MO_2 type oxide
	Oxide precipitates	$BaMO_3$ type oxide
		$BaMO_4$ type oxide
	Metallic precipitates	Mo-Me type alloy
		UMe_3 type intermetallic compounds
	Other solids	Other solids

Table 4

Results of burnup calculations using ORIGEN-2 code

6.2 wt.%-U235	Burnups 50.0 GWd/t 5.24 at.%		100.0 GWd/t 10.46 at.%		150.0 GWd/t 15.47 at.%	
Representative elements	mol%	wt.%	mol%	wt.%	mol%	wt.%
U (+Pu)	92.48	96.20	85.428	92.34	78.90	88.48
Ba (+Sr)	0.762	0.457	1.363	0.850	1.944	1.257
Zr (+Nb)	1.430	0.570	2.427	1.005	3.227	1.387
Mo (+Tc)	1.456	0.611	2.653	1.156	3.655	1.652
Ru	0.723	0.320	1.679	0.771	2.688	1.280
Rh	0.127	0.057	0.146	0.068	0.140	0.068
Pd	0.303	0.141	1.130	0.546	2.108	1.057
Y	0.208	0.081	0.319	0.129	0.392	0.164
La (+Am, Cm)	0.325	0.197	0.726	0.458	1.147	0.751
Ce (+Np)	0.747	0.457	1.348	0.858	1.797	1.186
Nd (+other REs)	1.436	0.905	2.779	1.820	3.998	2.716
TOTAL	100.00	100.00	100.00	100.00	100.00	100.00

Table 5

Calculated results at 1273 K

Burnup (GWd)	Oxygen potential (kJ/mol)	Equilibrium phases					
		MO_2	$BaMO_3$	$BaMO_4$	MoO_2	Mo-Me alloy	UMe_3
100	-200	○		○	○	○	
	-300	○		○	○	○	
	-400	○	○			○	○
	-500	○	○			○	○

Table 6

Compositions of MO_2 phase (M: U, Zr, Y, La, Ce, Nd) calculated in the present study

(mol%)	Oxygen potentials (kJ/mol)			
	-200	-300	-400	-500
UO_2	93.5	93.8	94.2	94.2
ZrO_2	2.70	2.67	2.12	2.11
Y_2O_3	0.18	0.18	0.18	0.18
La_2O_3	0.40	0.40	0.41	0.40
CeO_2	1.46	1.48	1.50	1.51
Nd_2O_3	1.53	1.53	1.55	1.55

Table 7

Compositions of $BaMO_3$ phase (M: U, Zr, Mo) calculated in the present study

(mol%)	Oxygen potentials (kJ/mol)			
	-200	-300	-400	-500
$BaUO_3$	-	-	58.9	60.5
$BaZrO_3$	-	-	38.6	39.5
$BaMoO_3$	-	-	2.46	0

Table 8

Compositions of $BaMO_4$ phase (M: U, Mo) calculated in the present study

(mol%)	Oxygen potentials (kJ/mol)			
	-200	-300	-400	-500
$BaUO_4$	5.10	5.10	-	-
$BaMoO_4$	94.9	94.9	-	-

Table 9

Compositions of Mo-Me (Me: Ru, Rh, Pd) alloy calculated in the present study

(mol%)	Oxygen potentials (kJ/mol)			
	-200	-300	-400	-500
Mo	0	0	51.9	58.9
Ru	56.8	56.6	33.3	37.3
Rh	4.94	4.93	2.89	3.24
Pd	38.2	38.1	11.9	0.51

Table 10

Chemical states of FP elements calculated in the present study

1273 K	Calculated results				PIE results [#]
	Oxygen potentials (kJ/mol)				
	-200	-300	-400	-500	
U	MO_2	MO_2	MO_2, $BaMO_3$, UMe_3	MO_2, $BaMO_3$, UMe_3	MO_2, $BaMO_3$
Zr			MO_2, $BaMO_3$	MO_2, $BaMO_3$	MO_2, $BaMO_3$
Y			MO_2	MO_2	MO_2
La					
Ce					
Nd					
Ba	$BaMO_4$	$BaMO_4$	$BaMO_3$	$BaMO_3$	$BaMO_3$
Mo	$BaMO_4$, MoO_2	$BaMO_4$, MoO_2	Mo-Me alloy	Mo-Me alloy	Mo-Me alloy
Ru	Mo-Me alloy	Mo-Me alloy	Mo-Me alloy, UMe_3	Mo-Me alloy, UMe_3	Mo-Me alloy
Rh					
Pd					

[#] The oxygen potential in the actual oxide fuel at 1273 K is about 350 to 400 kJ/mol.

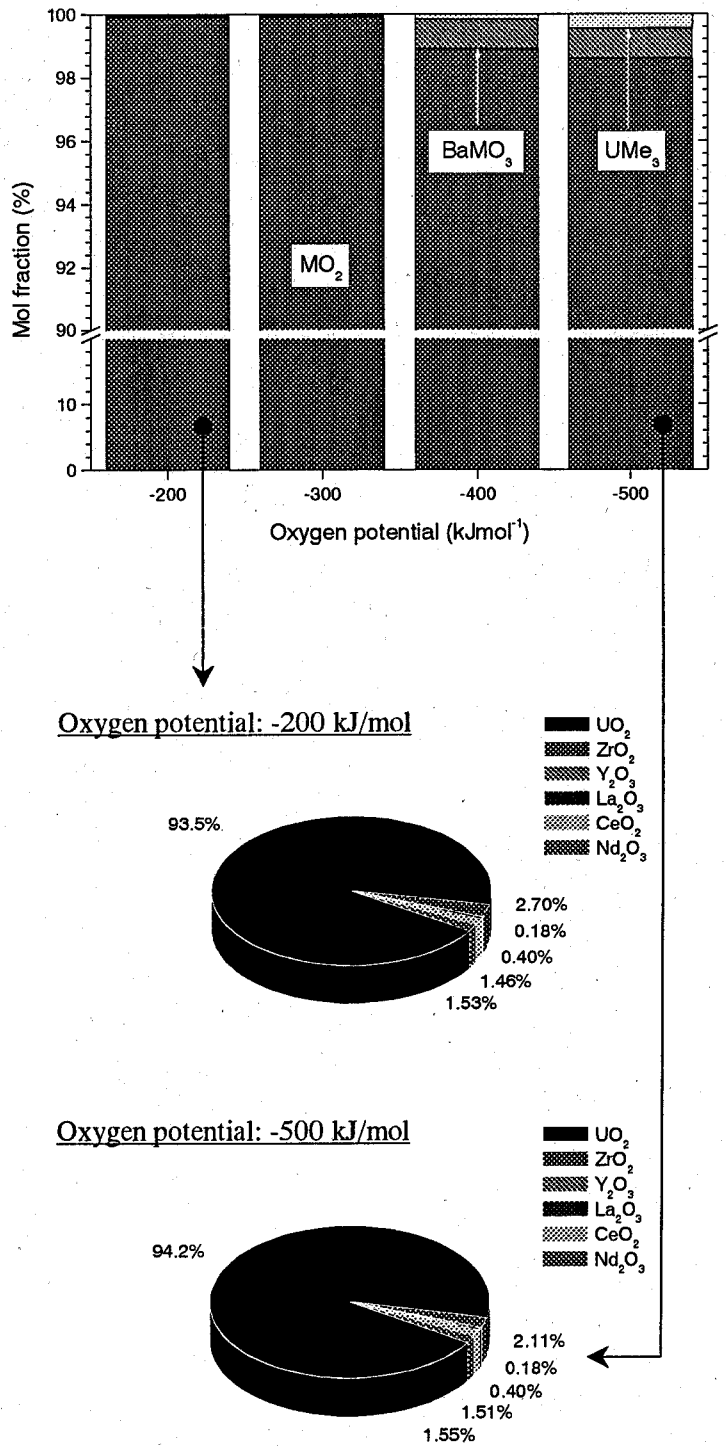

Figure 1. Chemical states of uranium and compositions of the MO_2 phase at the oxygen potentials of -200 and -500 kJ/mol.

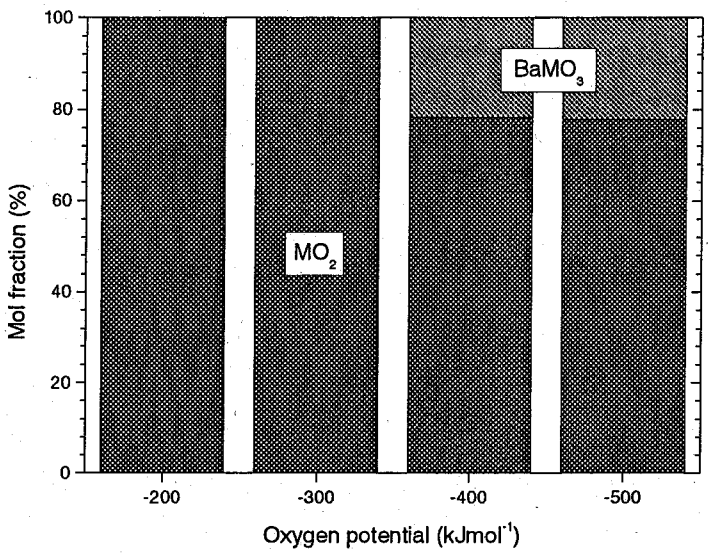

Figure 2. Chemical states of zirconium.

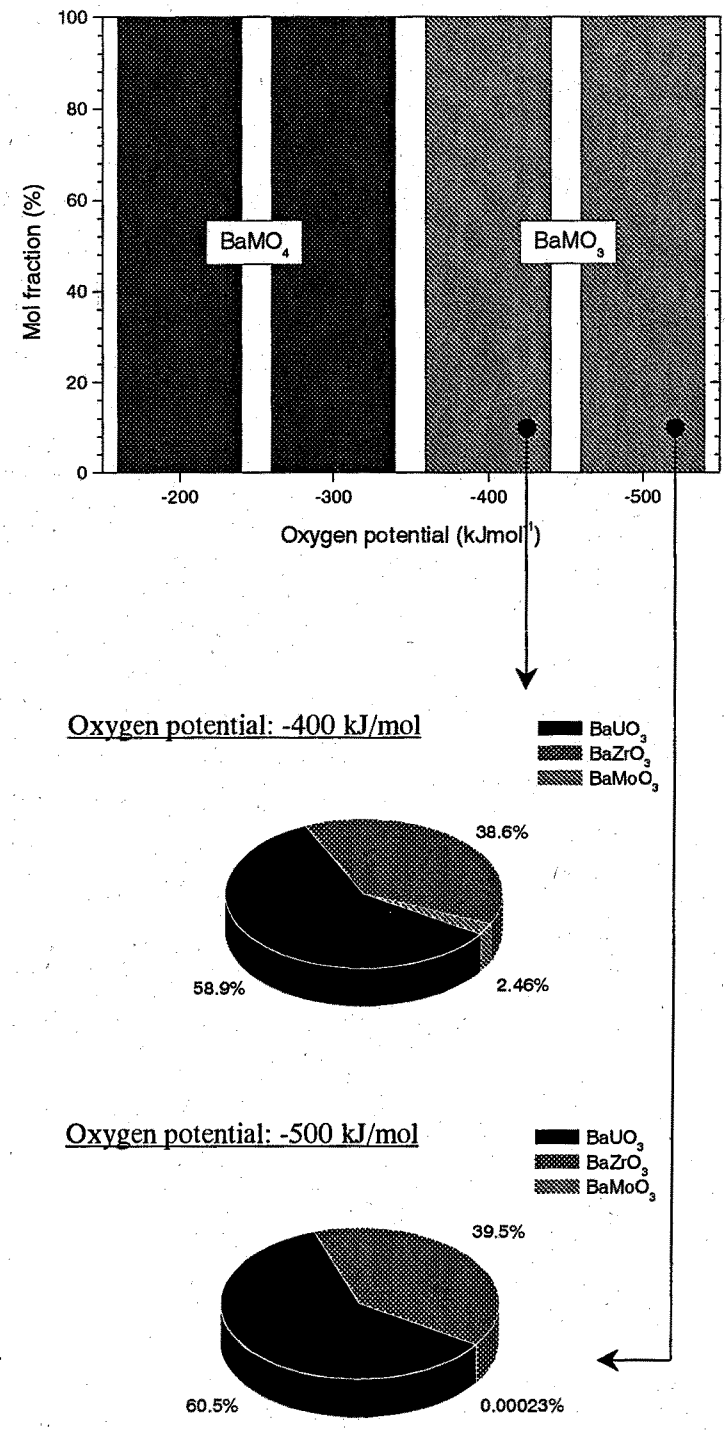

Figure 3. Chemical states of barium and compositions of the $BaMO_3$ phase at the oxygen potentials of -400 and -500 kJ/mol.

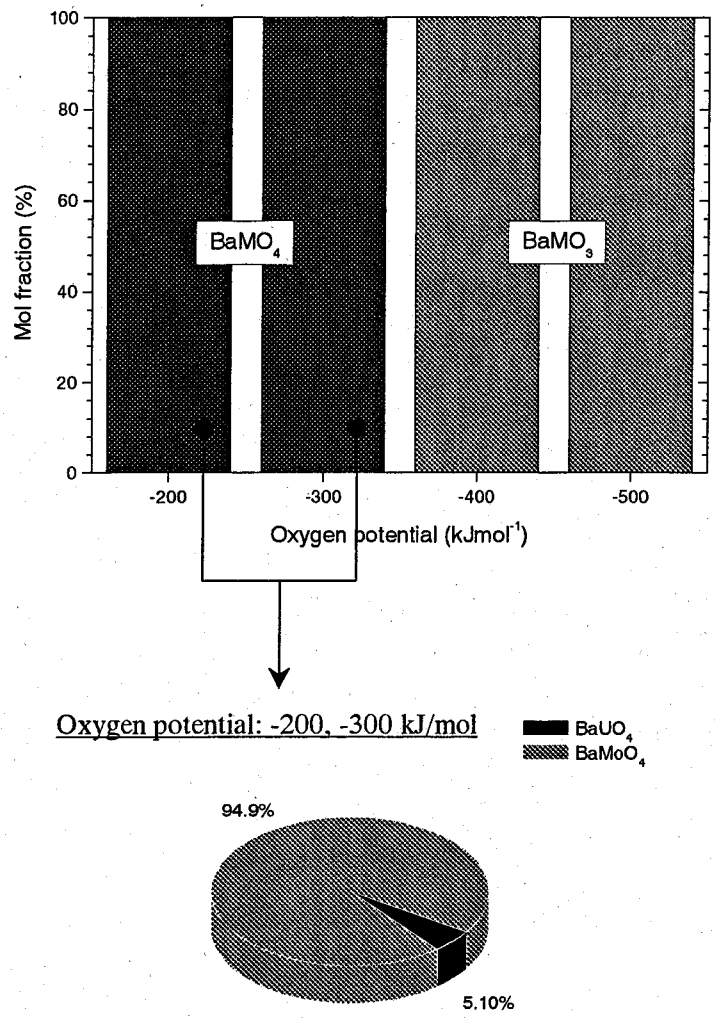

Figure 4. Chemical states of barium and compositions of the $BaMO_4$ phase at the oxygen potentials of -200 and -300 kJ/mol.

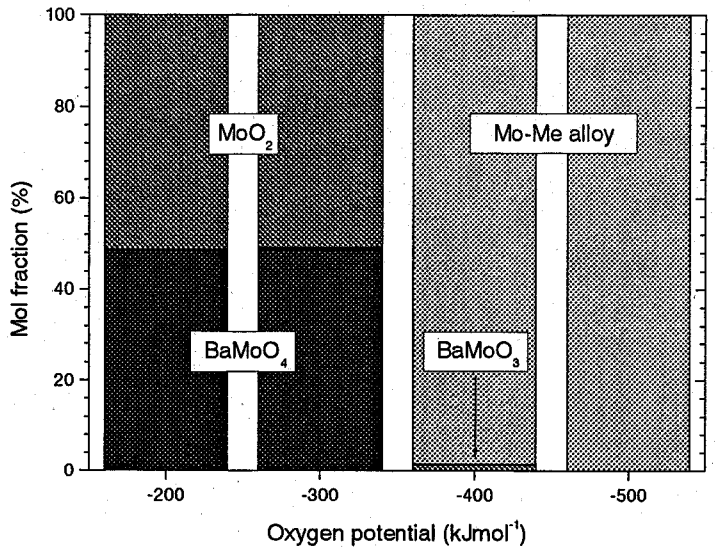

Figure 5. Chemical states of molybdenum.

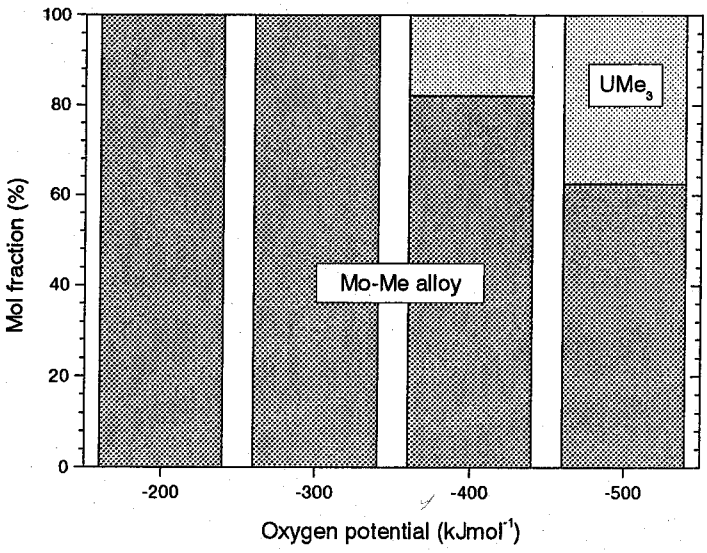

Figure 6. Chemical states of Me (Me: ruthenium, rhodium, and palladium).

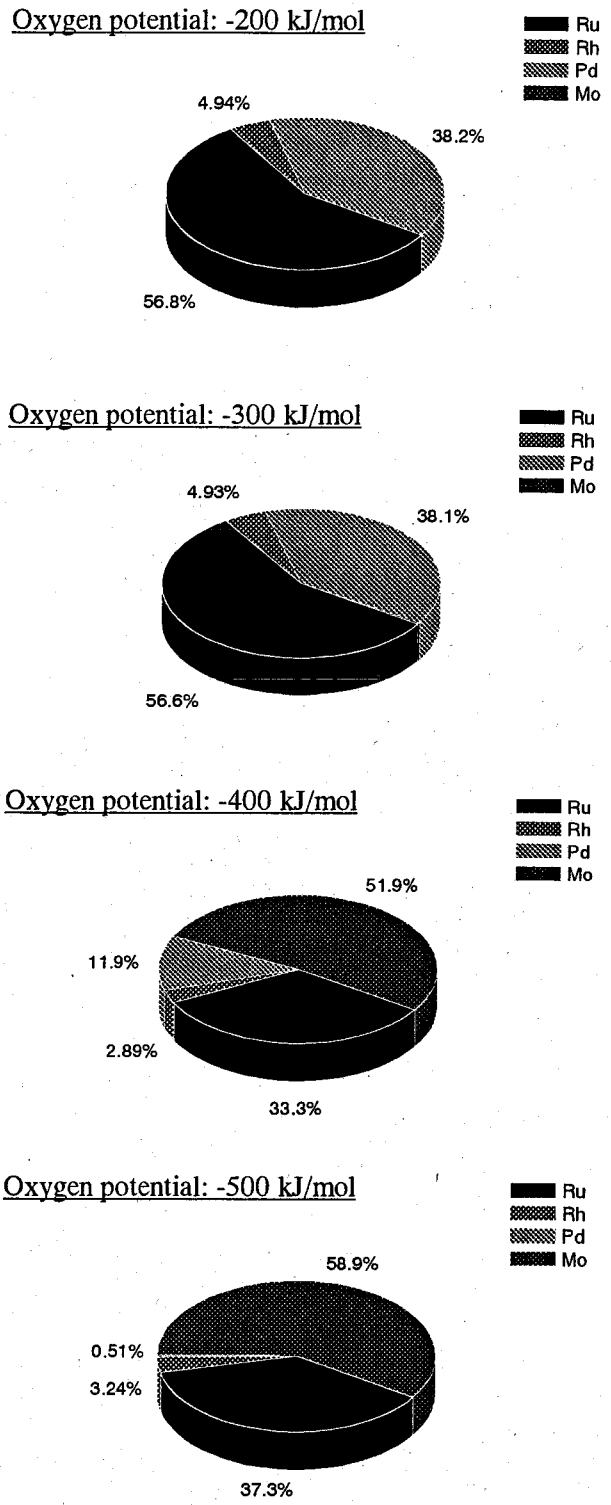

Figure 7. Compositions of the Mo-Me alloy under the various oxygen potentials.

3.1.2. Phase Equilibria of $BaUO_3$-$BaZrO_3$-$BaMoO_3$ System

3.1.2.1. Introduction

It is necessary to understand the behavior of fission product (FP) elements for evaluation of the reliability and safety of the irradiated oxide fuels. In particular, the FP elements precipitated in the fuel matrix such as oxide and metallic inclusions appear to affect the thermal and mechanical properties of the fuel. The gray oxide phase with a perovskite type structure, $(Ba,Sr)(U,Pu,Zr,RE,Mo)O_3$, has been observed in the irradiated mixed oxide (MOX) fuel [1,2], and their thermochemical properties are very important to evaluate the thermal and mechanical properties of the fuel.

The thermophysical properties have been examined for the related perovskite type oxides such as $BaUO_3$, $BaZrO_3$, and $Ba(U,Zr)O_3$ [3-6]. In order to evaluate the properties of the oxide inclusion more exactly, it is necessary to understand the chemical states of the phase, which is affected by various factors in the reactor such as the temperature and oxygen potential.

In the present study, therefore, the chemical states of the oxide inclusion, in short, phase equilibria in the $BaUO_3$-$BaZrO_3$-$BaMoO_3$ system, were studied under the various conditions by using a thermodynamic equilibrium calculation. The calculated results were compared with the previous reported post irradiation examination (PIE) results [7,8].

3.1.2.2. Calculation

The ChemSage program [9] was utilized to obtain the phase equilibria in the $BaUO_3$-$BaZrO_3$-$BaMoO_3$ system, by finding the minimum state of the total free energy of the system. The initial concentration of barium, uranium, zirconium, and molybdenum was calculated by ORIGEN-2 code for the burnup of 50-250 GWd/t, in which the stoichiometric uranium-plutonium mixed oxide $(U_{0.8}Pu_{0.2})O_2$ was taken as a loading fuel.

The chemical species treated in the present study are summarized in Table 1. The thermodynamic data were referred from the SGTE database attached to the ChemSage program and other references [5,10-12]. The gas phase, $(U,Zr,Mo)O_2$ phase, $Ba(U,Zr,Mo)O_3$ phase, and $Ba(U,Mo)O_4$ phase were adopted for the solution phases. The thermodynamic data of each solution phase were treated by an ideal solution model. In the present study, to evaluate the effect of the oxygen potential on the phase equilibria in the $BaUO_3$-$BaZrO_3$-$BaMoO_3$ system, the calculations were performed under the various conditions, in the temperatures at 1273 K and 1973 K and the oxygen potentials from -200 to -500 kJ/mol. The details for the calculation conditions are also given in Table 1.

3.1.2.3. Results and Discussion

The equilibrium phases obtained from the present calculation are shown in Table 2. It

is found that $(U,Zr.Mo)O_2$ phase, which corresponds to the fuel matrix phase, is always stable under the whole conditions. At 1273 K, $Ba(U,Zr.Mo)O_3$ phase, which corresponds to the oxide inclusion, does not exist as a stable phase under high oxygen potentials, because U_4O_9 and $Ba(U,Mo)O_4$ are more stable chemical species in these conditions. At 1973 K, however, $Ba(U,Zr.Mo)O_3$ phase is more stable than $Ba(U,Zr.Mo)O_4$ phase and U_4O_9 in the whole oxygen potential range. At both 1273 K and 1973 K, molybdenum metal is stable under low oxygen potentials.

The chemical composition of $Ba(U,Zr.Mo)O_3$ phase was also evaluated under the various conditions. The calculated results are plotted on the pseudo-ternary phase diagrams of $BaUO_3$-$BaZrO_3$-$BaMoO_3$ system as shown in Fig. 1 (for 1273 K) and Fig. 2 (for 1973 K). It is found that the concentration of $BaZrO_3$ increases with increasing burnup at both 1273 K and 1973 K. The calculated results at 1973 K show slightly higher $BaUO_3$ concentration than those at 1273 K. The oxygen potential affects the behavior of molybdenum significantly. Under low oxygen potentials, $BaMoO_3$ is scarcely included in $Ba(U,Zr.Mo)O_3$ phase, and the concentration of $BaMoO_3$ increases with the rise of oxygen potential.

The chemical composition of $(U,Zr.Mo)O_2$ phase (corresponding to the fuel matrix phase) was also evaluated. The calculated results are shown in Fig. 3 (for 1273 K) and Fig. 4 (for 1973 K). At both temperatures, it is confirmed that the fuel matrix phase is mainly composed of UO_2. The concentration of ZrO_2 increases with increasing burnup, and that of MoO_2 is affected by the oxygen potential. At 1973 K, MoO_2 is scarcely included in the fuel matrix phase under the oxygen potentials of -400 kJ/mol and below.

The calculated results for the chemical composition of $Ba(U,Zr.Mo)O_3$ phase were compared with the previous reported PIE results [1,7,13,14]. Sato et al. have studied the chemical composition of the oxide inclusion in the irradiated high burnup oxide fuel as shown in Fig. 5. It is found that the present calculated results well agree with the reported PIE results, in which $BaMoO_3$ is scarcely included in the oxide inclusion.

3.1.2.4. Conclusion

In order to understand the chemical states of the perovskite type gray oxide phase as the oxide inclusion in the high burnup oxide fuel, the phase equilibrium calculation between the selected FP elements and the fuel has been performed. To evaluate the chemical composition of the oxide inclusion, the thermodynamic data of the solid solution have been treated by the ideal solution model. The concentration of $BaZrO_3$ in the pseudo-ternary $BaUO_3$-$BaZrO_3$-$BaMoO_3$ system increases with increasing burnup at both 1273 K and 1973 K. The concentration of $BaUO_3$ in the system at 1973 K is higher than that at 1273 K. $BaMoO_3$ is scarcely included in the system and the concentration increases slightly with increasing the oxygen potential. These

calculated results well agree with the previous reported PIE results.

References

[1] H. Kleykamp, J. Nucl. Mater., 131 (1985) 221.

[2] H. Kleykamp, Nucl. Technol., 80 (1988) 412.

[3] S. Yamanaka, K. Kurosaki, T. Matsuda, and M. Uno, J. Nucl. Mater., 294 (2001) 99-103.

[4] K. Kurosaki, T. Matsuda, M. Uno, S. Kobayashi, and S. Yamanaka, Journal of Alloys and Compounds, 319 (2001) 271-275.

[5] T. Matsuda, S. Yamanaka, K. Kurosaki, M. Uno, and S. Kobayashi, J. Alloys and Compounds, 322 (2001) 77.

[6] S. Yamanaka, T. Matsuda, K. Kurosaki, and M. Uno, J. Nucl. Sci. Technol., Suppl. 3 (2002) 709.

[7] I. Sato, H. Furuya, T. Arima, K. Idemitsu, and K. Yamamoto, J. Nucl. Sci. Technol., 36 (1999) 775.

[8] I. Sato, H. Furuya, T. Arima, K. Idemitsu, and K. Yamamoto, J. Nucl. Mater., 273 (1999) 239.

[9] G. Eriksson and K. Hack, Metallurgical Transactions B, 21B (1990) 1013.

[10] SGTE Pure Substance Database (Edit. 1998), Provided by GTT Technol., Herzogenrath, Germany (1998).

[11] Japan Thermal Measurement Society, Thermodynamics data base for personal computer MALT2.

[12] E.H.P. Cordfunke and R.J.M. Konings, editor, "Thermochemical data for Reactor Materials and Fission Products", 1990, North-Holland, Amsterdam.

[13] H. Kleykamp, J.O. Paschoal, R. Pejsa, and F. Thummler, J. Nucl. Mater., 130 (1985) 426.

[14] J.O.A. Paschoal, Kernforschungszentrum Karlsruhe, report KfK-3473 (1983).

Table 1

Calculation conditions

Elements	Ba (+Sr) Mo Zr (+Nb) U (+Pu)	
Burnup conditions (GWd/t)	50, 150, 250	Fuel: $(U_{0.8}Pu_{0.2})O_2$ in a fast reactor
Oxygen potential (kJ/mol)	-200, -300, -400, -500	
Temperature (K)	1273, 1973	
Chemical forms	Gas phase	Ideal gas consisted of 25 kinds of gases
	$(U,Zr,Mo)O_2$ phase	Ideal solution of UO_2, ZrO_2, and MoO_2
	$Ba(U,Zr,Mo)O_3$ phase	Ideal solution of $BaUO_3$, $BaZrO_3$, and $BaMoO_3$
	$Ba(U,Zr)O_4$ phase	Ideal solution of $BaMoO_4$ and $BaUO_4$
	Other solids	Elemental substances and U_4O_9, etc

Table 2

Calculated results at 1273 K (a) and 1973 K (b)

(a) 1273 K

Burnup	Oxygen potential	Equilibrium phases				
(GWd)	(kJ/mol)	U_4O_9	$Ba(U,Mo)O_4$	$(U,Zr,Mo)O_2$	$Ba(U,Zr,Mo)O_3$	Mo
50	-200	○	○	○		
	-300		○	○		
	-400			○	○	
	-500			○	○	○
150	-200		○	○		
	-300		○	○	○	
	-400			○	○	○
	-500			○	○	○
250	-200		○	○		
	-300		○	○	○	
	-400			○	○	○
	-500			○	○	○

(b) 1973 K

Burnup	Oxygen potential	Equilibrium phases				
(GWd)	(kJ/mol)	U_4O_9	$Ba(U,Mo)O_4$	$(U,Zr,Mo)O_2$	$Ba(U,Zr,Mo)O_3$	Mo
50	-200			○	○	
	-300			○	○	
	-400			○	○	○
	-500			○	○	○
150	-200			○	○	
	-300			○	○	○
	-400			○	○	○
	-500			○	○	○
250	-200			○	○	
	-300			○	○	○
	-400			○	○	○
	-500			○	○	○

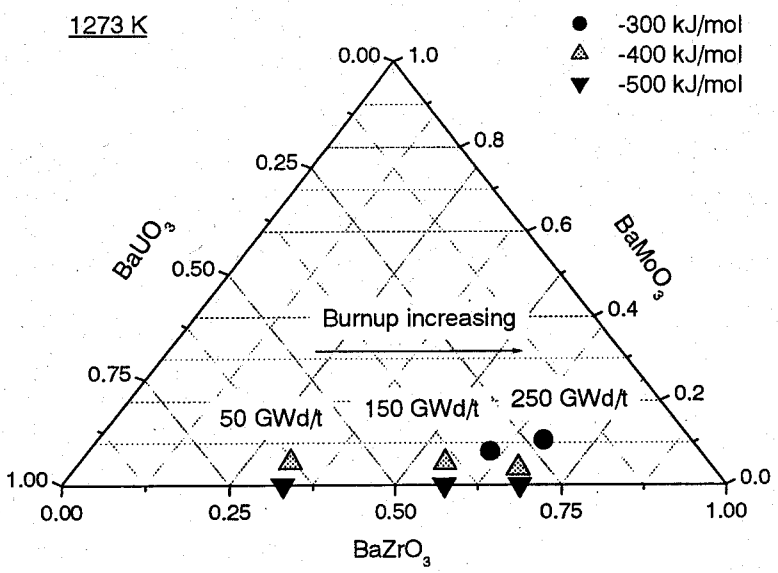

Figure 1. Phase equilibria in the $BaUO_3$-$BaZrO_3$-$BaMoO_3$ system at 1273 K.

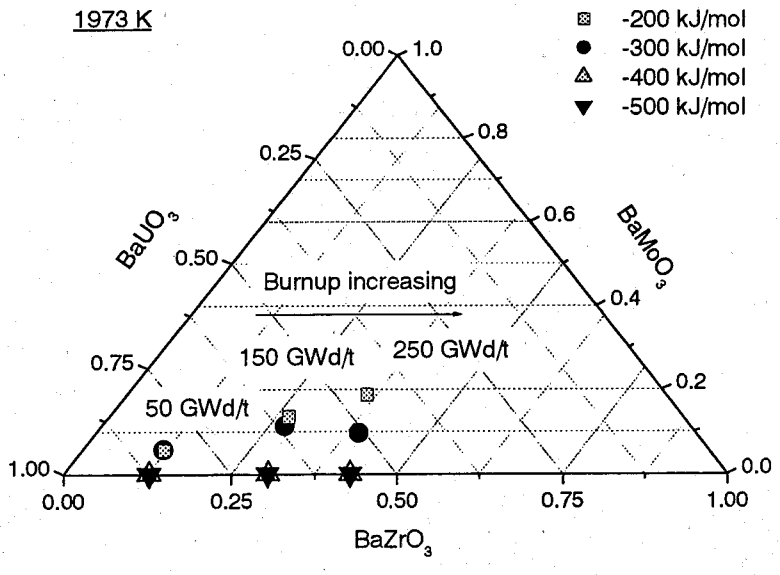

Figure 2. Phase equilibria in the $BaUO_3$-$BaZrO_3$-$BaMoO_3$ system at 1973 K.

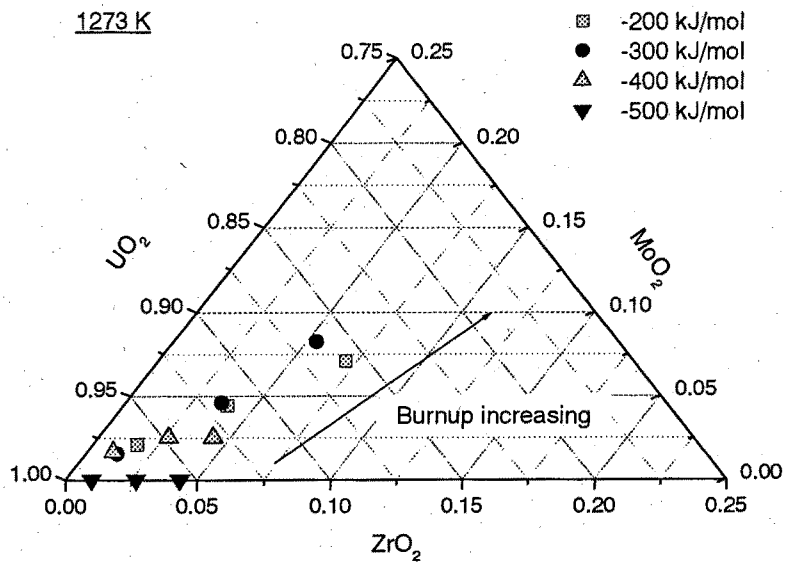

Figure 3. Phase equilibria in the UO_2-ZrO_2-MoO_2 system at 1273 K.

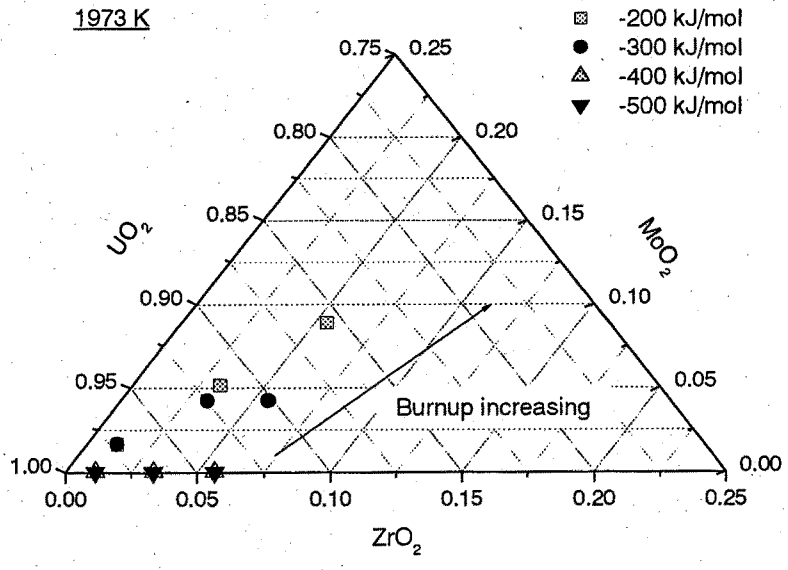

Figure 4. Phase equilibria in the UO_2-ZrO_2-MoO_2 system at 1973 K.

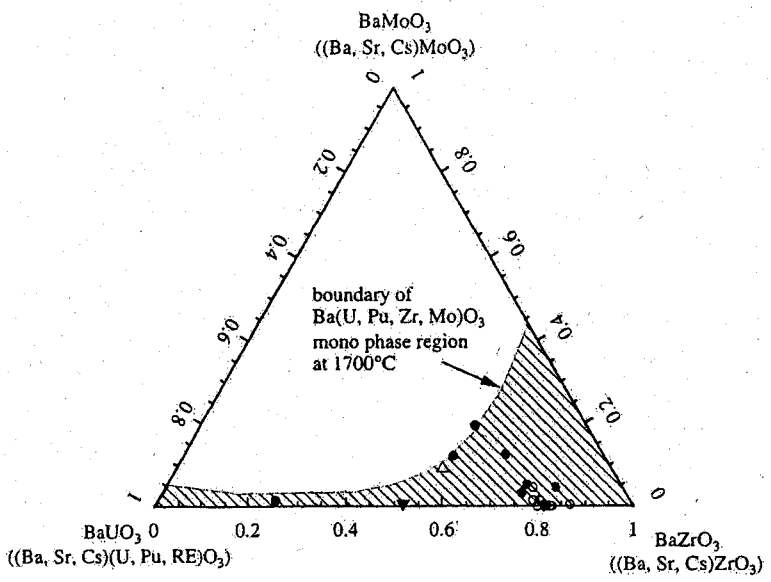

Figure 5. Compositions of the perovskite type oxides precipitated in the irradiated oxide fuels projected onto the $BaUO_3$-$BaZrO_3$-$BaMoO_3$ isothermal section at 1973 K [1,7,13,14].

3.2. Molecular Dynamics (MD) Studies of Oxide Nuclear Fuels

3.2.1. MD Studies of UO_2, PuO_2, and $(U,Pu)O_2$

3.2.1.1. Introduction

Thermal and mechanical properties of nuclear fuels are very important to evaluate pellet-cladding interactions (PCI). However, there is limited information on these properties for uranium-plutonium mixed oxide (MOX) fuel, due to the difficulties associated with the high radiation fields. Because the recycled fuel will be widely used in fast breeder reactors and/or transmutation reactors in the future, it is necessary to develop a new technique to evaluate the thermal and mechanical properties of the MOX fuel. Molecular dynamics (MD) calculations can be one useful technique, and provide information to understand the thermophysical properties of the fuel.

In recent years with the advance of computer simulation techniques, extensive MD studies [1,2,3] have been performed on UO_2 to understand its thermal properties. There are only a few studies of the MD simulation for PuO_2 and $(U,Pu)O_2$ solid solutions. However, these studies were limited to a few properties, or a small temperature range. In the present study, the MD calculations for UO_2, PuO_2, and $(U,Pu)O_2$ solid solution were performed to evaluate the thermal and mechanical properties of the MOX fuel.

3.2.1.2. Molecular Dynamics Calculation

The MD calculations for UO_2, PuO_2, and $(U,Pu)O_2$ were performed for a system of 324 ions (108 cations and 216 anions) initially arranged in a CaF_2 type crystal structure. The MD cell for UO_2 is shown in Fig. 1. In the present study, the calculations were performed by a molecular dynamics program based on MXDRTO [4]. The standard constant pressure-temperature (NPT) and constant volume-temperature (NVT) MD calculations at the thermodynamic equilibrium were performed. A quantum effect [5] was taken into account in the present calculation. In the $(U,Pu)O_2$ system, the desired number of plutonium ions was substituted randomly onto the uranium ion sites. The lattice, containing a fixed number of atoms, was assumed to repeat periodically throughout the material, and there was no edge or surface effect. The long-range coulomb interaction was treated with Ewald's summation [6]. The equations of motion were integrated using Verlet's algorithm [7] with on integration time step of 2.0×10^{-15} s. At the start of the calculation, the initial velocity of each atom was assumed to take random velocities, which was about 0.01 $Åfs^{-1}$.

The calculations were made in the temperature range from 300 K to 2500 K, and in the pressure range from 0.1 MPa to 1.5 GPa. The temperature and pressure of the system were controlled independently through a simple velocity scaling method. However, in calculating the thermal conductivities, a combination of the methods introduced by Andersen [8] and Nose [9]

were used to control the pressure and temperature, respectively. A 10000-step equilibrium run was made at the desired temperature and pressure. Although the number of steps was small, equilibrium was achieved as judged from the changes in the temperature (±3 %), pressure (±9 %), density (±0.02 %), and internal energy (±0.04 %). At 300 K, the mean square displacement of oxygen ions in the MD cell was within 0.02 $Å^2$, which is close to the magnitude of thermal vibrations at that temperature.

We employed the semi-empirical 2-body potential function proposed by Ida [10] for cation-anion interactions. In this potential, the f-electrons and relativistic effects are accounted for implicitly, but the 3-body effect is not accounted for. It would be desirable to use the 3-body (or beyond) potential. For the present study, however, the 2-body potential is sufficient though, because the system (fluorite structure) is relatively simple. The potential is a partially ionic model including a covalent contribution:

$$U_{ij}(r_{ij}) = \frac{z_i z_j e^2}{r_{ij}} + f_0(b_i + b_j)\exp(\frac{a_i + a_j - r_{ij}}{b_i + b_j}) - \frac{c_i c_j}{r_{ij}^6} + D_{ij}\{\exp[-2\beta_{ij}(r_{ij} - r_{ij}^*)] - 2\exp[-\beta_{ij}(r_{ij} - r_{ij}^*)]\} \quad (1)$$

where f_0 equals 4.186, Z_i and Z_j are the effective partial electronic charges on the ith and jth ions, r is the atom distance, r_{ij}^* is the bond length of the cation-anion pair in vacuum, and a, b, and c are the characteristic parameters depending on the ion species. In this potential function, D_{ij} and β_{ij} describe the depth and shape of this potential, respectively. The first term is the coulomb interaction, the second term denotes the core repulsion, and the third term, which is called Morse-type [11] potential, corresponds to the covalent contribution.

The parameters (a, b, and c) for oxygen ions given by Kawamura [12] were used in the present study. These parameters have been used in the studies of other oxides such as SiO_2, $MgSiO_4$, Al_2O_3, and $NaAlSiO_4$ [12]. The other parameters were determined by trial and error using the experimental values of the changes in the lattice parameters with temperature and pressure for UO_2, PuO_2, and $(U_{0.8}Pu_{0.2})O_2$. This semi-empirical approach to determine the potential parameters has given effective and realistic results for crystalline solids [4], and the MD studies using the same method are published [13-15]. Using the parameters so obtained, the linear thermal expansion coefficient (α), compressibility (β), heat capacity (C_P), and thermal conductivity (λ) of UO_2, PuO_2, and $(U_{0.8}Pu_{0.2})O_2$ were evaluated.

The thermal conductivity of the system was calculated by the Green-Kubo relations. Because the Green-Kubo theory is a statistical method, the NPT calculation was performed using the methods introduced by Andersen [8] and Nose [9]. Details of the Green-Kubo relations have been described in several other papers [16], so only the main points will be briefly described here.

The form of the thermal conductivity of the system is based on the integrated heat flux

[S(t)] autocorrelation function:

$$\lambda = \frac{V}{3k_B T^2}\int_0^{\infty}\langle S(t)\cdot S(0)\rangle dt, \tag{2}$$

where λ is the thermal conductivity, V is the volume of the system, T is the absolute temperature, and k_B is the Boltzmann constant. The heat flux S is described as:

$$S = \frac{1}{V}\left[\sum_j e_j v_j - \frac{1}{2}\sum_j\sum_{j=i} r_{ij}\left(f_{ij}\cdot v_j\right)\right], \tag{3}$$

and the instantaneous excess energy of atom j, e_j, is described as:

$$e_j = \left\{\frac{1}{2}m_j v_j^{\,2} + \frac{1}{2}\sum_{i=j} u\left(r_{ij}\right)\right\} - e_{av}, \tag{4}$$

where m_j and v_j are the mass and velocity of atom j, and r_{ij}, f_{ij}, and u are the interatomic distance, force, and potential between atom i and j. The autocorrelation function was calculated for 5×10^5 steps with time origins taken at every 10 steps.

The MD calculation conditions for UO_2, PuO_2, and $(U,Pu)O_2$ performed in the present study are summarized in Table 1.

3.2.1.3. Results and Discussion

The values of the parameters used in the interatomic potential in the present study are summarized in Table 2. The change in the lattice parameters of UO_2, PuO_2, and $(U_{0.8}Pu_{0.2})O_2$ with temperature obtained by the MD calculations under the pressure of 0.1 MPa are shown in Fig. 2, together with the experimental data [17,18]. The changes in the lattice parameter of UO_2 with pressure in the range from 0.1 MPa to 1.5 GPa at the temperatures of 300 K and 100 K are shown in Fig. 3. The variations with temperature and pressure in the calculated lattice parameter agree well with the reported experimental values. The change in the lattice parameter of $(U,Pu)O_2$ with Pu content is shown in Fig. 4. It is confirmed that the calculated lattice parameters of $(U,Pu)O_2$ solid solutions follow Vegard's law. These results indicate that the potential function used in the present calculations describes well the changes in the lattice parameter with both temperature and pressure.

Linear thermal expansion coefficients (α) of UO_2, PuO_2, and $(U_{0.8}Pu_{0.2})O_2$ can be obtained from the change in the lattice parameters with temperature. Although the calculated values of α are slightly lower (about 5 %) than the experimental data [17,18], the tendency of the temperature dependence is consistent with the experimental data.

The compressibility (β) at the pressures from 0.1 MPa to 1.5 GPa was evaluated up to about 2500 K from the change in lattice parameter with pressure. The temperature dependence of the calculated β for UO_2, PuO_2, and $(U_{0.8}Pu_{0.2})O_2$ are shown in Fig. 5, together with the experimental data [19,20]. For UO_2, the calculated β is in good agreement with the experimental

data, increasing with increasing temperature in a similar manner to the experimental data. This means that the MD cell of UO_2 becomes mechanically soft with increasing temperature. At high temperatures, the calculated β increases markedly. It is known that UO_2 becomes soft and the creep rate of UO_2 increases at high temperatures. This phenomenon is well reproduced by the present MD simulation. The β of stoichiometric PuO_2 has not been reported until now. It increases with increasing temperature. The marked increase of the calculated β at high temperatures is not observed for PuO_2. For $(U_{0.8}Pu_{0.2})O_2$, the calculated β (5.5×10^{-3} GPa) is slightly lower than literature data [20] (6.3×10^{-3} GPa) at room temperature, which is caused by the difference in the structures between the MD cell (a perfect single crystal) and the experimental specimen (polycrystalline). The calculated β of $(U_{0.8}Pu_{0.2})O_2$ increases markedly at high temperatures as did in UO_2.

Jackson [21] has showed that cation migration is assisted by anion diffuse transition (Bredig transition). The Bredig transition may occur at high temperatures in the MD cells of UO_2 and $(U_{0.8}Pu_{0.2})O_2$, and this would generate the marked increases of the calculated β.

By using the same parameters for the interatomic potential that have been determined from the lattice parameter variations, the heat capacities of UO_2, PuO_2, and $(U_{0.8}Pu_{0.2})O_2$ were evaluated. The heat capacity at constant pressure C_P can be evaluated approximately from the following relationship:

$$C_P = C_V + C_d + C_{el} + C_{sch} + C_{sp} + \cdots, \quad (5)$$

where C_V is the heat capacity at constant volume, C_d is the lattice dilation term, C_{el} is the conduction electronic term, C_{sch} is the Schottky term, and C_{sp} is the contribution from the formation of the small polarons. We have evaluated C_P for the 3 materials as follows:

$$C_P(UO_2) = C_V(MD) + C_d(MD) + C_{sch}(UO_2) + C_{sp}(UO_2), \quad (6)$$

$$C_P(PuO_2) = C_V(MD) + C_d(MD) + C_{sch}(PuO_2) + C_{sp}(UO_2), \quad (7)$$

$$C_P((U_{0.8}Pu_{0.2})O_2) = C_V(MD) + C_d(MD) + 0.8(C_{sch}(UO_2) + C_{sp}(UO_2)) + 0.2C_{sch}(PuO_2). \quad (8)$$

Only C_V and C_d can be evaluated from the results obtained by the MD calculations. C_{sch} (Schottky term) and C_{sp} (small polarons term) are taken from the data in literatures [22,23]. The conduction electron contribution is ignored, since UO_2, PuO_2, and $(U_{0.8}Pu_{0.2})O_2$ are considered to behave like insulators.

In the present study, C_V was evaluated from the variation of the internal energy of the system with temperature calculated by the NVT MD simulations. C_d was evaluated from the following relationship:

$$C_d = \frac{(3\alpha)^2 VT}{\beta}, \quad (9)$$

where V is the molar volume, α is the linear thermal expansion coefficient, β is the compressibility, and T is the absolute temperature. C_d was evaluated by using the calculated

values of α, V, and β obtained from the NPT MD simulations. Since the contributions of the conduction electrons, the Schottky defects, and the formation of the small polarons were not simulated in the present calculation, literature data [22] were used. For UO_2, the Schottky contribution to the internal energy (U) is given by:

$$U_{sch} = 1.46 \cdot t^2 \ \text{(kJ/mol)}, \tag{10}$$

where $t=10^{-3}T$ (K), and the contribution from the formation of the small polarons ($2U^{4+} \rightarrow U^{3+} + U^{5+}$) to the internal energy (U) is given by:

$$U_{sp} = 256 \cdot \exp\left(\frac{-10.79}{t}\right) \ \text{(kJ/mol)}. \tag{11}$$

In the present study, each contribution to the heat capacity was obtained from a differentiation of the internal energy by temperature.

The change in the calculated C_P with temperature for UO_2 is shown in Fig. 6, together with literature data [24-26]. In the temperature range from 300 K to 2500 K, the calculated C_P agrees well with both MALT-2 [25] and SGTE [26] data, which indicates that the potential function used in the present study describes well the change in the internal energy of UO_2 with temperature.

For PuO_2, C_P was calculated by adding C_d, C_{sch}, and C_{sp} (for UO_2) to C_V. C_V was calculated from the variation of the internal energy of the system with temperature by the NVT simulations, similar to the case of UO_2. The Schottky contribution to the heat capacity for PuO_2 has been reported by Manes [23]. It is known that C_P for PuO_2 is higher than that for UO_2. The main reason is that the Schottky contribution of PuO_2 to the heat capacity is larger than that for UO_2. Figure 7 shows the variation in the calculated C_P for PuO_2 with temperature, together with literature data [24-26]. This figure shows too poor agreement between the calculated C_P and that measured by Ralph [24]. The reason for the poor agreement is not understood yet. However, the calculated result is considered to be reasonable, because the agreement with other data (SGTE and MALT-2) can be observed in the figure.

For $(U_{0.8}Pu_{0.2})O_2$, C_P was obtained by adding C_d, C_{sch}, and C_{sp} to C_V. 80 % of the values of C_{sch} and C_{sp} for UO_2 and 20 % of the values of C_{sch} for PuO_2 were used. Figure 8 shows the results, together with literature data [24-26]. It is observed that the results agree with the Neumann-Kopp law. At about 2350 K, the calculated C_P shows a peak as already seen for UO_2, which indicates the occurrence of the Bredig transition in the simulated MD cells.

It has been reported [27] that a diffuse transition (Bredig transition) occurs at about 0.8 of the melting temperatures in many fluorite structure compounds ($SrCl_2$, PbF_2, ThO_2, UO_2). The Bredig transition is characterized by a smooth peak in the heat capacity [28], a dramatic rise in the electrical conductivity [29], and a rapid increase in disorder of the anion sublattice [30]. In the present study, the Bredig transition can be observed in the calculated C_V for UO_2 and

20 %-MOX but not for PuO_2. For example, the calculated C_V for UO_2 is shown in Fig. 9 as a function of temperature. The Bredig transition is observed in C_V, independently of the Schottky and other effects, which means that the Bredig transition can be reproduced by the potential effects.

The motion tracks of the ions for UO_2 unit cell at various temperatures are shown in Fig. 10. The large motion of oxygen ions is observed in the figure at 2500 K, and it is suggested that the MD cell of UO_2 becomes an oxygen superionic conductor at the temperature as confirmed by the neutron scattering experiments [31]. Ralph [24] has reported that the Bredig transition of UO_2 occurs at 2610 K (0.84 of the melting temperature), which is almost in agreement with the present calculation. This result provides further confirmation that our model can give a reasonable description of the atomic motion in UO_2 at high temperatures.

Clear existence of the Bredig transition in PuO_2 has not been reported. Ralph [24] concluded that it might occur in PuO_2, although his enthalpy data analysis did not detect a heat capacity peak for PuO_2. He pointed out that insufficient data in the vicinity of 0.8 of the absolute melting temperature may have been the reason. The motion track of the ions for PuO_2 unit cell at 2500 K is shown in Fig. 11, together with that of UO_2. In the present calculation, the Bredig transition does not occur in the simulated PuO_2 MD cell even at 2500 K (0.94 of the melting temperature). Therefore, it is concluded that the transition temperature might be very near to the melting temperature for PuO_2.

The thermal conductivity of UO_2, PuO_2, and $(U_{0.8}Pu_{0.2})O_2$ were evaluated by the MD calculation. Only the lattice contributions to the thermal conductivity, λ_{lat} could be included in the MD calculations. The λ_{lat} was obtained as the plateau value of the time integral of the auto-correlation function (ACF) of the energy current, $< S(t) \cdot S(0) >$. The ACF approaches zero and its time integral reaches a plateau value. Integrating ACF with respect to time gives the thermal conductivity. Details of these calculations are given in my previous reported papers [32-35].

For UO_2, the variation in the calculated thermal conductivity with temperature is shown in Fig. 12, together with literature data [36]. The high temperature electronic contribution to thermal conductivity, predicted by Harding [37], was added to the calculated value at 2000 K and 2500 K. The calculated values are in good agreement with the experimental values in the temperature range from 650 K to 2500 K, even though the simulated system is a perfect crystal. This indicates that our model can describe the phonon contribution to the thermal conductivity.

The calculated thermal conductivity of PuO_2 is shown in Fig. 13 as a function of temperature, together with the experimental data reported by Gibby [38]. The calculated values are in good agreement with the experimental data in the temperature range from 360 K to 2000 K, showing that the simulated system of PuO_2 models the phonon vibration well. This provides

further confirmation that the potential model of PuO_2 in the present study is reasonable for computing the thermal conductivity.

The calculated thermal conductivity of $(U_{0.8}Pu_{0.2})O_2$ is shown in Fig. 14 as a function of temperature, together with literature data [38-44]. 80% of the electronic contribution in UO_2 predicted by Harding [37] was added to the calculated values at 2000 K and 2500 K. The calculated values are in good agreement with the experimental values up to 2500 K, and are lower than those of both UO_2 and PuO_2.

Figure 15 shows the normalized thermal conductivity ($\lambda_{MOX}/\lambda_{UO2}$) at 360 K as a function of Pu content together with literature data [38]. The thermal conductivity of $(U,Pu)O_2$ decreases with increasing Pu content, and goes through a minimum value at about 30-40% Pu. This result indicates that the Pu ions mutually act as the phonon scattering centers in the MD cell, similar to the real materials.

3.2.1.4. Conclusion

The MD calculations have been performed for the oxide nuclear fuels, UO_2, PuO_2, and $(U,Pu)O_2$. The thermal and mechanical properties, viz. the linear thermal expansion coefficient, compressibility, heat capacity, and thermal conductivity have been evaluated by the MD calculations. The calculated results have been compared with the experimental data. The Morse-type potential function added to the Busing-Ida type potential proposed by Ida has been employed for the ionic interactions. The potential parameters have been determined by trial and error using the experimental values of the variations in the lattice parameters with temperature and pressure.

The simulated UO_2 system shows both the existence of the Bredig transition and a peak in the heat capacity at high temperatures, and provides thermal conductivities in the temperature range from 360 K to 2500 K. The variation in the calculated heat capacity of PuO_2 with temperature agrees well with the experimental data. The change in the calculated thermal conductivity of PuO_2 with temperature is also in good agreement with the experimental data. This indicates that the simulation model of PuO_2 gives a reasonable description of the phonon contribution to the thermal conductivity. The Bredig transition does not occur in the simulated PuO_2 system.

The thermal and mechanical properties of $(U,Pu)O_2$ have been evaluated from some basic properties of UO_2 and PuO_2 by using the MD techniques. The calculated lattice parameter of $(U_{0.8}Pu_{0.2})O_2$ closely follows Vegard's law. The calculated heat capacity and thermal conductivity of $(U_{0.8}Pu_{0.2})O_2$ are in good agreement with the experimental data. The simulated $(U_{0.8}Pu_{0.2})O_2$ cell also shows both the existence of the Bredig transition and a peak in the heat capacity at around 2350 K.

These results show the usefulness of the MD techniques for evaluation of the thermal and mechanical properties of the oxide nuclear fuel. The MD simulations will become a powerful method to evaluate the properties of the oxide fuels.

References

[1] C.R.A. Catlow, Proc. Roy. Soc., A353 (1977) 533.

[2] P.J.D. Lindan and M.J. Gillan, J. Phys. Condens. Matter., 3 (1991) 3929.

[3] S. Higuchi, J. Nucl. Sci. Technol., 35 (1998) 833-835.

[4] K. Kawamura and K. Hirao, "Material Design using Personal Computer", Shokabo, Tokyo, (1994).

[5] E. Wigner, Phys. Rev., 40 (1932) 749.

[6] P.P. Ewald, Ann. Phys., 64 (1921) 253.

[7] L. Verlet, Phys. Rev., 159 (1967) 98.

[8] H.C. Andersen, J. Chem. Phys., 72 (1980) 2384.

[9] S. Nose, J. Chem. Phys., 81 (1984) 511.

[10] Y. Ida, Phys. Earth Planet Interiors, 13 (1976) 97.

[11] P.M. Morse, Phys. Rev., 34 (1929) 57.

[12] K. Kawamura, "Molecular Dynamics Simulations", Springer Series in Solid-State Sciences, 103 (1992) 88.

[13] T. Katsumata, Y. Inaguma, M. Itoh, and K. Kawamura, Solid State Ionics, 108 (1998) 175.

[14] H. Inaba, R. Sagawa, H. Hayashi, and K. Kawamura, Solid State Ionics, 122 (1999) 95.

[15] H. Hayashi, R. Sagawa, H. Inaba, and K. Kawamura, Solid State Ionics, 131 (2000) 281.

[16] R. Zwanzig, Ann. Rev. Phys. Chem., 16 (1965) 67.

[17] D.G. Martin, J. Nucl. Mater., 152 (1988) 94.

[18] Thermophysical properties of matter, The TPRC data series vol. 5. IFI/Plenum Data Co., New York (1970).

[19] P. Browning, G.J. Hyland, and J. Ralph, High Temp.-High Press., 15 (1983) 169.

[20] A.W. Nutt and A.W. Allen, J. Am. Ceram. Soc., 53 (1970) 205.

[21] R.A. Jackson, A.D. Murray, J.H. Harding, and C.R.A. Catlow, Philosophical Magazine, A53 (1986) 27.

[22] G.J. Hyland and J. Ralph, High Temp.-High Press., 15 (1983) 179.

[23] L. Manes, "Plutonium 1970 and other actinides", Part 1, pp. 254.

[24] J. Ralph, J. Chem. Soc. Farady Trans., 2, 83 (1987) 1253.

[25] Japan Thermal Measurement Society, Thermodynamics Data Base for Personal Computer MALT 2, 1992.

[26] The SGTE Pure Substance and Solution databases, GTT-DATA SERVICES.

[27] A.S. Dworkin and M.A. Bredig, J. Phys. Chem., 72 (1968) 1277.

[28] W. Schroter and J. Nolting, J. Phys. Colloq., (Paris), C6 (41) (1980) 20.

[29] M.J. Gillan, UKAEA Harwell Report TP 1097.

[30] M.H. Dickens et al., J. Phys., C15 (1982) 4043.

[31] K. Clausen, W. Hayes, J.E. Macdonald, R. Osborn, and M.T. Hutchings, Phys. Rev. Letters, 52 (1984) 1238.

[32] K. Yamada, K. Kurosaki, M. Uno, and S. Yamanaka, J. Alloys and Compounds, 307 (2000) 1.

[33] K. Yamada, K. Kurosaki, M. Uno, and S. Yamanaka, J. Alloys and Compounds, 307 (2000) 10.

[34] K. Kurosaki, K. Yano, K. Yamada, M. Uno, and S. Yamanaka, J. Alloys and Compounds, 311 (2000) 305.

[35] K. Kurosaki, K. Yano, K. Yamada, M. Uno, and S. Yamanaka, J. Alloys and Compounds, in press (JALCOM6182).

[36] MATPRO-Version 11 (Revision 2), NUREG/CR-0497, TREE-1280, Rev. 2, August (1981).

[37] J.H. Harding and D.G. Martin, J. Nucl. Mater., 166 (1989) 233.

[38] R.L. Gibby, J. Nucl. Mater., 38 (1971) 163.

[39] Y. Philipponneau, J. Nucl. Mater., 188 (1992) 194.

[40] S. Fukushima, T. Ohmichi, A. Maeda, and M.Handa, J. Nucl. Mater., 16 (1983) 287.

[41] J.C. Van Crayonist and J.C. Weilbacher, Rapport SYRIA-3488 (1968).

[42] H.E. Schmidt, High-Temp.-High-Press., 3 (1971) 345.

[43] J.C. Weilbacher, Rapport SYRIA-4572 (1972).

[44] C.S. Olsen and G.A. Reymann, "THREE-NUREG-1005 (1976)", eds. P.E. MacDonald and L.B. Thompson.

Table 1

Calculation conditions of MD simulations for cubic fluorite type oxides, MO_2

		α	β	C_V	λ
System	Particles	324 particles (O^{2-}: 216, M^{4+}: 108[#])			
	Structure	Cubic fluorite			
	Boundary	3 dimensional periodic boundary condition			
Control	Temperature	Scaling	Scaling	Scaling	Nose
	Pressure	Scaling	Scaling	Scaling	Andersen
Step time		2f sec	2f sec	2f sec	2f sec
Number of steps		10,000	10,000	10,000	1,000,000

[#] The desired number of plutonium ions is substituted randomly onto the uranium ion sites.

Table 2

Values of the interatomic potential function parameters for UO_2, PuO_2, and $(U,Pu)O_2$

Ions	z	a	b	c	D_{ij}	β_{ij}	r_{ij}^*
O	-1.2	1.926	0.160	20			
					(for U-O pairs)		
U	2.4	1.659	0.160	0	18.0	1.25	2.369
					(for Pu-O pairs)		
Pu	2.4	1.229	0.080	0	13.0	1.56	2.339

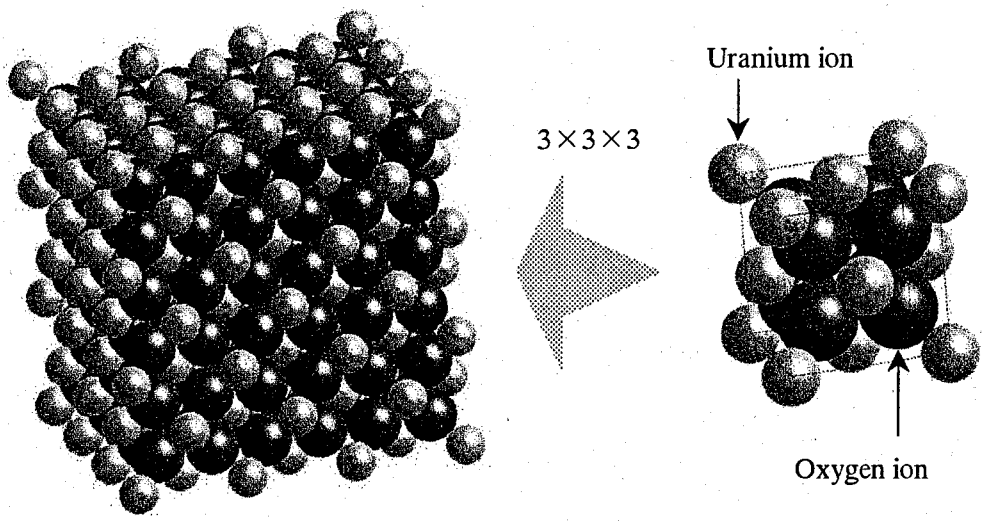

Figure 1. MD cell for UO_2.

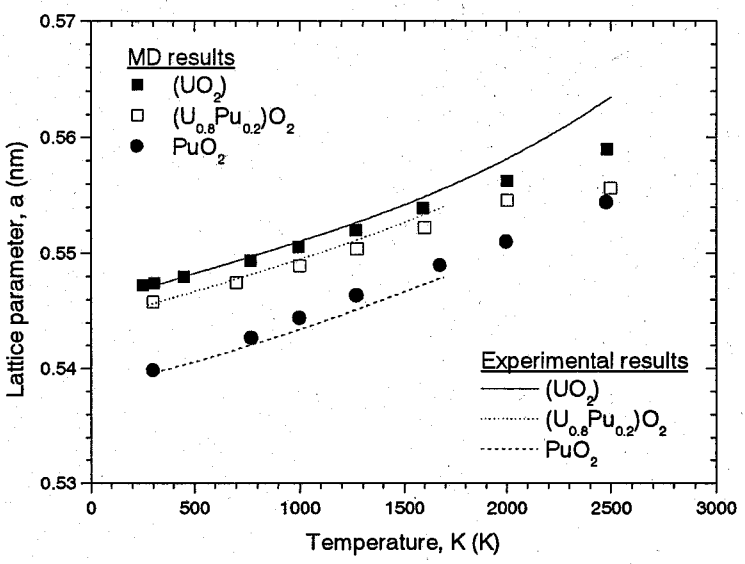

Figure 2. Calculated lattice parameters for UO_2, PuO_2, and $(U_{0.8}Pu_{0.2})O_2$ as a function of temperature.

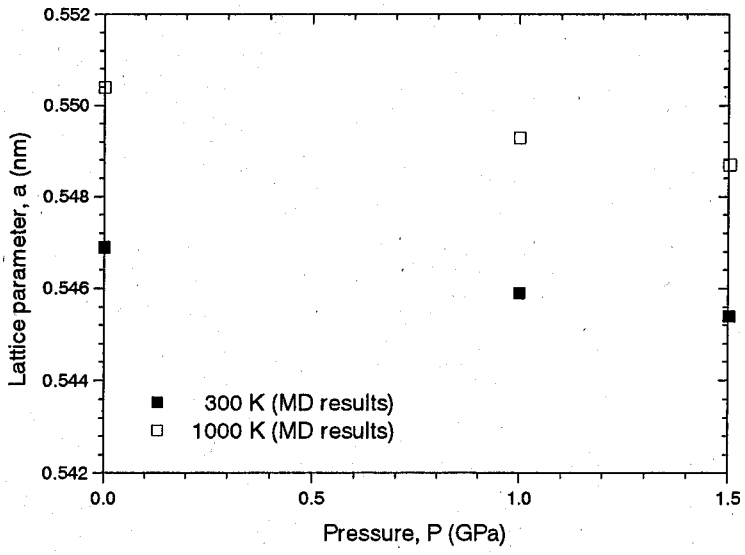

Figure 3. Calculated lattice parameters for UO_2 as a function of pressure.

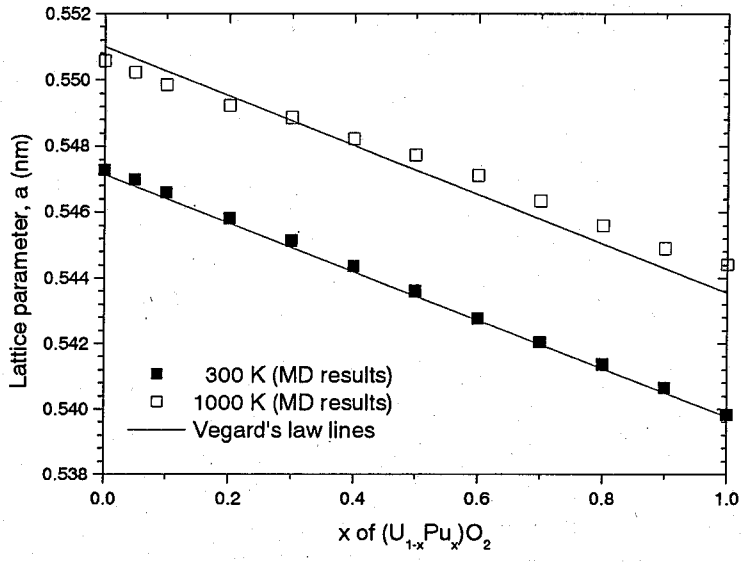

Figure 4. Calculated lattice parameters for $(U,Pu)O_2$ as a function of Pu content.

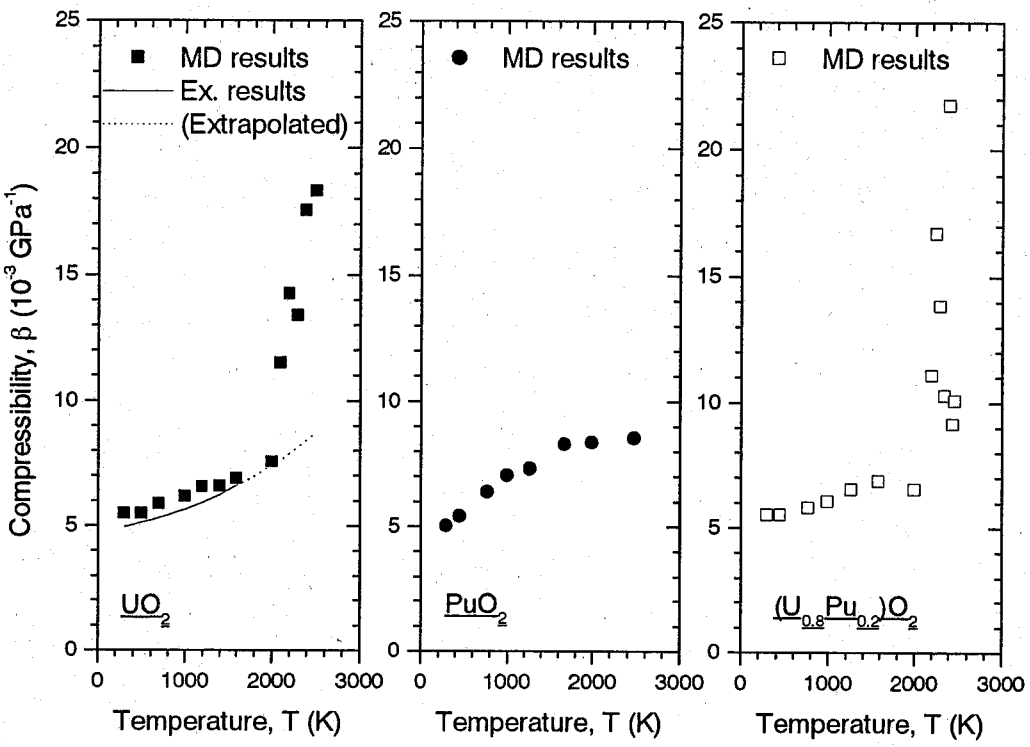

Figure 5. Calculated compressibility (β) for UO_2, PuO_2, and $(U_{0.8}Pu_{0.2})O_2$ as a function of temperature.

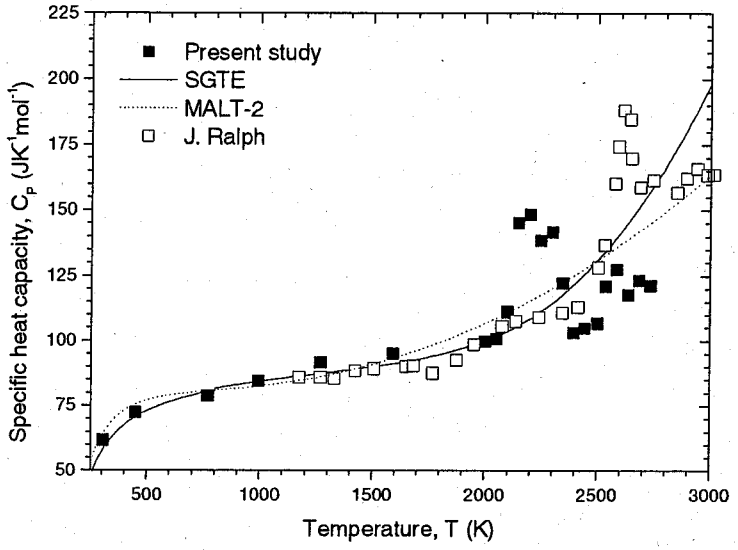

Figure 6. Temperature dependence of C_P for UO_2.

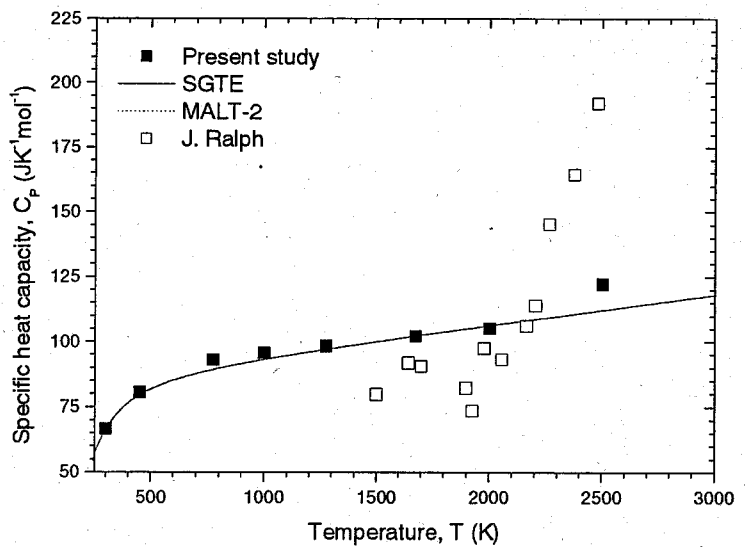

Figure 7. Temperature dependence of C_P for PuO_2.

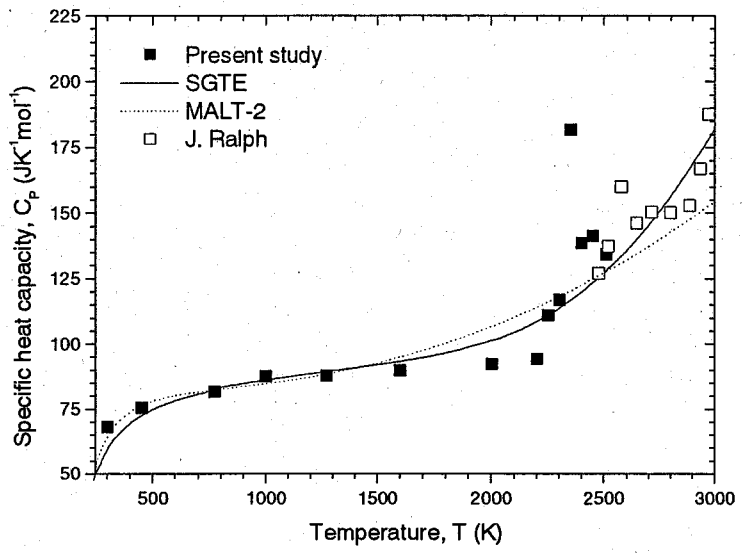

Figure 8. Temperature dependence of C_P for $(U_{0.8}Pu_{0.2})O_2$.

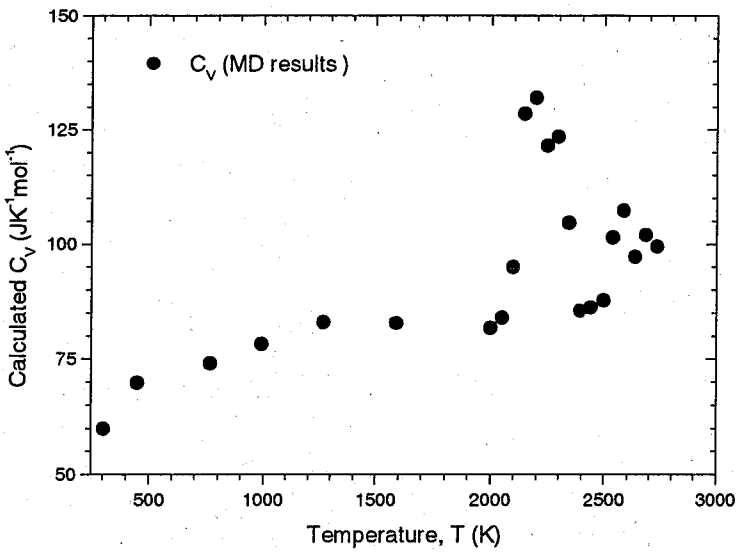

Figure 9. Calculated C_V for UO_2 as a function of temperature.

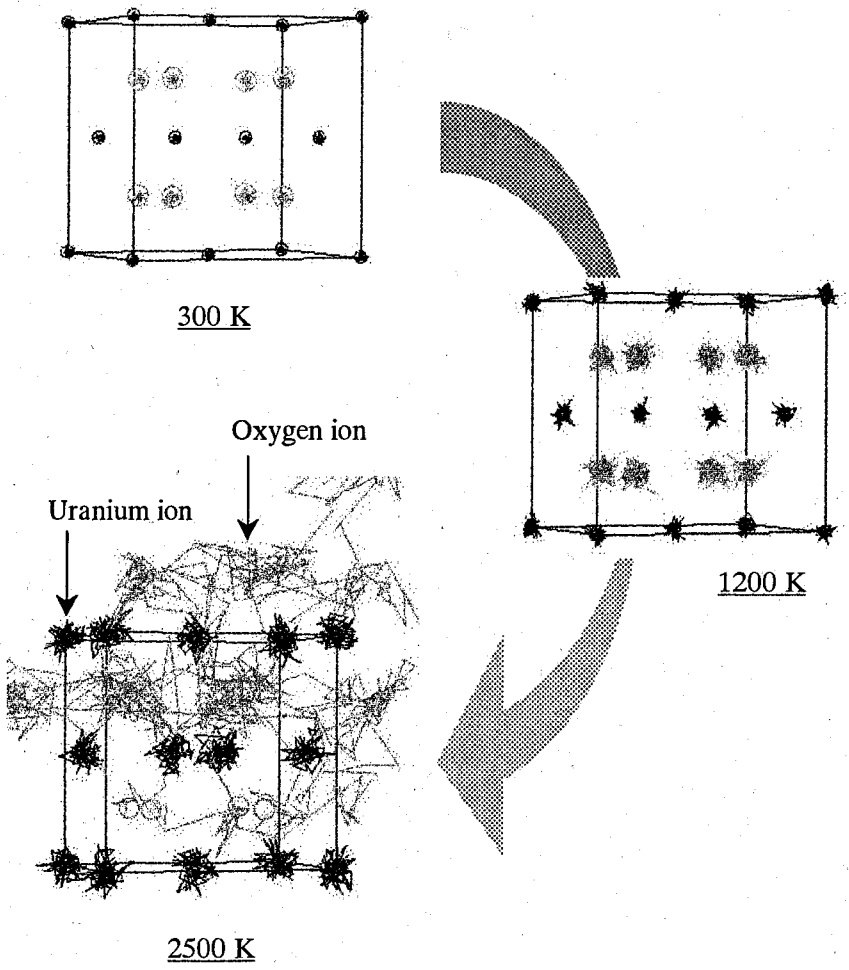

Figure 10. Motion tracks of ions for UO_2 at various temperatures.

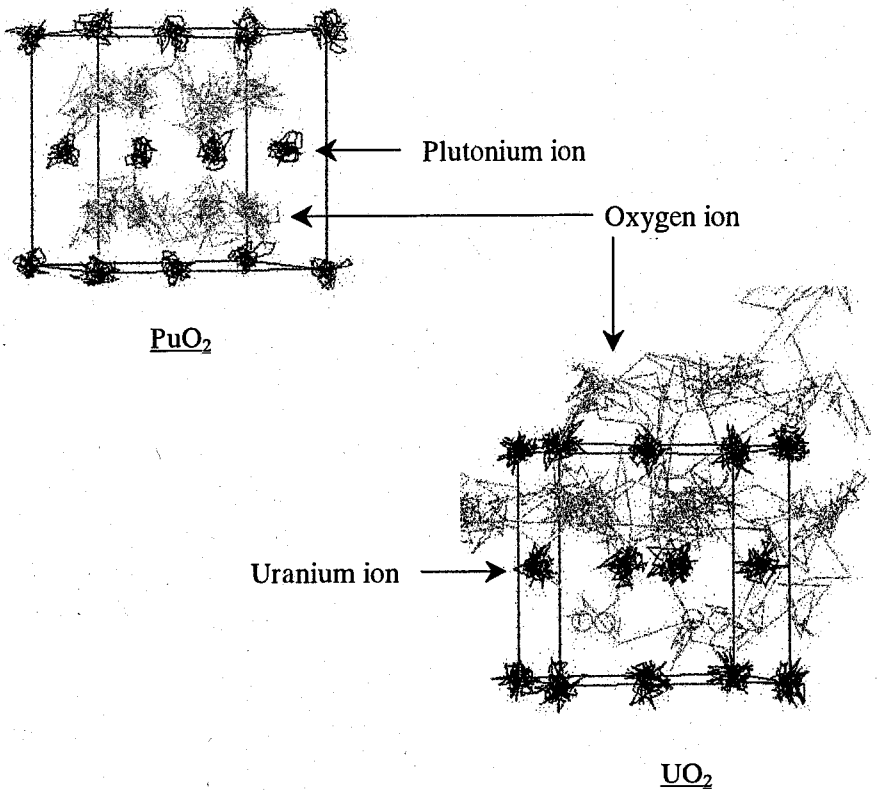

Figure 11. Motion tracks of ions for UO_2 and PuO_2 unit cells at 2500 K.

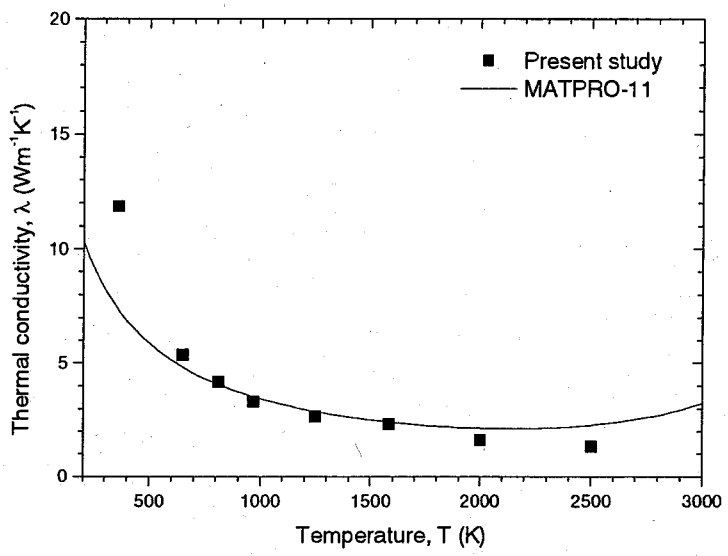

Figure 12. Temperature dependence of thermal conductivity for UO_2.

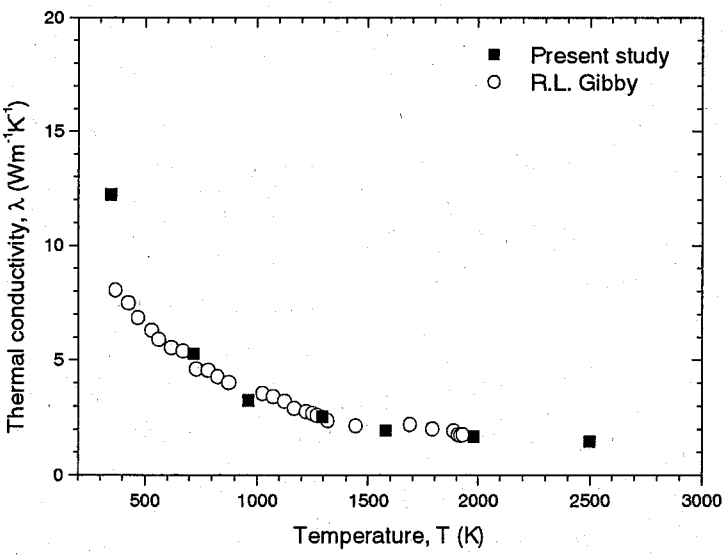

Figure 13. Temperature dependence of thermal conductivity for PuO_2.

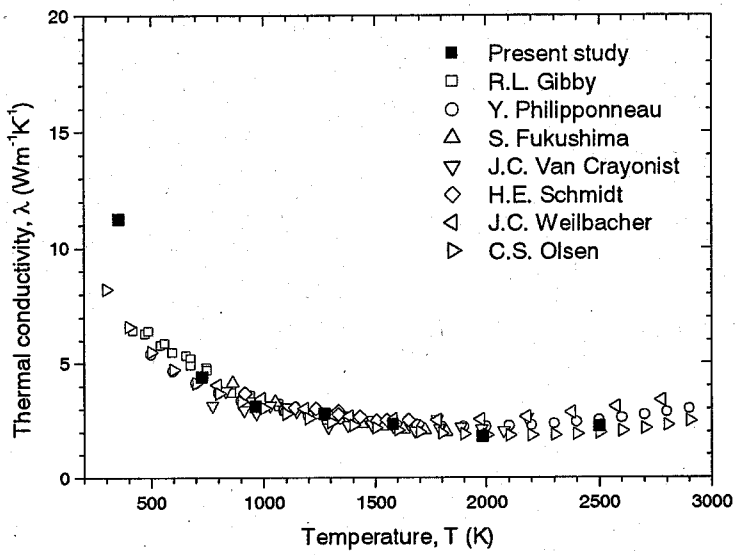

Figure 14. Temperature dependence of thermal conductivity for $(U_{0.8}Pu_{0.2})O_2$.

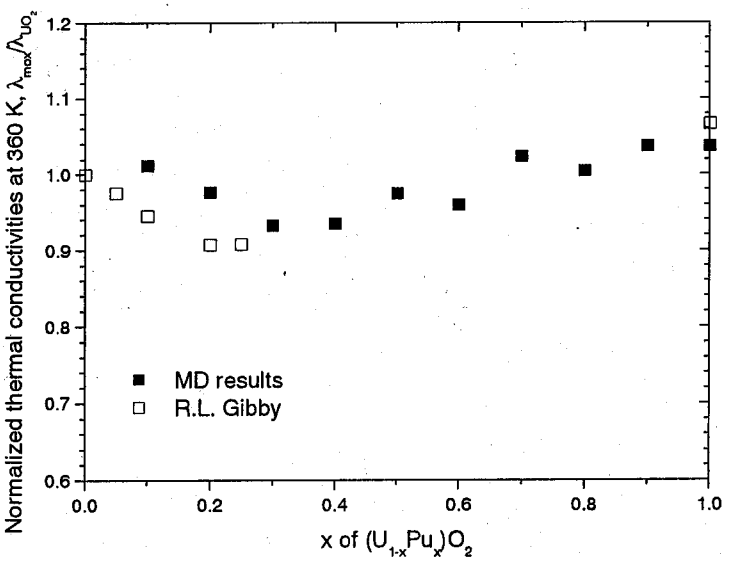

Figure 15. Normalized thermal conductivity ($\lambda_{MOX}/\lambda_{UO2}$) at 360 K of $(U,Pu)O_2$.

3.2.2. MD Studies of Perovskite Type Oxides

3.2.2.1. Introduction

In irradiated nuclear fuel, the fission product (FP) elements affect the thermal and mechanical properties of the fuel. In particular, the FP elements precipitated in the fuel matrix, such as oxide and metallic inclusions, appear to have an influence on the thermal and mechanical properties of the fuel. The gray oxide phase with the perovskite type structure of $(Ba,Sr)(U,Pu,Zr,RE,Mo)O_3$ has been observed in the irradiated oxide fuel as the oxide inclusion [1,2]. In our previous studies, several properties of the Ba and Sr series perovskite type oxides, specifically the melting point, thermal expansion coefficient, elastic moduli, Debye temperature, heat capacity, and thermal conductivity, have been studied [3-7].

On the other hand, recent advances in computer power and simulation techniques have allowed us to simulate the materials behavior on the atomic scale. For nuclear fuels, several molecular dynamics (MD) studies [8-15] of MOX and mixed nitride fuels have been performed by the authors to evaluate the various thermophysical properties. For other nuclear materials, such as precipitated FP compounds, however, there is no MD study.

In the present study, the MD calculations for Ba and Sr series perovskite type oxides, viz., $BaUO_3$, $BaZrO_3$, $BaCeO_3$, $BaMoO_3$, $SrZrO_3$, and $SrCeO_3$, are performed to evaluate the thermal and mechanical properties in the temperature range from 300 K to 2000 K. The anomalous properties, for example, the extremely low thermal conductivity of $BaUO_3$ are discussed by using the MD calculations. The calculated results are compared with the experimental data measured in the previous chapter of this thesis. The applicability of the MD method to evaluate the thermal and mechanical properties of the perovskite type oxides is discussed.

3.2.2.2. Molecular Dynamics Calculation

The calculation method and procedure are same as mentioned in previous section. For cubic perovskites, $BaUO_3$, $BaZrO_3$, and $BaMoO_3$, the MD calculation was performed for a system of 320 ions (O^{2-}: 192, U^{4+}, Zr^{4+}, or Mo^{4+}: 64, Ba^{2+}: 64). For orthorhombic perovskites, $BaCeO_3$, $SrZrO_3$, and $SrCeO_3$, the MD calculation was performed for a system of 160 ions (O^{2-}: 96, Zr^{4+} or Ce^{4+}: 32, Ba^{2+}: 32). For example, the MD cell for $BaUO_3$ is shown in Fig. 1. The calculation conditions for the cubic and orthorhombic perovskites are summarized in Tables 1 and 2, respectively. The calculation was performed by the MD program based on MXDRTO [16], and the quantum effect [17] was taken into account in the present calculation. The calculation was made in the temperature range from 300 K to 2000 K, and in the pressure range from 0.1 MPa to 1.5 GPa.

The partial ionic two body potential model reported in the previous papers [8-15] was

employed for the interatomic potential function. This potential function is proposed by Ida [18],

$$U_{ij}(r_{ij}) = \frac{z_i z_j e^2}{r_{ij}} + f_0(b_i + b_j)\exp(\frac{a_i + a_j - r_{ij}}{b_i + b_j}) - \frac{c_i c_j}{r_{ij}^6} + D_{ij}\{\exp[-2\beta_{ij}(r_{ij} - r_{ij}^*)] - 2\exp[-\beta_{ij}(r_{ij} - r_{ij}^*)]\} \quad (1)$$

The detail of the potential function is shown in the previous section.

The parameters (a, b, and c) for oxygen ions given by Kawamura [19] were used in the present study. These parameters have been used in the studies of other oxides such as SiO_2, $MgSiO_4$, Al_2O_3, and $NaAlSiO_4$ [19]. The other parameters were determined by trial and error using the experimental values of the changes in the lattice parameters with temperature and pressure for the perovskite type oxides measured by the present author. This semi-empirical approach to determine the potential parameters has given effective and realistic results for crystalline solids [16], and MD studies using the same method are reported [20-22]. Using the parameters so obtained, the linear thermal expansion coefficient (α_{lin}), compressibility (β), and heat capacity (C_P) were evaluated. The thermal conductivity (λ) of the system was calculated by the Green-Kubo relation in the temperature range from 300 K to 2000 K at a pressure of 0.1 MPa.

3.2.2.3. Results and Discussion

The values of the interatomic potential parameters used in the present study are summarized in Tables 3, 4, and 5. The variation in the lattice parameters of the cubic and orthorhombic perovskites with temperature evaluated by the MD calculations under the pressure of 0.1 MPa are shown in Figs. 2 and 3, respectively, together with the experimental data. The calculations were performed in the temperature range between 300 K and 2000 K. For the orthorhombic perovskites, the lattice parameter shown in Fig. 3 is the average value of the lattice parameters, a, b, and c. The calculated lattice parameters well agree with the experimental values. The variations in the lattice parameters of the cubic and orthorhombic perovskites with pressure evaluated by the MD calculations under the temperature of 300 K are shown in Figs. 4 and 5, respectively, together with the experimental data. The calculations were performed in the pressure range between 0.1 MPa and 1.5 GPa. The calculated lattice parameters well agree with the experimental data, as well as the case of the temperature dependence. These results indicate that the potential functions used in the present calculation describe well the changes in the lattice parameters with both temperature and pressure.

The linear thermal expansion coefficient (α_{lin}) and compressibility (β) of the perovskite type oxides can be evaluated from the variations of the lattice parameters with temperature and pressure. These results are shown in Tables 6 and 7, respectively, together with the experimental data. The linear thermal expansion coefficient and compressibility are the

values under the pressure of 0.1 MPa and at room temperature, respectively. It is confirmed that the calculated results are almost identical with the experimental data.

In the temperature range from 300 K to 2000 K, the heat capacity at constant pressure (C_P) was evaluated as sum of the heat capacity at constant volume (C_V) and lattice dilation team (C_d). The C_V was evaluated from the variation of the internal energy of the system with temperature calculated by the NVT MD simulations. The C_d was evaluated from the following relationship:

$$C_d = \frac{(3\alpha_{lin})^2 VT}{\beta}, \qquad (2)$$

where V is the molar volume, α_{lin} is the linear thermal expansion coefficient, β is the compressibility, and T is the absolute temperature. The C_d was evaluated by using the calculated values of α_{lin}, V, and β obtained from the NPT MD simulations.

The temperature dependence of the calculated C_V and C_V+C_d of the perovskite type oxides is shown in Figs. 6 to 11, together with the experimental and literature data [23,24]. In these figures, the dotted line indicates 15R from the Dulong-Petit law, in which R is the gas constant. In all figures, the calculated C_V agree well with 15R, which indicates that the potential function used in the present study describes well the change in the internal energy with temperature. The calculated results of C_V+C_d are almost identical with the experimental C_P values, except for $BaUO_3$. The calculated C_V+C_d of $BaUO_3$ is slightly lower than the experimental data, which is because that the calculated results do not contain other contributions such as the anharmonic contribution.

We have succeeded in reproducing a phase transition behavior in the MD simulation for $SrZrO_3$. In Fig. 10, a large peak is observed in both experimental C_P and calculated C_V curves at around 1000 K, which is caused by the phase transition from the orthorhombic structure to tetragonal structure of $SrZrO_3$ [25-27]. The temperature dependence of the linear thermal expansion coefficient (α_{lin}) of $SrZrO_3$ calculated by the MD method is shown in Fig. 12. It is also observed a peak in the calculated α_{lin} curve at around 1000 K, as observed in the experimental data.

The thermal conductivities of the perovskite type oxides were evaluated by the MD calculations in the temperature range between 300 K and 2000 K. Only the lattice contributions to the thermal conductivity, λ_{lat} can be evaluated in the present case. The λ_{lat} was obtained as the plateau value of the time integral of the auto-correlation function (ACF) of the energy current, $\langle S(t)\cdot S(0)\rangle$. The ACF approaches zero and its time integral reaches a plateau value. Integrating ACF with respect to time gives the thermal conductivity. Details of these calculations are given in the previous section.

The temperature dependence of the calculated thermal conductivities of the perovskite

type oxides is shown in Figs. 13 to 18, together with the experimental data. The calculated thermal conductivities decrease with increasing temperature, which indicates that the lattice thermal conductivity (λ_{lat}) can be evaluated by the MD calculation. The calculated thermal conductivities of $BaZrO_3$, $SrZrO_3$, and $SrCeO_3$ well agree with the experimental data, while those of $BaUO_3$ and $BaCeO_3$ are higher than the experimental data and that of $BaMoO_3$ is lower than the experimental data. For $BaMoO_3$, the electronic contribution to the thermal conductivity is larger than those of other perovskite type oxides, because of the larger electrical conductivity. It is considered that the difference between the calculated and experimental thermal conductivity of $BaMoO_3$ corresponds to the electronic contribution.

In chapter 2.2, the thermal and mechanical properties of the perovskite type oxides have been evaluated, and a unique property for $BaUO_3$ have been discovered. The relationships between several properties, such as the Young's modulus, Debye temperature, and melting temperature, of $BaUO_3$ show glass like characteristics, regardless of the simple crystal structure. The thermal conductivity of $BaUO_3$ is extremely lower than those of other perovskites, and also SiO_2 glass. The temperature dependence of the calculated thermal conductivities of $BaUO_3$ and $BaZrO_3$ is shown in Fig. 19. The calculated thermal conductivity of $BaUO_3$ is smaller than that of $BaZrO_3$, as with the case of experimental data.

The glass like characteristics, including the extremely low thermal conductivity, of $BaUO_3$ is explained by using MD simulations. The two body interatomic potentials for Ba and Sr series perovskite type oxides are shown in Figs. 20 and 21, respectively. In Fig. 20, it can be seen that the position and bottom form of the potential curve of U-O interaction are shallower and smoother than those of other interactions, which corresponds to that the bonding energy of U-O bond is smaller than those of other bonds. The motion tracks of some ions for $BaUO_3$ and $BaZrO_3$ unit cells at 300 K and 1000 K obtained from the MD calculations are shown in Figs. 22 and 23. It is observed that the motion of U ions in $BaUO_3$ is larger than that of Zr ions in $BaZrO_3$, which is based on the smaller bond strength of U-O interaction. From the MD simulations, it is found that $BaUO_3$ has larger phonon scattering probability than $BaZrO_3$, and this may be the reason of the glass like characteristics and extremely low thermal conductivity of $BaUO_3$.

3.2.2.4. Conclusion

The MD calculations have been performed for the perovskite type oxides, $BaUO_3$, $BaZrO_3$, $BaCeO_3$, $BaMoO_3$, $SrZrO_3$, and $SrCeO_3$. The thermal and mechanical properties, viz. the linear thermal expansion coefficient, compressibility, heat capacity, and thermal conductivity have been evaluated by the MD calculations, and the results have been compared with the experimental data. The Morse-type potential function added to the Busing-Ida type potential has

been employed for the ionic interactions. The potential parameters have been determined by trial and error using the experimental values of the variations in the lattice parameters with temperature and pressure.

The calculated linear thermal expansion coefficient (α_{lin}) and compressibility (β) are almost identical with the experimental data. The calculated results of C_V+C_d are almost identical with the experimental C_P values, except for $BaUO_3$. The calculated C_V+C_d of $BaUO_3$ is slightly lower than the experimental data, which is because that the calculated results do not contain other contributions such as the anharmonic contribution. The calculated thermal conductivities of $BaZrO_3$, $SrZrO_3$, and $SrCeO_3$ well agree with the experimental data, while those of $BaUO_3$, $BaCeO_3$, and $BaMoO_3$ are larger than the experimental data. The difference between the calculated and experimental thermal conductivity of $BaMoO_3$ corresponds to the electronic contribution. It is found from the MD simulations that the glass like characteristics and extremely low thermal conductivity of $BaUO_3$ are caused by the lower bond strength of U-O interaction than those of other bonds.

References

[1] H. Kleykamp, J. Nucl. Mater., 131 (1985) 221.

[2] H. Kleykamp, Nucl. Technol., 80 (1988) 412.

[3] K. Kurosaki, T. Matsuda, M. Uno, S. Kobayashi, and S. Yamanaka, J. Alloys and Compounds, 319, 271, (2001).

[4] S. Yamanaka, K. Kurosaki, T. Matsuda, and M. Uno, J. Nucl. Mater., 294, 99, (2001).

[5] T. Matsuda, S. Yamanaka, K. Kurosaki, M. Uno, and S. Kobayashi, J. Alloys and Compounds, 322, 77, (2001).

[6] S. Yamanaka, T. Matsuda, K. Kurosaki, and M. Uno, J. Nucl. Sci. Technol., Suppl. 3, 709-712, (2002).

[7] T. Matsuda, S. Yamanaka, K. Kurosaki, S. Kobayashi, and M. Uno, J. Nucl. Sci. Technol., Suppl. 3, 823-826, (2002).

[8] K. Yamada, S. Yamanaka, and M. Katsura, Technol. Reps. Osaka Univ., 48 (1998) 167.

[9] K. Yamada, K. Kurosaki, M. Uno, and S. Yamanaka, J. Alloys and Compounds, 307 (2000) 1.

[10] K. Yamada, K. Kurosaki, M. Uno, and S. Yamanaka, J. Alloys and Compounds, 307 (2000) 10.

[11] K. Kurosaki, K. Yano, K. Yamada, M. Uno, and S. Yamanaka, J. Alloys and Compounds, 297 (2000) 1.

[12] K. Kurosaki, K. Yano, K. Yamada, M. Uno, and S. Yamanaka, J. Alloys and Compounds, 311 (2000) 305.

[13] K. Kurosaki, K. Yano, K. Yamada, M. Uno, and S. Yamanaka, J. Alloys and Compounds, 313, 242, (2000).

[14] K. Kurosaki, K. Yano, K. Yamada, M. Uno, and S. Yamanaka, J. Alloys and Compounds, 319, 253, (2001).

[15] K. Kurosaki, K. Yano, K. Yamada, M. Uno, S. Yamanaka, K. Yamamoto, and T. Namekawa, J. Nucl. Mater., 294, 160, (2001).

[16] K. Kawamura and K. Hirao, "Material Design using Personal Computer", Shokabo, Tokyo, (1994).

[17] E. Wigner, Phys. Rev., 40 (1932) 749.

[18] Y. Ida, Phys. Earth Planet Interiors, 13 (1976) 97.

[19] K. Kawamura, "Molecular Dynamics Simulations", Springer Series in Solid-State Sciences, 103 (1992) 88.

[20] T. Katsumata, Y. Inaguma, M. Itoh, and K. Kawamura, Solid State Ionics, 108 (1998) 175.

[21] H. Inaba, R. Sagawa, H. Hayashi, and K. Kawamura, Solid State Ionics, 122 (1999) 95.

[22] H. Hayashi, R. Sagawa, H. Inaba, and K. Kawamura, Solid State Ionics, 131 (2000) 281.

[23] Japan Thermal Measurement Society, Thermodynamics Data Base for Personal Computer MALT2, (1992).
[24] The SGTE Pure Substance and Solution databases, GTT-DATA SERVICES.
[25] T. Matsuda, S. Yamanaka, K. Kurosaki, and S. Kobayashi, J. Alloys and Compounds, 351 (2003) 43.
[26] B.J. Kennedy, C.J. Howard, and B.C. Chakoumakos, Phys. Rev. B 59 (1999) 4023.
[27] C.J. Howard, K.S. Knight, B.J. Kennedy, and E. H. Kisi, J. Phys. Condens. Matter., 12 (2000) L677.

Table 1

Calculation conditions of MD simulations for cubic perovskites, ABO_3

		α	β	C_V	λ
System	Particles	320 particles (O^{2-}: 192, B^{4+}: 64, A^{2+}: 64)			
	Structure	Cubic perovskite			
	Boundary	3 dimensional periodic boundary condition			
Control	Temperature	Nose	Nose	Nose	Nose
	Pressure	Andersen	Andersen	No control	Andersen
Step time		2f sec	2f sec	2f sec	2f sec
Number of steps		10,000	10,000	10,000	1,000,000

Table 2

Calculation conditions of MD simulations for orthorhombic perovskites, ABO_3

		α	β	C_V	λ
System	Particles	160 particles (O^{2-}: 96, B^{4+}: 32, A^{2+}: 32)			
	Structure	Orthorhombic perovskite			
	Boundary	3 dimensional periodic boundary condition			
Control	Temperature	Nose	Nose	Nose	Nose
	Pressure	Andersen	Andersen	No control	Andersen
Step time		2f sec	2f sec	2f sec	2f sec
Number of steps		10,000	10,000	10,000	1,000,000

Table 3

Values of the interatomic potential function parameters for $BaUO_3$, $BaZrO_3$, $BaCeO_3$, and $BaMoO_3$

Ions	z	a	b	c	D_{ij}	β_{ij}	r_{ij}^*
O	-1.2	1.926	0.160	20			
					(for Ba-O pairs)		
Ba	1.2	1.771	0.195	0	4.08	1.12	3.106
					(for U-O pairs)		
U	2.4	1.659	0.160	0	8.91	1.21	2.190
					(for Zr-O pairs)		
Zr	2.4	1.274	0.180	15	4.73	4.32	2.193
					(for Ce-O pairs)		
Ce	2.4	1.333	0.096	0	0.01	0.01	2.197
					(for Mo-O pairs)		
Mo	2.4	1.682	0.120	15	0.24	0.06	2.193

Table 4

Values of the interatomic potential function parameters for $SrZrO_3$

Ions	z	a	b	c	D_{ij}	β_{ij}	r_{ij}^*
O	-1.2	1.926	0.160	20			
					(for Sr-O pairs)		
Sr	1.2	1.198	0.160	10	3.22	1.78	3.043
					(for Zr-O pairs)		
Zr	2.4	1.146	0.180	15	4.23	3.82	2.193

Table 5

Values of the interatomic potential function parameters for $SrCeO_3$

Ions	z	a	b	c	D_{ij}	β_{ij}	r_{ij}^*
O	-1.2	1.926	0.160	20			
					(for Sr-O pairs)		
Sr	1.2	1.638	0.120	10	10.1	1.78	3.043
					(for Ce-O pairs)		
Ce	2.4	1.296	0.096	0	0.01	0.01	2.199

Table 6

Calculated linear thermal expansion coefficient α_{lin} under atmospheric pressure of the perovskite type oxides

Compounds	Linear thermal expansion coefficient α_{lin} (K^{-1})		Temperature range
	Calculated value	Experimental value	
$BaUO_3$	1.07×10^{-5}	1.10×10^{-5}	300 K-700 K
$BaZrO_3$	6.12×10^{-6}	7.15×10^{-6}	300 K-700 K
$BaCeO_3$	1.10×10^{-5}	1.06×10^{-5}	300 K-600 K
	1.16×10^{-5}	1.12×10^{-5}	600 K-1000 K
$BaMoO_3$	8.26×10^{-6}	9.46×10^{-6}	300 K-700 K
$SrZrO_3$	8.83×10^{-6}	9.96×10^{-6}	600 K-1000 K
$SrCeO_3$	9.77×10^{-6}	1.11×10^{-5}	600 K-1000 K

Table 7

Calculated compressibility β at room temperature of the perovskite type oxides

Compounds	Compressibility β (GPa^{-1})		Pressure range
	Calculated value	Experimental value	
$BaUO_3$	1.16×10^{-2}	1.38×10^{-2}	0.1 MPa-1.5GPa
$BaZrO_3$	4.37×10^{-3}	7.86×10^{-3}	
$BaCeO_3$	1.01×10^{-2}	7.23×10^{-3}	
$BaMoO_3$	5.24×10^{-3}	6.48×10^{-3}	
$SrZrO_3$	4.35×10^{-3}	2.96×10^{-3}	
$SrCeO_3$	1.24×10^{-2}	1.56×10^{-2}	

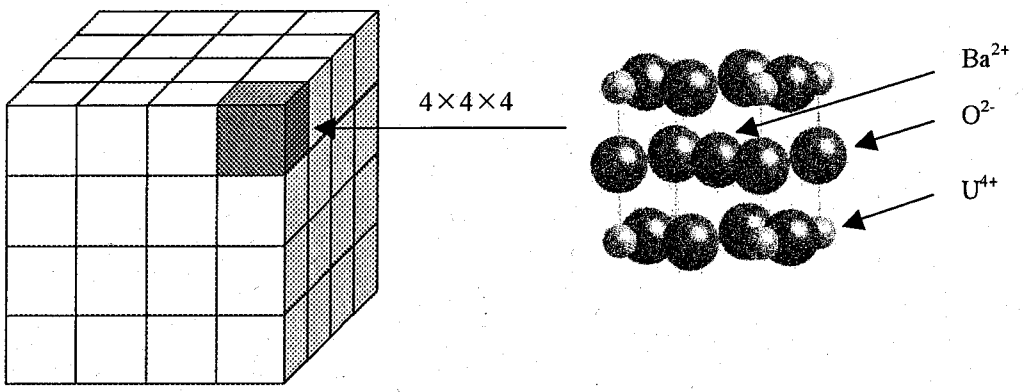

Figure 1. A MD cell for $BaUO_3$.

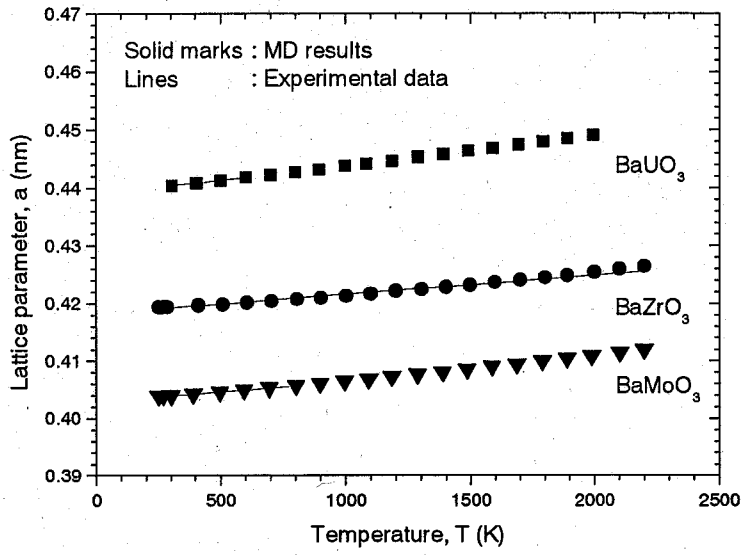

Figure 2. Temperature dependence of the lattice parameters of the cubic perovskites, $BaUO_3$, $BaZrO_3$, and $BaMoO_3$.

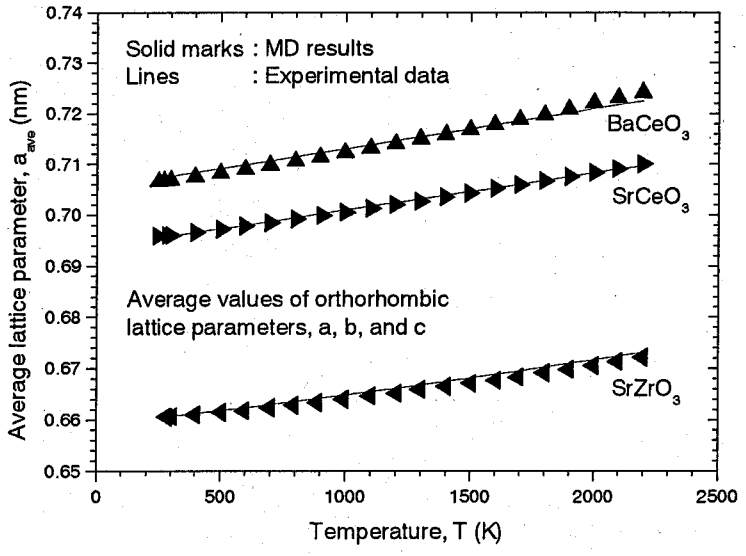

Figure 3. Temperature dependence of the average lattice parameters of the orthorhombic perovskites, $BaCeO_3$, $SrZrO_3$, and $SrCeO_3$.

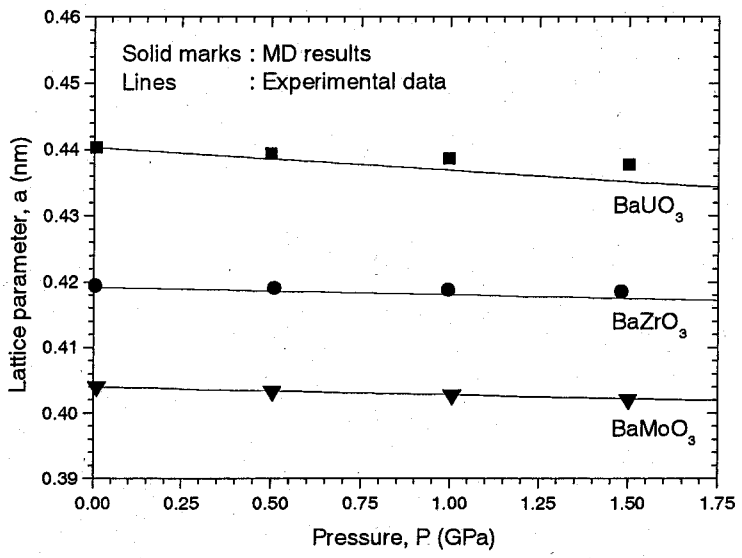

Figure 4. Pressure dependence of the lattice parameters of the cubic perovskites, $BaUO_3$, $BaZrO_3$, and $BaMoO_3$.

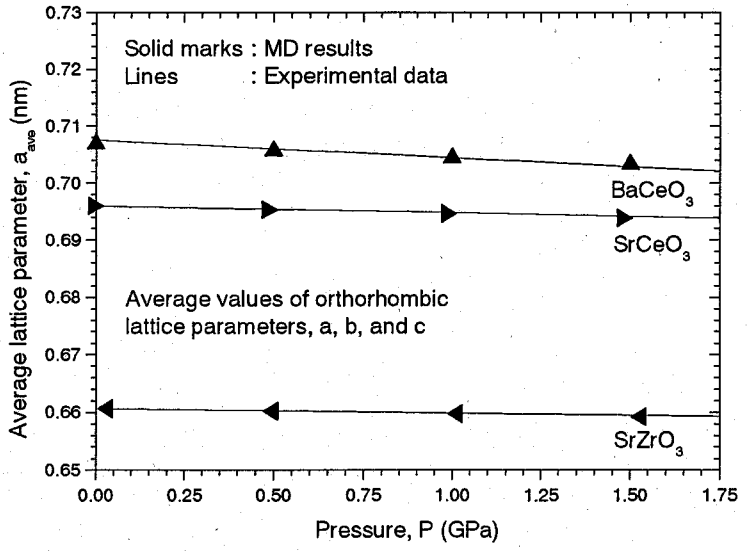

Figure 5. Pressure dependence of the average lattice parameters of the orthorhombic perovskites, $BaCeO_3$, $SrZrO_3$, and $SrCeO_3$.

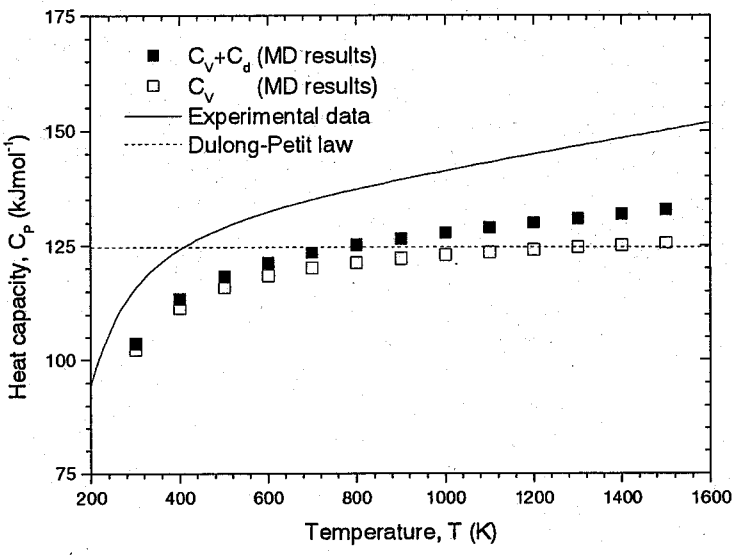

Figure 6. Temperature dependence of the heat capacity C_P of $BaUO_3$.

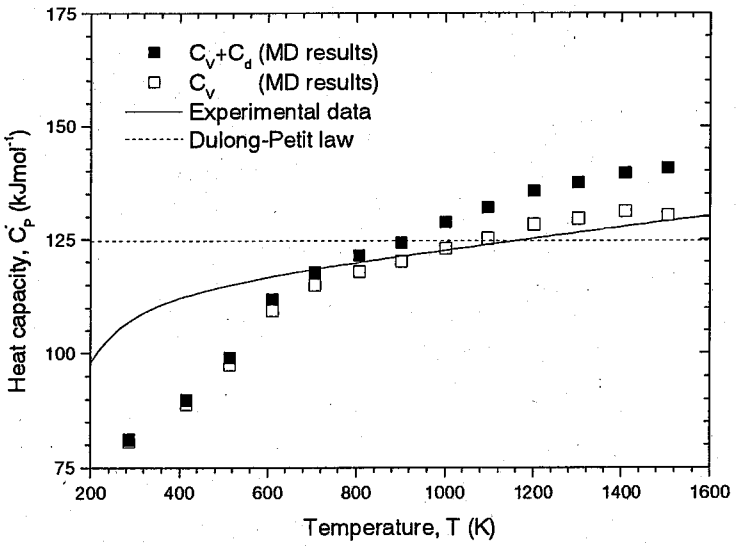

Figure 7. Temperature dependence of the heat capacity C_P of $BaZrO_3$.

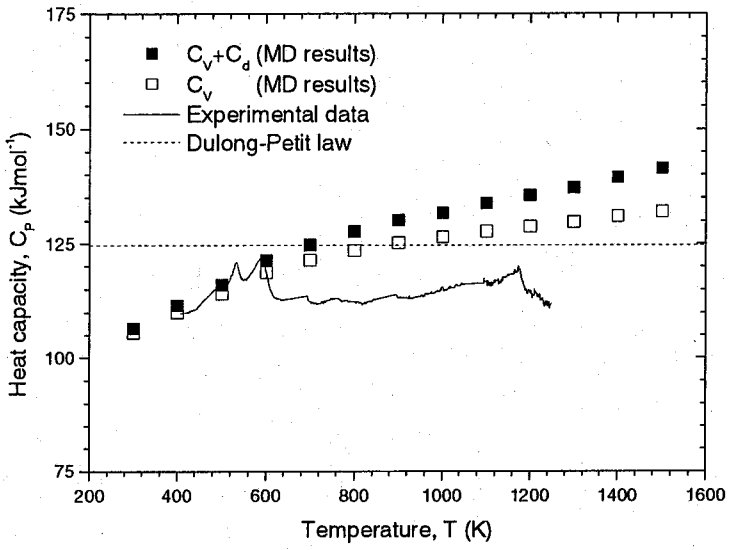

Figure 8. Temperature dependence of the heat capacity C_P of $BaCeO_3$.

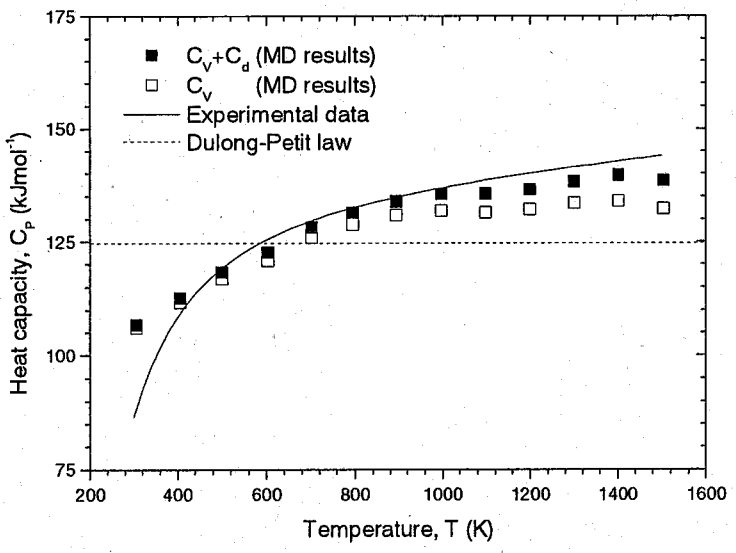

Figure 9. Temperature dependence of the heat capacity C_P of $BaMoO_3$.

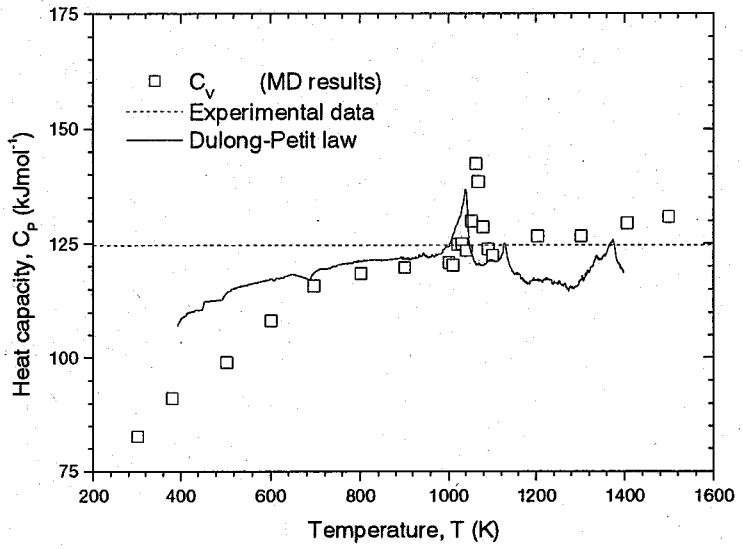

Figure 10. Temperature dependence of the heat capacity C_P of $SrZrO_3$.

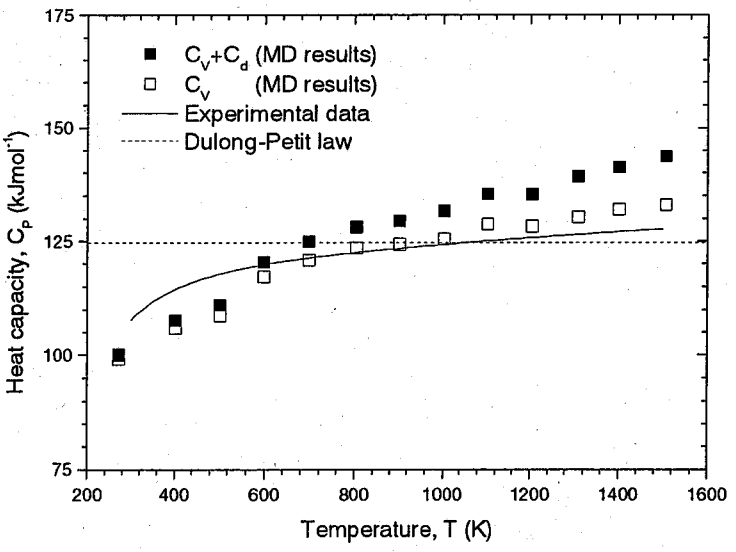

Figure 11. Temperature dependence of the heat capacity C_P of $SrCeO_3$.

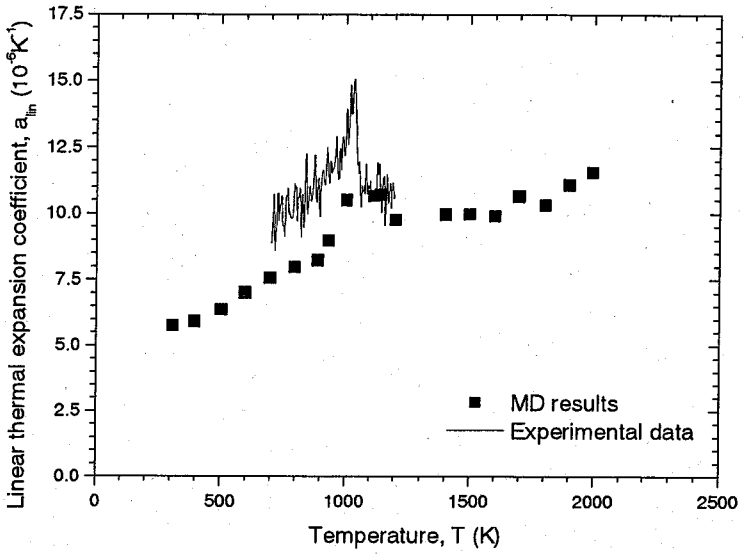

Figure 12. Temperature dependence of the linear thermal expansion coefficient α_{lin} of $SrZrO_3$.

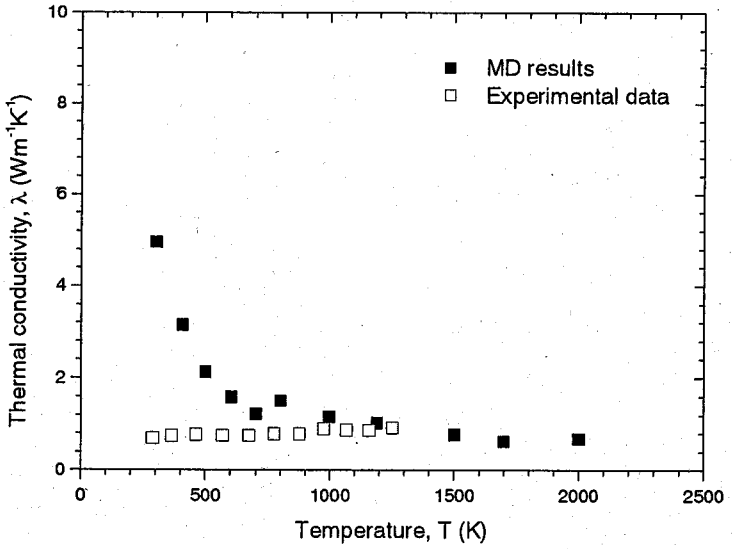

Figure 13. Temperature dependence of the thermal conductivity λ of $BaUO_3$.

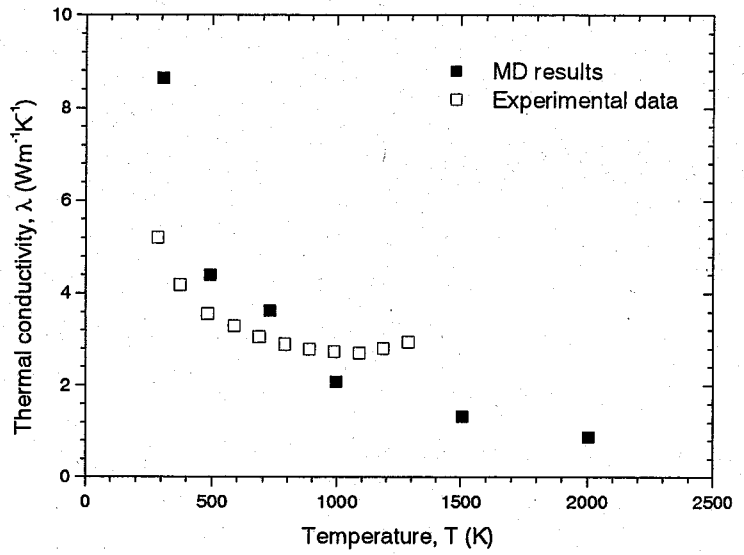

Figure 14. Temperature dependence of the thermal conductivity λ of $BaZrO_3$.

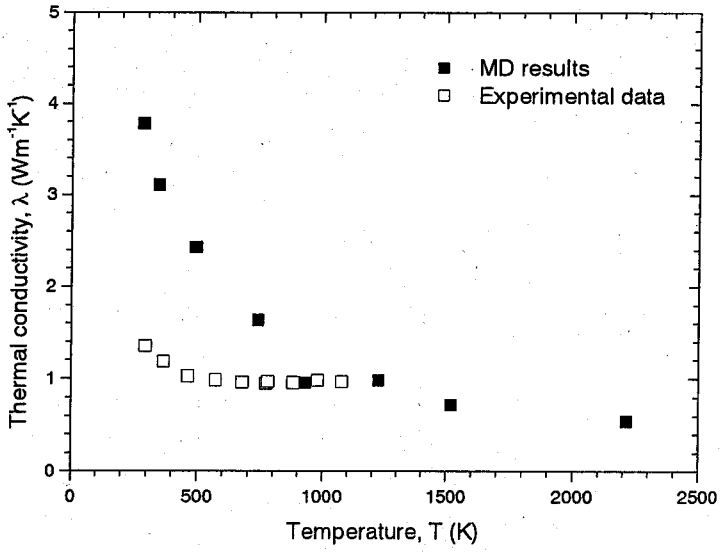

Figure 15. Temperature dependence of the thermal conductivity λ of $BaCeO_3$.

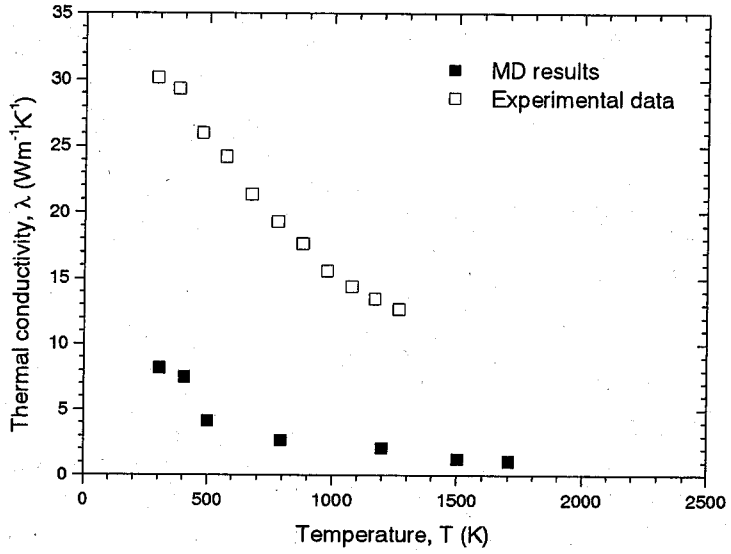

Figure 16. Temperature dependence of the thermal conductivity λ of $BaMoO_3$.

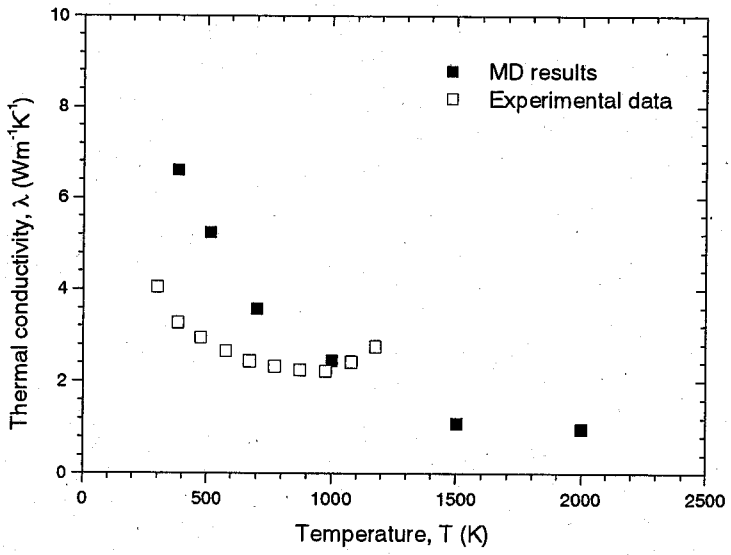

Figure 17. Temperature dependence of the thermal conductivity λ of $SrZrO_3$.

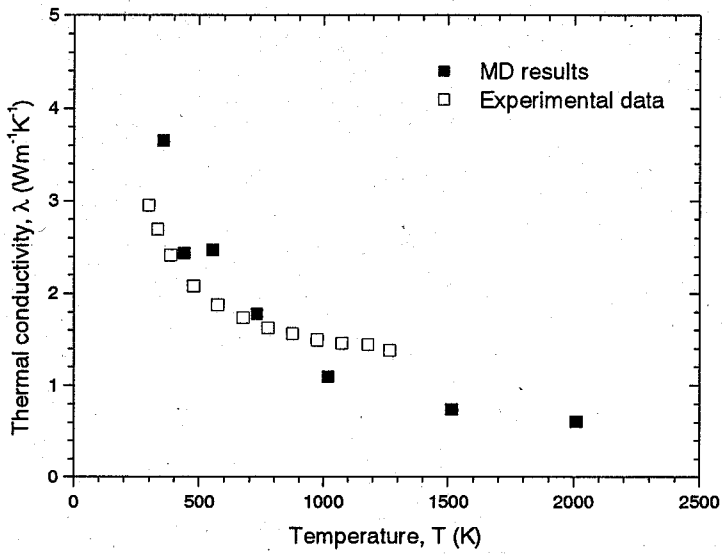

Figure 18. Temperature dependence of the thermal conductivity λ of $SrCeO_3$.

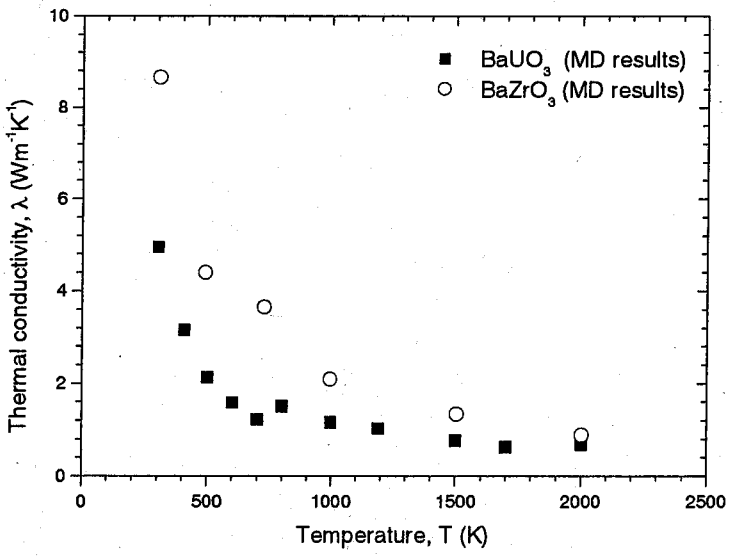

Figure 19. Temperature dependence of the calculated thermal conductivity λ of $BaUO_3$ and $BaZrO_3$.

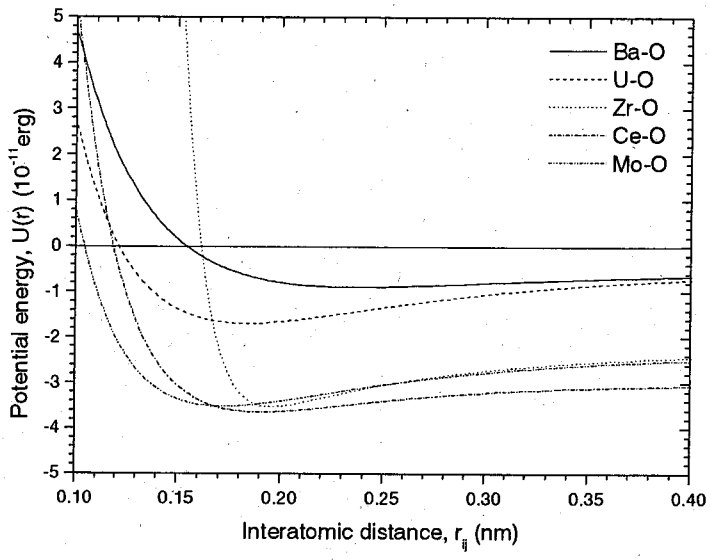

Figure 20. Two body interatomic potentials for Ba series perovskite type oxides.

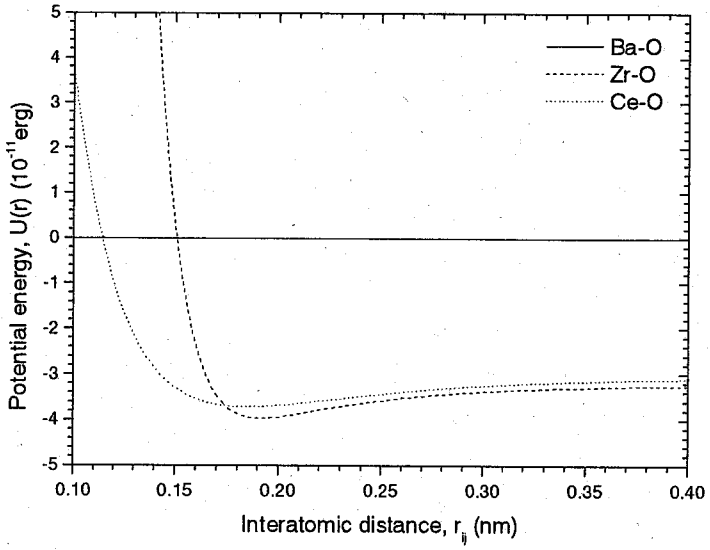

Figure 21. Two body interatomic potentials for Sr series perovskite type oxides.

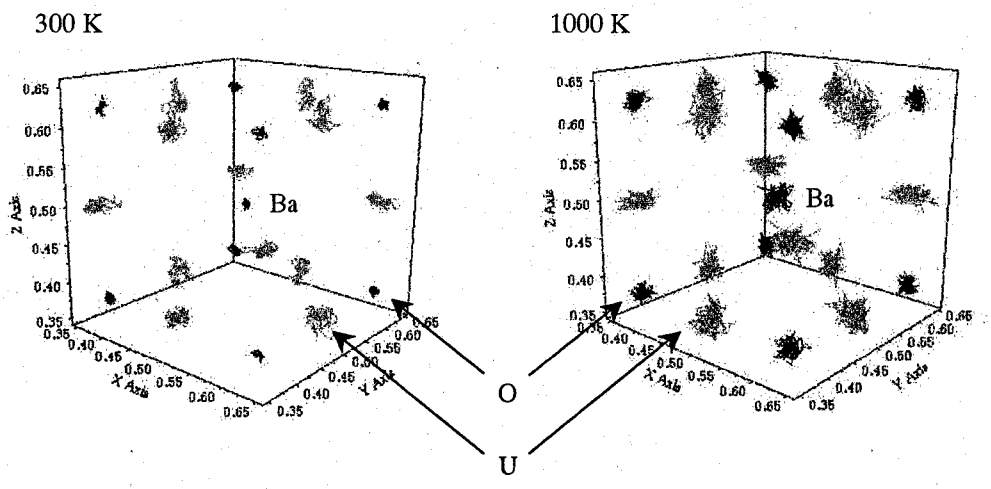

Figure 22. Motion tracks of some ions for $BaUO_3$ unit cells at 300 K and 1000 K.

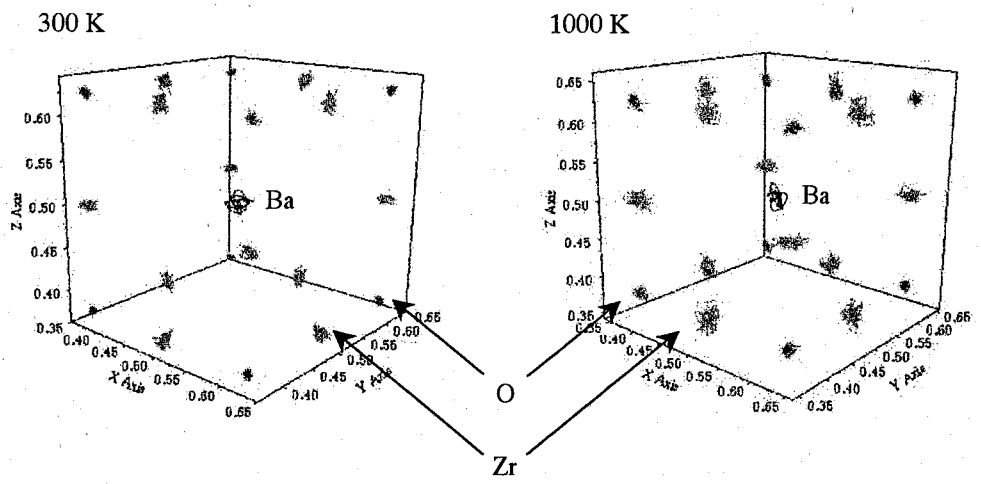

Figure 23. Motion tracks of some ions for $BaZrO_3$ unit cells at 300 K and 1000 K.

3.3. Phase Relation Assessment for O-Pu-U System

3.3.1. Introduction

Plutonium is one of the actinides formed by a neutron capture in ^{238}U during an irradiation of UO_2 in nuclear power plants. Recent technologies in present commercial PUREX installations have made it possible to recover the plutonium efficiently from the spent nuclear fuel, and disposition of the recovered plutonium is acknowledged as one of the most urgent issues at the world level for proliferation resistance [1].

Possible plutonium deposition scheme includes utilisation of plutonium in the nuclear reactors. Burning fissile actinides, such as plutonium, in the nuclear reactors requires inactive materials acting as diluents in the fuel pins to soften the high fission density and high fuel temperatures. Various oxides, carbides, and nitrides have been studied as a candidate to form either a homogeneous solid solution or a heterogeneous two-phase microstructure with the fuel [1-5].

Among these schemes, utilisation of plutonium as mixed oxide fuel (MOX: PuO_2+UO_2) seems most promising and practical since the technology for the commercial utilization of the UO_2 fuel has already been established. In addition, the very completed review on the thermophysical properties of the MOX fuel by Carbajo et al. [6] shows that various researchers have carried out intensive studies on the MOX fuel.

Phase relation assessment for O-Pu-U system is of interest to the present study. In order to evaluate the thermodynamic properties of the oxide fuels, it is very important to understand the phase relation of the O-Pu-U system. Thermodynamic modelling was utilised for the assessment of the system based on the CALculation of PHAse Diagram (CALPHAD) technique [7], which enables us to predict not only the phase behaviour but also the thermodynamic properties in highly complex multi-component systems based on the Gibbs energy of the components. This technique has been successfully applied for such systems as O-Pu-Zr [8] and O-U-Zr [9].

In the present study, the thermodynamic modelling was carried out for the O-Pu-U system based on the data for O-Pu [8], O-U [9] and Pu-U [10] binary systems. In the first part of the present study, the non-ideal stoichiometric PuO_2-UO_2 pseudo binary system was assessed based on the phase diagram and heat capacity data. In the second part, the deviation from the ideal model in the non-stoichiometric fluorite structure phase was discussed with respect to the oxygen potential data. A possible ternary phase diagrams for the O-Pu-U system were also calculated.

3.3.2. Calculation

3.3.2.1. Thermodynamic Modelling

Thermodynamic modelling was performed using the program named POLY-3 included in Thermo-Calc [11]. The quantity stored in the data for the calculation is Gibbs energy of formation for phases, G-H^{SER} (J/mol), referred to a given reference state. In general, it is expressed as:

$$G - H^{SER} = a + bT + cT\ln T + dT^2 + eT^3 + fT^{-1} + \ldots \quad (1)$$

,where a, b, c, d, e, and f are constants, T represents temperature in Kelvin, and SER indicates "stable element reference" and is defined by the use of $H_{298.15\,K}$, and $S_{0\,K}$ for the stable state of the phase at 298.15 K and 1 bar. In the present calculations, Eq. 1 was directly applied to the pure substances and stoichiometric compounds.

The Gibbs energy of a solid solution phase applied in the present study consists of such terms as reference (G^{ref}), ideal (G^{id}) and excess (G^{ex}) Gibbs energies as follows:

$$G = G^{ref} + G^{id} + G^{ex} \quad (2)$$

,where G^{ref} is the contribution of pure components of the phase to the Gibbs energy, G^{id} is the ideal mixing contribution known as ideal entropy of mixing, and G^{ex} is the contribution due to non-ideal interactions between the components known as excess Gibbs energy of mixing.

These contributions, G^{ref}, G^{id}, and G^{ex} to the Gibbs energy were expressed with the general multi-sublattice model proposed by Sundman et al. [12] in the present study. This model takes account the preferential occupation of the atoms in the lattice that occurs when atoms are sufficiently different in size, electronegativity, or charge. As shown in Fig. 1, in a simple case of a fluorite structure (FCC_C1) phase with a formula $(A, B)_1(C)_2$, the reference (G^{ref}), ideal (G^{id}), and excess (G^{xs}) Gibbs energies are expressed as Eqs. 3, 4, and 5, respectively.

$$G^{ref} = y^1_A y^2_C G^0_{AC} + y^1_B y^2_C G^0_{BC} \quad (3)$$

$$G^{id} = RT\left\{N^1\left(y^1_A \ln y^1_A + y^1_B \ln y^1_B\right)\right\} \quad (4)$$

$$G^{ex} = y^1_A y^1_B y^2_C \left\{L^0_{A,B:C} + L^1_{A,B:C}\left(y^1_A - y^1_B\right) + L^2_{A,B:C}\left(y^1_A - y^1_B\right)^2 + \ldots\right\} \quad (5)$$

,where y^s_i represents the site fraction of component "i" on sublattice "s", G^0_{ij} is the Gibbs energy of the pure "ij" phase in question, and N^s is the total number of the site on the sublattice "s". L^n_{ij} are constants known as interaction parameters described by using Redlich-Kister type polynomial [13].

The Redlich-Kister polynomial is usually used to describe the excess Gibbs energy of metallic liquid solutions. However, when one of the elements is not metallic, such as oxides, an associated model [14] and an ionic liquid model [15] can both be used to describe the thermodynamic properties of the liquid phase. The associated model defines as ideal reference one random mixture of atoms and associated species (A, B, A_iB_j, ...). The ionic liquid model defines two sublattices $(A^{+a}, \ldots)_P(B^{-b}, \ldots, V^Q, \ldots, A_iB_j, \ldots)_Q$, in which one is occupied by cations and the other is occupied by anions, and also there are vacancies with a negative charge

Q and neutral species. P and Q are the numbers of sites on the cation and anion sublattice, respectively. P and Q are calculated from the electrical neutrality. The ionic liquid model was used to describe the liquid phase in the present study.

3.3.2.2. Phases and Thermodynamic Data Used in the Present Study

The phases appear in the O-Pu-U system are α-Pu, β-Pu, γ-Pu, δ-Pu, δ'-Pu, ε-Pu (γ-U), α-U, β-U, ζ, η, Pu_2O_3, $PuO_{1.52}$, α-$PuO_{1.61}$, PuO_{2-x} ($UO_{2\pm x}$), U_4O_9, U_3O_8, UO_3, Liquid, and Gas. The sublattice models of the phases used for the calculation are summarized in Table 1.

The tthermodynamic modelling of the O-Pu-U system requires thermodynamic data of its three binary systems, O-Pu, O-U, and Pu-U. The thermodynamic data for O-U [9] and Pu-U [10] systems are available in literature. A set of data for O-Pu system was evaluated in the present study. In the data for these binary systems, the Gibbs energy data for the pure substance are originated from the SGTE (Scientific Group Thermodata Europe) database [16]. The data for some of the oxides are also taken from the SGTE database [17]. The interaction parameters for the liquid phases in the O-U and Pu-U systems from the literature were for the associated model and the general multi-sublattice model, respectively. The parameters for the liquid phase in O-U system were reassessed using a least-square method to give the same Gibbs energy curves for the ionic liquid model. That in Pu-U system was directly applicable to the ionic liquid model.

The use of the data from different binary systems causes the introduction of additional Gibbs energy parameters. In the present calculation, seven additional interaction parameters were to be introduced: $L(Pu^{4+}, U^{4+})_P(O^{-2})_Q$, $L(U^{4+})_P(O^{2-}, Pu_2O_3)_Q$ and $L(U^{4+})_P(VA^{Q-}, Pu_2O_3)_Q$ for the liquid phase, and $L(Pu, U)_1(O)_2$, $L(Pu, VA)_1(O)_2$, $L(Pu, U)_1(VA)_2$ and $L(Pu, VA)_1(VA)_2$ for the fluorite structure (FCC_C1) phase.

3.3.3. Results and Discussion

3.3.3.1. O-Pu, O-U, and Pu-U Binary Systems

The calculated binary phase diagrams of O-Pu, O-U, and Pu-U systems are shown in Figs. 2, 3, and 4, together with generally recommended phase diagrams. The calculated and recommended phase diagrams show a very good agreement. Figures 5, 6, and 7 compare the calculated oxygen potentials in $UO_{2\pm x}$ and PuO_{2-x} phases with experimental data reported in literatures [9,18-21], respectively. The calculated oxygen potentials indicate a good agreement with the experimental ones. Therefore, it is considered that the assessed thermodynamic parameters are reasonable to simulate the general feature of the O-Pu, O-U, and Pu-U binary systems, with respect to the phase diagrams and oxygen potentials of the $UO_{2\pm x}$ and PuO_{2-x} phases.

3.3.3.2. PuO_2-UO_2 Pseudo-Binary System

PuO_2 and UO_2 are totally miscible in the all composition range, because both PuO_2 and UO_2 form only a cubic (fluorite) structure phase up to their melting temperature and the ionic radii of Pu^{4+} and U^{4+} in the fluorite structure are very similar (Pu^{4+}: 0.096 nm, U^{4+}: 0.100 nm [22]). Therefore, only a fluorite structure phase and a liquid phase appear in the stoichiometric PuO_2-UO_2 pseudo-binary system.

The ideality of the PuO_2-UO_2 system is unclear. Beauvy has studied PuO_2-UO_2 solid solution and shown a possibility of its deviation from the ideality [23]. This experimental study focuses on the solid solution in the low PuO_2 composition range (up to 20 mol% of PuO_2) and includes the heat capacity data up to 873 K. On the other hand, Carbajo et al. has mentioned in their very completed review on the thermophysical properties of the MOX fuel that the solid solution in the PuO_2-UO_2 system are almost ideal [6]. They have also recommended determination of the heat capacity of the PuO_2-UO_2 solid solution from the composition following the Neumann-Kopp rule.

Figure 8 compares the calculated heat capacity of PuO_2, UO_2, and $(Pu_{0.25}U_{0.75})O_2$, together with the experimental data after Gibby et al. [24]. The calculation was demonstrated treating the PuO_2 and UO_2 form an ideal solid solution. The calculated and experimental values show a very good agreement. The deviation in the high temperature region attributes to the limit of the data (up to about 2700 K) for the thermodynamic data of solid PuO_2.

Figure 9 compares the phase diagram calculated in the present work with that recommended in literature [6] for the PuO_2-UO_2 system in the low PuO_2 composition range. The calculation was demonstrated treating the PuO_2 and UO_2 form ideal solid and liquid solutions. The calculated and recommended phase diagrams show a very good agreement even in the low PuO_2 composition range, in which a possibility of deviation from the ideality was pointed out [23]. Therefore, it is concluded that the deviation from the ideality in the PuO_2-UO_2 system is negligibly small. It is reasonable to treat the phases in this pseudo binary system as ideal solutions: $L(Pu^{4+}, U^{4+})_P(O^{-2})_Q = 0$ and $L(Pu, U)_1(O)_2 = 0$.

3.3.3.3. O-Pu-U Ternary System

For further assessment of the fluorite structure phase, especially for the non-stoichiometric region, thermodynamic modelling of O-Pu-U ternary system was demonstrated using the data of its three binary systems, O-Pu, O-U, and Pu-U. Because of the lack of the thermodynamic information, the additional interaction parameters for the liquid phase, $L(U^{4+})_P(O^{2-}, Pu_2O_3)_Q$ and $L(U^{4+})_P(VA^{Q-}, Pu_2O_3)_Q$ were tentatively assessed as 0 (ideal solution). Therefore, the interaction parameters assessed in this section are: $L(Pu, VA)_1(O)_2$,

$L(Pu, U)_1(VA)_2$, and $L(Pu, VA)_1(VA)_2$ for the fluorite structure (FCC_C1) phase.

The modelling was demonstrated firstly assuming all the additional interaction parameters for the fluorite structure phase as 0 (the ideal mixture of the data for the O-Pu, O-U, and Pu-U), and the oxygen potentials both in hyper- and hypo-stoichiometric region were calculated to compare with the experimental data available in literatures [18,25-30]. Figure 10 compares the calculated oxygen potential in the fluorite structure phase in the hyper-stoichiometric region with the experimental data. At any temperatures, the values calculated using the data of the ideal mixture of O-Pu, O-U, and Pu-U binary systems are larger than those experimentally obtained [30]. It suggests that the data for O-Pu, O-U, and Pu-U binary systems cannot be mixed ideally to model the fluorite structure phase. Therefore, it is necessary to introduce the additional interaction parameters. Figure 10 also indicates the oxygen potential calculated using the assessed parameters, and the assessed data shows a very good agreement with the experimental ones.

Figure 11 also compares the oxygen potential in the fluorite structure phase but in the hypo-stoichiometric region. Similarly in the hyper-stoichiometric region, the values obtained using the data of the ideal mixture of O-Pu, O-U, and Pu-U binary systems differ from those experimentally obtained [18,28] in any of the compositions and temperatures. On the other hand, the values obtained using the assessed data shows a very good agreement with the experimental ones. The assessed interaction parameters are indicated in Table 2, together with the other data for the fluorite structure phase utilised in the present modelling.

The ternary phase diagram for the O-Pu-U system is available in literature, as shown in Fig. 12, for the limited composition and temperature region [31]. Important features of this diagram regarding the fluorite structure phase, which is the special concern of the present study, are (i) FCC MO_{2+x} phase in U rich region becomes wider as temperature rises and (ii) FCC MO_2 + BCC MO_{2-x} region becomes much smaller as temperature rises. Using the assessed interaction parameters, ternary phase diagrams for the O-Pu-U system were calculated. Figure 13 indicates the calculated results for both 773 K and 1273K. The tie lines in the zoomed diagrams, (b) and (d), are excluded to make it easier see the phase regions. It should be noted that the FCC_C1 phase in U rich region and FCC_C1 + $PuO_{1.61}$ (BCC MO_{2-x}) regions become wider and smaller, respectively, as temperature rises similarly to Fig. 12. We can conclude that the calculated diagrams, therefore the assessed data, reproduce the general feature of the ternary phase diagram well for 773 K and 1273K. It is noticeable that the fluorite structure (FCC_C1) phase tends to expand towards hyper- and hypo-stoichiometric direction in the U and Pu rich regions, respectively, as temperature rises.

3.3.4. Conclusion

The tthermodynamic modelling has been carried out for the O-Pu-U system and the deviation from the ideal model in the fluorite structure phase was assessed based on the data for O-Pu, O-U, and Pu-U binary systems. For the O-Pu, O-U, and Pu-U binary systems, the assessed thermodynamic parameters are reasonable to simulate the general feature of the O-Pu, O-U, and Pu-U binary systems, with respect to the phase diagrams and oxygen potentials of the $UO_{2\pm x}$ and PuO_{2-x} phases. For the stoichiometric PuO_2-UO_2 pseudo binary system, the calculation for the heat capacity and phase diagram treating the PuO_2 and UO_2 form an ideal solid solution provides very good agreement with the experimental data available in literatures. Therefore, the deviation from the ideal model in the PuO_2-UO_2 system should be negligibly small and that it is reasonable to treat the phases in this pseudo binary system as ideal solutions.

For the non-stoichiometric fluorite structure phase, the thermodynamic modelling has been demonstrated firstly assuming all the additional interaction parameters for the fluorite structure phase are 0 (the ideal mixture of the data for the O-Pu, O-U, and Pu-U). The results suggest that the data for O-Pu, O-U, and Pu-U binary systems cannot be mixed ideally to model the fluorite structure phase. The interaction parameters have been assessed, and the oxygen potential calculated using the assessed parameters shows very good agreement with the experimental ones both in hyper- and hypo-stoichiometric regions. Using the assessed interaction parameters, the ternary phase diagrams for the O-Pu-U system have been also calculated. The calculated phase diagrams reproduce the general feature of the ternary phase diagram well for 773 K and 1273 K.

References

[1] F. Vettraino, G. Magnani, T. La Torretta, E. Marmo, S. Coelli, L. Luzzi, P. Ossi, and G. Zappa, J. Nucl. Mater., 274 (1999) 23-33.

[2] H. Kleykamp, J. Nucl. Mater., 275 (1999) 1-11.

[3] W.L. Gong, W. Lutze, and R.C. Ewing, J. Nucl. Mater., 277 (2000) 239-249.

[4] N. Nitani, T. Yamashita, T. Matsuda, S.-i. Kobayashi, and T. Ohmichi, J. Nucl. Mater., 274 (1999) 15-22.

[5] H. Zhang, M.E. Huntelaar, R.J.M. Konings, and E.H.P. Cordfunke, J. Nucl. Mater., 249 (1997) 223-230.

[6] J.J. Carbajo, G.L. Yoder, S.G. Popov, and V.K. Ivanov, J. Nucl. Mater., 299 (2001) 181-198.

[7] N. Saunders and A.P. Miodownik, in "CALPHAD (Calculation of Phase Diagrams): A Comprehensive Guide," Pergamon Materials Series Vol. 1, Pergamon, Oxford, UK, 1998.

[8] H. Kinoshita, M. Uno, and S. Yamanaka, J. Alloys Comp., in press.

[9] P.Y. Chevalier and E. Fischer, J. Nucl. Mater., 257 (1998) 213-255.

[10] M. Kurata, Calphad, 23 (1999) 305-337.

[11] B. Sundman, "Thermo-Calc User's Guide," Royal Institute of Technology, Sweden (1995).

[12] B. Sundman and J. Agren, J. Phys. Chem. Solids, 42 (1981) 297-301.

[13] O. Redlich and A. T. Kister, Ind. Eng. Chem., 40 (1948) 345-348.

[14] A.S. Jordan, Metall. Trans., 1 (1970) 239-249.

[15] M. Hillert, B. Jansson, B. Sundman, and J. Agren, Metall. Trans. A, 16A (1985) 261-266.

[16] A.T. Dinsdale, CALPHAD, 11 (1991) 317-425.

[17] SGTE Pure Substance Database (Edition 1998), Provided by GTT Technologies, Herzogenrath, Germany 1998.

[18] R.E. Woodley, J. Nucl. Mater., 96 (1981) 5-14.

[19] M. Tetenbaum, Am. Ceram. Soc. Symp. Ser., 216 (1983) 109-122.

[20] C.A. Alexander, data presented at the Libby-Cockcraft Exchange Meeting on Phase Diagrams and Thermodynamics of Fuel Materials, May (1968).

[21] T.M. Besmann et al., Trans. Am. Nucl. Soc., 45 (1983) 280-281.

[22] R.D. Shannon, Acta. Crystallogr., A32 (1976) 751-767.

[23] M. Beauvy, J. Nucl. Mater., 188 (1992) 232-238.

[24] R.L. Gibby, L. Leibowitz, J.F. Kerrisk, and D.G. Clifton, J. Nucl. Mater., 50 (1974) 155-161.

[25] T.L. Markin and E.J. McIver, in "Plutonium 1965," Ed. by A.E. Kay and M.B. Waldron, Chapman and Hall, London (1967) pp. 845-857.

[26] R.E. Woodley, J. Am. Ceram. Soc., 56[3] (1973) 116-119.

[27] G.R. Chilton and I.A. Kirkham, in "Plutonium 1975 and Other Actinides," Ed. by H. Blank

and R. Linder, Elsevier, New York, and North Holland Publ. Co., Amsterdam (1976) P.171.

[28] R.E. Woodley, J. Nucl. Mater., 74 (1978) 290-296.

[29] R.E. Woodley and M.G. Adamson, J. Nucl. Mater., 82 (1979) 65-75.

[30] G.R. Chilton and J. Edwards, in "Thermodynamics of Nuclear Materials 1979," Vol. I, IAEA Vienna (1980) pp. 357-368.

[31] "The Plutonium-Oxygen and Uranium-Plutonium-Oxygen Systems: A Thermodynamic Assessment," Technical Report Series No. 79, IAEA Vienna, (1967).

Table 1

Phases in O-Pu-U system used in the present modelling

Phase	Sublattice model
α-Pu	$(Pu)_1$
β-Pu	$(Pu, U)_1$
γ-Pu	$(Pu, U)_1$
δ-Pu	$(Pu, U)_1(VA)_1$
δ'-Pu	$(Pu, U)_1$
ε-Pu, . -U	$(Pu, U)_1(VA)_3$
α-U	$(Pu, U)_1$
β-U	$(Pu, U)_1$
ζ	$(Pu, U)_1$
η	$(Pu, U)_1$
Pu_2O_3	$(Pu)_2(O)_3$
$PuO_{1.52}$	$(Pu)_{100}(O)_{152}$
. -$PuO_{1.61}$	$(Pu)_{100}(O)_{161}$
PuO_{2-X}, $UO_{2\pm X}$	$(Pu, U, VA)_1(O, VA)_2$
U_4O_9	$(U)_4(O)_9$
U_3O_8	$(U)_3(O)_8$
UO_3	$(U)_1(O)_3$
Liquid	$(Pu^{4+}, U^{4+})_P(O^{2-}, VA^{Q-}, Pu_2O_3, O)_Q$ $\begin{cases} P=2y_{O2-}+Qy_{VA} \\ Q=4y_{Pu4+}+4y_{U4+} \end{cases}$
Gas	$(O_2)_1$

Table 2

Gibbs energy parameters for the fluorite structure phase used in the present modelling

Gibbs energy		Parameters (J/mol)	Temperature (K)
G_{PuO2}	=	-1087288.7 +505.66828T -83.319199TlnT $-5.8418\times10^{-3}T^2$ $-2.2924167\times10^{-11}T^3$ +913505T^{-1}	298<T<4000
G_{PuVA2}	=	+42603.691 +80.301382T -18.1258TlnT -0.02241T^2	298<T<400
	=	+33394.038 +236.786603T -42.4187TlnT -0.00134493T^2	400<T<944
	=	$+2.63443\times10^{-7}T^3$ +579325T^{-1} +35537.844 +232.961553T -42.248TlnT	944<T<4000
G_{UO2}	=	-1112055.29 +433.851907T -74.6514TlnT –0.00610305T^2	289<T<1500
	=	$+1.7213\times10^{-7}T^3$ +649010T^{-1} -1707426.87 +4369.94495T -604.679TlnT	1500<T<2670
	=	+0.205276T^2 $-1.58314833\times10^{-5}T^3$ +126580500T^{-1} -1303255.56 +1218.63701T -167.038TlnT	2670<T<4000
G_{UVA2}	=	+41592.266 +130.955151T -26.9182TlnT +0.00125156T^2	298<T<955
	=	$-4.426050\times10^{-6}T^3$ +38568T^{-1} +27478.2 +292.121093T-48.66TlnT	955<T<4000
G_{VAO2}	=	+93038.3 -51.0061T -22.2720TlnT –0.0101978T^2 $+1.32369\times10^{-6}T^3$ –76730.0T^{-1}	298<T<1000
	=	+86862.5 +25.3198T -33.6276TlnT –0.0011916T^2 $+1.35620\times10^{-8}T^3$ +525810T^{-1}	1000<T<3300
	=	+72026.5 +62.5193T -37.9072TlnT –0.000850486T^2 $+2.14420\times10^{-8}T^3$ +8766400T^{-1}	3300<T<4000
G_{VAVA2}	=	+0	298<T<4000
$L^0_{Pu:O,VA}$	=	+90000+68T	298<T<4000
$L^1_{Pu:O,VA}$	=	-935000-196T	298<T<4000
$L^2_{Pu:O,VA}$	=	+787200	298<T<4000
$L^0_{U:O,VA}$	=	+88353.17-32.37686T	298<T<4000
$L^1_{U:O,VA}$	=	+42858.36	298<T<4000
$L^0_{VA:O,VA}$	=	+0	298<T<4000
$L^0_{Pu,U:O}$	=	+0	298<T<4000
$L^0_{Pu,VA:O}$	=	-205000	298<T<4000
$L^1_{Pu,VA:O}$	=	+0	298<T<4000
$L^2_{Pu,VA:O}$	=	+600000	298<T<4000
$L^0_{U,VA:O}$	=	+184216.70+135.94271T	298<T<4000
$L^1_{U,VA:O}$	=	-1422742.46	298<T<4000
$L^2_{U,VA:O}$	=	+782551.16	298<T<4000
$L^0_{Pu,U:VA}$	=	-340000	298<T<4000
$L^1_{Pu,U:VA}$	=	+1189000	298<T<4000
$L^2_{Pu,U:VA}$	=	-1500000	298<T<4000
$L^0_{Pu,VA:VA}$	=	+0	298<T<4000
$L^0_{U,VA:VA}$	=	+0	298<T<4000

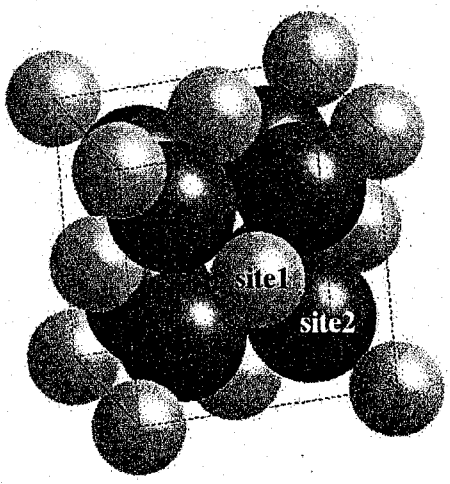

Figure 1. Image of sublattice model for a fluorite structure phase with a formula $(A, B)_1(C)_2$: site 1 is occupied by atoms A or B; site 2 is occupied by atom C. The Gibbs energy of this solution phase is expressed based on the site fractions of A (y^1_A) and B (y^1_B) and the Gibbs energies of A_1C_2 (G^0_{AC}) and B_1C_2 (G^0_{BC}) using Eqs. 2, 3, 4, 5, and 6.

(a)

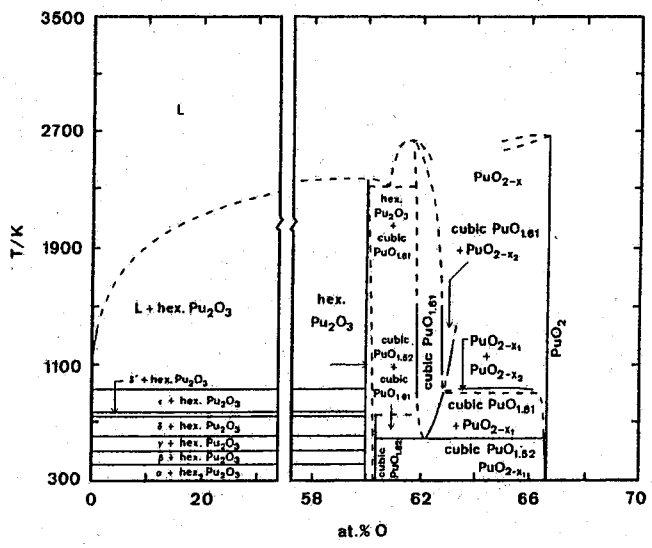

(b)

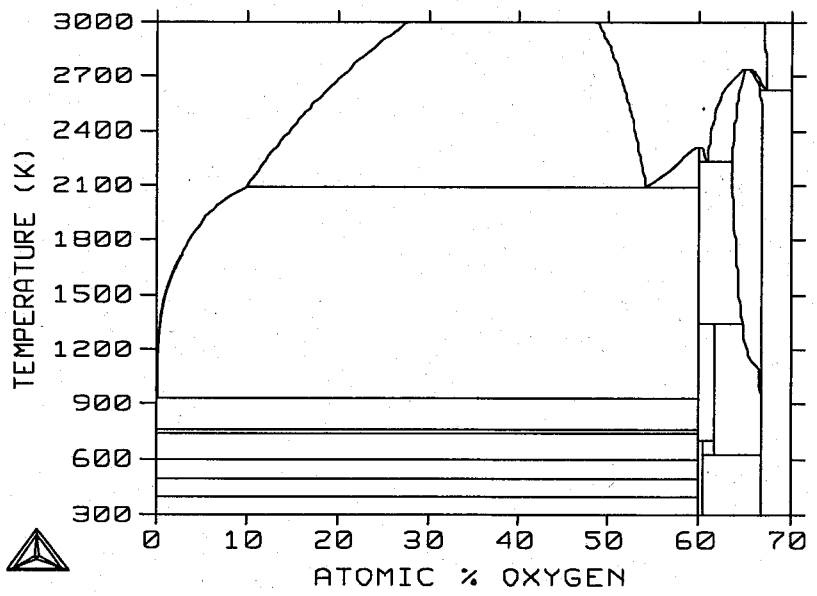

Figure 2. O-Pu binary phase diagram: (a): calculated results and (b): literature data.

(a)

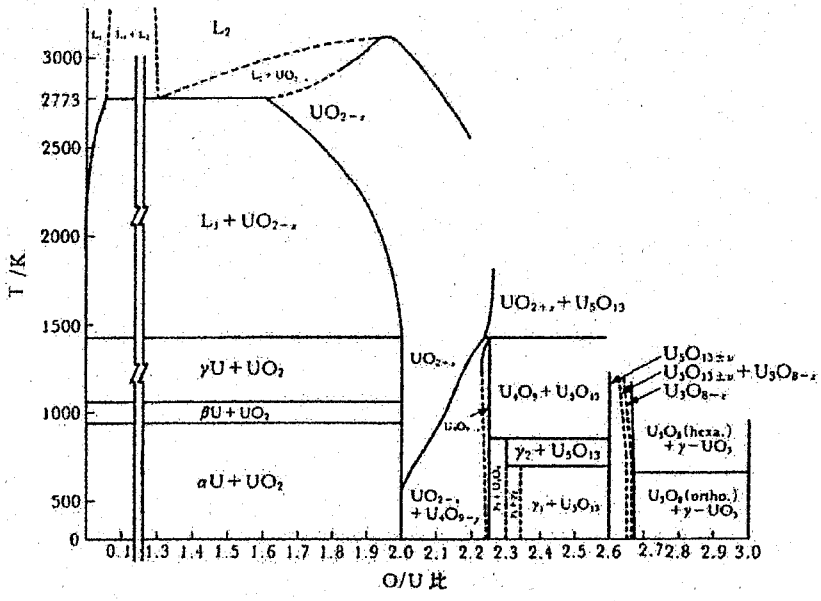

(b)

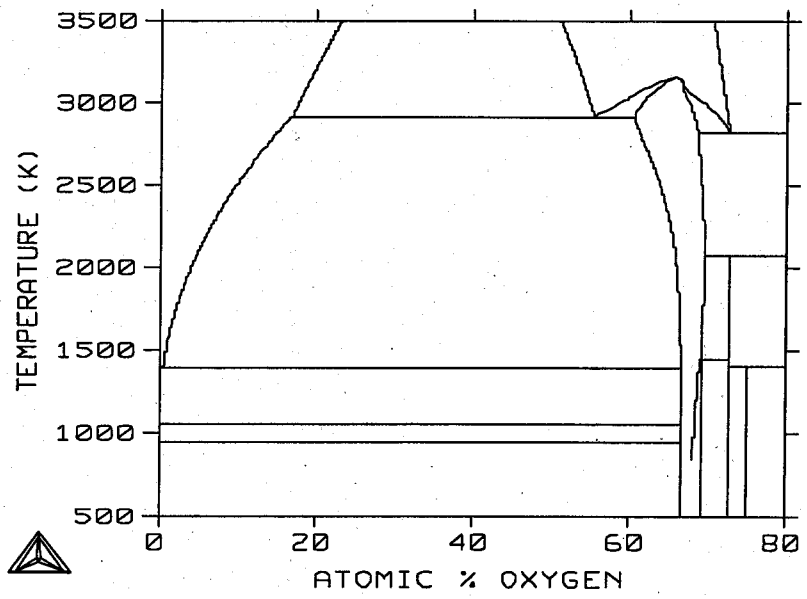

Figure 3. O-U binary phase diagram: (a): calculated results and (b): literature data.

(a)

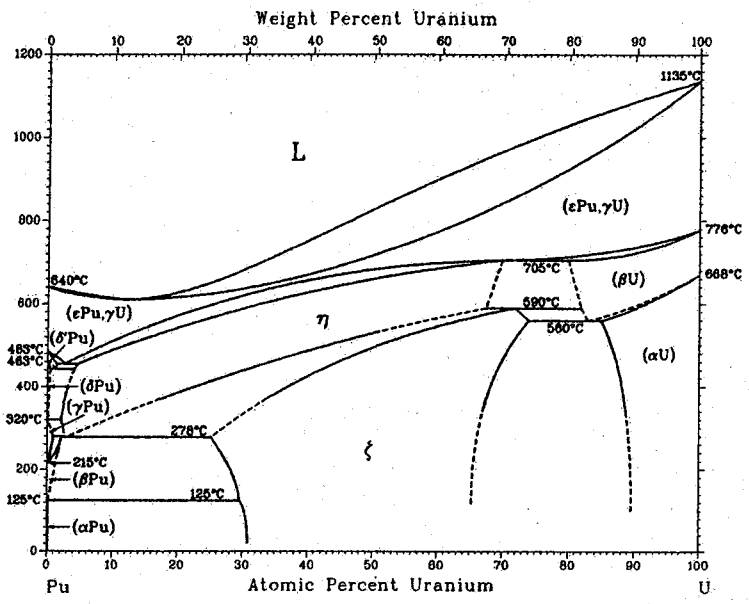

(b)

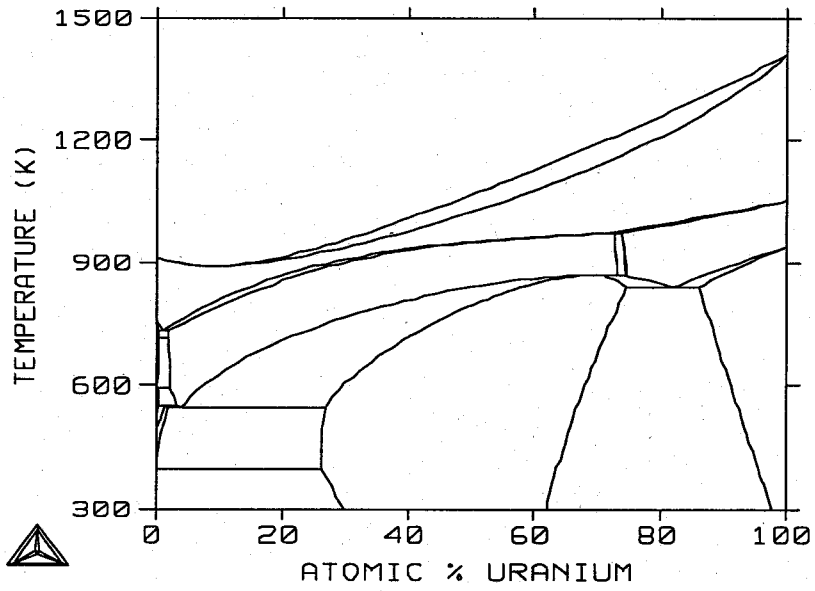

Figure 4. Pu-U binary phase diagram: (a): calculated results and (b): literature data.

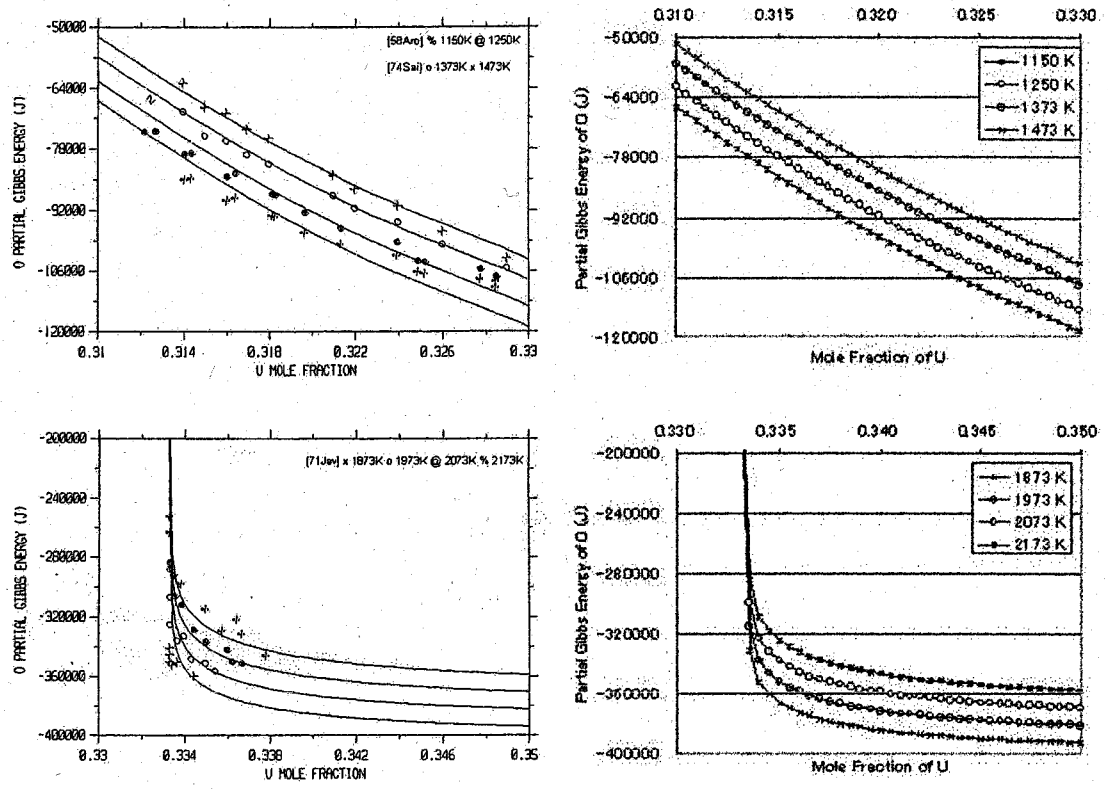

Figure 5. Oxygen potentials of $UO_{2\pm X}$ phase at various temperatures (Comparisons between calculated results and literature data).

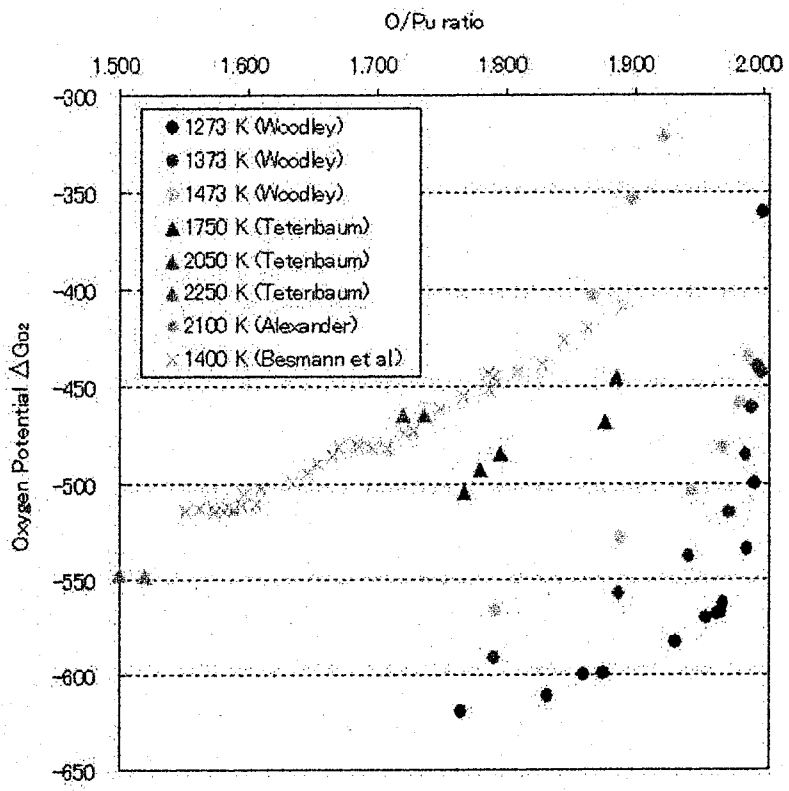

Figure 6. Oxygen potentials (kJ/mol) of PuO_{2-X} phase at various temperatures (Literature data).

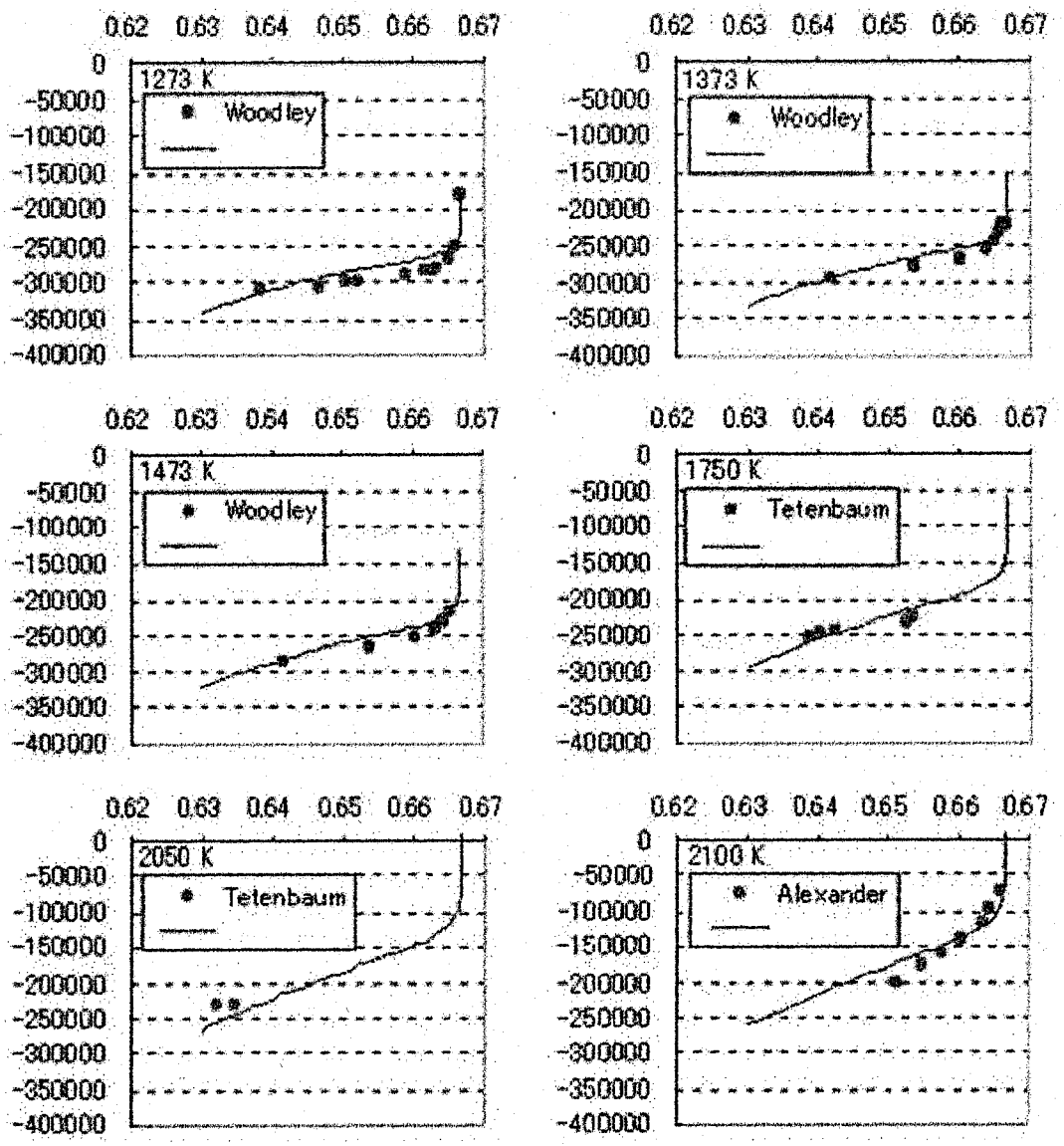

Figure 7. Oxygen potentials (Joule per one oxygen atom) of PuO_{2-x} phase at various temperatures: comparisons between calculated results (line) and literature data (dot).

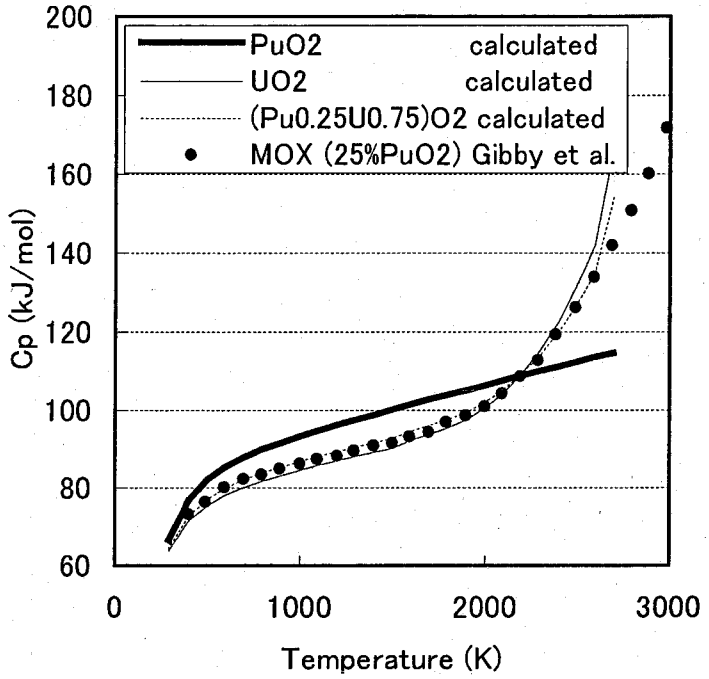

Figure 8. Heat capacity of PuO_2, UO_2, and $(Pu_{0.25}U_{0.75})O_2$.

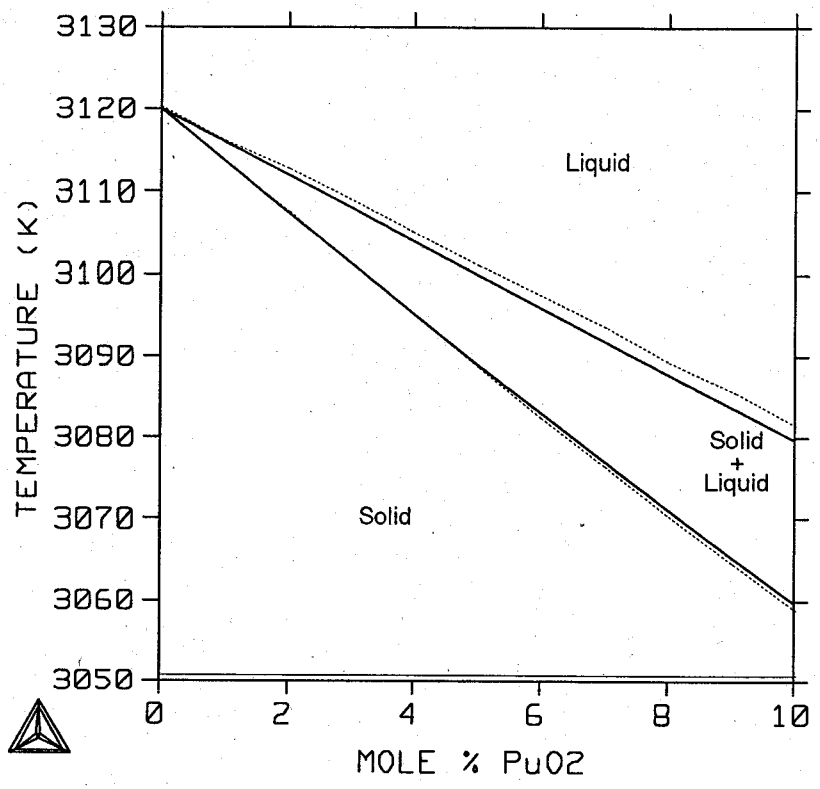

Figure 9. Phase diagram for the PuO_2-UO_2 pseudo-binary system in the low PuO_2 composition range.

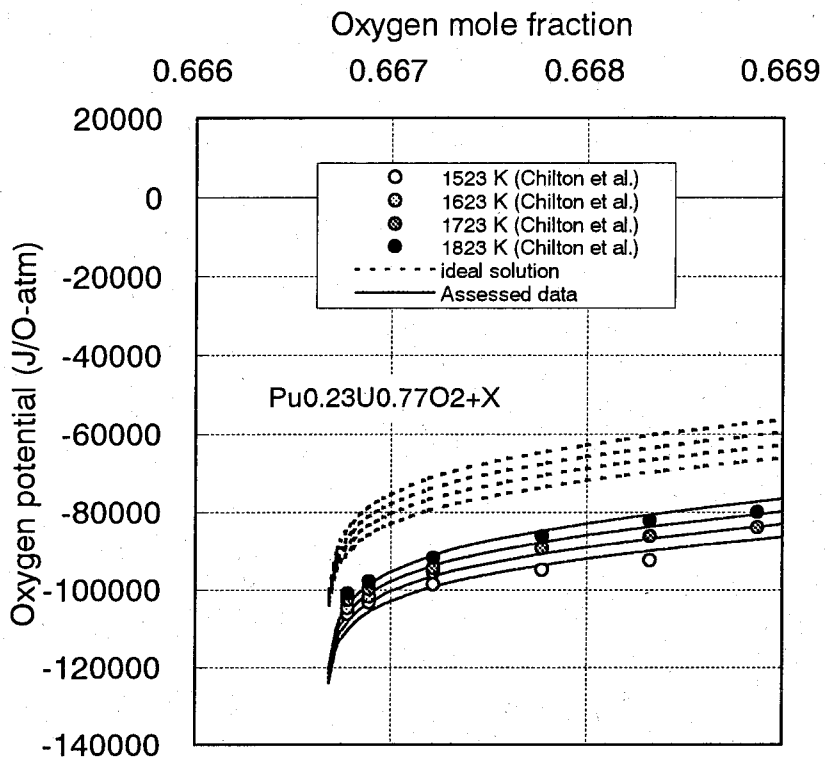

Figure 10. Oxygen potential of fluorite structure phase in the O-Pu-U ternary phase in hyper-stoichiometric region: $Pu_{0.23}U_{0.77}O_{2+X}$.

(a)

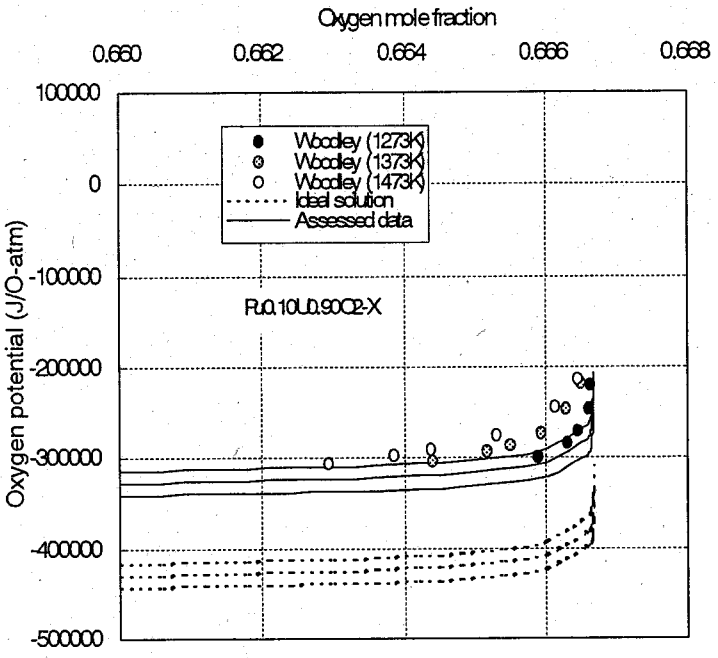
Oxygen mole fraction
0.660
0.662
0.664
0.666
0.668
100000
0
-100000
-200000
-300000
-400000
-500000
Oxygen potential (J/O-atm)
Wbodley (1273K)
Wbodley (1373K)
Wbodley (1473K)
Ideal solution
Assessed data
R:0.10U:0.90O2-X

(b)

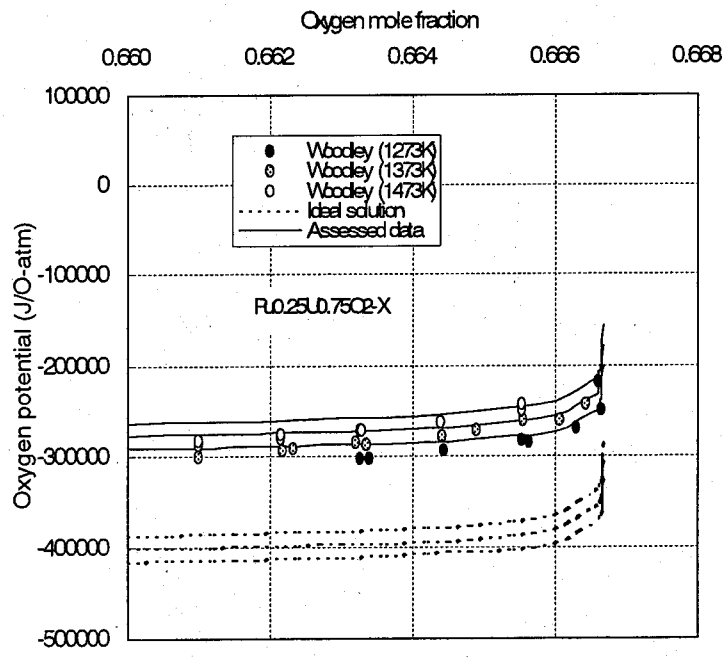
Oxygen mole fraction
0.660
0.662
0.664
0.666
0.668
100000
0
-100000
-200000
-300000
-400000
-500000
Oxygen potential (J/O-atm)
Wbodley (1273K)
Wbodley (1373K)
Wbodley (1473K)
Ideal solution
Assessed data
R:0.25U:0.75O2-X

(c)

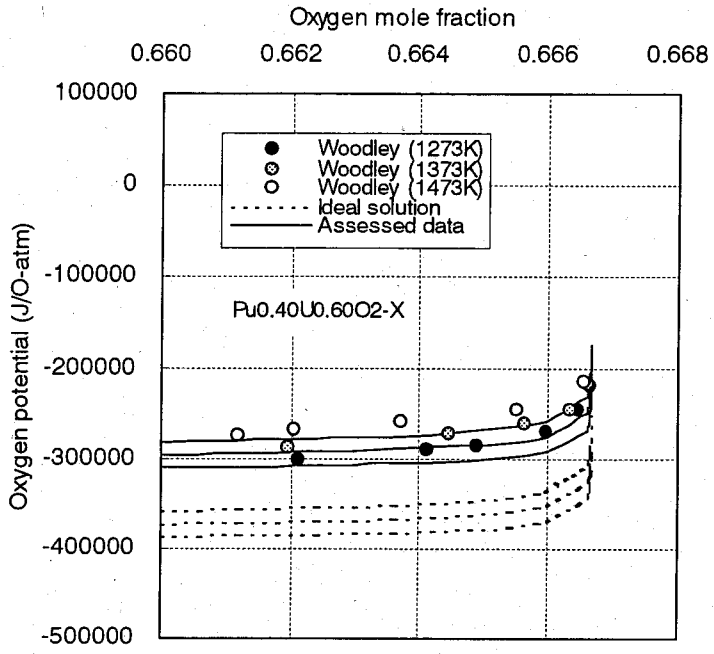

Figure 11. Oxygen potential of fluorite structure phase in the O-Pu-U ternary phase in hypo-stoichiometric region: (a) $Pu_{0.10}U_{0.90}O_{2-X}$, (b) $Pu_{0.25}U_{0.75}O_{2-X}$ and (c) $Pu_{0.40}U_{0.60}O_{2-X}$.

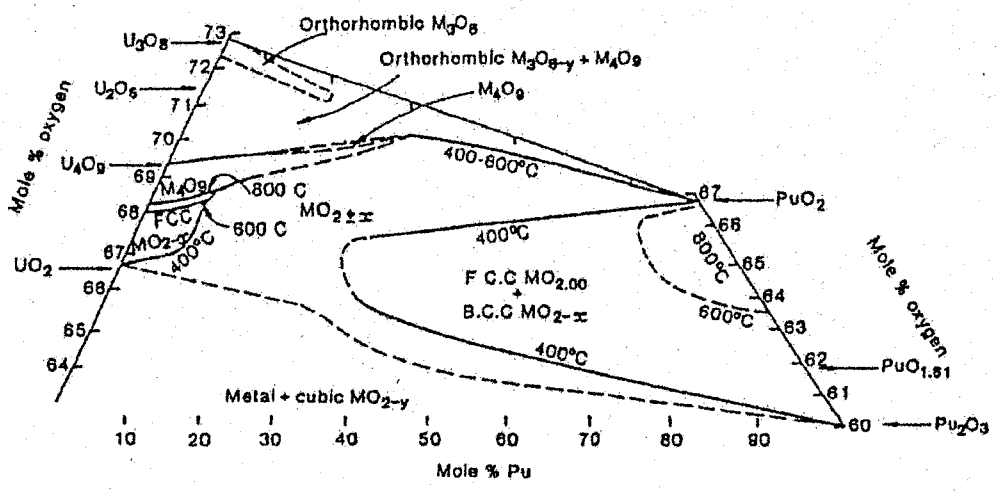

Figure 12. O-Pu-U ternary phase diagram [31].

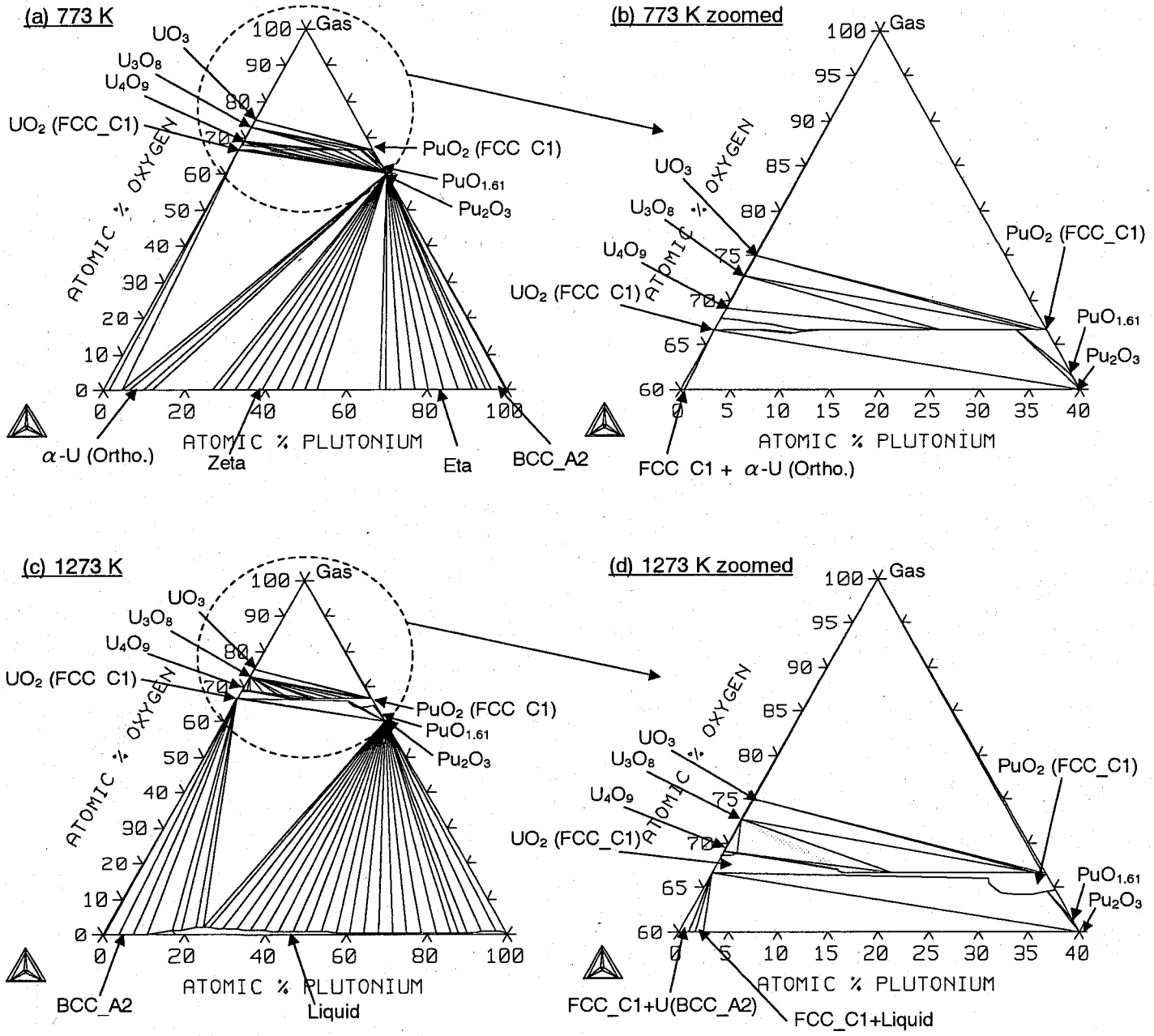

Figure 13. Ternary phase diagram for O-Pu-U system: (a) 773 K, (b) 773 K zoomed in high oxygen composition region, (c) 1273 K and (d) 1273 K zoomed in high oxygen composition region. Tie lines in the zoomed diagrams are excluded to make it easier see the phase regions.

3.4. Thermal and Mechanical Properties Modeling of High Burnup Oxide Fuels

3.4.1. Thermal Conductivity Modeling of High Burnup Oxide Fuels

3.4.1.1. Introduction

The thermal conductivity of a nuclear fuel under irradiation is very important to evaluate the safety of the fuel. In the high burnup oxide fuel, a number of fission product (FP) elements are produced, which affect the thermal and mechanical properties of the fuel. In particular, the FP elements precipitated in the fuel matrix such as the oxide and metallic inclusions appear to have an influence on the thermal conductivity of the fuel [1-5].

The thermal conductivities of the oxide and metallic inclusions have been reported in the previous chapters of this thesis. It was found that the thermal conductivity of $BaUO_3$ (simulated material for the oxide inclusion) is about one-tenth that of UO_2 [6-8], while that of Mo-Ru-Rh-Pd alloy (simulated material for the metallic inclusion) is about two to eight times higher than that of UO_2 [9]. However, the quantitative evaluation about the effect of these inclusions on the thermal conductivity of the irradiated fuel has been scarcely reported.

A finite element method (FEM) is one of the powerful numerical techniques to evaluate the physical properties of various materials. This method is superior to the older analytical techniques, which are limited by the geometric constants and tractable mathematical equations. With the finite elements, it is possible to include the micro-structural parameters that are extremely difficult or impossible to model analytically.

In the present study the thermal conductivity of the high burnup oxide fuel containing the oxide and metallic inclusions has been evaluated by the FEM analysis. The quantitative discussion about the effect of the oxide and metallic inclusions on the thermal conductivity of the fuel has also been performed.

3.4.1.2. Calculation

For the FEM calculation, as indicated in Fig. 1, a model with a cubic matrix with spherical dispersed phases was proposed. The spheres were randomly dispersed without touching each other and protruding from the cube. From this cubic model, a cross-section was arbitrary selected and this two-dimensional (2D) plane was used as the object of the analysis. The geometry on this objective plane was then expressed with tetragonal elements and utilized for the FEM analysis using a commercially available FEM program, MARC/MENTAT II [10]. In the calculation, the upper and lower boundary of the objective plane were taken adiabatic, the right boundary of the plane had a fixed temperature T_1, and the left one received a fixed quantity of heat flux Q (0.5 Wm^{-2}). In this case, the thermal gradient is generated in a horizontal direction (x-direction), and an averaged temperature of the left boundary T_x, which is slightly higher than T_1, can be obtained. The thermal conductivity of this 2D plane λ_x was calculated by

using following relationship:

$$\lambda_x = \frac{Q \cdot x}{T_x - T_1}, \tag{1}$$

where x is the distance between the left and right boundaries. By setting T_1 to an arbitrary temperature, the thermal conductivity at any temperature can be evaluated. The y-direction thermal conductivity λ_y was also calculated, and the average of λ_x and λ_y was used as the result obtained from the calculation.

As described in the former section, in the present study, the FEM program calculates a two-dimensional (2D) thermal conductivity and its temperature profile. However, the actual heat flux in the actual materials exists in a three-dimensional (3D) space, and the extra degree of freedom in the heat flux causes the 3D thermal conductivity to be larger than the 2D one. Therefore, it is necessary to convert the obtaining 2D thermal conductivity to the 3D one.

In the present study, the conversion was performed using the following equation proposed by Bakker [11]:

$$\frac{1-\{1-(\lambda_d/\lambda_m)\}\cdot V_d - (\lambda_{2D}/\lambda_m)}{1-\{1-(\lambda_d/\lambda_m)\}\cdot V_d - (\lambda_{3D}/\lambda_m)} = r, \tag{2}$$

where V_d is the volume fraction of the dispersed phase, λ_{2D} and λ_{3D} represent 2D and 3D thermal conductivity, and "r" is the constant affected by the shape of the dispersed phase. Bakker have also obtained "r" with various dispersed phase shape and concentration [12]. Based on the Bakker's study, we proposed the following equation for "r" in spherical dispersing case:

$$r = 1.02 + \frac{1}{(\lambda_d/\lambda_m)+1.12}. \tag{3}$$

By using above two equations, the 2D thermal conductivity was converted to the 3D one.

In the present study, the effect of the oxide and metallic inclusions, existing in the high burnup oxide fuel pellet, on the thermal conductivity of the pellet is evaluated. We employed $(U_{0.8}Pu_{0.2})O_2$ [13] and $(M_{0.94}Nd_{0.06})O_2$ (M: $U_{0.8}Pu_{0.2}$) [14] for the fuel matrix materials, and $BaUO_3$ [6] and Mo-Ru-Rh-Pd alloy [9] for the inclusions. The dispersed phase size were determined from a post irradiation examination (PIE) result of 9.6 at.% burnup MOX fuel [4], in which the inclusions with the diameter of about 25 μm were observed. The volume concentration of the inclusions was calculated from the amount of the FP elements at the burnup of 10 at.%. In the present study, 2.5 vol.% of the spherical inclusions with the diameter of 25 μm were dispersed in the fuel matrix cube with a size of 400x400x400 μm. To evaluate the temperature dependence of the thermal conductivity, the FEM analysis were performed at 500, 1000, 1500, and 2000 K. The detail for the calculation conditions are summarized in Table 1, and the 2D plane used in the present study is shown in Fig. 2.

3.4.1.3. Results and Discussion

The thermal conductivities [6,9,13,14] used in the input data for the present FEM analysis are shown in Fig. 3. In the FEM analysis, $(U_{0.8}Pu_{0.2})O_2$ and $(M_{0.94}Nd_{0.06})O_2$ (M: $U_{0.8}Pu_{0.2}$) correspond to the matrix phases, and $BaUO_3$ and Mo-Ru-Rh-Pd alloy correspond to the dispersed inclusions. The thermal conductivities of $(U_{0.8}Pu_{0.2})O_2$ and $(M_{0.94}Nd_{0.06})O_2$ (M: $U_{0.8}Pu_{0.2}$) were corrected to 95 % of the theoretical density by using Maxwell-Eucken and Schulz's equations [15-17]. It is found from this figure that the thermal conductivity of $(U_{0.8}Pu_{0.2})O_2$ decreases about 30 % by dissolving 6 at.% neodymium.

The calculated results obtained from the FEM analysis are shown in Fig. 4. It can be recognized that the calculated thermal conductivity of the system is slightly decreased by dispersing $BaUO_3$ inclusions, while is slightly increased by dispersing Mo-Ru-Rh-Pd alloy inclusions. The quantitative evaluation about the effect of the inclusions on the thermal conductivity of the system was also performed, and its result is shown in Fig. 5. The rates of the variation caused by the inclusions are evaluated to be about 1-3 % decreasing in $BaUO_3$ dispersing case and about 2-8 % increasing in Mo-Ru-Rh-Pd alloy dispersing case, respectively. It is found that the effect of the precipitated FP elements is about one order lower than that of the dissolved FP elements on the thermal conductivity of the high burnup oxide fuel.

3.4.1.4. Conclusion

In order to evaluate the effect of the precipitated FP elements on the thermal conductivity of the irradiated fuel, the thermal conductivity of the fuel containing the oxide and metallic inclusions has been evaluated by using the FEM analysis. $(U_{0.8}Pu_{0.2})O_2$ and $(M_{0.94}Nd_{0.06})O_2$ (M: $U_{0.8}Pu_{0.2}$) have been employed as the fuel matrix, and $BaUO_3$ and Mo-Ru-Rh-Pd alloy as the inclusions. 2.5 vol.% of the inclusions have been dispersed in the matrix, which corresponds to about 10 at.% burnup. In $BaUO_3$ dispersing case, about 1-3 % decreasing is observed in the thermal conductivity of the system, while in Mo-Ru-Rh-Pd alloy dispersing case, about 2-8 % increasing is observed. It is found that the effect of the precipitated FP elements is about one order lower than that of the dissolved FP elements on the thermal conductivity of the high burnup oxide fuel.

References

[1] J.H. Davies and F.T. Ewart, J. Nucl. Mater., 41(1971) 143.

[2] H. Kleykamp, J. Nucl. ater., 131 (1985) 221.

[3] H. Kleykamp, Nucl. Technol., 80 (1988) 412.

[4] I. Sato, H. Furuya, T. Arima, K. Idemitsu, and K. Yamamoto, J. Nucl. Sci. Technol., 36 (1999) 775.

[5] I. Sato, H. Furuya, T. Arima, K. Idemitsu, and K. Yamamoto, J. Nucl. Mater., 273 (1999) 239.

[6] S. Yamanaka, K. Kurosaki, T. Matsuda, and M. Uno, J. Nucl. Mater., 294 (2001) 99-103.

[7] K. Kurosaki, T. Matsuda, M. Uno, S. Kobayashi, and S. Yamanaka, Journal of Alloys and Compounds, 319 (2001) 271-275.

[8] S. Yamanaka, T. Matsuda, K. Kurosaki, and M. Uno, J. Nucl. Sci. Technol., Suppl. 3 (2002) 709.

[9] S. Yamanaka and K. Kurosaki, Journal of Alloys and Compounds, in press (JALCOM8412).

[10] K. Oizumi, "How to use MARC/MENTAT", (in Japanese) SENAC, Vol. 31, No. 3 (1998) 39-43.

[11] K. Bakker, Int. J. Heat Transfr, Vol.40, No.15 (1997) 3503-3511.

[12] K. Bakker, H. Kwast, and E. H. P. Cordfunke, J. Nucl. Mater., 226 (1995) 128-143.

[13] Y. Philipponneau, J. Nucl. Mater., 188 (1992) 194.

[14] S. Fukushima, T. Ohmichi, A. Maeda, and M. Handa, J. Nucl. Mater., 116 (1983) 287.

[15] J.C. Maxwell, Treaties on Electricity and Magnetism, Vol. 1, 3rd ed., Oxford Univ. Press (1891), reprinted by Dover, New York (1954).

[16] A.E. Eucken, Forsch. Gebiete Ingenieurw. B3, Forschungsheft, No. 353 (1932) 16.

[17] B. Schulz, High Temperatures – High Pressures, 13 (1981) 649-660.

Table 1

Calculation conditions of the FEM analysis

Matrix phases	$(U_{0.8}Pu_{0.2})O_2$ $(M_{0.94}Nd_{0.06})O_2$ (M: $(U_{0.8}Pu_{0.2})O_2$)
Dispersed phases	$BaUO_3$ Mo-Ru-Rh-Pd alloy
3D cubic size (μm)	400x400x400
Dispersed phase diameter (μm)	25*
Dispersed phase volume fraction (vol.%)	2.5**
Left boundary heat flux (Wm^{-2})	0.5
Analysis temperature (K)	500, 1000, 1500, 2000 K

*: observed in irradiated fuel at 9.6 at.% burnup

**: corresponding to about 10 at.% burnup

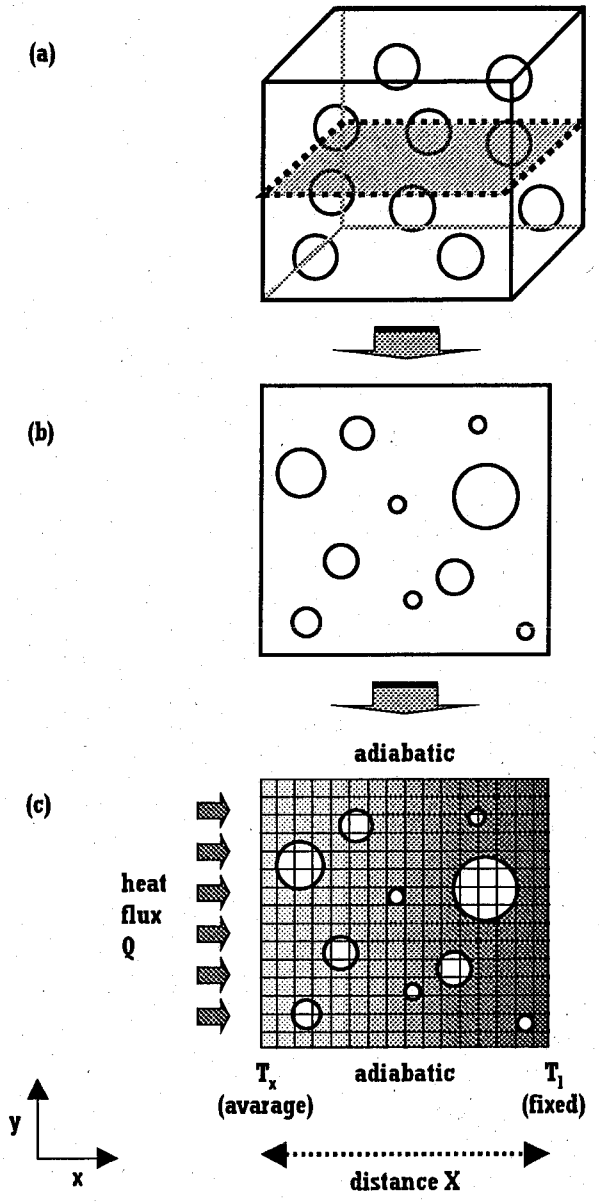

Figure 1. Thermal conductivity modeling procedure.

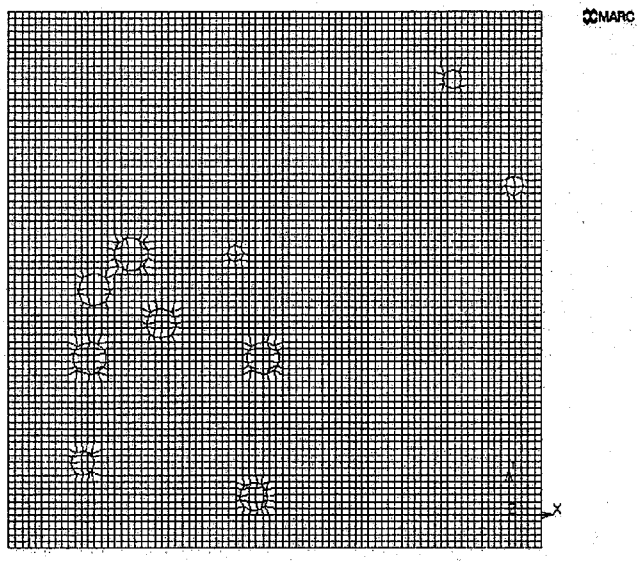

Figure 2. 2D plane used in the present study (2.5 vol.% of the inclusion).

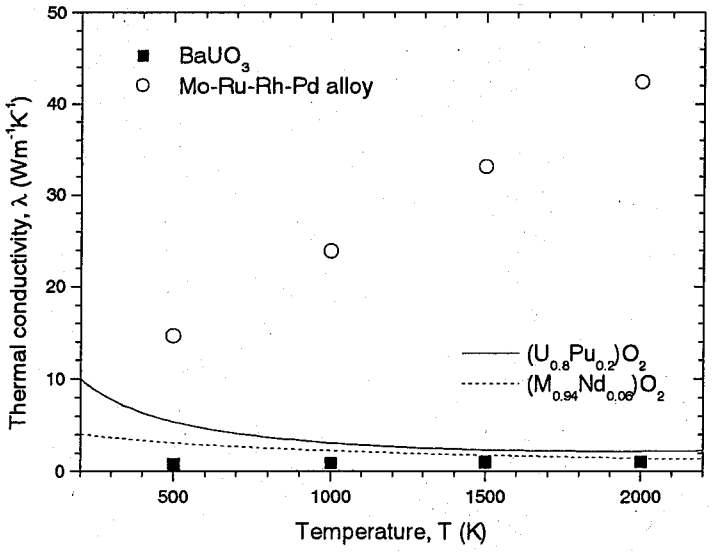

Figure 3. Thermal conductivities of $(U_{0.8}Pu_{0.2})O_2$, $(M_{0.94}Nd_{0.06})O_2$ (M: $(U_{0.8}Pu_{0.2})O_2$), $BaUO_3$, and Mo-Ru-Rh-Pd alloy.

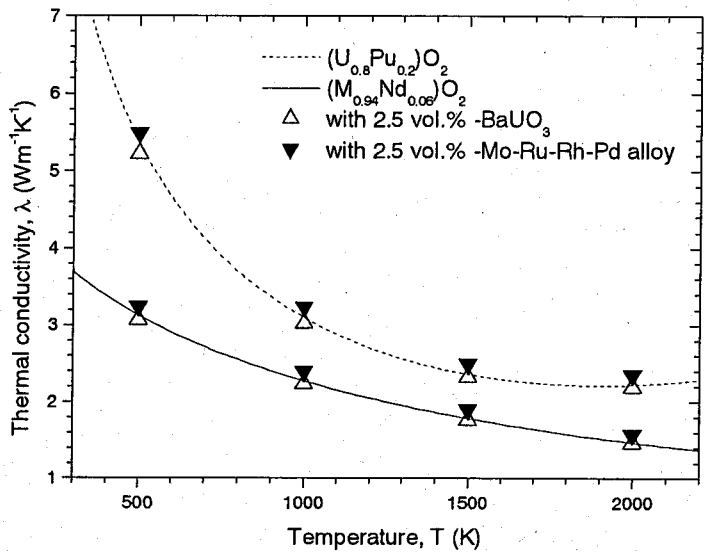

Figure 4. Thermal conductivities of $(U_{0.8}Pu_{0.2})O_2$ and $(M_{0.94}Nd_{0.06})O_2$ (M: $(U_{0.8}Pu_{0.2})O_2$) including 2.5 Vol.% of $BaUO_3$ or Mo-Ru-Rh-Pd alloy.

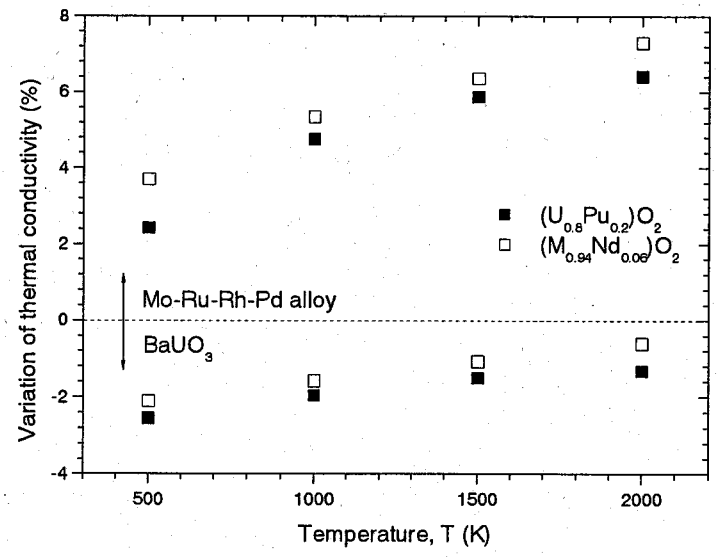

Figure 5. Effect of oxide and metallic inclusions on thermal conductivities of $(U_{0.8}Pu_{0.2})O_2$ and $(M_{0.94}Nd_{0.06})O_2$ (M: $(U_{0.8}Pu_{0.2})O_2$).

3.4.2. Young's Modulus Modeling of High Burnup Oxide Fuels

3.4.2.1. Introduction

As described in the previous chapters, the elastic modulus of the nuclear fuel is one of the most important factors to utilize for extending burnup. The lower elastic modulus of the nuclear fuel is one of the major stumbling to maintain the structural integrity of the fuel. In order to utilize the nuclear fuel for extending burnup, it is necessary to understand the effective elastic modulus in term of the effect of the fission product (FP) elements.

The effect of the solid state FP elements on the mechanical properties have been studied in Chapter 2.1. From the results of the ultra sonic pulse echo measurement, it was found that the elastic modulus, such as the Young's modulus, of the high burnup oxide fuel decrease with increasing the FP content (equivalent to the burnup). The degradation rates in the Young's modulus and shear modulus are about 6.5 % and 7 % with increasing burnup of 50 GWd/t.

In the present section, therefore, the Young's modulus of the high burnup oxide fuel containing the oxide FP inclusions has been evaluated by the finite element method (FEM) analysis. The quantitative discussion about the effect of the oxide inclusions on the Young's modulus of the fuel pellet has been also performed.

3.4.2.2. Calculation

The fundamental procedure of the FEM analysis is same as that described in the previous section. The high burnup oxide fuel was modeled as a cubic matrix with spherical dispersed inclusions corresponded to the oxide precipitates. The spheres were randomly dispersed in the cubic matrix without touching each other and from the cube. From this cube, a cross-section is arbitrary selected and this two-dimensional (2D) plane was used as the object of the analysis. The volume fractions of the spheres were selected to be 5, 15, and 25 %. The 2D planes used in the present study are shown in Fig. 1. The geometry of the elements is basically square, but the elements around the spherical dispersed phase have various geometries.

A commercially available FEM program, MARC/MENTAT II [1] was used for the FEM analysis. In this calculation, the Young's modulus was analyzed using a plane-strain approximation accomplished by the following boundary conditions. The nodes along the bottom edge of the mesh are fixed in the Y direction but allowed in the X direction. A load is then applied to the top edge of the mesh in the Y direction with a very small strain.

In the FEM calculation, the Young's modulus and Poisson's ratio of the matrix phase and the precipitated oxide inclusion are required. The Young's modulus and Poisson's ratio used for the input data of this analysis are summarized in Table 1. As the results of the nanoindentation described in Chapter 2.3, the Young's moduli of $(U_{0.9}Ce_{0.1})O_2$ as the matrix phase and $BaUO_3$ as the oxide inclusion were 205.1 GPa and 140.7 GPa, respectively. For the

Poisson's ratio, the literature values of 0.3136 for $(U_{0.9}Ce_{0.1})O_2$ [2] and 0.2390 for $BaUO_3$ [3] were used in this analysis.

According to the continuum dynamics with three dimensions, for an elastic deformation, the relationship between the stress and strain is expressed as:

$$\varepsilon_x = \frac{\sigma_x}{E} - \nu\frac{\sigma_y}{E} - \frac{\sigma_z}{E}, \quad (1)$$

$$\varepsilon_y = \frac{\sigma_y}{E} - \nu\frac{\sigma_z}{E} - \frac{\sigma_x}{E}, \quad (2)$$

$$\varepsilon_z = \frac{\sigma_z}{E} - \nu\frac{\sigma_x}{E} - \frac{\sigma_y}{E}, \quad (3)$$

where ε is the strain, σ is the stress, ν is the Poisson's ratio, and E is the Young's modulus. When the stress in the X direction is zero, then the above equations became:

$$\varepsilon_x = -\frac{\nu}{E}(\sigma_y + \sigma_z), \quad (4)$$

$$\varepsilon_y = -\frac{1}{E}(\sigma_y - \nu\sigma_z), \quad (5)$$

$$\varepsilon_z = \frac{1}{E}(\sigma_z - \nu\sigma_y). \quad (6)$$

In the present case, the plane stress must be discussed; therefore the stain in the Z direction is considered to be small compared with those of in the X and Y directions. The Poisson's ratio and Young's modulus can be expressed as:

$$\nu = \frac{\varepsilon_x}{\varepsilon_y + \varepsilon_x}, \quad (7)$$

$$E = -\frac{\sigma_y}{\varepsilon_x}\nu(1+\nu). \quad (8)$$

The shear modulus, G is expressed as follows:

$$G = \frac{E}{2(1+\nu)}. \quad (9)$$

3.4.2.3. Results and Discussion

The calculated results obtained from the FEM analysis are shown in Fig. 2. In this figure, the effect of the oxide inclusions on the calculated elastic modulus and Poisson's ratio are shown in the relative values. In order to confirm the error of the calculated results associated with the arrangement of the oxide inclusions, each calculation was duplicated performing analysis in two different directions (x- and y- directions). As the result of these duplicated calculations, the error associated with the arrangement of the oxide inclusions is not clearly

confirmed up to 25 vol.%. The relative values of the calculated elastic modulus and Poisson's ratio are almost one, regardless of the volume fraction of the oxide inclusions. Therefore, it is confirmed that the oxide inclusions have little influence on the mechanical properties of the high burnup oxide fuel up to the volume fraction of 25 %.

Figure 3 shows the Young's modulus of the high burnup simulated oxide fuel (SIMFUEL) as a function of the burnup described in Chapter 2.1, together with the FEM result. In this case, the SIMFUEL with simulated burnup of 150 GWd/t corresponds to about 4 vol.% of the oxide inclusions in the FEM analysis. The reduction rates in the elastic moduli of the SIMFUEL are about 6.5 % per 50 GWd/t burnup for the shear modulus and about 7 % per 50 GWd/t burnup for the Young's modulus, respectively. From the FEM analysis, the effect of the oxide inclusions on the elastic moduli of the fuel is vanishingly small (within 1 % per 25 vol.% of the oxide inclusions). It is found that the effect of the precipitated FP elements on the mechanical properties of the fuel is quite lower than that of the dissolved FP elements.

3.4.2.4. Conclusion

In order to evaluate the effect of the precipitated FP elements on the mechanical properties of the irradiated fuel, the Young's modulus of the fuel containing the oxide inclusions has been evaluated by using the FEM analysis. $(U_{0.9}Ce_{0.2})O_2$ and $BaUO_3$ have been employed as the fuel matrix and oxide inclusion, respectively. It is found that the effect of the oxide inclusions on the Young's modulus of the irradiated fuel is vanishingly small (within 1 % per 25 vol.% of the oxide inclusions), and quite lower than that of the dissolved FP elements.

References

[1] K. Oizumi, "How to use MARC/MENTAT", (in Japanese) SENAC, Vol. 31, No. 3 (1998) 39-43.

[2] K. Yamada, S. Yamanaka, T. Nakagawa, M. Uno, and M. Katsura, J. Nucl Mater., 247 (1997) 289.

[3] S. Yamanaka, K. Kurosaki, T. Matsuda, and M. Uno, J. Nucl. Mater., 294 (2001) 99.

Table 1

Young's modulus and Poisson's ratio of $(U_{0.9}Ce_{0.1})O_2$ and $BaUO_3$ used in the FEM analysis

	Young's modulus, E (GPa)[#]	Poisson's ratio, ν
$(U_{0.9}Ce_{0.1})O_2$	205.1	0.3136 [2]
$BaUO_3$	140.7	0.2390 [3]

The Young's moduli are determined in Chapter 2.3.

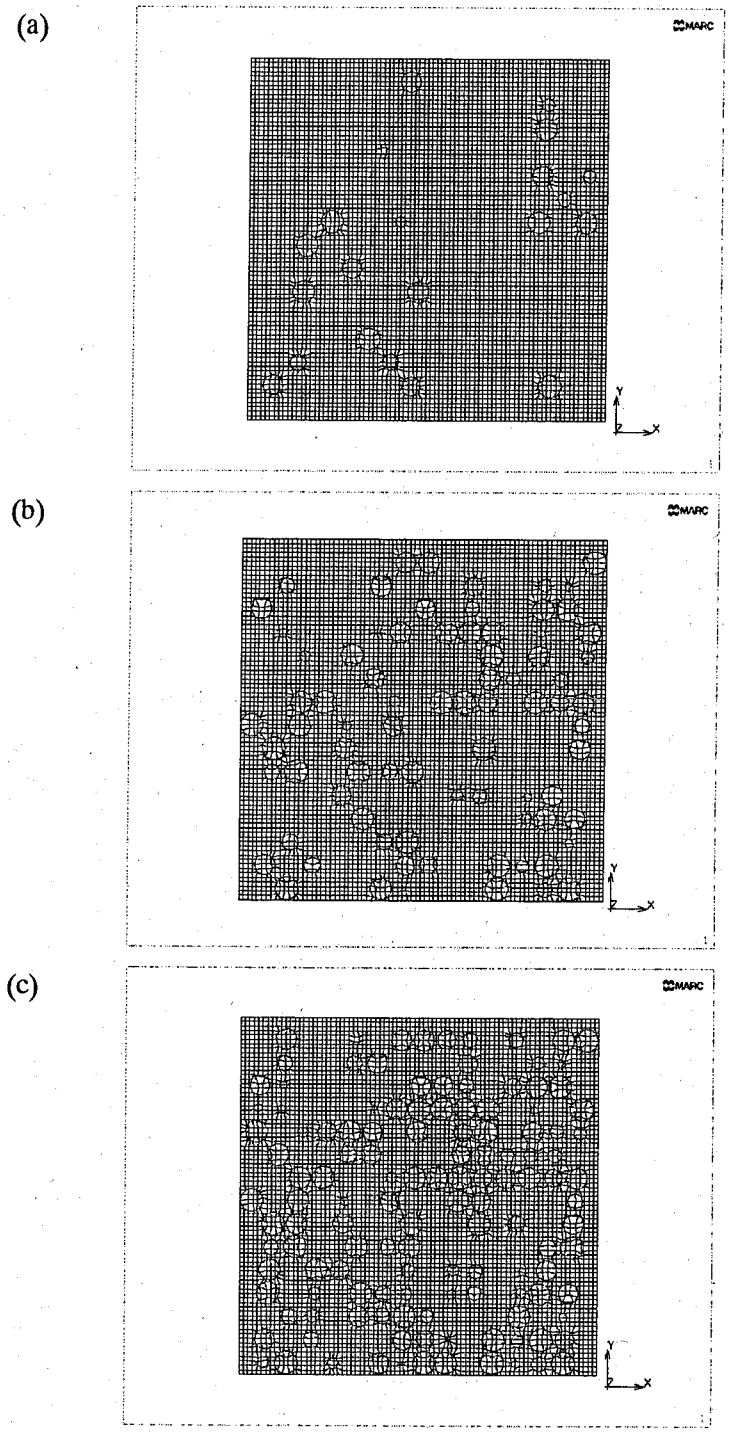

Figure 1. 2D planes used in the present study. (a), (b), and (c) correspond to 5, 15, and 25 vol.% of the inclusion, respectively.

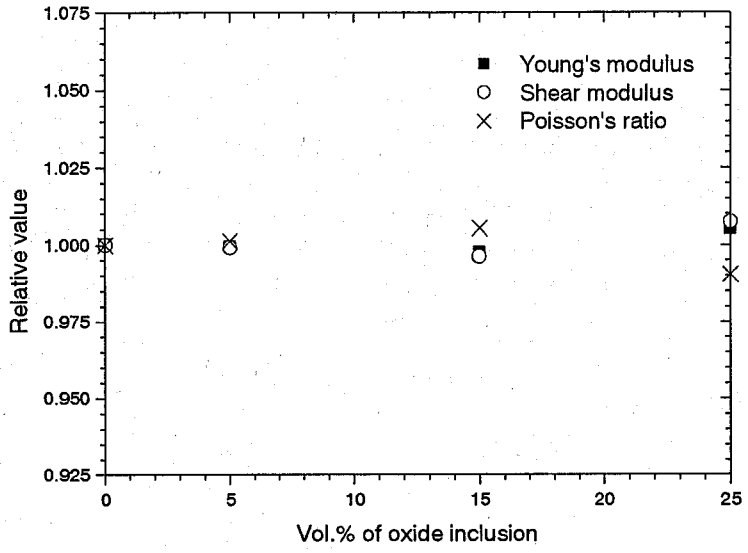

Figure 2. Calculated elative values of the elastic moduli and Poisson's ratio as a function of the volume fraction of the oxide inclusions.

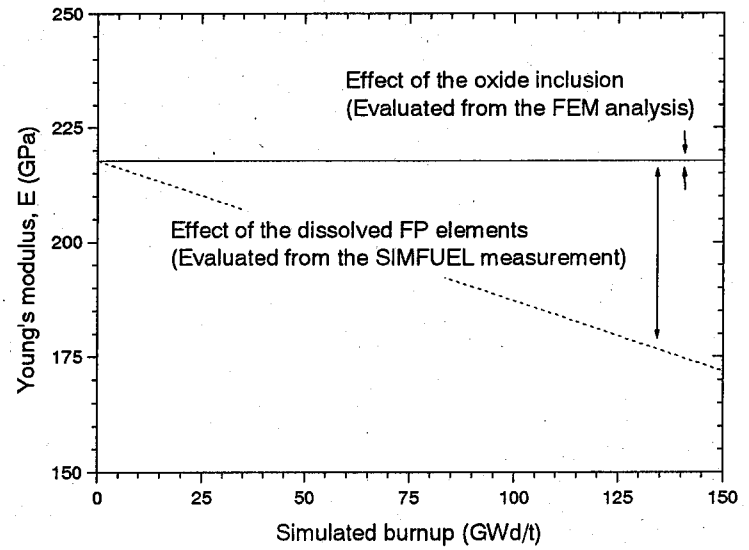

Figure 3. Effect of the solid state FP elements on Young's modulus of the irradiated oxide fuel.

Chapter 4

Summary

4. Summary

In the present study, the thermal and mechanical properties of the high burnup oxide fuel have been studied by the experimental measurements of the simulated materials and computer simulations. The effects of the solid state fission product (FP) elements on the properties of the high burnup oxide fuels have been evaluated.

In Chapter 2, the simulated fuel materials have been prepared and their thermal and mechanical properties have been measured.

The simulated high burnup UO_2 based fuel (SIMFUEL) has been prepared and their thermal and mechanical properties have been studied. The phase equilibria of the SIMFUEL annealed at three kinds of oxygen potential have been studied by using the X-ray diffraction analysis, SEM observation, EDX analysis, and oxygen chemical analysis. The lattice parameter of the matrix phase linearly decreases from 0.5470 nm (corresponds to that of UO_2) with increasing both the burnup and annealing oxygen potential, which corresponds to literature data. The O/U ratio of UO_{2+x} annealed under the oxygen potentials of -390, -340 and -220 kJ/mol at 1400 K are 2.000, 2.002 and 2.030, respectively. The specific heat capacity of the SIMFUEL increases proportionally with increasing the simulated burnup. The specific heat capacity of the SIMFUEL slightly increases with increasing the oxygen content. The thermal conductivity of the SIMFUEL decreases with increasing the simulated burnup. The reduction rate of the thermal conductivity appears to be small with increasing the simulated burnup. The excess oxygen decreases the thermal conductivity of the SIMFUEL. The elastic moduli and Vickers hardness of the SIMFUEL decrease with increasing the simulated burnup. The effects of the annealing oxygen potential on the mechanical properties of the SIMFUEL are not clearly confirmed.

The thermal and mechanical properties of the oxide and metallic inclusions have been studied. The thermophysical properties of $BaUO_3$, $BaZrO_3$, $BaCeO_3$, and $BaMoO_3$ have been measured and the relationships between the properties have been studied. The thermal expansions of $BaUO_3$ and $BaCeO_3$ nearly equal that of UO_2, while $BaZrO_3$ and $BaMoO_3$ show slightly lower thermal expansion. In the relationship between α_l and T_m, the product of α_l and T_m for $BaUO_3$ shows slightly higher value (= 0.027) than those for $BaZrO_3$ and $BaCeO_3$, while that for $BaMoO_3$ shows slightly lower value (= 0.017). In the relationship between E and $q(RT_m/V_m)$, $BaZrO_3$, $BaCeO_3$, and $BaMoO_3$ show similar characteristics and the proportionality is almost identical. Although $BaUO_3$ has the same crystal structure as $BaZrO_3$ and $BaMoO_3$, the proportionality between E and $q(RT_m/V_m)$ is almost identical with that of SiO_2 glass. It is confirmed that the measured C_P of $BaZrO_3$ is nearly consistent with the (C_h+C_d) evaluated from the thermal expansion coefficient, compressibility, and Debye temperature. On the other hand, the measured C_P of $BaUO_3$ is higher than the (C_h+C_d), indicating the existence of other contributions. The thermal conductivities of $BaUO_3$, $BaZrO_3$, and $BaCeO_3$ are lower than that of

UO_2 in the whole temperature range, especially that of $BaUO_3$ shows the extremely low values. The thermal conductivity at room temperature of $BaUO_3$ is around 1 $Wm^{-1}K^{-1}$, which is about 10 times lower than that of UO_2. On the other hand, $BaMoO_3$ shows the extremely high values, in which the thermal conductivity at room temperature of $BaMoO_3$ is around 30 $Wm^{-1}K^{-1}$, which is caused by the high electronic contribution to the thermal conductivity. The thermophysical properties, especially the thermal conductivity, of the Mo-Ru-Rh-Pd alloys with the compositions of $Mo_{35}Ru_{31}Rh_9Pd_{25}$, $Mo_{20}Ru_{54}Rh_{15}Pd_{11}$, $Mo_{30}Ru_{43}Rh_{14}Pd_{13}$, and $Mo_{43}Ru_{34}Rh_{12}Pd_{11}$ have been studied. The relationship between the micro-Vickers hardness and the Young's modulus for the alloys shows the metallic characteristics. The thermal conductivities of all the alloys almost linearly increase with increasing temperature, showing the metallic behavior. Above about 1000 K, the thermal conductivities are tenfold or above larger than that of UO_2. It is confirmed that the characteristics of the mechanical and thermal properties of the Mo-Ru-Rh-Pd alloys differ from that of UO_2.

In order to obtain the nanoscale mechanical properties such as the reduced modulus and nanohardness of the oxide nuclear fuels, the nanoindentation tests have been performed. For the reduced modulus, there is no difference between the single crystal and pellet for UO_2. The nanohardness of the polycrystalline UO_2 pellet is lower than that of UO_2 single crystal. Both the reduced modulus and nanohardness of the polycrystalline $(U,Ce)O_2$ pellet decrease with CeO_2 content. The same tendency is observed in the nanoscale mechanical properties of $(U,Ce)O_2$ as that in the bulk-mechanical properties obtained from the ultrasonic pulse echo measurement. The nanoindentation tests have also been performed for the SIMFUEL to evaluate the nanoscale mechanical properties. The nanoindentation method enables in situ measurements of the nanomechanical properties of the matrix phase and oxide inclusion observed in the high burnup oxide fuel.

In Chapter 3, the characteristics of the oxide nuclear fuels have been evaluated by the computer simulations.

In order to understand the chemical states of the FP elements in the high burnup oxide fuel, the phase equilibrium calculation has been performed using ChemSage program. Although the free energy of each solution phase is treated as the ideal solution model, the calculated results almost agree with the PIE results. In order to understand the chemical states of the perovskite type gray oxide phase in the high burnup oxide fuel, the phase equilibrium calculation between the selected FP elements and fuel has also been performed. The concentration of $BaZrO_3$ in the pseudo-ternary $BaUO_3$-$BaZrO_3$-$BaMoO_3$ system increases with increasing burnup at both 1273 K and 1973 K. $BaMoO_3$ is scarcely included in the system and the concentration increases slightly with increasing the oxygen potential. It is found that the multi-component and multi-phase thermodynamic equilibrium calculation between the fuel and

FP elements system is an effective tool for understanding the phase equilibria of the high burnup oxide fuel.

The molecular dynamics (MD) calculations have been performed to UO_2, PuO_2, $(U,Pu)O_2$ solid solution, and the perovskite type oxides. The applicability of the MD method to evaluation of the thermal and mechanical properties of the oxide nuclear fuels has been studied. The thermophysical properties, viz. the linear thermal expansion coefficient, compressibility, heat capacity, and thermal conductivity have been evaluated by the MD calculations, and the results have been compared with the experimental data obtained in the present study. The Morse-type potential function added to the Busing-Ida type potential has been employed for the ionic interactions. The potential parameters have been determined by trial and error using the experimental values of the variations in the lattice parameters with temperature and pressure. The simulated UO_2 system shows both the existence of the Bredig transition and a peak in the heat capacity at high temperatures, and provides the thermal conductivity in the temperature range from 360 K to 2500 K. The variation in the calculated heat capacity of PuO_2 with temperature agrees well with the experimental data. The change in the calculated thermal conductivity of PuO_2 with temperature is also in good agreement with the experimental data. This indicates that the simulation model of PuO_2 gives a reasonable description of the phonon contribution to the thermal conductivity. The Bredig transition does not occur in the simulated PuO_2 system. The thermal and mechanical properties of $(U,Pu)O_2$ have been evaluated from some basic properties of UO_2 and PuO_2 by using the MD techniques. The calculated lattice parameter of $(U_{0.8}Pu_{0.2})O_2$ closely follows Vegard's law. The calculated heat capacity and thermal conductivity of $(U_{0.8}Pu_{0.2})O_2$ are in good agreement with the experimental data. The simulated $(U_{0.8}Pu_{0.2})O_2$ cell also shows both the existence of the Bredig transition and a peak in the heat capacity at about 2350 K. The MD calculations have also been performed for the perovskite type oxides, $BaUO_3$, $BaZrO_3$, $BaCeO_3$, $BaMoO_3$, $SrZrO_3$, and $SrCeO_3$. The calculated linear thermal expansion coefficient and compressibility are almost identical with the experimental data. The calculated results of C_V+C_d are almost identical with the experimental C_P values, except for $BaUO_3$. The calculated C_V+C_d of $BaUO_3$ is slightly lower than the experimental C_P data, which is because that the calculated results do not contain other contributions such as the anharmonic contribution. The calculated thermal conductivities of $BaZrO_3$, $SrZrO_3$, and $SrCeO_3$ well agree with the experimental data, while those of $BaUO_3$ and $BaCeO_3$ are higher than the experimental data, and that of $BaMoO_3$ is lower than the experimental data. The difference between the calculated and experimental thermal conductivity of $BaMoO_3$ corresponds to the electronic contribution. These results show the usefulness of the MD techniques for evaluation of the thermal and mechanical properties of the oxide nuclear fuel. The MD simulations will become a powerful method to evaluate the properties of the oxide

fuel.

The thermodynamic modelling has been carried out for the O-Pu-U system. The possible ternary phase diagrams for the O-Pu-U system have been calculated. For the O-Pu, O-U, and Pu-U binary systems, the assessed thermodynamic parameters are reasonable to simulate the general feature of the O-Pu, O-U, and Pu-U binary systems, with respect to the phase diagrams and oxygen potentials of the $UO_{2\pm x}$ and PuO_{2-x} phases. For the stoichiometric PuO_2-UO_2 pseudo binary system in which PuO_2 and UO_2 are assumed to form an ideal solid solution, the calculation for the heat capacity and phase diagram provides very good agreements with the experimental data available in literatures. For the non-stoichiometric fluorite structure phase, the thermodynamic modelling has been demonstrated firstly assuming that all the additional interaction parameters for the fluorite structure phase are 0 (the ideal mixture of the data for the O-Pu, O-U, and Pu-U binary systems). The results suggest that the data for O-Pu, O-U, and Pu-U binary systems cannot be mixed ideally to model the non-stoichiometric fluorite structure phase. The interaction parameters have been assessed, and the oxygen potential of $(U,Pu)O_{2\pm x}$ calculated from the assessed parameters shows very good agreement with the experimental ones both in hyper- and hypo-stoichiometric regions. Using the assessed interaction parameters, the ternary phase diagram for the O-Pu-U system has been calculated. The calculated phase diagram reproduces the general feature of the ternary phase diagram well at 773 K and 1273 K.

The thermal and mechanical properties modeling of the high burnup oxide fuels with the oxide and metallic inclusions have been performed by using the finite elements method (FEM). The quantitative discussion about the effect of the oxide and metallic inclusions on the thermal conductivity and Young's modulus of the fuel has been performed. For the thermal conductivity modeling, $(U_{0.8}Pu_{0.2})O_2$ and $(M_{0.94}Nd_{0.06})O_2$ (M: $U_{0.8}Pu_{0.2}$) have been employed as the fuel matrix, and $BaUO_3$ and Mo-Ru-Rh-Pd alloy as the inclusions. In $BaUO_3$ dispersing case, about 1-3 % decreasing is observed in the thermal conductivity of the system, while in Mo-Ru-Rh-Pd alloy dispersing case, about 2-8 % increasing is observed. It is found that the effect of the precipitated FP elements is about one order lower than that of the dissolved FP elements on the thermal conductivity of the fuel. For the Young's modulus modeling case, $(U_{0.9}Ce_{0.2})O_2$ and $BaUO_3$ have been employed as the fuel matrix and oxide inclusion, respectively. It is found that the effect of the oxide inclusion on the Young's modulus of the high burnup oxide fuel is vanishingly small (within 1 % per 25 vol.% of the oxide inclusions), and quite lower than that of the dissolved FP elements.

Acknowledgment

I would like to express my greatest appreciation to Prof. Dr. Shinsuke Yamanaka for his suggestion and encouragement. I would like to express my appreciation to Prof. Dr. Shigehiro Nishijima, Assoc. Prof. Dr. Takao Yamamoto, and Assoc. Prof. Dr. Masayoshi Uno for their valuable comments. I would like to express my appreciation to Assist. Prof. Mr. Hiroaki Muta, Res. Assoc. Dr. Ayami Miura, Res. Assoc. Miss Atsuko Kosuga, and Miss Kazuko Terasoma for their kind support. I would like to express my appreciation to Dr. Tetsushi Matsuda (Nuclear Fuel Industries, Ltd.) and Dr. Isamu Sato (Japan Nuclear Cycle Development Institute) for their comments. I would like to grateful to all members of the Yamanaka Laboratory, especially Dr. Kazuhiro Yamada, Dr. Hajime Kinoshita, Mr. Kimihiko Yano, Mr. Ryo Ohshima, Mr. Shinji Yoshida, Mr. Taku Oyama, Mr. Yoshiyuki Saito, Miss Sumiko Masuo, and Mr. Mitsuhiro Imamura for their assistance. I would like to thank my family for their encouragement.

Research Achievements

List of Publications

Relevant Papers

1. Evaluation of Thermal Properties of Mixed Oxide Fuel by Molecular Dynamics
   Kazuhiro Yamada, Ken Kurosaki, Masayoshi Uno, and Shinsuke Yamanaka
   Journal of Alloys and Compounds, Vol. 307, pp. 1-9, (2000).

2. Evaluation of Thermal Properties of Uranium Dioxide by Molecular Dynamics
   Kazuhiro Yamada, Ken Kurosaki, Masayoshi Uno, and Shinsuke Yamanaka
   Journal of Alloys and Compounds, Vol. 307, pp. 10-16, (2000).

3. Thermoelectric properties of $BaUO_3$
   Ken Kurosaki, Tetsushi Matsuda, Masayoshi Uno, Shin-ichi Kobayashi, and Shinsuke Yamanaka
   Journal of Alloys and Compounds, Vol. 319, pp. 271-275, (2001).

4. Thermophysical properties of $BaUO_3$
   Shinsuke Yamanaka, Ken Kurosaki, Tetsushi Matsuda and Masayoshi Uno
   Journal of Nuclear Materials, Vol. 294, pp. 99-103, (2001).

5. Molecular dynamics study of mixed oxide fuel
   Ken Kurosaki, Kazuhiro Yamada, Masayoshi Uno, Shinsuke Yamanaka, Kazuya Yamamoto, and Takashi Namekawa
   Journal of Nuclear Materials, Vol. 294, pp. 160-167, (2001).

6. Thermal conductivity of $(U,Ce)O_2$ with and without Nd or Zr
   Ken Kurosaki, Ryo Ohshima, Masayoshi Uno, Shinsuke Yamanaka, Kazuya Yamamoto, and Takashi Namekawa
   Journal of Nuclear Materials, Vol. 294, pp. 193-197, (2001).

7. Heat capacity measurement of $BaUO_3$
   Tetsushi Matsuda, Shinsuke Yamanaka, Ken Kurosaki, Masayoshi Uno, and Shin-ichi Kobayashi
   Journal of Alloys and Compounds, Vol. 322, pp. 77-81, (2001).

8. Mechanical properties of $(U,Ce)O_2$ with and without Nd or Zr
Shinsuke Yamanaka, Shinji Yoshida, Ken Kurosaki, Masayoshi Uno, Kazuya Yamamoto, and Takashi Namekawa
Journal of Alloys and Compounds, Vol. 327, pp. 281-284, (2001).

9. Thermo-chemical and -physical properties of $BaMO_3$
Shinsuke Yamanaka, Tetsushi Matsuda, Ken Kurosaki, and Masayoshi Uno
Journal of Nuclear Science and Technology, Supplement 3, Nov., pp. 709-712, (2002).

10. Electronic states of $BaUO_3$
Yoshiyuki Kawaharada, Hirokazu Kobayashi, Ken Kurosaki, Masayoshi Uno, Shinsuke Yamanaka, and Hirohide Nakamatsu
Journal of Nuclear Science and Technology, Supplement 3, Nov., pp. 784-786, (2002).

11. Phase equilibria in the $BaUO_3$-$BaZrO_3$-$BaMoO_3$ system
Ken Kurosaki, Shinsuke Yamanaka, Tetsushi Matsuda, and Masayoshi Uno
Journal of Nuclear Science and Technology, Supplement 3, Nov., pp. 807-810, (2002).

12. Thermal conductivities of uranium intermetallic compounds
Ken Kurosaki, Hirokazu Kobayashi, Masayoshi Uno, and Shinsuke Yamanaka
Journal of Nuclear Science and Technology, Supplement 3, Nov., pp. 811-814, (2002).

13. A molecular dynamics study on $BaUO_3$
Ken Kurosaki, Taku Oyama, Tetsushi Matsuda, Masayoshi Uno, and Shinsuke Yamanaka
Journal of Nuclear Science and Technology, Supplement 3, Nov., pp. 815-818, (2002).

14. Heat capacities of $BaMO_3$
Tetsushi Matsuda, Shinsuke Yamanaka, Ken Kurosaki, Shin-ichi Kobayashi, and Masayoshi Uno
Journal of Nuclear Science and Technology, Supplement 3, Nov., pp. 823-826, (2002).

15. Thermal conductivity modeling of high burnup MOX fuel
Shinsuke Yamanaka, Sumiko Masuo, Ken Kurosaki, and Masayoshi Uno
Journal of Nuclear Science and Technology, Supplement 3, Nov., pp. 862-865, (2002).

16. High temperature phase transitions of $SrZrO_3$

Tetsushi Matsuda, Shinsuke Yamanaka, Shin-ichi Kobayashi, and Ken Kurosaki
Journal of Alloys and Compounds, Vol. 351, pp. 43-46, (2003).

17. Thermal properties of $SrCeO_3$
Shinsuke Yamanaka, Tetsushi Matsuda, Shin-ichi Kobayashi, and Ken Kurosaki
Journal of Alloys and Compounds, Vol. 352, pp. 52-56, (2003).

18. Thermophysical properties of Mo-Ru-Rh-Pd alloys
Shinsuke Yamanaka, and Ken Kurosaki
Journal of Alloys and Compounds, Vol. 353, pp. 269-273, (2003).

19. Thermodynamic modelling and phase stability assessment of MO_{2-X} oxides with a fluorite structure
Hajime Kinoshita, Daigo Setoyama, Yoshiyuki Saito, Masayuki Hirota, Ken Kurosaki, Masayoshi Uno, and Shinsuke Yamanaka
The Journal of Chemical Thermodynamics, Vol. 35, pp. 719-731, (2003).

20. Heat capacities and thermal conductivities of perovskite type $BaZrO_3$ and $BaCeO_3$
Shinsuke Yamanaka, Tsuyoshi Hamaguchi, Taku Oyama, Tetsushi Matsuda, Shin-ichi Kobayashi, and Ken Kurosaki
Journal of Alloys and Compounds, Vol. 359, pp. 1-4, (2003).

21. Thermophysical properties of $BaZrO_3$ and $BaCeO_3$
Shinsuke Yamanaka, Masaki Fujikane, Tsuyoshi Hamaguchi, Hiroaki Muta, Taku Oyama, Tetsushi Matsuda, Shin-ichi Kobayashi, and Ken Kurosaki
Journal of Alloys and Compounds, Vol. 359, pp. 109-113, (2003).

22. SPM によるナノ領域の機械特性評価
山中伸介，黒崎　健
日本セラミックス協会誌，(印刷中)．

23. Nanoindentation studies of UO_2 and $(U,Ce)O_2$ solid solutions
Ken Kurosaki, Yoshiyuki Saito, Hiroaki Muta, Masayoshi Uno, and Shinsuke Yamanaka
Journal of Nuclear Materials, submitted, (July 10, 2003).

24. Phase Relation Assessment for O-Pu-U Ternary System

Shinsuke Yamanaka, Hajime Kinoshita, and Ken Kurosaki
Journal of Nuclear Materials, submitted, (July 12, 2003).

25. Thermophysical properties of perovskite type strontium cerate and zirconate
Shinsuke Yamanaka, Ken Kurosaki, Taku Oyama, Hiroaki Muta, Masayoshi Uno, Tetsushi Matsuda, and Shin-ichi Kobayashi
Journal of the American Ceramic Society, submitted, (August 4, 2003).

26. Molecular dynamics studies of perovskite type strontium cerate and zirconate
Ken Kurosaki, Shinsuke Yamanaka, Taku Oyama, Hiroaki Muta, Masayoshi Uno, Tetsushi Matsuda, and Shin-ichi Kobayashi
Journal of the American Ceramic Society, submitted, (August 4, 2003).

27. Thermoelectric properties of perovskite type barium molybdate
Ken Kurosaki, Taku Oyama, Hiroaki Muta, Masayoshi Uno, and Shinsuke Yamanaka
Journal of Alloys and Compounds, to be submitted.

28. Preparation and phase equilibria of simulated high burnup UO_2 based fuel
Ken Kurosaki, Yoshiyuki Saito, Hiroaki Muta, Yoshiaki Ishii, Masayoshi Uno, and Shinsuke Yamanaka
Journal of Nuclear Materials, to be submitted.

29. Thermal properties of simulated high burnup UO_2 based fuel
Ken Kurosaki, Yoshiyuki Saito, Hiroaki Muta, Yoshiaki Ishii, Masayoshi Uno, and Shinsuke Yamanaka
Journal of Nuclear Materials, to be submitted.

30. Mechanical properties of simulated high burnup UO_2 based fuel
Ken Kurosaki, Yoshiyuki Saito, Hiroaki Muta, Yoshiaki Ishii, Masayoshi Uno, and Shinsuke Yamanaka
Journal of Nuclear Materials, to be submitted.

31. Nanoindentation studies of simulated high burnup UO_2 based fuel
Ken Kurosaki, Yoshiyuki Saito, Hiroaki Muta, Masayoshi Uno, and Shinsuke Yamanaka
Journal of Nuclear Materials, to be submitted.

32. Thermophysical properties of barium series perovskite type oxides
Shinsuke Yamanaka, Ken Kurosaki, Taku Oyama, Hiroaki Muta, Masayoshi Uno, Tetsushi Matsuda, and Shin-ichi Kobayashi
Journal of the American Ceramic Society, to be submitted.

33. Molecular dynamics studies of barium series perovskite type oxides
Ken Kurosaki, Shinsuke Yamanaka, Taku Oyama, Hiroaki Muta, Masayoshi Uno, Tetsushi Matsuda, and Shin-ichi Kobayashi
Journal of the American Ceramic Society, to be submitted.

Other Papers

1. Reactions of Uranium Nitride with Platinum-Family Metals
Masayoshi Uno, Ken Kurosaki, and Akira Nakamura
Journal of Nuclear Materials, Vol. 247, pp. 322-327, (1997).

2. Phase Equilibria in the Ternary URu_3-URh_3-UPd_3 System
Ken Kurosaki and Masayoshi Uno
Journal of Alloys and Compounds, Vol. 271-273, pp. 641-644, (1998).

3. Formation of the Cu_3Au Type Solid Solution of UPd_3 by Doping a Small Amount of URu_3
Ken Kurosaki and Masayoshi Uno
Journal of Alloys and Compounds, Vol. 274, pp. 222-228, (1998).

4. A Molecular Dynamics Study on the Heat Capacity of Uranium Mononitride
Ken Kurosaki, Kimihiko Yano, Kazuhiro Yamada, Masayoshi Uno, and Shinsuke Yamanaka
Journal of Alloys and Compounds, Vol. 297, pp. 1-4, (2000).

5. A Molecular Dynamics Study on the Thermal Conductivity of Uranium Mononitride
Ken Kurosaki, Kimihiko Yano, Kazuhiro Yamada, Masayoshi Uno, and Shinsuke Yamanaka
Journal of Alloys and Compounds, Vol. 311, pp. 305-310, (2000).

6. A Molecular Dynamics Study on Plutonium Mononitride
Ken Kurosaki, Kimihiko Yano, Kazuhiro Yamada, Masayoshi Uno, and Shinsuke Yamanaka
Journal of Alloys and Compounds, Vol. 313, pp. 242-247, (2000).

7. Thermoelectric properties of $CoSb_3$
Yoshiyuki Kawaharada, Ken Kurosaki, Masayoshi Uno, and Shinsuke Yamanaka
Journal of Alloys and Compounds, Vol. 315, pp. 193-197, (2001).

8. Thermoelectric properties of $NaCo_2O_4$
Ken Kurosaki, Hiroaki Muta, Masayoshi Uno, and Shinsuke Yamanaka
Journal of Alloys and Compounds, Vol. 315, pp. 234-236, (2001).

9. Re-evaluation of the phase relationship between plutonium and zirconium dioxides
H. Serizawa, K. Nakajima, Yasuo Arai, T. Yamashita, Ken-ichi Kuramoto, Hajime Kinoshita, Shinsuke Yamanaka, Masayoshi Uno, and Ken Kurosaki
Progress in Nuclear Energy, Vol. 38, pp. 237-240, (2001).

10. A molecular dynamics study on uranium-plutonium mixed nitride
Ken Kurosaki, Kimihiko Yano, Kazuhiro Yamada, Masayoshi Uno, and Shinsuke Yamanaka
Journal of Alloys and Compounds, Vol. 319, pp. 253-257, (2001).

11. Thermal properties of zirconium hydride
Shinsuke Yamanaka, Kazuhiro Yamada, Ken Kurosaki, Masayoshi Uno, Kiyoko Takeda, Hiroaki Anada, Tetsushi Matsuda, and Shin-ichi Kobayashi
Journal of Nuclear Materials, Vol. 294, pp. 94-98, (2001).

12. Some properties of a lead vanado-iodoapatite $Pb_{10}(VO_4)_6I_2$
Masayoshi Uno, Makoto Shinohara, Ken Kurosaki, and Shinsuke Yamanaka
Journal of Nuclear Materials, Vol. 294, pp. 119-122, (2001).

13. Thermal properties of Mo_3Te_4
Ken Kurosaki, Atsuko Kosuga, Masayoshi Uno, and Shinsuke Yamanaka,
Journal of Nuclear Materials, Vol. 294, pp. 179-182, (2001).

14. Characteristics of zirconium hydride and deuteride
Shinsuke Yamanaka, Kazuhiro Yamada, Ken Kurosaki, Masayoshi Uno, Kiyoko Takeda, Hiroyuki Anada, Tetsushi Matsuda, and Shin-ichi Kobayashi
Journal of Alloys and Compounds, Vol. 330-332, pp. 99-104, (2002).

15. Electronic states of hydrogen in zirconium oxide
Takanori Nishizaki, Mihoko Okui, Ken Kurosaki, Masayoshi Uno, Shinsuke Yamanaka, Kiyoko Takeda, and Hiroyuki Anada
Journal of Alloys and Compounds, Vol. 330-332, pp. 307-312, (2002).

16. Analysis of the electronic structure of zirconium hydride
Shinsuke Yamanaka, Kazuhiro Yamada, Ken Kurosaki, Masayoshi Uno, Kiyoko Takeda, Hiroyuki Anada, Tetsushi Matsuda, and Shin-ichi Kobayashi
Journal of Alloys and Compounds, Vol. 330-332, pp. 313-317, (2002).

17. Photoelectrochemical study of hydrogen in zirconium oxide
Mihoko Okui, Takanori Nishizaki, Masayoshi Uno, Ken Kurosaki, Shinsuke Yamanaka, Kiyoko Takeda, and Hiroyuki Anada
Journal of Alloys and Compounds, Vol. 330-332, pp. 645-648, (2002).

18. Thermoelectric properties of Mo_3Te_4
Ken Kurosaki, Atsuko Kosuga, Masayoshi Uno, and Shinsuke Yamanaka
Journal of Alloys and Compounds, Vol. 334, pp 317-323, (2002).

19. Thermoelectric properties of Ti- and Sn-doped α-Fe_2O_3
Hiroaki Muta, Ken Kurosaki, Masayoshi Uno, and Shinsuke Yamanaka
Journal of Alloys and Compounds, Vol. 335, pp 200-202, (2002).

20. Hydrogen solubility in uranium intermetallic compounds with Fe_2P type structure
Shinsuke Yamanaka, Takehiro Maruyama, Ken Kurosaki, and Masayoshi Uno
Journal of Nuclear Science and Technology, Supplement 3, Nov., pp. 642-644, (2002).

21. Physico-chemical properties of Fe_2P-type uranium intermetallic compounds
Shinsuke Yamanaka, Masayoshi Uno, T. Tsuzuki, Ken Kurosaki, Yasushi Hoshino, and Wataru Saiki
Journal of Nuclear Science and Technology, Supplement 3, Nov., pp. 645-648, (2002).

22. High temperature thermoelectric properties of $(Fe_{1-x}V_x)_3Al$ Heusler type compounds
Yoshiyuki Kawaharada, Ken Kurosaki, and Shinsuke Yamanaka
Journal of Alloys and Compounds, Vol. 349, pp. 37-40, (2003).

23. Thermophysical properties of layered rare earth copper oxides
Shinsuke Yamanaka, Hirokazu Kobayashi, and Ken Kurosaki
Journal of Alloys and Compounds, Vol. 349, pp. 269-272, (2003).

24. Thermoelectric properties of layered rare earth copper oxides
Shinsuke Yamanaka, Hirokazu Kobayashi, and Ken Kurosaki
Journal of Alloys and Compounds, Vol. 349, pp. 321-324, (2003).

25. Physical properties of $Mo_{6-x}Ru_xTe_8$ and $Mo_6Te_{8-x}S_x$
Shinsuke Yamanaka, Atsuko Kosuga, and Ken Kurosaki
Journal of Alloys and Compounds, Vol. 350, pp. 288-291, (2003).

26. Thermoelectric properties of rare earth doped $SrTiO_3$
Hiroaki Muta, Ken Kurosaki, and Shinsuke Yamanaka
Journal of Alloys and Compounds, Vol. 350, pp. 292-295, (2003).

27. Thermoelectric properties of Ni- and Zn-doped Nd_2CuO_4
Ken Kurosaki, Hirokazu Kobayashi, and Shinsuke Yamanaka
Journal of Alloys and Compounds, Vol. 350, pp. 340-343, (2003).

28. Thermophysical properties of Tl_9BiTe_6 and $TlBiTe_2$
Ken Kurosaki, Atsuko Kosuga, and Shinsuke Yamanaka
Journal of Alloys and Compounds, Vol. 351, pp. 14-17, (2003).

29. Thermoelectric properties of Chevrel phase $Mo_6Te_{8-x}S_x$
Ken Kurosaki, Atsuko Kosuga, and Shinsuke Yamanaka
Journal of Alloys and Compounds, Vol. 351, pp. 208-211, (2003).

30. Thermoelectric properties of $TlBiTe_2$
Ken Kurosaki, Atsuko Kosuga, and Shinsuke Yamanaka
Journal of Alloys and Compounds, Vol. 351, pp. 279-282, (2003).

31. Thermophysical properties of Fe_2VAl
Yoshiyuki Kawaharada, Ken Kurosaki, and Shinsuke Yamanaka
Journal of Alloys and Compounds, Vol. 352, pp. 48-51, (2003).

32. Thermoelectric properties of Tl_9BiTe_6
Shinsuke Yamanaka, Atsuko Kosuga, and Ken Kurosaki
Journal of Alloys and Compounds, Vol. 352, pp. 275-278, (2003).

33. Thermoelectric properties of Fe-V-Si Heusler type compounds
Yoshiyuki Kawaharada, Hironori Uneda, Ken Kurosaki, and Shinsuke Yamanaka
Journal of Alloys and Compounds, Vol. 359, pp. 216-220, (2003).

34. Thermoelectric properties of constantan/spherical SiO_2 and Al_2O_3 particles composite
Hiroaki Muta, Ken Kurosaki, Masayoshi Uno, and Shinsuke Yamanaka
Journal of Alloys and Compounds, in press.

35. Nanoindentation of Zirconium oxide films prepared at near a/b transformation temperature
Mihoko Okui, Masayoshi Uno, Ken Kurosaki, and Shinsuke Yamanaka
Journal of Alloys and Compounds, accepted for publication.

36. High temperature thermoelectric properties of NiZrSn Half-Heusler compounds
Yoshiyuki Kawaharada, Hironori Uneda, Hiroaki Muta, Ken Kurosaki, and Shinsuke Yamanaka
Journal of Alloys and Compounds, accepted for publication.

37. Thermoelectric properties of doped $BaTiO_3$-$SrTiO_3$ solid solution
Hiroaki Muta, Yoshiyuki Kawaharada, Ken Kurosaki, Masayoshi Uno, and Shinsuke Yamanaka
Journal of Alloys and Compounds, in press (JALCOM10258).

38. Thermoelectric properties of thallium antimony telluride
Ken Kurosaki, Hironori Uneda, Hiroaki Muta, and Shinsuke Yamanaka
Solid State Communications, submitted, (July 10, 2003).

Bulletins and Reports

1. Phase Equilibria in the Ternary U-Me-N (Me:Ru, Rh, Pd) System
Masayoshi Uno and Ken Kurosaki
Technology Reports of the Osaka University, Vol. 47, No. 2289, pp. 187-194, (1997).

2. Chemical States of Fission Products in Irradiated Uranium- Plutonium Mixed Oxide Fuel
Ken Kurosaki, Masayoshi Uno and Shinsuke Yamanaka
Technology Reports of the Osaka University, Vol. 49, No. 2341, pp. 29-35, (1999).

3. Study on Hydrogen Diffusivity in Zirconium Oxide
Takanori Nishizaki, Shinsuke Yamanaka, Ken Kurosaki, K Tateishi and Masayoshi Uno
Technology Reports of the Osaka University, Vol. 49, No. 2352, pp. 119-125, (1999).

4. Physico-Chemical Properties of $BaUO_3$
Shinsuke Yamanaka, Masayoshi Uno, Ken Kurosaki, Kazuhiro Yamada, and Hajime Kinoshita
KURRI Progress Report 1999, Published by The Research Reactor Institute, Kyoto University, pp. 192, (2000).

5. Crystal Structure and Physicochemical Properties of Actinide Complex Oxides
Shinsuke Yamanaka, Masayoshi Uno, and Ken Kurosaki,
KURRI Progress Report 2000, Published by The Research Reactor Institute, Kyoto University, pp. 178, (2001).

6. Phonon Glass Characteristics of Perovskite Type Uranium Oxides
Shinsuke Yamanaka, Masayoshi Uno, and Ken Kurosaki,
KURRI Progress Report 2001, Published by The Research Reactor Institute, Kyoto University, pp. 184, (2002).

7. Hiroshi Horiike, Akihiro Suzuki, and Ken Kurosaki, "Measurement of Stainless Steel Erosion/Corrosion in a Lithium Loop, JAERI-Tech, 2003-005, pp. 218-222, March 2003.

8. Phonon Glass Characteristics of Perovskite Type Uranium Oxides
Shinsuke Yamanaka, Masayoshi Uno, and Ken Kurosaki,
KURRI Progress Report 2002, Published by The Research Reactor Institute, Kyoto University, in press.

List of Presentations

International Conference and Symposium

1. Reactions Between Uranium Nitrides and Platinum Family Metals
   9th Symposium on Thermodynamics of Nuclear Materials (STNM-9) in 14th IUPAC CONFERENCE ON CHEMICAL THERMODYNAMICS (ICCT-96), Osaka, Japan, August 25-30, 1996.

2. Reactions of Uranium Nitride with Platinum-Family Metals in the Pseudo-Ternary System
   Actinides '97, Kongresshaus Baden-Baden, Baden-Baden, Germany, September 21-26, 1997.

3. Molecular dynamics study on mixed oxide fuel
   10th Symposium on Thermodynamics of Nuclear Materials (STNM-10) in 16th IUPAC CONFERENCE ON CHEMICAL THERMODYNAMICS (ICCT2000), Dalhousie University, Halifax, Canada, August 6-11, 2000.

4. Phase equilibria in the $BaUO_3$-$BaZrO_3$-$BaMoO_3$ system
   Actinides 2001, Hayama, Japan, November 4-9, 2001.

5. Heat capacities of Tl_9BiTe_6 and $TlBiTe_2$
   17th IUPAC CONFERENCE ON CHEMICAL THERMODYNAMICS (ICCT2002), University of Rostock, Rostock, Germany, July 28-August 02, 2002.

6. Fabrication of Oxide Nanohole Array and its Application
   International Symposium on 21st Century COE Program, Osaka University, Osaka, Japan, March 11-12, 2003.

7. Fabrication of Oxide Nanohole Array and its Application
   International Symposium on Nanotechnology and Materials for the Environment, Pacifico Yokohama, Yokohama, Japan, March 26-27, 2003.

8. Nanoindentation Study of Oxide Nuclear Fuels
   105th Annual Meeting & Exposition of The American Ceramics Society, Gaylord Opryland, Nashville, Tennessee, USA, April 27-30, 2003.

9. Mechanical Properties of $SrZrO_3$ and $SrceO_3$
   The 5th International Meeting of Pacific Rim Ceramic Societies, Nagoya Congress Center,

Nagoya, Japan, September 29-October 2, 2003, accepted for presentation.

10. Molecular Dynamics Studies of Ba- and Sr-Series Perovskite type oxides
The 5th International Meeting of Pacific Rim Ceramic Societies, Nagoya Congress Center, Nagoya, Japan, September 29-October 2, 2003, accepted for presentation.

11. Thermoelectric Properties of Thallium Compounds
The 5th International Meeting of Pacific Rim Ceramic Societies, Nagoya Congress Center, Nagoya, Japan, September 29-October 2, 2003, accepted for presentation.

12. Thermoelectric Properties of Ternary Thallium Compounds
2003 MRS Fall Meeting, Hynes Convention Center and Sheraton Boston Hotel, Boston, Massachusetts, USA, December 1-5, 2003, submitted.

13. Thermal Properties of Perovskite Type Strontium Oxides
28th International Cocoa Beach Conference and Exposition on Advanced Ceramics & Composites, Doubletree and Hilton Hotels, Cocoa Beach, Florida, USA, January 25-30, 2004, submitted.

14. Nanoindentation Studies of Oxide Single Crystals
28th International Cocoa Beach Conference and Exposition on Advanced Ceramics & Composites, Doubletree and Hilton Hotels, Cocoa Beach, Florida, USA, January 25-30, 2004, submitted.

Domestic Meeting

1. Reactions of uranium mononitride with platinum-family metals (2)
-Reaction between UN and Pd-
Fall Meeting of the Atomic Energy Society of Japan, Tohoku University, September 23-25, 1996, (K12).

2. Reactions of uranium mononitride with platinum-family metals (4)
-Reaction of UN with (Ru, Rh, Pd) in the pseudo-ternary and quaternary systems-
Fall Meeting of the Atomic Energy Society of Japan, Okinawa Convention Center, October 14-17, 1997, (I74).

3. Chemical states of FPs in uranium-plutonium mixed nitride fuels (I)
-Variation of chemical states of FPs with burnup-
Fall Meeting of the Atomic Energy Society of Japan, Fukui University of Technology, September 28-30, 1998, (I45).

4. Physico-chemical properties of perovskite type oxides (1)
Annual Meeting of the Atomic Energy Society of Japan, Ehime University, March 28-30, 2000, (J49).

5. Physico-chemical properties of perovskite type oxides (2)
-Thermoelectric properties of $BaUO_3$-
Fall Meeting of the Atomic Energy Society of Japan, Aomori University, September 15-17, 2000, (K15).

6. Physico-chemical properties of perovskite type oxides (6)
-Molecular dynamics studies on $BaUO_3$-
Annual Meeting of the Atomic Energy Society of Japan, Musashi Institute of Technology, March 27-29, 2001, (J50).

7. Physicochemical properties of high burnup MOX fuel (1)
-Chemical states of oxide precipitates in high burnup MOX fuel-
Fall Meeting of the Atomic Energy Society of Japan, Hokkaido University, September 19-21, 2001, (K24).

8. Nanoscale properties of nuclear materials
-Nanoindentations and SPM studies of UO_2-
Annual Meeting of the Atomic Energy Society of Japan, Kobe University of Mercantile Marine, March 27-29, 2002, (N27).

9. Development of LWR-MOX vibro-packed fuel (3)
-Thermal conductivity analysis-
Fall Meeting of the Atomic Energy Society of Japan, Iwaki Meisei University, September 14-16, 2002, (E6).

10. Thermoelectric properties of Chevrel phase Mo_3Te_4

The Japan Institute of Metals, Annual Fall Meeting, Osaka University, November 2-4, 2002, (141).

11. Thermoelectric properties of Tl-Bi-Te compounds
The Japan Institute of Metals, Annual Fall Meeting, Osaka University, November 2-4, 2002, (142).

12. Physical properties of perovskite type oxides 3
-Mechanical properties of Ba-based compounds-
Annual Meeting of The Ceramic Society of Japan, Tokyo Metropolitan University, March 22-24, 2003, (1J08).

13. Physical properties of perovskite type oxides 4
- Molecular dynamics studies of $BaUO_3$-
Annual Meeting of The Ceramic Society of Japan, Tokyo Metropolitan University, March 22-24, 2003, (1J10).

14. Thermoelectric properties of $TlSbTe_2$
The Japan Institute of Metals, Annual Spring Meeting, Chiba University, March 27-29, 2003, (658).

15. Thermochemical and Thermophysical Properties of Simulated High Burnup BWR Fuels (2)
-Preparation and Characteristics of the SIMFUEL-
Fall Meeting of the Atomic Energy Society of Japan, Shizuoka University, September 24-26, 2003, (accepted for presentation).

16. Thermoelectric properties of AgTlTe
The Japan Institute of Metals, Annual Spring Meeting, Hokkaido University, October 11-13, 2003, (accepted for presentation).

List of Award

1. Ando Incentive Prize for the Study of Electronics, "Fabrication of Oxide Nanohole Array and its Application", July 2003.

List of Patents

1. 発明の名称：酸化物ナノホールアレイ、およびその製造方法ならびにその用途
   特許出願人：財団法人大阪産業振興機構
   発明者　　：山中伸介、濱口豪、宇埜正美、黒崎健
   出願年月日：2002 年 12 月 21 日
   番号　　：特願 2002-383495

2. 発明の名称：基盤付酸化物ナノホールアレイ、およびその製造方法並びにその用途
   特許出願人：財団法人大阪産業振興機構
   発明者　　：山中伸介、濱口豪、宇埜正美、黒崎健、牟田浩明、釘宮公一
   出願年月日：2003 年 7 月 22 日
   番号　　：特願 2003-277714